RESPONSE PROPERTIES AND CRITICAL PHENOMENA OF DISORDERED MATERIALS

A Dissertation

Presented to the Faculty of the Graduate School

of Cornell University

in Partial Fulfillment of the Requirements for the Degree of

Doctor of Philosophy

by

Stephen Joseph Thornton

December 2025

RESPONSE PROPERTIES AND CRITICAL PHENOMENA OF DISORDERED MATERIALS

Stephen Joseph Thornton, Ph.D.

Cornell University 2025

There has been renewed interest in the response properties of disordered materials in recent years. Understanding the "jamming" of hard or soft particles, considered as a zero-temperature phase transition, has led to the development of new techniques in statistical physics. Related phase transitions that occur in disordered elastic networks may hold the key to understanding the highly tunable systems frequently seen in biology. To address these problems, we investigate the scaling properties and extract the universal predictions of a dynamical mean-field theory, the coherent potential approximation (CPA), that describes the phase behavior in inhomogeneous elastic systems quite well (Chapter 2). We make comparisons to measurements of charge density fluctuations in strange metals, which also show featureless response (Chapter 3). We follow up on these universal predictions from the CPA by showing the existence and origin of logarithmic corrections to scaling in two dimensions (Chapter 4). We also perform simulations of an anisotropically diluted version of the triangular lattice and analyze the non-mean-field behavior as a crossover between two distinct universality classes of rigidity transitions as isotropy is broken (Chapter 5). We extract universal scaling functions for Ising models using modern non-perturbative techniques (Chapter 6). Finally, we comment on the topological defects that are possible in the many nematic phases of bent-core liquid crystals (Chapter 7).

BIOGRAPHICAL SKETCH

Stephen J. Thornton was informed that he should write this section in the third-person voice, which he finds kind of funny. He attended Penn State for undergrad starting in 2015, and graduated in 2019 with a B.S. in Astronomy & Astrophysics, a B.S. in Mathematics, a B.S. in Physics, and an M.A. in Mathematics. For his M.A. work, he primarily focused on the singular behavior of certain PDEs. He then attended the Ph.D. program in Physics at Cornell University from 2019 to 2025 and focused on critical phenomena in disordered elastic systems.

He is not aware of any relation to the more famous Stephen T. Thornton (of *Classical Dynamics of Particles and Systems* fame). However, he is grateful to have a distinct middle initial.

This work is dedicated to my fiancée, Neti Bhatt, who made graduate school tolerable.

ACKNOWLEDGEMENTS

I would like to acknowledge the many people who made the past six years of my life interesting. As I was getting started with research, I frequently had very nice interactions with Jim Sethna, Danilo Liarte, Itai Cohen, Jaron Kent-Dobias, David Hathcock, and Debanjan Chowdhury. Debanjan's group in particular had many insightful comments on all of my projects, especially Felipe Mendez-Valderrama, Sunghoon Kim, Sridhar Prabhu, Xuepeng Wang, Zihao Qi, Seth Musser, Keiran Lewellen, and Rohit Mukherjee. I had many pleasant research conversations with the postdocs, especially Itay Griniasty and Jason Kim. Anna Barth, Japheth Omonira, Kaarthik Varma, Thomas Wyse Jackson, Navneet Singh, Sully Bailey-Darland, and Eric Dufresne provided me with brilliant, high-quality experiments, simulation data, and conversations. Collaborations with Bulbul Chakraborty, Moumita Das, and Eleni Katifori were very helpful in my early learning of principles of soft matter systems. Discussions with Leo Radzihovsky at the Boulder School were important in my understanding of liquid crystals and led to a very nice collaborative work. William Wang was a fantastic undergraduate and talented computer scientist, and I very much enjoyed our collaboration on anisotropic rigidity percolation.

One of the highlights of my experience was my development as an instructor. For this, I owe Phil Krasicky and Bert Fulbright (for introductory mechanics) and Jim Sethna (for grad stat mech) a great deal. I particularly enjoyed the opportunity to develop exam exercises for the statistical mechanics course. Meeting the first-year graduate students and learning about their research interests also helped motivate me in my own research.

For contributions to the intangible parts of my thesis, I must thank Lopa Bhatt and Raghav Chaturvedi, Pat Thornton, Chloe Thornton, and Sage Rose-

mary Thornton. For introducing me to gardening and cooking, and for generally making my life enjoyable, I owe a great debt to my fiancée Neti Bhatt.

TABLE OF CONTENTS

LIST OF TABLES

LIST OF FIGURES

CHAPTER 1

INTRODUCTION

I have placed a cutoff Λ that separates projects that I will write about from projects that I will not. Projects that live above Λ include: disorder in Heisenberg magnets with Landau-Lifshitz dynamics, coarsening in BKT models, applications of machine learning to discover energy functionals and predict temperature/discover hidden order, strain stiffening of fiber networks at large strains, continuous phase separation of biopolymers, and acoustic perturbations of shear thickening suspensions. For projects that live below Λ, see the Chapters below. As is typical, the projects that live above Λ contribute to my understanding of the projects below, but I have chosen to integrate them out.

Each chapter has at least two sections. The first sections are devoted to soft introductions, derivations of necessary formulas, or illustrative examples. The final section of each chapter is the reformatted full text of a manuscript that is either published or to be submitted. The appendices associated with each chapter are generally the appendices associated with the manuscript that is the final section of that chapter.

CHAPTER 2

UNIVERSAL SCALING FUNCTIONS FOR VISCOELASTIC MATTER FROM A DYNAMICAL MEAN-FIELD THEORY

2.1 The coherent potential approximation for random spring networks

We have been broadly interested in the response properties of disordered networks that undergo phase transitions from a rigid state to a floppy state. This is a phase transition that occurs at zero temperature. It is also a transition that is detected in the response properties of the network, rather than in the average configuration of the nodal (translational) degrees of freedom. Suppose we have an infinite set of nodes organized throughout space. The nodes could be arranged in a regular pattern or placed randomly with some finite density. Connect nodes with linear springs to all neighbors that are a distance at most R away. If enough connections are formed throughout the network, we imagine that the network would have a linear elastic regime: for any infinitesimal strain ϵ, the network will relax to produce an elastic energy $C\epsilon^2/2$.

We now imagine that we start removing bonds at random. At (ordinary) percolation, the network falls apart (there is no connected component that can span edge-to-edge in the infinite system). Here, the network is floppy, since there is no connected set of bonds that can transmit stress. However, long before we disconnect the network, the lattice is already floppy in general. Most of the bonds in the tenuously connected random network do not contribute to transmitting loads for any given applied strain. Tracking the rigid component

of the network, there is a location in phase space where the rigid component is first severed by removing an important bond, so that *stress* cannot propagate from edge-to-edge in the infinite system. This point is called *rigidity percolation*, and it has been the subject of some intense study over the years [1, 2, 3, 4, 5, 6, 7, 8, 9]. One typical model is the aforementioned bond dilution model: we have a Hamiltonian H with quenched disorder

$$H = \frac{1}{2} \sum_{\langle ij \rangle} k_{ij} \left| \mathbf{u}_i - \mathbf{u}_j \right|^2, \quad k_{ij} \sim p\ \delta\left(k_{ij} - k\right) + (1-p)\ \delta\left(k_{ij}\right). \tag{2.1}$$

The Latin characters i, j label the nodes in the network. The sum is performed over the set $\langle ij \rangle$ of pairs of connected nodes in the network with all bonds (often, nearest neighbors). The vectors $\mathbf{u}_i$ are the positions of the nodes in d dimensions. The stiffness of the spring connecting i to j is k_{ij}, which is a random variable. k_{ij} is drawn from some distribution; for a typical bond dilution model each $k_{ij} = k$ with probability p and $k_{ij} = 0$ with probability $1-p$; the bonds are independently randomly placed. The properties of the model are investigated as a function of p, the parameter in the probability distribution for k_{ij} that controls the average number of connections.

To determine average response properties of the network, one draws samples from the distribution of quenched disorder in the Hamiltonian and then computes the average physical quantity over the drawn Hamiltonian samples. One can compute average moduli, average dynamical Green's functions, average higher-order correlations, etc. Because this model has a phase transition in its response at some value $0 < p < 1$ for a typical rigid network, the average response properties will show interesting singularities and lend themselves well to being described using the usual language of critical phenomena: critical exponents, scaling functions, etc.

Interestingly, this model has Newtonian equations of motion that describe its dynamics unambiguously. Depending on whether the network is submerged in molasses (giving viscous damping), or whether the springs contribute damping when nodes are forced together quickly (giving a Galilean-invariant damping), or whether the network is undamped, one can deterministically compute the dynamics of the nodes for a given disorder realization under arbitrary forces, and so one can compute average Green's functions without additional input. This leads directly, near the phase transition, to estimates of dynamical critical exponents z. In thermodynamically controlled critical phenomena, like the Ising model, one has no dynamical laws a priori. The theory of dynamical critical phenomena [10] in these cases usually proceeds by assuming one approaches equilibrium through some overdamped process that depends upon gradients of the free energy with respect to the order parameter. One then imposes conservation laws, and finds different dynamical critical exponents depending upon which conservation laws are imposed, leading to the well-known Models A-J.[1]

We will study one class of these bond dilution models numerically in Chapter 5. We can start by making some estimates of properties of the model by using an interesting mean-field theory. Let us start with a regular lattice, described by a dynamical matrix D_{ij}. We are going to estimate the average response properties of the lattice by replacing the random springs with a new spring k_{EM} which best captures the response properties of the diluted network. Clearly, $k_{\mathrm{EM}} \leq k$: as we dilute the network, the effective value of the connecting springs is reduced so that the effective network is less stiff. This kind of replacement is usually called an *effective medium theory*, since the disordered medium is replaced by a homogeneous effective medium. We will proceed to find the optimal value of

[1]Some of these letters don't have models since some sets of conservation laws were shown to have the same universal features.

k_{EM} by requiring the effective medium flex in a similar way under an imposed load as the average flex of the random network. The procedure described below closely follows the technique discussed in [1].

First, consider the effective medium network with all bonds equal in strength to k_{EM}. Single out a pair of nodes that are connected (I will call this pair $\langle 12 \rangle$). Now apply a uniform bulk stress to the network (for instance, a dilational stress). The nodes move outward from their equilibrium positions. In particular, the bond associated with $\langle 12 \rangle$ extends by a distance δu_m.

Next, we replace the bond connecting $\langle 12 \rangle$ with a single "wrong bond" k_{ij} of arbitrary strength (eventually, this bond will be averaged over the distribution of bond disorder that we would like to investigate). We simultaneously apply a force f to the two nodes to keep the lattice in its original position under the uniform stress. We have that

$$f + \delta u_m k_{\mathrm{EM}} = \delta u_m k_{ij} \implies f = \delta u_m \left(k_{ij} - k_{\mathrm{EM}} \right) \tag{2.2}$$

since we have force balance after this procedure. This entire process is illustrated in Figure 2.1.

We would like to understand how the lattice flexes under the insertion of a single wrong bond. We will do this using a superposition principle.

Case 1: if we take the unstressed lattice with the bond connecting $\langle 12 \rangle$ replaced by k_{ij}, and apply the force f to the two nodes, the lattice will flex, and the nodes will move apart by some amount δu. If we were to apply the uniform stress to the rest of the lattice, the nodes $\langle 12 \rangle$ will move apart all the way to δu_m by definition of f.

Case 2: if one takes the complete effective medium lattice under the uniform

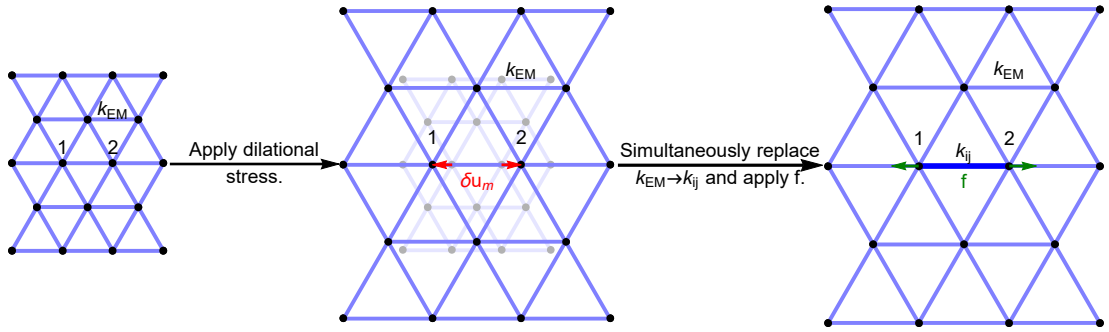

Figure 2.1: We take the effective medium lattice (shown as triangular) and place it under a dilational stress, leading nodes 1 and 2 to separate by δu_m. Next, we replace the bond between nodes 1 and 2 with the bond k_{ij} and simultaneously apply a force f so that none of the nodes move. The relationship between f, δu_m, k_{EM}, and k_{ij} is given by Equation 2.2.

stress and replaces the bond connecting $\langle 12 \rangle$ with the bond k_{ij} *without* applying any other forces, the lattice flexes by δu. This is because applying f across the bond k_{ij} causes a further displacement δu by the definition of δu given in Case 1 and superposition. These steps are shown in Figure 2.2.

Using the mental picture given by Case 2, δu is the "fluctuation" in the relative displacement between the nodes that is due to the introduction of a single "wrong bond" k_{ij}. However, we can compute the relationship between f and δu using the mental picture given by Case 1. The mean-field-like expression will be closed by requiring that $\langle \delta u \rangle = 0$, giving an equation for the k_{EM}. This is the statement that, under an arbitrary load, replacement of any spring in the effective medium by a random spring drawn from the disorder distribution will *on average* not flex the network. This means that the flex of the effective medium network is doing a good job of approximating the flex of a network with a random collection of springs. However, it is still an approximation in that we only replace a single link with a random bond. Higher-cluster computations have been performed by others [11]. This approximation is equivalent to the *coherent*

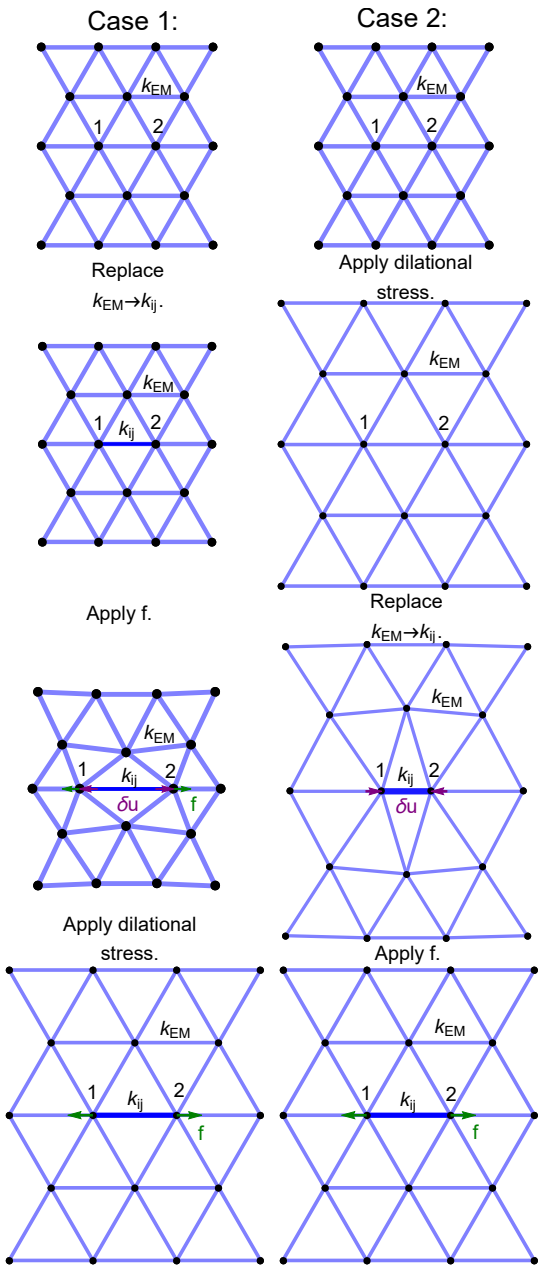

Figure 2.2: Two orderings of replacing a bond, applying f, and applying the dilational stress. By a superposition argument, the lattice flex δu is identical in each case. Case 2 argues that $\langle \delta u \rangle = 0$ is a good condition to use to set the value of k_{EM}. Case 1 gives a method to compute the relationship between f and δu. Illustrated here is the situation where $k_{ij} > k_{\text{EM}}$.

potential approximation, which is used to treat impurity scattering in other problems with quenched disorder in the Hamiltonian and can be placed on firmer diagrammatic foundations. It represents a resummation of an infinite subclass of diagrams with impurity scattering lines which do not cross (called the non-crossing approximation) [11, 12]. It can also be viewed as the saddle point of a nonlinear sigma model coming from a replica field theory for heterogeneous elasticity [13]. In this latter setup, renormalization of the theory can be achieved to investigate classical wave localization near two dimensions for infinitesimal disorder, which is a different transition that occurs in these systems.

We need to close our set of mean-field equations. To relate f to δu, we start with the unstressed effective medium lattice with the bond connecting $\langle 12 \rangle$ replaced with k_{ij}. Upon applying f across the nodes $\langle 12 \rangle$, we can imagine the forces that arise from the flex to balance f coming from two places: first, there is a force that comes from a lattice which is entirely regular and comprised of springs of strength k_{EM}. The effective stiffness of this is k_{EM}/a^*, where a^* has to do with the geometry of connections in the unit cell, but the effective spring is proportional to the only microscopic stiffness k_{EM}. We will compute a^* exactly later. Second, there is a correction from removing one of the springs k_{EM} and adding a spring k_{ij}. This can be thought of as adding another spring, connected in parallel with the first, with strength $k_{ij} - k_{\mathrm{EM}}$. Hence, the effective stiffness is $k_{\mathrm{EM}}/a^* + k_{ij} - k_{\mathrm{EM}}$. The philosophy behind this decomposition is shown in Figure 2.3.

Upon applying the force f, the nodes $\langle 12 \rangle$ move apart by δu. Hence,

$$f = \delta u \left(\frac{k_{\mathrm{EM}}}{a^*} + k_{ij} - k_{\mathrm{EM}} \right). \tag{2.3}$$

However, we also have an expression for f from Equation 2.2. Equating these

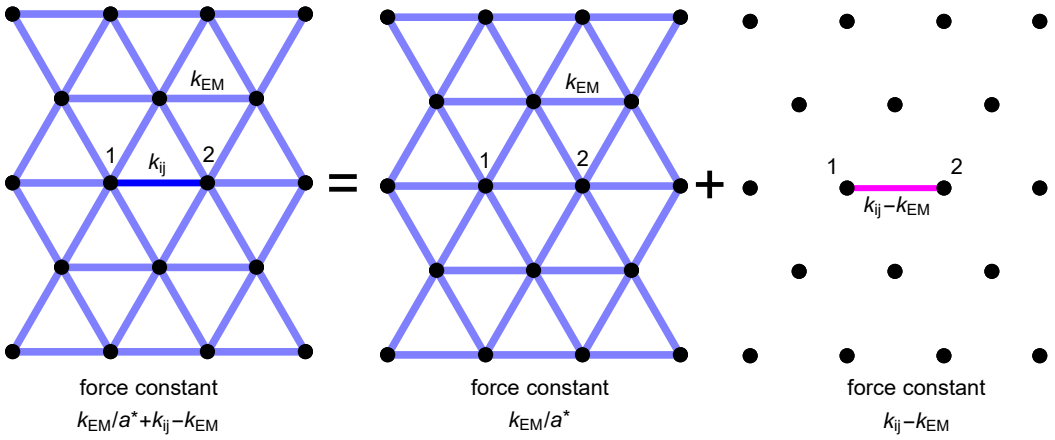

Figure 2.3: The decomposition of the lattice perturbed by a single bond into a regular lattice and a single bond. This decomposition makes it easier to compute a^* and hence to find the exact relationship between f and δu.

and solving for δu gives

$$\delta u = \delta u_m \frac{k_{ij} - k_{\text{EM}}}{k_{\text{EM}}/a^* + k_{ij} - k_{\text{EM}}}. \tag{2.4}$$

We now treat k_{ij} as a random variable, and set the average $\langle \delta u \rangle = 0$ as discussed above. The quantity δu_m depends upon the arbitrary load we placed on the original lattice but not on k_{ij}, and so it drops out of the expression. We end up with a closed set of equations for the k_{EM}:

$$\left\langle \frac{k_{ij} - k_{\text{EM}}}{k_{\text{EM}}/a^* + k_{ij} - k_{\text{EM}}} \right\rangle = 0. \tag{2.5}$$

Now we can compute a^* using the perfect lattice filled with k_{EM}. I will use superscripts to refer to node labels and subscripts to refer to indices of tensors (which when repeated, are contracted). The force on node i is

$$f_k^i = -\frac{\partial U}{\partial u_k^i} = -\sum_j D_{k\ell}^{ij} u_\ell^j \tag{2.6}$$

where the dynamical matrix $D_{k\ell}^{ij}$ is

$$D_{k\ell}^{ij} = \begin{cases} -k_{\text{EM}} \hat{r}_k^{ij} \hat{r}_\ell^{ij}, & i \neq j \\ k_{\text{EM}} \sum_{m \neq i} \hat{r}_k^{im} \hat{r}_\ell^{im}, & i = j \end{cases} \tag{2.7}$$

and $\hat{r}^{ij}$ is the unit vector pointing from node i to node j. We can use the Fourier transform to invert these equations, giving

$$\tilde{u}_k = -\tilde{D}^{-1}_{k\ell}\tilde{f}_\ell \tag{2.8}$$

where the $\sim$ variables are Fourier transforms of the real-space variables and are functions of the reciprocal space coordinates q_i. The dynamical matrix in Fourier space is

$$\tilde{D}_{k\ell} = \sum_{ij} D^{ij}_{k\ell} e^{iq_n\left(r^i_n - r^j_n\right)} = k_{\mathrm{EM}} \sum_{\hat{\delta}} \left(1 - e^{iaq_n\hat{\delta}_n}\right)\hat{\delta}_k\hat{\delta}_\ell \tag{2.9}$$

where $\hat{\delta}$ is a unit vector pointing in the direction of one of the connections in the unit cell and a is the nearest-neighbor separation. We now imagine putting a force across nodes 1 and 2 of arbitrary magnitude f_2. This corresponds to choosing a force acting on every node i of

$$f^i_k = f_2\hat{r}^{12}_k\left(\delta^{i1} - \delta^{i2}\right). \tag{2.10}$$

Now we can compute its Fourier transform:

$$\tilde{f}_k = \sum_i f^i_k e^{iq_n r^i_n} = f_2\hat{r}^{12}_k\left(e^{iq_n r^1_n} - e^{iq_n r^2_n}\right). \tag{2.11}$$

We know that nodes 1 and 2 will separate by some amount δu_2 along $\hat{r}^{12}$. We can compute this quantity in real space by undoing the Fourier transform and using the relationship between the displacements and forces in Fourier space:

$$\begin{aligned}
u^2_i - u^1_i &= \frac{1}{N}\sum_{\boldsymbol{q}} \tilde{u}_i e^{-iq_n r^2_n} - \frac{1}{N}\sum_{\boldsymbol{q}} \tilde{u}_i e^{-iq_n r^1_n} = \frac{1}{N}\sum_{\boldsymbol{q}}\left(e^{-iq_n r^2_n} - e^{-iq_n r^1_n}\right)\tilde{u}_i \\
&= -\frac{1}{N}\sum_{\boldsymbol{q}}\left(e^{-iq_n r^2_n} - e^{-iq_n r^1_n}\right)\tilde{D}^{-1}_{i\ell}\tilde{f}_\ell \\
&= -\frac{f_2}{N}\sum_{\boldsymbol{q}}\left(e^{-iq_n r^2_n} - e^{-iq_n r^1_n}\right)\left(e^{iq_m r^1_m} - e^{iq_m r^2_m}\right)\tilde{D}^{-1}_{i\ell}\hat{r}^{12}_\ell \\
&= \frac{f_2}{N}\sum_{\boldsymbol{q}}\left(2 - e^{iq_n(r^2_n - r^1_n)} - e^{-iq_n(r^2_n - r^1_n)}\right)\tilde{D}^{-1}_{i\ell}\hat{r}^{12}_\ell \\
&= \frac{f_2}{N}\sum_{\boldsymbol{q}}\left(2 - e^{iaq_n\hat{r}^{12}_n} - e^{-iaq_n\hat{r}^{12}_n}\right)\tilde{D}^{-1}_{i\ell}\hat{r}^{12}_\ell.
\end{aligned} \tag{2.12}$$

The distance that these nodes have separated is δu_2. We define a^* by $f_2 = (k_{\mathrm{EM}}/a^*)\,\delta u_2$, or $a^* = (k_{\mathrm{EM}}/f_2)\,\delta u_2$. Hence

$$a^* = \frac{k_{\mathrm{EM}}}{f_2}\delta u_2 = \frac{k_{\mathrm{EM}}}{f_2}\hat{r}_i^{12}\left(u_i^2 - u_i^1\right) = \frac{k_{\mathrm{EM}}}{N}\sum_{\boldsymbol{q}}\left(2 - e^{iaq_n\hat{r}_n^{12}} - e^{-iaq_n\hat{r}_n^{12}}\right)\hat{r}_i^{12}\tilde{D}_{i\ell}^{-1}\hat{r}_\ell^{12}. \quad (2.13)$$

Now we use a trick: for the completely randomly diluted lattice, all bonds are equivalent. We have singled out a bond $\hat{r}^{12}$ which is only one of the nearest-neighbor directions in the unit cell. We can replace $\hat{r}^{12}$ everywhere with $\hat{\delta}$ and average over the different $\hat{\delta}$ directions.[2] With z different nearest neighbors, this becomes

$$\begin{aligned} a^* &= \frac{1}{z}\frac{1}{N}\sum_{\boldsymbol{q}} k_{\mathrm{EM}}\sum_{\hat{\delta}}\left(2 - e^{iaq_n\hat{\delta}_n} - e^{-iaq_n\hat{\delta}_n}\right)\hat{\delta}_i\hat{\delta}_\ell\tilde{D}_{i\ell}^{-1} \\ &= \frac{2}{z}\frac{1}{N}\sum_{\boldsymbol{q}} k_{\mathrm{EM}}\sum_{\hat{\delta}}\left(1 - e^{iaq_n\hat{\delta}_n}\right)\hat{\delta}_i\hat{\delta}_\ell\tilde{D}_{i\ell}^{-1} \end{aligned} \quad (2.14)$$

since $\hat{\delta}$ and $-\hat{\delta}$ are equivalent. But now the object inside the sum over wavevectors can be recognized as the Fourier transform of the dynamical matrix, leading to the stunningly simple expression

$$a^* = \frac{2}{z}\frac{1}{N}\sum_{\boldsymbol{q}}\tilde{D}_{\ell i}\tilde{D}_{i\ell}^{-1} = \frac{1}{\widetilde{z}}\frac{1}{N}\sum_{\boldsymbol{q}}\tilde{D}_{\ell i}\tilde{D}_{i\ell}^{-1} = \frac{d}{\widetilde{z}}, \quad (2.15)$$

where $\widetilde{z} = z/2$ is the number of bonds per node.

We are interested in a generalization of this argument to finite frequencies. In nearly all steps, the static force f can be replaced by a sinusoidal force with frequency ω with no consequence. For instance, the self-consistent expression for k_{EM} in terms of a^* remains identical. However, in computing a^*, the relationship between the force and the displacement in Fourier space (Equation 2.8) is now given by the Green's function $\tilde{G}_{ij} = \left(\tilde{D} - \mathbb{I}m\omega^2\right)^{-1}_{ij}$ rather than directly by the inverse dynamical matrix itself. Following the same steps in the derivation, the

[2] In cases where bonds are occupied with different probabilities in different directions, a generalization is needed. There could be different values of a^* for different directions, for instance.

quantity a^* is then

$$a^* = \frac{1}{\widetilde{z}} \frac{1}{N} \sum_{\boldsymbol{q}} \tilde{D}_{\ell i} \tilde{G}_{i\ell}. \tag{2.16}$$

In an infinite system, we can make the replacement

$$\frac{1}{N} \sum_{\boldsymbol{q}} \longrightarrow \frac{1}{s_{\mathrm{BZ}}} \int_{\mathrm{BZ}} \mathrm{d}^d q \tag{2.17}$$

giving

$$a^* = \frac{1}{\widetilde{z}} \frac{1}{s_{\mathrm{BZ}}} \int_{\mathrm{BZ}} \mathrm{d}^d q \; \tilde{D}_{\ell i} \tilde{G}_{i\ell}. \tag{2.18}$$

which allows us to compute this quantity for a general Bravais lattice at arbitrary frequencies. Note that the dynamical matrix and the Green's function are both written in terms of k_{EM}, and so they enter nontrivially into the self-consistent expression.

To complete the story for the bond dilution model, we can average the quantity in Equation 2.5 over the bimodal distribution of bond disorder where k_{ij} is k with probability p and 0 with probability $1 - p$. This gives

$$\left\langle \frac{k_{ij} - k_{\mathrm{EM}}}{k_{\mathrm{EM}}/a^* + k_{ij} - k_{\mathrm{EM}}} \right\rangle = p \; \frac{k - k_{\mathrm{EM}}}{k_{\mathrm{EM}}/a^* + k - k_{\mathrm{EM}}} + (1 - p) \, \frac{-k_{\mathrm{EM}}}{k_{\mathrm{EM}}/a^* - k_{\mathrm{EM}}} = 0. \tag{2.19}$$

This can be solved for a^* to show

$$\frac{p - k_{\mathrm{EM}}/k}{1 - k_{\mathrm{EM}}/k} = a^* = \frac{1}{\widetilde{z}} \frac{1}{s_{\mathrm{BZ}}} \int_{\mathrm{BZ}} \mathrm{d}^d q \; \tilde{D}_{\ell i} \tilde{G}_{i\ell}. \tag{2.20}$$

Let us now locate the phase transition at $\omega = 0$. The self-consistent equation can be solved exactly for k_{EM}, assuming $\tilde{G}_{i\ell}$ can be inverted at $\omega = 0$ (so $k_{\mathrm{EM}} \neq 0$).[3] We have

$$k_{\mathrm{EM}} = \begin{cases} k \frac{p - d/\widetilde{z}}{1 - d/\widetilde{z}}, & p > p_c \equiv d/\widetilde{z} \\ 0, & p \leq p_c \equiv d/\widetilde{z} \end{cases} \tag{2.21}$$

[3] We can do this more safely using the finite frequency form of $\tilde{G}_{i\ell}$ and then taking $\omega \to 0$ to verify these expressions for k_{EM}.

so k_{EM} vanishes linearly with p at $p_c \equiv d/\overline{z}$. When the frequency becomes nonzero, it is possible that the only solution for k_{EM} has an imaginary part. For the effective medium Green's function to be analytic in the upper half-plane (which is necessary for causality), the imaginary part of k_{EM} must be nonpositive. The CPA incorporates the loss of coherence of phonons due to impurity scattering into an effective dissipation. The full dynamical scaling behavior will be investigated in the manuscript and Chapter 4. First, it is useful to recall how universal predictions can be extracted from mean-field theories.

2.2 An instructive example of universal predictions: from mean-field theory to Landau

Before focusing on the specific example of effective medium theories for disordered elastic systems, which have more nontrivial scaling behavior, it is useful to perform a calculation in the same spirit for a more familiar problem: a mean-field theory for the Ising model. The Ising model is a simplified model of a magnet. "Spins," which can take values $s_i \in \{-1, +1\}$ (pointing down or up) are arranged in a particular graph structure. To replicate the paramagnetic-ferromagnetic transition, one prefers configurations of spins with adjacent spins pointing in the same direction. The spin states are taken to occur with likelihood

$$P(\{s_i\}) \propto \exp\left(-\beta H(\{s_i\})\right), \tag{2.22}$$

where H is the Hamiltonian, which maps spin configurations to their energies. This distribution ensures that lower energy states are preferred. The degree of preference is controlled by β, the inverse temperature, so that at very "cold" temperatures $\beta \gg 1$ a typical configuration has very low energy. For an Ising

model in a uniform field on a lattice with nearest-neighbor interactions, the Hamiltonian is

$$H(\{s_i\}) = -J \sum_{\langle ij \rangle} s_i s_j - h \sum_i s_i, \tag{2.23}$$

where the sum $\sum_{\langle ij \rangle}$ is performed over nearest-neighbor spins, J is the energy scale of the coupling between adjacent spins, and h is an external field that gives a preferred direction of spin alignment. To detect the paramagnetic-ferromagnetic transition that occurs upon lowering the temperature, one tracks an order parameter

$$m = \frac{1}{N} \left\langle \sum_i s_i \right\rangle \tag{2.24}$$

which gives the average direction of a spin (one can track this value as $h \to 0^+$, for instance, to eliminate the degeneracy between upward and downward pointing states). An approximate way to detect the phase transition in this model is through the following mean-field theory: first, we assume that the average spin has magnitude m. We will then self-consistently compute m by requiring that a spin s_i, feeling all neighbors of magnitude m (a "mean field"), has average value m when allowed to fluctuate. The first assumption removes the interaction of spins in the energy functional:

$$H = -J \sum_{\langle ij \rangle} s_i s_j - h \sum_i s_i \approx -\frac{Jz}{2} \sum_i s_i m - h \sum_i s_i = \sum_i -\left(\frac{Jz}{2} m + h \right) s_i = \sum_i H_{\text{eff}}(s_i). \tag{2.25}$$

The interacting problem has factorized into a single-site problem. To self-consistently solve for m, we require that the average value of s_i is m, where the energy functional for s_i is $H_{\text{eff}}(s_i)$:

$$m = \langle s_i \rangle = \frac{\sum_{s_i \in \{-1,+1\}} s_i \exp(-\beta H_{\text{eff}}(s_i))}{\sum_{s_i \in \{-1,+1\}} \exp(-\beta H_{\text{eff}}(s_i))} = \tanh\left(\beta \left(\frac{Jz}{2} m + h \right) \right). \tag{2.26}$$

Hence, according to our mean-field theory, the average magnetization per spin

m as a function of inverse temperature β should be the solution to the self-consistent equation

$$m = \tanh\left(\beta\left(\frac{Jz}{2}m + h\right)\right). \tag{2.27}$$

How does this tell us that there is a phase transition? The solution set for m changes as we vary β. This can be seen graphically by plotting each side of the equation and tracking intersections. Let us restrict ourselves to the case where $h = 0$ for now. Intuitively, $\tanh(x)$ is an S-shaped curve that crosses through 0 when $x = 0$, so $m = 0$ is always a solution. The paramagnetic-ferromagnetic transition occurs when β is increased sufficiently so that the S-shaped curve of $\tanh(x)$ is steeper near the origin than x, since it then intersects the line $y = x$ at three locations: 0, and two other places symmetric about the origin. Because $\tanh(x) \approx x - x^3/3 + \ldots$, the slope of our function near the origin is simply $\beta Jz/2$. Hence, the transition occurs at

$$\frac{\beta_c Jz}{2} = 1 \implies \beta_c = \frac{2}{Jz} \implies k_B T_c = \frac{Jz}{2}. \tag{2.28}$$

There are some obvious trends that the mean-field theory does seem to capture: the critical temperature increases if we increase the energy scale of spin-spin interactions J or the number of neighbors z. However, we do not expect the mean-field theory to be quantitatively accurate, since we ignore the fluctuations of the spins that spin s_i interacts with. Indeed, this mean-field theory completely misses the fact that the Ising model has no transition at finite temperature in 1 spatial dimension. It is also quantitatively *wrong* about the location of the transition for the square lattice Ising model: past the first step in the derivation of the mean-field theory, there is essentially no reference to the connectivity properties or loop structure of the lattice on which the spins live.

The mean-field theory does, however, make some predictions about the phase transition that are accurate in high enough spatial dimensions (so that the fluctuations that were ignored do not modify the critical properties). These are the *universal* predictions of the model, and they include critical exponents (power laws with which certain parameters diverge or go to zero) and shapes of scaling functions. These predictions are broadly insensitive to the specifics of the model being studied, and allow phase transitions to be sorted into "universality classes" which share critical exponents and scaling functions. The machinery of the renormalization group seeks to explain the empirical observation of universality. For now, we will use this extremely simple mean-field theory for the Ising model to extract universal predictions: the critical exponents and scaling function associated with the magnetization.

We know from our graphical analysis of the self-consistent equation for m when $h = 0$ that m vanishes continuously as $T \to T_c^-$. We expect that

$$m \sim \left(\frac{T_c - T}{T_c}\right)^{\beta} \equiv (-t)^{\beta}, \tag{2.29}$$

where β is a critical exponent (not to be confused with the inverse temperature). To extract this critical exponent, we first set $h = 0$ in the self-consistent equation and then rewrite the equation in terms of T_c and t:

$$m = \tanh\left(\frac{Jz}{2k_{\mathrm{B}}T}m\right) = \tanh\left(\frac{Jz}{2\left(k_{\mathrm{B}}T - k_{\mathrm{B}}T_c + k_{\mathrm{B}}T_c\right)}m\right) = \tanh\left(\frac{Jzm}{2k_{\mathrm{B}}T_c}\frac{1}{1 + (T/T_c - 1)}\right) \tag{2.30}$$

or, using the expression for $k_{\mathrm{B}}T_c$ and t,

$$m = \tanh\left(\frac{m}{1+t}\right). \tag{2.31}$$

Close to the transition, m and t are both small, so the argument of $\tanh(x)$ is

small. We can then expand $\tanh(x)$ to cubic order:

$$m \approx \frac{m}{1+t} - \frac{1}{3}\left(\frac{m}{1+t}\right)^3 \implies \frac{1}{3}\left(\frac{m}{1+t}\right)^2 \approx -t. \tag{2.32}$$

Taking the square root and dropping terms higher-order in t gives

$$m \sim \pm\sqrt{3}\,(-t)^{1/2}, \tag{2.33}$$

so that the mean-field prediction is that $\beta = 1/2$. When multiple variables are relevant near a critical point, such as t and h, we expect from renormalization group arguments that the magnetization should behave as

$$m/m_0 \sim (-t)^{\beta}\,\mathcal{M}_{\pm}\left(\frac{h/h_0}{|t|^{\beta\delta}}\right), \tag{2.34}$$

where δ is another critical exponent and $\mathcal{M}_{\pm}(x)$ is a *universal scaling function* that all transitions in the same universality class share. Here the two branches are for $t > 0$ and $t < 0$, respectively. By using the mean-field theory for the Ising model, we can extract the mean-field prediction for both δ and the shape of $\mathcal{M}_{\pm}(x)$. Before we begin this exercise, we know the situation close to the critical point when $h = 0$. We can define an *invariant scaling combination* formed between the magnetization m and the temperature t as

$$M \equiv \frac{m/\sqrt{3}}{|t|^{1/2}}. \tag{2.35}$$

The $\sqrt{3}$ represents a non-universal amplitude of the magnetization. Then from the above analysis, we know that $M = \pm 1$ when $t < 0$ and $M = 0$ when $t > 0$. This tells us that

$$\mathcal{M}_{+}(0) = 0, \quad \mathcal{M}_{-}(0) = \pm 1. \tag{2.36}$$

More precisely, we will see that

$$\lim_{x \to 0^{\pm}} \mathcal{M}_{-}(x) = \pm 1. \tag{2.37}$$

This is simply the statement that the magnetization is not continuous across the line $h = 0$ when $t < 0$ since there are two equally satisfactory values of m which can be approached by taking the external field to 0 coming from above or below. We can solve for the exponent δ and the shape of the scaling function $\mathcal{M}_{\pm}(x)$ using the self-consistent equation leaving h arbitrary. First, I rewrite the self-consistent equation in terms of t, m, and $h/h_1 \equiv h/k_B T_c$:

$$m = \tanh\left(\frac{1}{1+t}\left(m + \frac{h}{h_1}\right)\right). \tag{2.38}$$

We will write a scaling solution when all of m, t, and h/h_1 are small, so that we are close to the $t = 0$, $h = 0$ critical point where m vanishes continuously. This again justifies our expansion of $\tanh(x)$ for small values of its argument. Let us perform this expansion in a more principled way. Using the expected form of the scaling function, we can write

$$M \equiv \frac{m/\sqrt{3}}{|t|^{1/2}} \implies m = \sqrt{3} M |t|^{1/2}, \quad H \equiv \frac{h/\left(h_1\sqrt{3}\right)}{|t|^{\beta\delta}} \implies h/h_1 = \sqrt{3} H |t|^{\beta\delta}, \tag{2.39}$$

replacing m and h/h_1 with their scaling forms M and H before performing a principled expansion in small t (the extra factor of $\sqrt{3}$ in the invariant scaling combination H is chosen for later convenience). If the scaling is chosen correctly, then the self-consistent equation will reduce in the limit $t \to 0$ to a simple formula involving only the invariant scaling combinations M and H. We first have

$$\sqrt{3} M |t|^{1/2} = \tanh\left(\frac{1}{1+t}\left(\sqrt{3} M |t|^{1/2} + \sqrt{3} H |t|^{\beta\delta}\right)\right). \tag{2.40}$$

We now fix M and H while sending $t \to 0$:

$$\sqrt{3} M |t|^{1/2} \approx \frac{1}{1+t}\left(\sqrt{3} M |t|^{1/2} + \sqrt{3} H |t|^{\beta\delta}\right) - \frac{1}{3}\left(\frac{1}{1+t}\left(\sqrt{3} M |t|^{1/2} + \sqrt{3} H |t|^{\beta\delta}\right)\right)^3. \tag{2.41}$$

Now multiply each side by $1 + t$, and subtract the common terms $\sqrt{3}M\,|t|^{1/2}$ that appear on each side:

$$\sqrt{3}M\,|t|^{1/2} + \sqrt{3}Mt\,|t|^{1/2} \approx \sqrt{3}M\,|t|^{1/2} + \sqrt{3}H\,|t|^{\beta\delta} - \frac{1}{3}\left(\frac{1}{1+t}\right)^2\left(\sqrt{3}M\,|t|^{1/2} + \sqrt{3}H\,|t|^{\beta\delta}\right)^3 \tag{2.42}$$

$$\sqrt{3}Mt\,|t|^{1/2} \approx \sqrt{3}H\,|t|^{\beta\delta} - \frac{1}{3}\left(\frac{1}{1+t}\right)^2\left(\sqrt{3}M\,|t|^{1/2} + \sqrt{3}H\,|t|^{\beta\delta}\right)^3 \tag{2.43}$$

Now we require some asymptotic analysis to self-consistently determine the proper value for the unknown exponent $\beta\delta$. As $t \to 0$, the LHS $\sim t^{3/2}$. For a nontrivial scaling limit, then, the RHS must also $\sim t^{3/2}$. Expanding the terms on the RHS, we have terms that scale like $t^{\beta\delta}$, $t^{3/2}$, $t^{1+\beta\delta}$, $t^{1/2+2\beta\delta}$, $t^{3\beta\delta}$, and higher-order powers of t coming from both the expansion of $(1+t)^{-1}$ and further terms in the power series of $\tanh(x)$ that we have already ignored. For a nontrivial scaling limit, then, we must have $\beta\delta = 3/2$, so that the leading-order term involving H scales with the same exponent as the leading-order terms involving M. If we choose $\beta\delta < 3/2$, then the leading-order term involving H vanishes more slowly than every other term and the self-consistent equation is the trivial $H = 0$ (this indicates that the improper invariant scaling combination was chosen). If $\beta\delta > 3/2$, then all terms involving H enter as corrections to scaling and we recover the analysis performed when we set $h = 0$ (this also indicates that the improper invariant scaling combination was chosen). Choosing the only nontrivial option $\beta\delta = 3/2$ and then sending $t \to 0$ gives

$$\sqrt{3}Mt\,|t|^{1/2} \approx \sqrt{3}H\,|t|^{3/2} - \sqrt{3}M^3\,|t|^{3/2} \tag{2.44}$$

or, dividing by $\sqrt{3}\,|t|^{3/2}$,

$$M^3 \pm M - H = 0. \tag{2.45}$$

This is an implicit definition of a scaling function $\mathcal{M}_\pm(H)$. Since $\beta = 1/2$, we conclude that the mean-field prediction is that $\delta = 3$.

Is it possible that the predictions of the mean-field theory are exactly correct? Certainly not. The mean-field theory purports to describe the magnetization everywhere as a function of temperature and external field. But the mean-field equation we derived depends on the structure of the lattice only through the coordination number z, while geometric effects (longer-ranged interactions induced by chains of nearest-neighbor interactions, closed loops on the lattice) are certainly important for an exact description of the phase behavior.

Is it possible that these predictions for the values of the critical exponents and the shape of the scaling function are true asymptotically close to the transition? This is more likely to be true. This simplified model of a phase transition replicates the transition from a paramagnetic to a ferromagnetic phase through a pitchfork bifurcation. The most generic possible pitchfork bifurcation will give an exponent $\beta = 1/2$. This can be seen through the fact that we only needed to expand $\tanh(x)$ to cubic order, and all symmetric functions undergoing a bifurcation of this form have similar expansions. To lend credibility to this assertion, let us consider an even further simplified Landau theory for the magnetization, ignoring all spatial fluctuations in m:

$$F(m) = f_0 + am^2 + gm^4 - hm, \tag{2.46}$$

where F is the free energy, h is the external field coupling linearly to m in the free energy, and a changes sign as T passes through T_c to drive the transition at $h = 0$. Near T_c, the most generic form of a is an analytic function of T, and so $a \sim a_0 (T - T_c)$ with $a_0 > 0$. The equilibrium value of the magnetization is found through minimization of $F(m)$ with respect to m:

$$\frac{\mathrm{d}F}{\mathrm{d}m} = 0 = 2am + 4gm^3 - h \sim 2a_0 (T - T_c) m + 4gm^3 - h. \tag{2.47}$$

When $h = 0$, we can write

$$2a_0 (T - T_c) m + 4gm^3 = 0 \implies m^3 \sim \frac{a_0}{2g} (T_c - T) m. \tag{2.48}$$

When $T > T_c$, $m = 0$ is the only real solution. When $T < T_c$ there are three real solutions, but only the nonzero solutions sit in the minima of the free energy. This leads, for $T < T_c$, to

$$m \sim \pm \sqrt{\frac{a_0 T_c}{2g}} (-t)^{1/2} \tag{2.49}$$

and so the Landau theory agrees with the mean-field prediction of $\beta = 1/2$. We can now repeat the same procedure as above to determine the Landau theory's prediction for δ and the shape of the universal scaling function: we define

$$M \equiv \sqrt{\frac{2g}{a_0 T_c}} \frac{m}{|t|^{1/2}} \implies m = \sqrt{\frac{a_0 T_c}{2g}} M |t|^{1/2}, \quad H \equiv \frac{h/h_0}{|t|^{\beta\delta}} \implies h = h_0 H |t|^{\beta\delta} \tag{2.50}$$

with h_0 a non-universal quantity to be set for convenience and $\beta\delta$ a universal quantity to be determined. Inserting these into the self-consistent equation from the Landau theory gives

$$2a_0 T_c t \sqrt{\frac{a_0 T_c}{2g}} M |t|^{1/2} + 4g \left(\frac{a_0 T_c}{2g} \right)^{3/2} M^3 |t|^{3/2} - h_0 H |t|^{\beta\delta} = 0. \tag{2.51}$$

The prefactors of the first two terms simplify to the same combination of parameters:

$$\sqrt{\frac{2}{g}} (a_0 T_c)^{3/2} Mt |t|^{1/2} + \sqrt{\frac{2}{g}} (a_0 T_c)^{3/2} M^3 |t|^{3/2} - h_0 H |t|^{\beta\delta} = 0. \tag{2.52}$$

The equation is greatly simplified if we choose

$$h_0 \equiv \sqrt{\frac{2}{g}} (a_0 T_c)^{3/2}. \tag{2.53}$$

Then there are three terms. The first two scale as $\sim t^{3/2}$, while the last scales as $t^{\beta\delta}$. For a nontrivial scaling limit, then, we choose $\beta\delta = 3/2$, and so the Landau theory also agrees with the mean-field value of $\delta = 3$. Furthermore, simplification

of this expression then leads to the self-consistent relation

$$M^3 \pm M - H = 0, \tag{2.54}$$

which is an implicit definition of a universal scaling function $\mathcal{M}_{\pm}(H)$: the *same* function as the one that was found through an asymptotic expansion of the mean-field theory. This is a sort of "universality" of mean-field theories, more trivial than the concept of universality classes in more complex theories of critical phenomena.

The mean-field theory and the Landau theory predict the same critical exponents and shapes of scaling functions close to the transition; it is in this sense that these aspects of the theories are "universal:" even if we do not have a perfect theory for the phases, there are predictions that reasonably similar models will share. These predictions are robust to a large class of "irrelevant" changes to the models: for instance, one could imagine an Ising model with next-nearest-neighbor interactions. A simplified model of this transition would likely incorporate the additional interactions into a downward renormalization of the nonuniversal critical temperature, T_c, but aspects of the transition dealing with the pitchfork bifurcation, such as the values for critical exponents and shapes of scaling functions asymptotically close to the transition, would remain the same.

The mean-field theory and the Landau theory only make accurate universal predictions in some cases. For the Ising model, the critical exponents associated with the transition are mean-field-like in $d \geq 4$, but take other values in lower dimensions. This discrepancy is attributed to the effects of fluctuations that are ignored in treating the transition using a single-site problem. In high numbers of spatial dimensions, these fluctuations are unimportant for the predictions of universal features like critical exponents, but below an *upper critical dimension*

the critical exponents themselves are modified from the values given by mean-field theories, and more sophisticated techniques to keep track of interactions are necessary (see Chapter 6).

It is with this philosophy that we approach the analysis of an approximate theory for a rigidity transition that occurs in randomly diluted elastic networks. The self-consistent equations that come from the theory in this case determine the best values for homogeneous elastic constants in the disordered medium. Past work on these models focuses on their success in describing the phase behavior deep into the elastic phase and also in the prediction of the location of the rigidity transition. Others have done detailed simulations close to the transition in diluted elastic networks, finding non-mean-field critical exponents. We seek to identify the universal predictions of this model: critical exponents, shapes of scaling functions, etc. In this case, the model makes many more predictions than the Landau theory for the Ising model: all of linear response of disordered elastic solids can be determined from the Green's function of the theory.

In the following manuscript, I assisted in the derivations of scaling functions and in the numerical verifications of the scaling forms. Additionally, I generated many of the figures that appear, including the RegionPlots for the asymptotic behavior of the response functions. Danilo Liarte and Jim Sethna had the idea to extract universal predictions for response functions close to a jamming transition following Danilo's earlier postdoctoral work [2]. Eric Schwen and Itai Cohen brought valuable comments on experimental realizations of such systems, and Debanjan Chowdhury was important in technical discussions of response functions and later extensions of this framework to understand electronic density response in strange metals (Chapter 3).

2.3 Universal scaling for disordered viscoelastic matter near the onset of rigidity

This is a reformatted version of a manuscript appearing on the arXiv as "Universal scaling for disordered viscoelastic matter near the onset of rigidity," which was later edited and published as Phys. Rev. E 106, L052601 (2022) under the same title [9].

2.3.1 Abstract

The onset of rigidity in interacting liquids, as they undergo a transition to a disordered solid, is associated with a rearrangement of the low-frequency vibrational spectrum. In this letter, we derive scaling forms for the singular dynamical response of disordered viscoelastic networks near both jamming and rigidity percolation. Using effective-medium theory, we extract critical exponents, invariant scaling combinations and analytical formulas for universal scaling functions near these transitions. Our scaling forms describe the behavior in space and time near the various onsets of rigidity, for rigid and floppy phases and the crossover region, including diverging length and time scales at the transitions.

2.3.2 Main text

Jamming [14] and Rigidity Percolation (RP) [15] provide suitable frameworks to characterize the fascinating invariant scaling behavior exhibited by several classes of disordered viscoelastic materials near the onset of rigidity [16]. Both are often described by elastic networks near the Maxwell limit of mechanical

stability [17], and represent transitions from a rigid phase to a floppy one when the average coordination number z falls below the isostatic value z_c. RP appears in network glasses [18], fiber networks [19, 5] and soft colloidal gels [20], and is described in terms of networks in which bonds are randomly removed; the bulk modulus vanishes [4] at the transition [1, 22, 23]. Jamming is also a ubiquitous phenomenon arising in systems ranging from amorphous solids and glasses [24] to cell tissues [25] and deep learning [26]. Jamming is commonly described in terms of sphere packings that possess a finite bulk modulus $B > 0$ at the transition. Recently, it was shown that jamming can be described as a multi-critical point that terminates a line of continuous transitions associated with rigidity percolation and that there is a deep connection between the universal scaling forms for both transitions [2]. Determining explicit formulas for the susceptibilities and space-time correlations has been challenging, however, since there is a scarcity both of comprehensive numerical data and of analytic models for these transitions (with the exception of jamming in high dimensions [27, 28, 29]). Here, we leverage the analytically-tractable effective-medium theory (EMT) of Ref. [2] to fill this gap and extract explicit equations for these universal forms.

At jamming [14], two-dimensional disk packings form a disordered contact network [blue lines in Fig. 2.4(a)] that supports compression but not shear. Mimicking compression by randomly adding next-nearest neighbor bonds between disks [red N-bonds in Fig. 2.4(a)] and/or randomly removing B-bonds can lead to either jamming or RP depending on the population for each type of bond [2].

[4] Different types of lattices do not *appear* to have the same universal RP behavior. For instance, isotropic periodic Maxwell lattices (in which $z = z_c = 2D$ where D is the dimension) can have $B, G > 0$ (as in the kagome lattice), where G is the shear modulus, or $B = 0$ and $G > 0$ (as in the twisted-kagome lattice, see e.g. [21]), which suggests that these lattices do not belong to the same RP universality class. However, if these lattices have extra bonds so that $z > 2D$, arbitrary protocols to randomly dilute these networks without specifically targeting particular bonds will lead to a continuous transition for both B and G.

A simpler model that yields the same scaling behavior consists of randomly placing 'B' and 'N'-bonds between nearest and next-nearest neighbor pairs of sites [blue and red solid lines in Fig. 2.4(b)] of a periodic honeycomb lattice. This network describes a diluted version of a 3-sub-lattice system consisting of a honeycomb lattice [shaded blue in Fig. 2.4(b)] and two triangular lattices (shaded red; here we show only the bonds of one triangular lattice). Detailed knowledge of the mechanical behavior of periodic lattices allowed the development of an EMT at finite dimension [5] for jamming [2] and for the crossover from jamming to RP, valid in both rigid and floppy states. We will employ these results to derive explicit solutions for the critical scaling of the susceptibilities of disordered viscoelastic matter near jamming and RP. Our analysis not only allows for quick assessment of scale-invariant behavior of quantities such as viscosities and correlations (without the need for computationally-expensive simulations); it also serves as an example of how one may analyze rigidity transitions for which the universality class has not been determined.

Figure 2.4(c) shows the phase diagram of the honeycomb-triangular lattice (HTL) model in terms of occupation probability of nearest neighbor B bonds and next-nearest neighbor N bonds. Rigid (yellow) and floppy regions are separated by an RP line that terminates in a multicritical jamming point J (red disk). From Fig. 2.4(c), one can also extract definitions for the scaling variables δp_{B} and δp, chosen so that $\delta p = 0$ at RP, and δp_{B} is also zero at jamming.

RP should generically be codimension one, because only one constraint (isostaticity) needs to be satisfied. In the HTL model of Fig. 2.4(b), jamming is codimension two. But the jump in bulk modulus characteristic of jamming here

[5] See also Refs. [30, 31] for calculations in finite dimension based on the nonaffine response of amorphous solids.

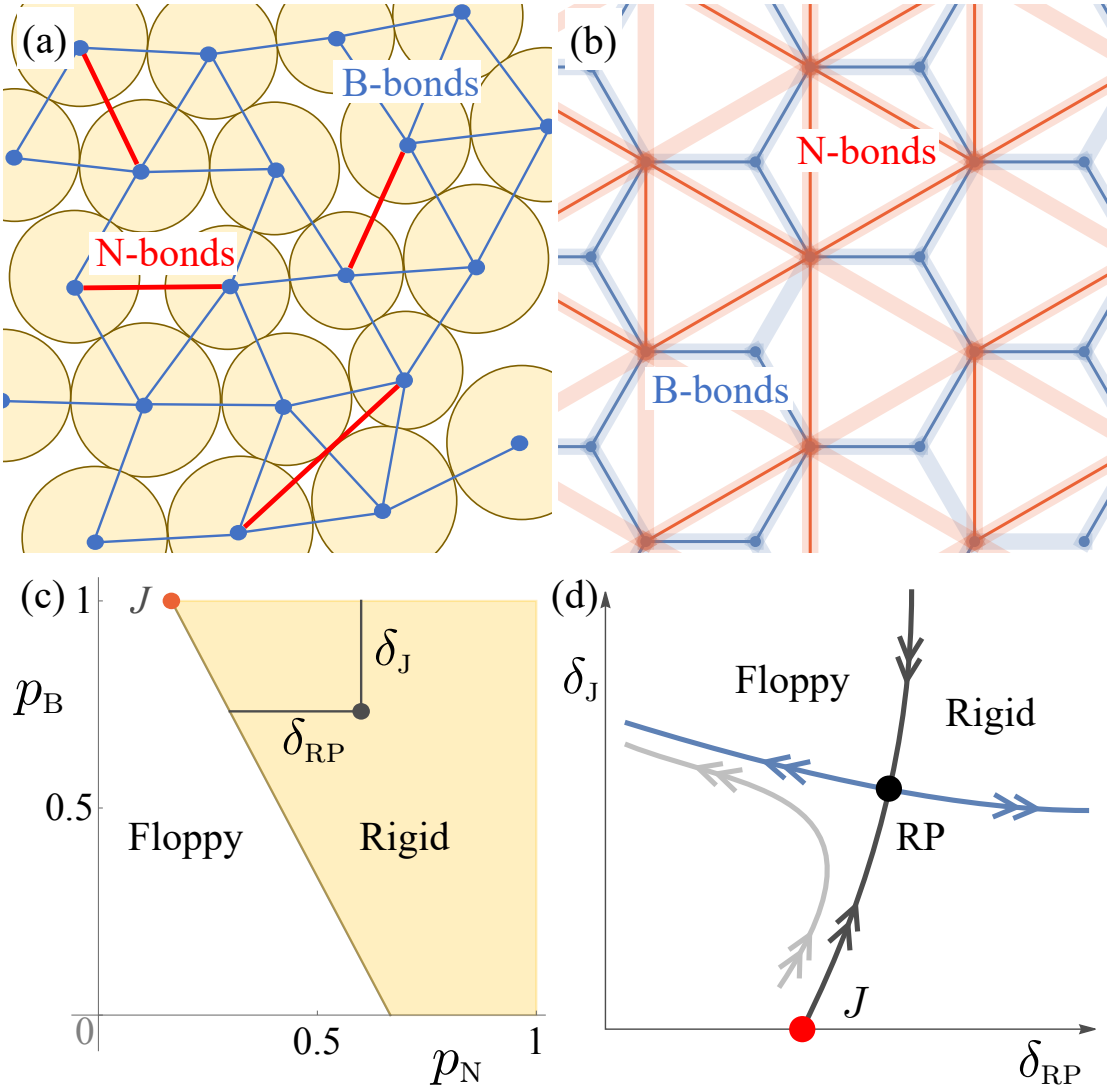

Figure 2.4: (a) Jammed disk packing, underlying contact network (B-bonds in blue) and randomly added next-nearest neighbor N-bonds (red). (b) HTL model with nearest and next-nearest neighbor bonds (solid blue and red lines) connecting sites of a honeycomb lattice. Faint blue and red lines show underlying honeycomb and triangular lattices, respectively. (c) Phase diagram of the HTL model in terms of occupation probabilities for B and N-bonds. The yellow region corresponds to the rigid state, and is separated from the floppy state by an RP line ending at a jamming point J (red disk). (d) Conjecture for a crossover flow diagram projected into $\delta p \times \delta p_B$ space. J (red disk) and RP (black disk) represent fixed points of a putative renormalization-group scheme. The blue, black and gray lines represent the unstable manifold, the critical line and a sample trajectory, respectively.

demands a complete honeycomb lattice; one can see that if the three orientations of hexagon bonds were independently populated, the jamming transition would be codimension four (their three probabilities set to one plus isostaticity). This special tuning of the system to favor the bulk modulus is echoed in the jamming of frictionless spheres, where the first state of self stress [32] leads to a jump in the bulk modulus because the conjugate degree of freedom (a uniform compression) was used to tune the system to the rigidity transition. As evidence for this, shear jamming of frictionless spheres has a jump in a single anisotropic modulus [33].

We conjecture that there is a class of disordered elastic systems for which a renormalization-group scheme leads to the typical crossover flow diagram [34] (projected in $\delta p \times \delta p_{\mathrm{B}}$ space) illustrated in Fig. 2.4(d). The scaling variable $\delta p \propto \Delta z \equiv z - z_c$ must be relevant for both jamming and RP, but the depletion probability of the B-lattice δp_{B} is relevant only for jamming. This behavior is captured by the direction of the arrows coming in and out of the putative jamming and RP fixed points (red and black disks, respectively) in Fig. 2.4(d). A system near the J fixed point ($\delta p_{\mathrm{B}}, |\delta p| \ll 1$) will be controlled either by J if a crossover variable $\delta p_{\mathrm{B}}/|\delta p|^{\varphi} \ll 1$ for some exponent φ, or by RP if $\delta p_{\mathrm{B}}/|\delta p|^{\varphi} \gg 1$, i.e. for trajectories such as the gray line passing sufficiently close to the critical line (black solid line.) Though δp_{B} does not have a direct interpretation in the jamming of sphere packings [except for the network model of Fig. 2.4(a)], there might be variables that play a similar role, such as attractive interactions in soft gels [35].

We now introduce a scaling ansatz for the longitudinal response func-

tion [36] near jamming:

$$\frac{\chi_{\mathrm{L}}}{\chi_0} \approx |\delta p|^{-\gamma} \mathcal{L}\left(\frac{q/q_0}{|\delta p|^{\nu}}, \frac{\omega/\omega_0}{|\delta p|^{z\nu}}, \frac{\delta p_{\mathrm{B}}/\delta_0}{|\delta p|^{\varphi}}\right), \tag{2.55}$$

where q is the wavevector, ω is the frequency, γ, ν, z and φ are critical exponents for the susceptibility, correlation length, correlation time, and crossover behavior, respectively [34, 37], and $\mathcal{L}$ is a universal scaling function. The constants χ_0, q_0, ω_0 and δ_0 are nonuniversal scaling factors. Many other properties can be derived from $\mathcal{L}$ (Table 2.2). Such space-time susceptibilities, and the corresponding structure and correlation functions, are the fundamental linear response quantities for materials. They have been well studied in glassy systems, but have hitherto not been a focus in the study of jamming or RP. Baumgarten et al. [38] and Hexner et al. [39] have studied the static response of frictionless jammed spheres to a sinusoidal perturbation; they find diverging length scales that are different from the ones presented here. Because our system is on a regular lattice, and particularly because our analysis replaces the disordered lattice with a uniform one, it is natural for us to fill this gap.

Our approach goes beyond previous work [40] in two aspects. First, rather than starting with an ansatz for the free energy in terms of the excess contact number Δz, excess packing fraction $\Delta\phi$, shear stress ϵ and system size N, we consider the longitudinal response in terms of δp, q, ω and δp_{B}. Our variable δp is proportional to Δz. Though we do not consider an explicit dependence of χ_{L} on ϵ or $\Delta\phi$ [6], we can extract equivalent expressions for moduli and correlations from the dependence of χ_{L} on q. Importantly, the inclusion of ω in our analysis allows us to predict dynamical properties such as viscosities.

[6] Note that δp does not change with lattice deformation for our system. This contrasts with the case of compressed disks in which Δz can vary with $\Delta\phi$. We assume fixed (quenched) disorder in our model.

Second, we use EMT [2] to derive and validate both the universal exponents and the universal scaling functions ($\mathcal{L}$), for both jamming and RP. This form of EMT is based on the coherent-potential approximation [41, 1] (CPA), and is known to reproduce well results obtained from simulations of randomly-diluted lattices with two-body [7] harmonic interactions [42, 21], even for undamped [22, 2] and overdamped dynamics [43, 44]. Although the CPA involves mean-field-like uncontrolled approximations, it preserves the topology of the original lattices — an essential ingredient that ultimately allows one to describe jamming. Here we focus on the longitudinal response, since the full response of isotropic elastic systems can be decomposed into longitudinal and transverse components, and the latter has the same scaling form near both jamming and RP as the longitudinal response near RP; see [45].

We use the long wavelength limit of the longitudinal response χ_{L} along with EMT results from Ref. [2] to derive critical exponents (see Table A.1) and the universal scaling function $\mathcal{L}$ in Eq. (A.17) (see [45]),

$$\mathcal{L}(u, v, w) = \left[\frac{u^2}{1 + w/\left(\sqrt{1 - \tilde{v}(v)} \pm 1 \right)} - \tilde{v}(v) \right]^{-1} , \tag{2.56}$$

where $\tilde{v}(v) = v^2$ and $i\,v$ for undamped and overdamped dynamics, respectively, and the plus and minus signs correspond to solutions in the elastic and floppy states, respectively. Equation (2.56) embodies the central results of this paper. From Eqs. (A.17) and (2.56), we will extract the universal behavior of the elastic moduli, viscosities as well as the density response and correlation functions (dynamic structure factor). Though it is not certain that these functions are as universal as critical exponents, recent simulations of compressed hyperspheres [46] indicate that critical amplitudes calculated using mean-field mod-

[7] A more sophisticated version of EMT is needed to reproduce the scaling behavior of randomly-diluted lattices with three-body forces such as bending [23].

	γ	z	ν	φ	β_{B}	γ_{B}
Jamming	2	1 (2)	1	1	0	1 (2)
Rigidity Percolation	2	2 (4)	1/2	-	1	0 (1)

Table 2.1: Critical exponents for the longitudinal susceptibility (γ), correlation length (ν), correlation time (z) and crossover behavior (φ) near jamming and RP for undamped and overdamped (between parentheses if different from undamped) dynamics. The exponents β_{B} and γ_{B} can be derived from γ, ν and z (see Table 2.2), and describe power-law singularities for the bulk modulus and viscosity, respectively.

els at infinite dimension are preserved for low-dimensional jammed packings.

For $|\delta p| \ll \delta p_{\text{B}}$ [$w \gg 1$ in Eq. (2.56)], our model exhibits RP criticality: δp_{B} becomes an irrelevant variable, and $\mathcal{L}(u, v, w) \to \bar{\mathcal{L}}(u, v)$, with

$$\bar{\mathcal{L}}(u, v) = \left[u^2 \left(\sqrt{1 - \tilde{v}(v)} \pm 1\right) - \tilde{v}(v)\right]^{-1}. \tag{2.57}$$

Here the change in $\mathcal{L}$ is accompanied by a change in the critical exponents ν and z (see Table A.1). Note that the exponent $z\nu$ depends only on the type of dynamics, but the exponent ν equals 1 and 1/2 for jamming and RP, respectively.

Our formulation of Eqs. (A.17-A.22) represents a deliberate effort to emphasize model-independent (universal) features. Note e.g. that our model definition of the non-universal scaling factor q_0 is different for jamming and RP; the latter involves a term that increases as one moves away from the jamming multicritical point. Besides, our formulation allows for the suitable incorporation of analytic corrections to scaling [47, 48, 34, 49], which can be added in a case-by-case basis. In general, we expect these corrections to appear through the introduction of nonlinear scaling fields, $u_q(q, \omega, \delta_{\text{J}}) = q/q_0 + \ldots$, $u_\omega(q, \omega, \delta_{\text{J}}) = \omega/\omega_0 + \ldots$, $u_{\text{J}}(q, \omega, \delta_{\text{J}}) = \delta_{\text{J}}/\delta_0 + \ldots$, which would replace q/q_0, ω/ω_0 and $\delta_{\text{J}}/\delta_0$ in Eq. (A.17). Here the dots represent higher-order terms and perhaps linear terms in the other

variables (rotating the axes). These nonlinear scaling fields can be viewed as the difference between the lab parameters and Nature's natural variables, or as the coordinate transformation removing the (hypothetical) nonlinear terms in the renormalization group to their hyperbolic normal form [49]. In order to use our scaling predictions to describe behavior far from the critical point, one must first determine the appropriate scaling fields u_q, u_ω and u_J for the particular system.

Equation (A.17) implies that solutions for $|\delta p|^\gamma \chi_\mathrm{L}$ as a function of one of the three invariant scaling combinations (the other two kept constant) should lie on the curves given by Eqs. (2.56) and (A.22), respectively. Hence, plots for different values of $|\delta p|$ should collapse for several paths approaching jamming or RP. Figure A.3 shows an example of a scaling collapse plot of the rescaled longitudinal response as a function of rescaled frequency for overdamped dynamics at fixed $q/|\delta p|^\nu$ and $\delta_\mathrm{J}/|\delta p|^\varphi$, and for paths approaching jamming (first row) and RP (second row) from both the rigid and floppy phases (see inset in each panel). Real parts are in blue; imaginary (dissipative) parts in red. The solid and dashed curves are the asymptotic universal scaling predictions [Eqs. (2.56) and (A.22)] at two different values of the wavevector scaling variable $q/|\delta p|^\nu$. Although there are model-specific predictions for the nonuniversal scaling factors, we choose them to best fit the collapsed data.

The collapses of Fig. A.3 not only validate our universal scaling forms; they indicate an interesting crossover to a regime dominated by dissipation (the imaginary part of χ_L in red) as the frequency increases. Note that the real part $\mathcal{L}'(v)$ plateaus and the imaginary part $\mathcal{L}''(v)$ (the dissipation) vanishes at low frequency v. At high frequency, both $\mathcal{L}'$ and $\mathcal{L}''$ decay to zero, but $\mathcal{L}'$ decays faster than $\mathcal{L}''$, except in the limit of very large u and v, where both $\mathcal{L}'$ and $\mathcal{L}''$

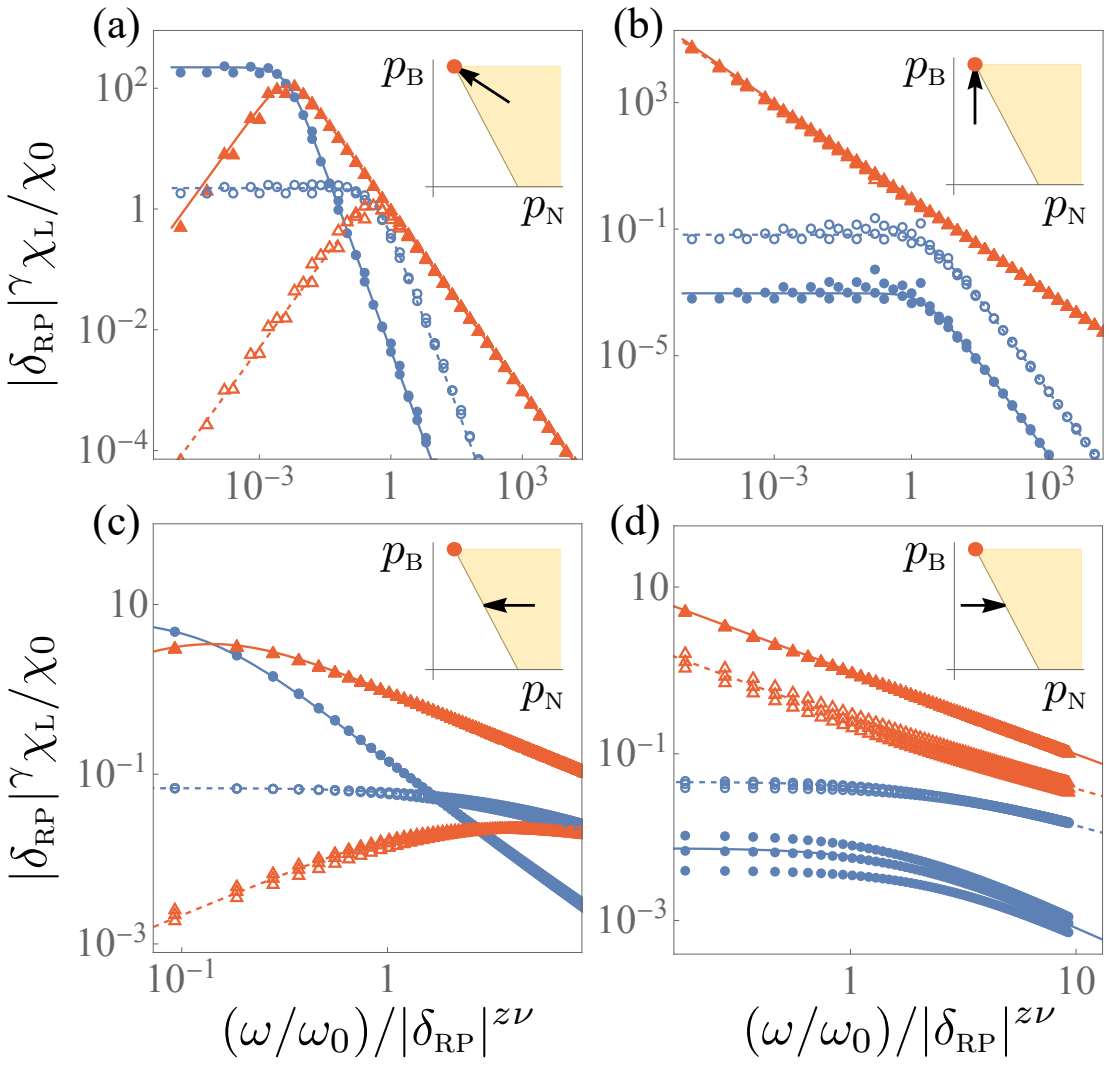

Figure 2.5: Scaling collapse plots showing the universal behavior of the longitudinal response as a function of rescaled frequency near jamming (first row) and RP (second row), for overdamped dynamics. Blue disks and red triangles are full solutions of the EMT equations for the real and imaginary parts of $|\delta p|^\gamma \chi_L/\chi_0$, respectively. Solid and dashed curves are the universal scaling predictions of Eqs. (2.56) and (A.22). We consider points approaching jamming and RP along the paths indicated in the inset graphs of each panel. We use $q/|\delta p|^\nu = 0.1$ (closed symbols) and 1 (open symbols) in all panels, and $\delta p_B/|\delta p|^\varphi$ equal to $\sqrt{5}/4$ from the rigid side (a), and equal to 2 from the floppy side (b). Full solutions run at $|\delta p| = 10^{-2}$, 10^{-3}, and 10^{-4} for RP and a range $|\delta p| \in [5\times10^{-2}, 5\times10^{-6}]$ for jamming show convergence to our universal asymptotic predictions.

decay as $v^{-1/2}$. Hence, there is a frequency ω in which $\mathcal{L}' \sim \mathcal{L}''$, and above which the response is dominated by the dissipative imaginary part. From Eq. (2.56), we find that $\omega \sim D^* q^2$ in this regime, leading to the definition of an effective diffusion constant $D^* \sim |\delta p|^{(z-2)\nu}$. Using the exponents shown in Table A.1, we find that $D^* \sim O(1)$ and $\sim |\delta p|$ for jamming and RP, respectively. In terms of rescaled variables, this crossover happens at $v \sim u^2$ for both transitions. In the liquid phase [(b) and (d)], $\mathcal{L}'$ behaves as in the elastic phase, but $\mathcal{L}''$ diverges rather than vanishing at low v due to the predominant viscous response of the fluid state.

Equations (2.56) and (A.22) also imply that our universal functions for the longitudinal response $\mathcal{L}(u, v, w)$ and $\bar{\mathcal{L}}(u, v)$ generally behave as $u^\alpha v^\beta$ with the exponents α and β depending on the region in the u (rescaled wavector) $\times$ v (rescaled frequency) plane. To illustrate and map this global behavior, we show in Fig. A.4 the power-law regions for which $\mathcal{L}(u, v, w) \propto u^\alpha v^\beta$ and $\bar{\mathcal{L}}(u, v) \propto u^\alpha v^\beta$, with (α, β) very close to their asymptotic values. The first and second rows correspond to our scaling forms for jamming and RP, respectively. To generate each panel, we numerically calculate the exponents using $f_\alpha \equiv \partial \log \mathcal{L} / \partial \log u$ and $f_\beta \equiv \partial \log \mathcal{L} / \partial \log v$ for jamming and similar formulas for RP. We then plot the regions in which $|f_\alpha - \alpha| < 0.1$ and $|f_\beta - \beta| < 0.1$, for several values of α and β.

Figure A.4 offers a vivid pictorial view allowing an easier assessment of the global behavior associated with our universal forms for jamming and rigid percolation. By comparing the two rows, notice how the change in universality class is also reflected in the behavior of the universal scaling functions. For instance, although jamming and RP exhibit similar qualitative features for the

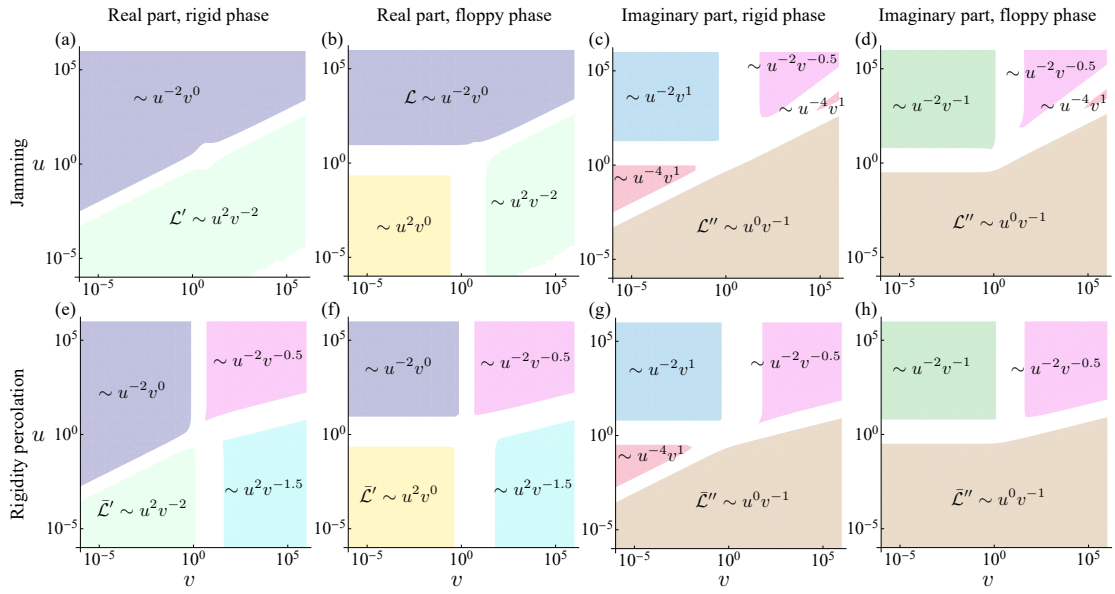

Figure 2.6: **Overdamped asymptotic exponents for universal longitudinal response.** Diagram in the u (rescaled wavevector) $\times v$ (rescaled frequency) plane, showing regions of distinct power-law behavior of the jamming (first row) and RP (second row) universal scaling functions for overdamped dynamics in both the rigid and floppy phases. The first and second (third and fourth) columns correspond to the real (imaginary) parts of $\mathcal{L}$ and $\bar{\mathcal{L}}$. We use $w = 1$ for jamming.

imaginary part [(c), (d), (g) and (h)], RP shows additional regimes for the real part, which do not appear in jamming [compare e.g. (a) and (e) or (b) and (f)].

In the Supplementary Material, we present results for undamped dynamics that are analogous to Figs. A.3 and A.4 in this letter. The full solutions of our effective-medium theory equations also converge to our universal scaling functions, except in the limit of very low frequencies. In fact, the asymptotic solutions derived in [2] do not capture the small but nonzero imaginary parts of the effective spring constants at frequencies smaller than $\sim \omega^*$ (the characteristic crossover to isostaticity) when there is no damping. This feature has important consequences for energy dissipation in systems believed to exhibit behavior related to RP. The corrections to scaling appear as singular perturbations to the self-consistency equations and vanish as powers of $|\delta p|$ in dimen-

Y	y	$\mathcal{Y}$
B	$\beta_B \equiv \gamma - 2\nu$	$\mathcal{B} = (\partial \mathcal{L}^{-1}/\partial u)/(2\,u)$
ζ	$-\gamma_B \equiv \gamma - (2+z)\nu$	$\mathcal{Z} = (1/v)\,\mathrm{Im}\,[\mathcal{B}]$
Π	$2\nu - \gamma$	$\mathcal{P} = u^2\mathcal{L}$
S	$(2+z)\nu - \gamma$	$\mathcal{S} = (1/v)\,\mathrm{Im}[\mathcal{P}]$

Table 2.2: Critical exponent y and universal scaling function $\mathcal{Y}$ describing the singular behavior of the bulk modulus B and viscosity ζ, density response Π and correlation function S, according to Eq. (A.35).

sions larger than three. Moreover, the scaling variables contain logarithms in two dimensions. This analysis is beyond the scope of the present work, and will be presented in a separate manuscript.

Equations (A.17) and (2.56) determine the scaling behavior of several quantities characterized by the general form,

$$\frac{Y}{Y_0} = |\delta p|^y \, \mathcal{Y}\left(\frac{q/q_0}{|\delta p|^\nu}, \frac{\omega/\omega_0}{|\delta p|^{z\nu}}, \frac{\delta p_B/\delta_0}{|\delta p|^\varphi}\right), \tag{2.58}$$

where in Table 2.2 we present explicit expressions for the exponent y and universal function $\mathcal{Y}$ describing the bulk modulus (B), viscosity (ζ), density response (Π) and correlation function (S). The behavior near RP is obtained by replacing $\mathcal{Y}$ and $\mathcal{L}$ in the third column of Table 2.2 by $\bar{\mathcal{Y}}$ and $\bar{\mathcal{L}}$ (now functions of u and v only), respectively, along with appropriate changes for the exponents (see Table A.1). The scaling behavior of the shear modulus and viscosity near jamming and RP is the same as that of B and ζ, respectively, near RP.

To illustrate the broad applicability of our scaling forms, we discuss our results for the density-density correlation — the structure function for isotropic fluids at $q \neq 0$. Figure 2.7(a) shows a 3D plot of the universal function $\bar{\mathcal{S}}(u, v)$ (see Table 2.2) for undamped fluids near RP.

At fixed u, $\bar{\mathcal{S}}(u, v)$ has a maximum (blue dashed line) at $v = v^* \approx O(1)$ [i.e.

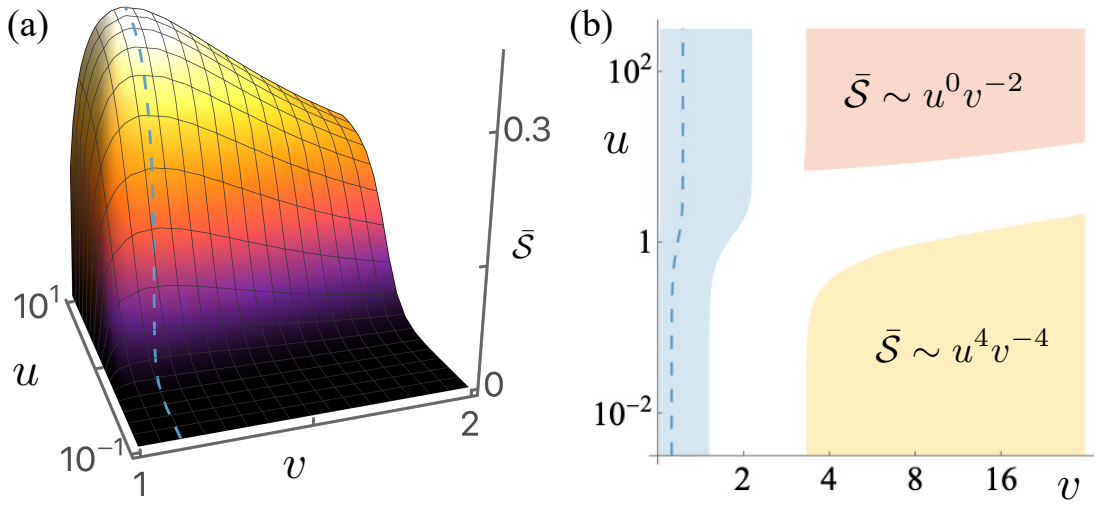

Figure 2.7: (a) 3D plot of the universal scaling function for the correlation function $\bar{\mathcal{S}}(u, v)$, for undamped fluids near RP. The blue dashed line corresponds to the rescaled frequency v^* (the boson peak) at which $\bar{\mathcal{S}}(u, v)$ is maximum for fixed rescaled wavevector u. (b) $u \times v$ diagram showing the boson peak (blue dashed line) and power-law regions for which $\mathcal{S}(u, v) \propto u^\alpha v^\beta$, with (α, β) close to their asymptotic values $(0, -2)$ (red) and $(4, -4)$ (yellow). In the blue region the condition $\bar{\mathcal{S}}(u, v) > \bar{\mathcal{S}}(u, v^*)/2$ is satisfied.

$\omega^* \propto \delta p$] (see [9]), which coincides with the crossover from Debye to isostatic behavior, interpreted as the paradigmatic boson peak [50, 51, 52, 53] of glasses [54]. Near jamming or RP, this point marks the onset of the enhancement of the population of low-energy modes [55] leading to a flat density of states at low frequency [55, 2]. At fixed v, $\bar{\mathcal{S}}$ plateaus at a value of u of $O(1)$ (i.e. at $q \propto |\delta p|^{1/2}$). Our explicit formulas also provide a simple tool to map the global behavior of many quantities of interest. For example, Fig. 2.7(b) shows a diagram in terms of rescaled wavevector u and frequency v marking the boson peak (blue-dashed line) and regions where $\bar{\mathcal{S}}(u, v)$ exhibits power-law behavior. The blue region indicates the neighborhood of the boson peak, in which $\bar{\mathcal{S}}(u, v) > \bar{\mathcal{S}}(u, v^*)/2$, and the red and yellow regions show power-law regimes in u and v.

Near jamming, the two-time density-density correlation function $S_{nn}(r-r', t-$

t') in real space is given by,

$$S_{nn}(r, r', t, t')/S_0 \approx |\delta p|^{(2+D)\nu-\gamma} \mathcal{S}\left(\frac{(r-r')/\ell_0}{|\delta p|^{-\nu}}, \frac{(t-t')/t_0}{|\delta p|^{-z\nu}}, \frac{\delta p_B/\delta_0}{|\delta p|^{\varphi}}\right), \tag{2.59}$$

where ℓ_0 and t_0 are nonuniversal scaling factors, and

$$\mathcal{S}(\rho, s, w) = \int d\mathbf{u}\, dv\, e^{i(u\cdot\rho - vs)}\, \frac{\mathrm{Im}\,\mathcal{P}(u, v, w)}{v}, \tag{2.60}$$

where ρ and s are arguments for the universal scaling function $\mathcal{S}$ associated with the re-scaled distance and time, respectively. The behavior near RP is obtained by replacing $\mathcal{S}$ and $\mathcal{P}$ by $\bar{\mathcal{S}}$ and $\bar{\mathcal{P}}$, respectively, along with appropriate changes for the exponents (see Table A.1). Equation (A.61) and the corresponding equation for RP lead to definitions of diverging length and time scales, $\ell = |\delta p|^{-\nu}\ell_0$ and $\tau = |\delta p|^{-z\nu}t_0$, respectively. Our characteristic length scale diverges as $|\delta p|^{-1}$ for jamming, and as $|\delta p|^{-1/2}$ for RP. These divergences should be compared with traditional definitions of $\ell_c \sim |\Delta z|^{-1/2}$ and $\ell^* \sim |\Delta z|^{-1}$, as discussed in the literature [56, 57, 58, 38, 39], Note that ν in our paper should not be confused with exponents for the finite-size scaling of the probability density $\Delta \sim L^{1/\nu}$, as reported in [59].

In this letter, we have combined scaling theory and the EMT of Ref. [2] to produce analytical formulas for universal scaling functions for the longitudinal dynamical response near both jamming and RP. Our equations can be used to determine the space-time dependence of universal functions for several quantities (such as moduli, viscosities and correlations) near the onset of rigidity in both the solid and liquid phases. A direct approach to experimentally validate our predictions consists of using 3D printers to fabricate and perform experiments on the disordered elastic networks illustrated in Figs. 2.4(a) and (b). We

also expect these scaling forms to apply to more traditional glass forming systems such as colloidal suspensions. Here, in addition to more standard scattering measurements, new techniques for measuring 3D particle positions and even stresses with high precision may make it feasible to measure these functional forms and test our predictions [60, 61, 62, 63]. In such suspensions, we expect that the scaling functions will capture the behavior in the elastic regime. However, our theory is built on a fixed network topology and lacks some features of the liquid phase. Annealed rather than quenched disorder [34] (or even intermediate disorder [64]) could be needed to describe viscoelastic fluids. An extension of our analysis includes an investigation [65] of the intriguing connections between the featureless low-energy modes in our system and the unconventional particle-hole continuum measured using momentum and energy-resolved spectroscopic probes in certain strange metals [66, 67]. Other extensions could include the incorporation of anisotropic bond occupation [3], which plays a major role in the crossover scaling of thickening suspensions near frictional jamming [68] and that can lead to simpler models for both shear jamming [69] and thickening [70], as well as the incorporation of random stress fields, which can elucidate the unjamming of colloidal suspensions (such as titanium dioxide) due to activity [71].

2.3.3 Acknowledgments

We thank Andrea Liu, Bulbul Chakraborty, Daniel Hexner, Eleni Katifori, Emanuela del Gado, Itay Griniasty, Matthieu Wyart, Meera Ramaswamy, Peter Abbamonte, Sean Ridout, Tom Lubensky and Xiaoming Mao for useful conversations. This work was supported in part by NSF DMR-1719490 (SJT and JPS),

NSF CBET Award # 2010118 (DBL, ES, JPS, and IC) and NSF CBET Award # 1509308 (ES and IC). DBL also thanks financial support through FAPESP grants # 2016/01343-7 and # 2021/14285-3. DC is supported by a faculty startup grant at Cornell University.

CHAPTER 3

ANALOGIES BETWEEN GRANULAR MATERIALS AND HIGH-TEMPERATURE SUPERCONDUCTORS

3.1 Strange metals and strange response

Much interest has formed in recent years regarding high-temperature superconductors. Materials with very complicated chemical compositions have been synthesized in efforts to push the superconducting temperature ever higher, with the eventual goal of a stable room-temperature superconductor at ambient pressure. The superconducting phase of any material is typically quite boring. In the cuprates, for instance, many of the superconducting phases are well-described by a Ginzburg-Landau theory. Outside of the superconducting phase, however, these materials show a rich sequence of phases, depending upon the chemical composition (dopant concentration). A typical phase diagram consists of a Fermi liquid-like phase (though even this is controversial), a "strange metal" phase, a pseudogap phase, and an antiferromagnetic phase. The characterization of the phase behavior is typically qualitative, and aside from the true antiferromagnetic ordering, there do not appear to be sharp phase transitions that separate the phases (Figure 3.1).

Superimposed on top of these phases is the superconducting dome, which is named after its semicircular shape. At low and high concentrations of (hole) dopants, the superconducting temperature is heavily suppressed. At some optimal dopant concentration, the superconducting temperature is maximal. Invariably, above the superconducting temperature at optimal doping, the cuprates enter a "strange metal" phase, which is usually said to be characterized by a T-

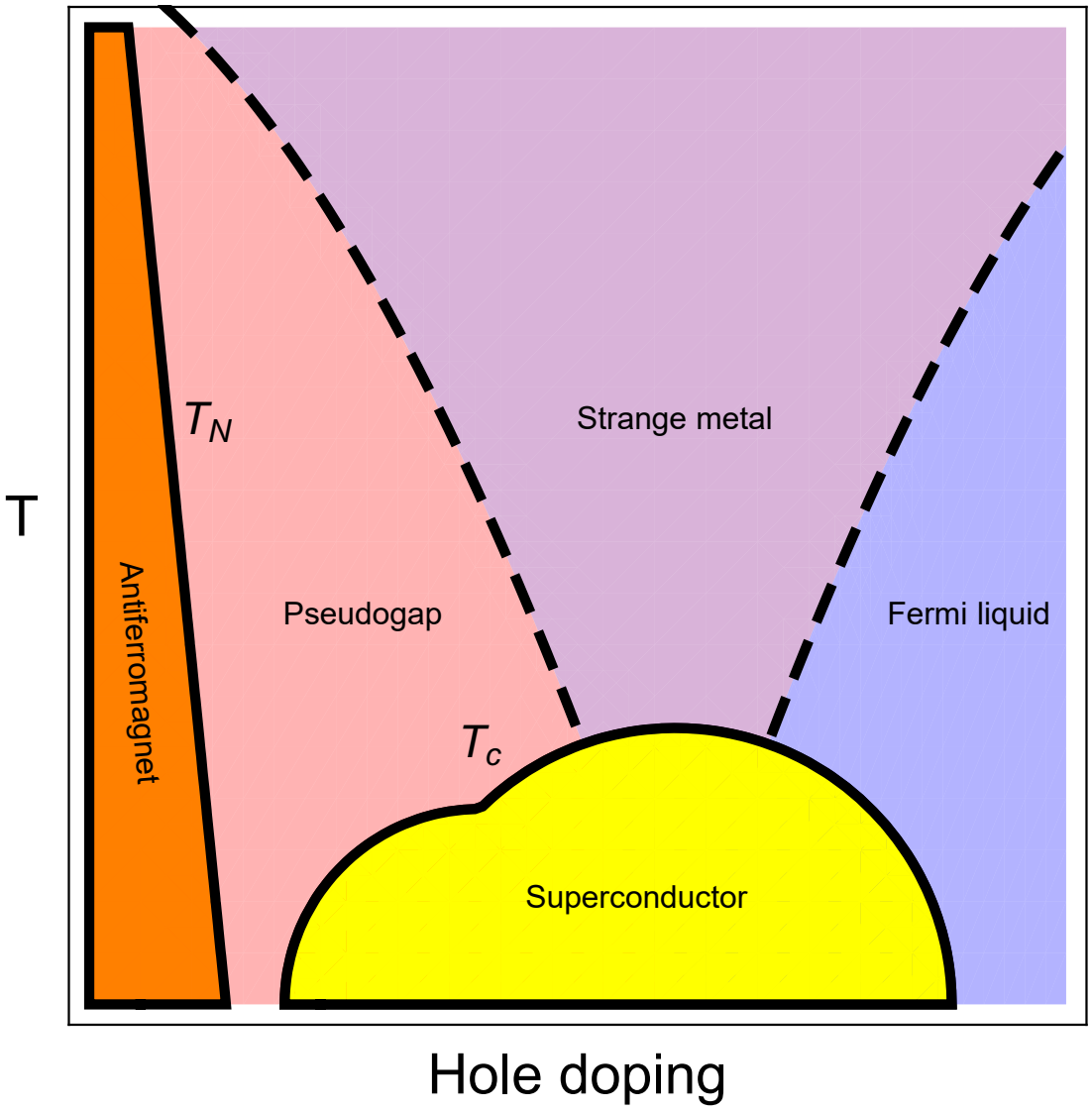

Figure 3.1: A schematic of the phase diagram of a high-temperature superconductor as hole doping and temperature is varied. T_c is maximal at optimal doping. A point at zero temperature inside the superconducting dome appears to control the crossover from Fermi liquid to strange metal.

linear resistivity $\rho \sim T$ over a wide range of temperatures in contrast to the scattering in ordinary metals $\rho \sim T^2$. Experimental measurements of other response properties of high-temperature superconductors in this phase have been performed to shed light upon the microscopic origin of this unusual behavior [66, 67]. In particular, momentum-resolved electron energy loss spectroscopy (M-EELS) can be used to extract full susceptibilities, mapping energy losses ω at different q to $\chi''(q,\omega)$ and using the Kramers-Kronig relation to reconstruct the full $\chi(q,\omega)$.

These experiments reveal a structure to the electronic density fluctuations that is quite unlike that of an ordinary metal. In the ordinary (charged) Fermi liquid, there are generally two types of excitations. Particle-hole excitations occur when electrons are excited from their place within the Fermi sea to a location outside of the Fermi sea. These kinds of excitations are kinematically constrained since the Fermi sea is largely filled, so free electrons can only be excited to locations outside of the Fermi surface. Their energies are constrained to satisfy [12]

$$\frac{\hbar^2 q^2}{2m} - \frac{\hbar^2 k_{\mathrm{F}} q}{m} \leq \hbar\omega \leq \frac{\hbar^2 q^2}{2m} + \frac{\hbar^2 k_{\mathrm{F}} q}{m} \implies \left(\frac{q}{k_{\mathrm{F}}}\right)^2 - 2\left(\frac{q}{k_{\mathrm{F}}}\right) \leq \frac{\hbar\omega}{E_{\mathrm{F}}} \leq \left(\frac{q}{k_{\mathrm{F}}}\right)^2 + 2\left(\frac{q}{k_{\mathrm{F}}}\right), \quad (3.1)$$

which can also be determined by examining where the imaginary part of the Lindhard function is nonzero. Aside from these excitations, the charged Fermi liquid also features plasmons, whose dispersion can be computed within the RPA as the location of the pole in the response function:

$$\omega(q) = \sqrt{\frac{3\hbar^2 k_{\mathrm{F}}^2}{5m^2} q^2 + \omega_{\mathrm{P}}^2} \implies \frac{\hbar\omega(q)}{E_{\mathrm{F}}} = \sqrt{\frac{12}{5}\left(\frac{q}{k_{\mathrm{F}}}\right)^2 + \left(\frac{\omega_{\mathrm{P}}}{E_{\mathrm{F}}}\right)^2}, \quad (3.2)$$

where the plasma frequency $\omega_{\mathrm{P}} = \sqrt{4\pi e^2 n_0/m}$ is related to the charge e, number density n_0, and mass m of the carriers. At higher values of q, the plasmon's

dispersion inevitably takes it into the region of particle-hole excitations, and the plasmon ultimately rapidly decays into particle-hole excitations and loses its quasiparticle status in a process known as Landau damping (see Figure 3.2). Although these calculations are performed for the free electron gas, metals that behave as Fermi liquids show many of these features due to the generality of the argument for the plasmon's existence (Goldstone's theorem + Anderson-Higgs mechanism). Under the assumptions of adiabatic continuity, quasielectrons and quasiholes also are generated in Fermi liquids, and so density response probes of ordinary metals show a sharply dispersing plasmon over a range of q before the plasmon is heavily overdamped by the continuum of particle-hole excitations.

In the strange metal, even down to $q \sim 0.1$ r.l.u., there is no evidence of a plasmon [66, 67]. There are slow changes in the shape of $\chi''(q, \omega)$ if one measures down to $q \sim 0.05$ r.l.u., but nothing close to what is seen in ordinary Fermi liquids occurs here. If the arguments of Goldstone's theorem still apply, one is led to conclude that there is a continuum of very low-energy excitations in the strange metal into which the plasmonic mode can decay. Unlike the particle-hole continuum in Fermi liquids, the excitations must extend to much lower wavevectors than the particle-hole continuum in Fermi liquids. Microscopic theories that predict such a continuum of excitations have been lacking.

The measured featureless response functions, however, look superficially similar to the featureless response functions that are measured close to the jamming transition, where compressed collections of particles first form a disordered contact network and the resulting amorphous material can first support a bulk strain. In a continuum elastic membrane, there are certainly phonons

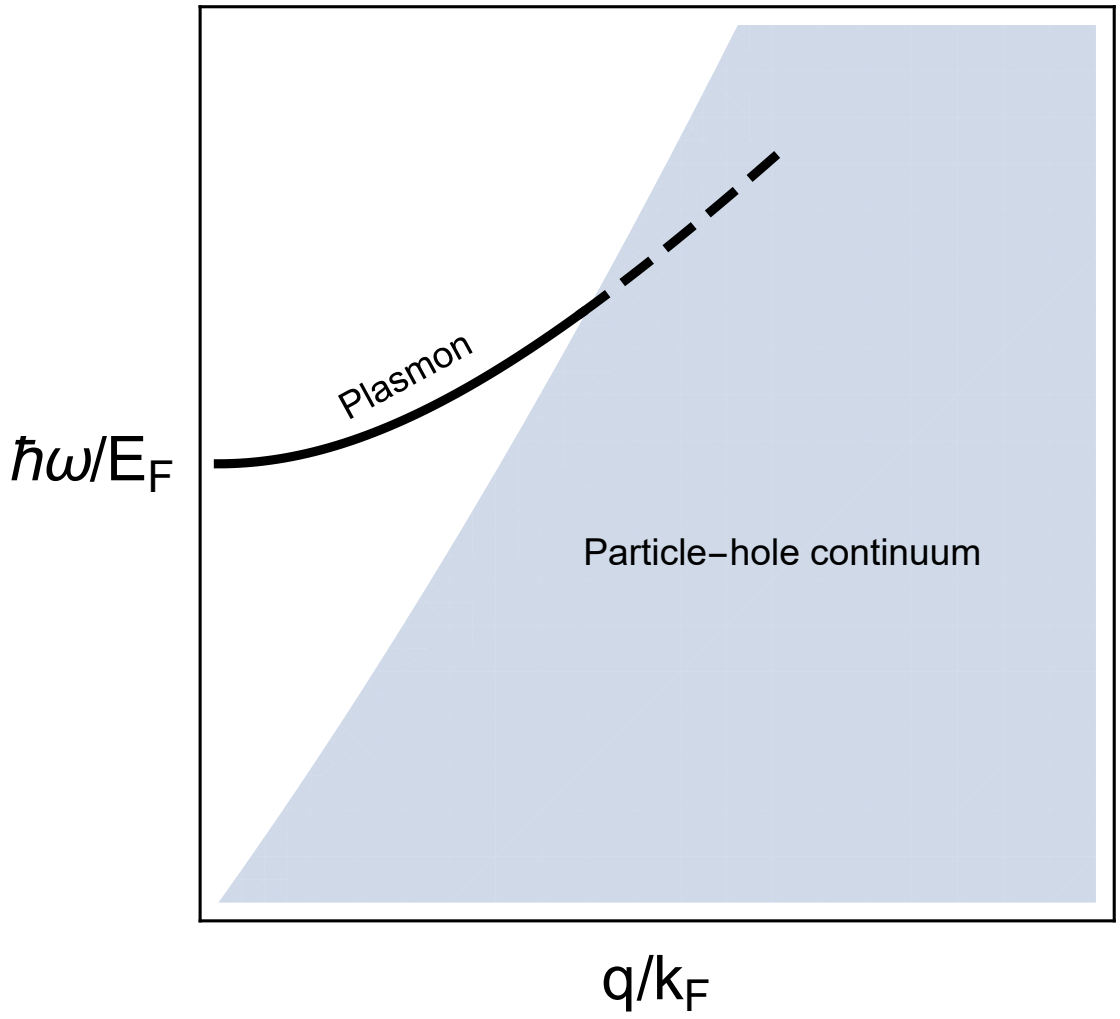

Figure 3.2: Summary of the excitations in a charged Fermi liquid. The plasmon decays into the particle-hole continuum via Landau damping.

that must exist by Goldstone's theorem. However, in the heavily disordered amorphous solid close to its unjamming transition, these phonons are heavily damped by the disorder intrinsic in the tenuously connected network that transmits stress through the material. The situation is similar in elastic networks close to their rigidity percolation transition. To detect the vibrational excitations in the case of elastic networks, one can examine the spectrum of normal modes and compute the density of states at each frequency. Close to rigidity percolation, there are large, rigid sections of the lattice connected by only a single bond

to a rigid backbone (there are also zero modes that arise from disconnected sections of the network, but these are often ignored). The density of states near the transition correspondingly becomes flat down to a very low frequency $\omega_\star$ that is set by the distance to the transition. In this way, the damping of the phonon that is induced by the disorder can be viewed as a decay into the many low-lying vibrational modes that exist near the transition. The nature of these low-lying modes is controlled by the universal features of the critical point.

Correspondingly, the universal existence of the strange metal phase of high-temperature superconductors is often attributed to the existence of a zero-temperature quantum critical point. This critical point is presumably shielded from experiments by the superconducting dome, but the universal features associated with the critical point can still control material properties deep into the strange metal phase. With this picture in mind, we investigate whether the universal properties of the response near the rigidity percolation critical point investigated in Chapter 2 are sufficient to describe features of the susceptibility measured for a strange metal. In both cases, we have a zero-temperature critical point that controls the onset of a spectrum of low-frequency excitations that leads to the decay of the Goldstone modes. The response in the strange metal also shows interesting changes as the dopant concentration is modified, which we are able to partially explain through a mapping from dopant concentration to bond occupation probability in an elastic network model.

In contrast to other attempts to describe the featureless continuum using e.g. holographic techniques [72], our analysis predicts that a sharply dispersing plasmon should exist at q lower than that measured in the experiment. It also makes some predictions about the crossover into the pseudogap phase which

we do not investigate in detail (largely because we do not believe the effective medium theories used to generate the response functions on the floppy side of the transition are accurate even for the rigidity problem they purport to solve). The predictions of the theory are imperfect. At asymptotically large q (which can be made arbitrarily small by changing the distance to the critical point), the shape of the imaginary part of the response is largely q-independent as in the experiment. However, the experiment shows a plateau in the response over a range of frequencies followed by a $\sim \omega^{-2}$ decay that seemingly violates f-sum rules. Other theories have plausible alternative explanations for this, including that the f-sum rule is rendered finite by a logarithmic term $\sim \omega^{-2} \log^{-2} \omega$ [73]. We reproduce the plateau by assuming long-wavelength inhomogeneities that serve to average the susceptibilities over a range of distances to the critical point. Far from the critical point, this averaging process is essentially irrelevant. However, when the scale of the disorder is comparable to the distance to the critical point, the imaginary part of the response function contains a featureless plateau similar to the experiment before crossing over to an anomalous $\sim \omega^{-1}$ falloff, also indicating violation of f-sum rules. This eventually crosses over into an $\sim \omega^{-3}$ decay at an energy scale that is controlled by the distance to the critical point in the elastic membrane, rendering the f-sum rules finite.

Although the microscopic origin of the low-energy excitations that lead to the destruction of the plasmon in BSCCO remain mysterious, the picture of a continuum of low-lying excitations that is controlled by the zero-temperature quantum critical point remains a promising avenue for future research. It would suffice to develop a quantum theory with a zero-temperature transition in the same universality class as those seen in high-temperature superconductors to

describe the crossover from Fermi liquid to strange metal.[1] The comparisons between the universal scaling forms of the susceptibilities near this transition would then proceed identically to the classical-quantum correspondence that we investigate in our manuscript. Such a microscopic understanding of the relevant physics might get us closer to designing materials with higher T_c.

In the following manuscript, I generated all figures and helped to edit the text. I also searched through the parameter space of δp (distance to the critical point) and σ (width of the distribution of long-wavelength disorder) to generate response functions that agreed well with the features that were seen in the M-EELS experiment. Danilo Liarte and Jim Sethna were invaluable in their comments on the different types of response functions and the applicability of the universal forms to the experimentally measured density response. Debanjan Chowdhury had the idea to apply our previously developed jamming response functions to the decidedly quantum problem of strange metals and wrote the full first draft of the manuscript. Peter Abbamonte performed the M-EELS experiments on BSCCO that we sought to describe, provided valuable insight into the specifics of the experiment and the extraction of momentum-resolved response functions, and assisted in the later stages of edits to the manuscript.

3.2 Jamming and unusual charge density fluctuations of strange metals

This is a reformatted version of the manuscript appearing as Nature Communications 14, Article number: 3919 (2023) [65].

[1] This is obviously hard.

3.2.1 Abstract

The strange metallic regime across a number of high-temperature superconducting materials presents numerous challenges to the classic theory of Fermi liquid metals. Recent measurements of the dynamical charge response of strange metals, including optimally doped cuprates, have revealed a broad, featureless continuum of excitations, extending over much of the Brillouin zone. The collective density oscillations of this strange metal decay into the continuum in a manner that is at odds with the expectations of Fermi liquid theory. Inspired by these observations, we investigate the phenomenology of bosonic collective modes and the particle-hole excitations in a class of strange metals by making an analogy to the phonons of classical lattices falling apart across an unconventional jamming-like transition associated with the onset of rigidity. By making comparisons to the experimentally measured dynamical response functions, we reproduce many of the qualitative features using the above framework. We conjecture that the dynamics of electronic charge density over an intermediate range of energy scales in a class of strongly correlated metals can be at the brink of a jamming-like transition.

3.2.2 Introduction

A hallmark of numerous interacting phases of quantum matter are their long-lived collective excitations (such as phonons, magnons, and skyrmions). Microscopically, these collective modes require a coherent motion of the constituent particles in the system. While such modes often have a long lifetime at low energies, they are prone to decay once they encounter the multi-particle contin-

uum at high energies. Even in weakly interacting metals, there are two kinds of long-lived excitations — the plasmon, which represents a collective (longitudinal) density fluctuation, and single-electron like quasiparticle excitations near the Fermi surface. The plasmon eventually decays at large enough momentum and frequency (i.e. for $\omega > \omega_\star(q)$) into the multi-particle continuum due to purely kinematic reasons. Within Landau's original formulation of Fermi liquid (FL) theory for electrically neutral fermions (e.g. as in liquid Helium-3) [74], the zero-sound mode is associated with a collective oscillation of the entire Fermi surface and has properties that are qualitatively similar to a longitudinal acoustic phonon. The sound mode gets renormalized into the plasmon mode in the presence of Coulomb interactions. It is natural to consider the fate of collective modes and their possibly unconventional decay into multi-particle continua in the regime of strong interactions.

Recent advances in the experimental technique of momentum-resolved electron energy-loss spectroscopy (M-EELS) [75] have made it possible to measure the dynamical charge response of numerous strongly correlated materials over a broad range of frequencies and momenta [66, 67, 76]. Focusing specifically on the strange metal regime of a cuprate material (BSCCO), these experiments report evidence of a featureless particle-hole continuum extending over most of the Brillouin zone (BZ), while being independent of temperature and doping. Remarkably, the unconventional continuum persists up to the highest measurable energies and accounts for more than 99% of the total spectral weight in the $f-$sum rule [66, 67]. Perhaps the most noteworthy observation is the absence of a sharply dispersing plasmon in the BZ (except for a narrow range of momenta, $q \lesssim 0.05$ r.l.u., near the $\Gamma-$point [77, 78]), as it decays into the featureless continuum. Evidence for such a continuum has been reported in earlier Raman studies

[79, 80] and recent M-EELS measurements in other strongly interacting metals (e.g. Sr_2RuO_4 [76]). The microscopic origin for the decay of the plasmon into such continua remains unclear. Recent theoretical works have utilized solvable lattice electronic models [81] to analyze the unconventional particle-hole continuum [82] and the anomalous decay of plasmons [73] in the strongly correlated regime of certain non-Fermi liquid metals; see Ref. [83] for a complementary holographic computation of plasmon decay.

In addition to the anomalous dynamics of the charge density fluctuations, the normal metallic state across a number of strange metals exhibits universal scattering lifetimes [85, 86, 87, 88] and violates the Mott-Ioffe-Regel limit with increasing temperature [89, 90], suggesting an absence of electronic quasiparticles with a long mean-free path and lifetime. A satisfactory theoretical explanation for the complex and universal aspects of this phenomenology does not presently exist starting from microscopic models.

These results point to the intriguing possibility of the strongly interacting electron fluid forming a collective and self-organized, nearly jammed state. At intermediate energy scales, it is conceivable that certain aspects of the dynamical response associated with the collective modes can be understood by drawing analogies to a strongly correlated classical liquid. By analyzing the universal behavior of such a liquid near the onset of rigidity (Fig. 3.3(a)) and a detailed comparison to recent M-EELS experiments in cuprates, we conjecture that the intermediate-scale charge-dynamics in strange metals belongs in the family of a class of theories with critical rigidity correlations. This brings together a new class of problems under the umbrella of jamming, which includes rigidity transitions observed in colloids and granular materials [14, 69], living

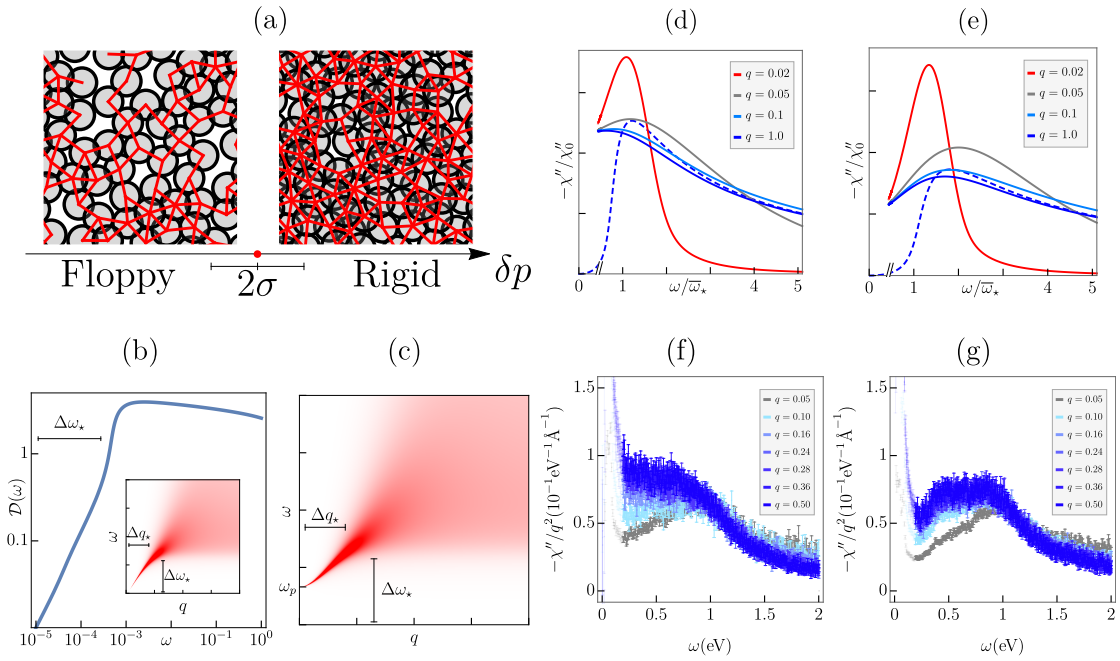

Figure 3.3: **Charge-density response near onset of rigidity and in strange metals.** (a) A random network of bonds (red) displayed in a rigid vs. floppy system, on either side of a continuous rigidity percolation (RP) transition; the critical properties near RP are distinct from a jamming transition associated with random packings of hard spheres [14]. We hypothesize that the two-particle density response over a broad range of intermediate energies near the hole-doping induced transition associated with the electrons near optimal doping in cuprates [84] can be described as a rigidity-type transition. (b) The vibrational density of states, $\mathcal{D}(\omega)$, as a function of frequency (ω) at a fixed distance from the RP critical point $\delta p = 10^{-3}$. The plateau in $\mathcal{D}(\omega)$ onsets for $\omega > \Delta\omega_\star \sim |\delta p|$. Inset: The polarization function, $\Pi''(q,\omega)$, in the absence of Coulomb interactions, as a function of q and ω, revealing the acoustic collective mode and its damping inside the continuum. (c) The density response function, $\chi''(q,\omega)$, (including the Coulomb interaction) with $\omega_p = 0.66\,|\delta p|$. The response functions, $\chi''(q,\omega)$, averaged over a range of $|\delta p| \leq \sigma$ (see (a)) as a function of ω for different q at a fixed distance (δp) from RP for (d) $|\delta p| = 1.1 \times 10^{-3}$, $\sigma = 0.9 \times 10^{-3}$, and (e) $|\delta p| = 1.6 \times 10^{-3}$, $\sigma = 0.9 \times 10^{-3}$. The plasma frequency is chosen to be at $\omega_p = 0.5\,\overline{\omega}_\star$. The dashed line represents the q-independent shape of the imaginary part of the susceptibility in the absence of disorder. Frequencies in (d) and (e) are rescaled by the same scaling frequency $\overline{\omega}_\star$ associated with the average distance to the transition δp; see the Methods section for details. Experimental data from M-EELS [66] demonstrating the overall q-independent shape of the continuum for (f) optimally doped BSCCO and (g) overdoped BSCCO. Error bars represent statistical (Poisson) error. The lowest frequencies show the lattice phonon, which we do not describe in our framework.

tissues [25, 91], elastic networks [1, 5, 2, 21], dislocation systems [92, 93], deep learning [26], and analogues of metal-insulator transitions for interacting quantum bosons [94]. Quenched randomness in geometrically frustrated magnets has also been shown to produce a jammed spin liquid [95], which is known to display unconventional spin-dynamics [96].

In this manuscript we address the question of what phenomenon might give rise to a largely momentum-independent continuum such as that observed in M-EELS experiments. We conjecture that these observations might be connected to phenomena characteristic of the rigidity transition in granular media [14]. Near such a transition, the vibrational density of states develops an anomalous, nearly frequency-independent plateau [55, 50]. This paper will be concerned with addressing the similarities between the experimentally measured density correlations of strange metals and the calculated density correlations near the onset of rigidity, based on our recent analysis of the density response near a rigidity transition [9].

3.2.3 Results

The onset of rigidity in classical liquids (but without any long-range crystalline order) has a complex dynamical signature. The transition is associated with a singular rearrangement of the low-energy vibrational spectrum of the nearly rigid solid [14]; see Fig. 3.3(b). These low-energy excitations will become the analog of the unconventional particle-hole continuum in the strange metal that we described above. Moreover, the longitudinal phonons in these viscoelastic systems can decay into this continuum of low-energy vibrational excitations,

much like the plasmons do in the cuprate strange metal.

Starting with scaling forms for the longitudinal susceptibility that were derived recently by some of us [9, 45], we will write down a coarse-grained effective description for the long-wavelength and low-frequency bosonic excitations in a liquid at the brink of rigidity percolation (RP); see Fig. 3.3(a). Percolation is a transition in connectivity; rigidity percolation is a transition from elastic to floppy, with a dramatic peak in low-energy excitations we believe common to strange metals. We will extend our formalism to analyze the inelastic density-density response using the predictions of our scaling theory and make direct comparisons with the M-EELS results, highlighting the similarities between the mechanism for anomalous decay of the plasmon into the continuum at momenta away from the $\Gamma-$point. Given the relatively large energy-scales over which the charge response has been probed, it is likely that the quantum critical collective modes associated with various forms of broken symmetries that emerge at low-energies [84] do not play a fundamental role in the interpretation of the M-EELS experiments.

Our starting point is based on a recently proposed scaling ansatz for the dynamical susceptibilities near classical jamming and RP [9, 45]. There has been a dearth of solvable models in finite dimensions where universal features of the dynamical susceptibilities can be analyzed in a reliable fashion; we utilized the tractable effective medium theory [2] to compute these in Ref. [9, 45] and obtained their explicit analytical forms. Given that the strange metals where the anomalous density fluctuations have been observed are quasi two-dimensional, we will model our system as a stack of weakly coupled two-dimensional layers. The individual layers are described in terms of a randomly percolated lattice

of harmonic springs (Fig. 3.3(a)); the connection to the density fluctuations of an underlying electronic fluid will be made explicit later. For our present discussion, we will start specifically with the longitudinal part of the displacement response, Ξ_L, near RP,

$$\Xi_L(q,\omega) \approx -|\delta p|^{-\gamma}\mathcal{L}\left(\widetilde{q},\widetilde{\omega}\right), \tag{3.3a}$$

$$\widetilde{q} \equiv \frac{q}{|\delta p|^{\nu}},\ \widetilde{\omega} \equiv \frac{\omega}{|\delta p|^{z\nu}}, \tag{3.3b}$$

where q and ω represent the wavevector and frequency, respectively, and $|\delta p|$ represents the deviation away from the critical point. The critical exponents for susceptibility, correlation length, and correlation time are denoted γ, ν and z, respectively. For RP, our calculation leads to $\gamma = 2$, $z = 2$ and $\nu = 1/2$. In two-dimensions, the above scaling form has additional dependence on the logarithms of the scaling variables which do not qualitatively affect any of our results; a detailed discussion of the origin of these additional logarithms will be discussed elsewhere (see Sec. I of the Supplementary Information [97] for more details). $\mathcal{L}\left(\widetilde{q},\widetilde{\omega}\right)$ is a universal scaling function whose explicit form appears in the Methods section. In all of our subsequent analysis and in our comparison with the experimental results, $\Xi_L(q,\omega)$ will play a central role. Near RP, the transverse response, $\Xi_T\left(q,\omega\right)$, has the same universal scaling form as $\Xi_L\left(q,\omega\right)$ but with different non-universal constants.

The onset of rigidity is tied to a significant rearrangement of the vibrational density of states, $\mathcal{D}(\omega)$; see Fig. 3.3(b) and Methods for a definition. Near RP, $\mathcal{D}(\omega) \sim \omega$ for $\omega \lesssim \Delta\omega_\star \sim |\delta p|$ (up to additional logarithms). For $\omega \gtrsim \Delta\omega_\star$, $\mathcal{D}(\omega)$ has a remarkably flat continuum as a function of ω over several orders of magnitude of frequencies; see Fig. 3.3(b). The physical origin of this low-energy continuum is related to the boson peak that demarcates a crossover from Debye

to isostatic behavior, and is a recurring feature in the physics of glassy systems [50, 52, 53]. From the point of view of our analogy to the excitations in the strange metal, these modes are naturally interpreted as the particle-hole continuum. This analogy will become more direct when we analyze the nature of the collective excitations — these are the phonons of the solid becoming floppy, which turn into the plasmon in the strange metal with the inclusion of Coulomb interactions — and their decay into the flat $\mathcal{D}(\omega)$ near RP.

In order to make the analogy between classical liquids and their vibrational excitations to the collective modes in strange metals, we need a precise relationship between the longitudinal susceptibility (Ξ_L) and the electron density correlation functions. As in the jellium model, we assume the negatively charged electronic liquid co-exists with a uniform oppositely charged (static) background to maintain electrical neutrality; we are only interested in the dynamics of the former. In the proposed model, the changes in the local displacement, $\mathcal{U}$, are tied to a local fluctuation of the electronic number density. More precisely,

$$n(\boldsymbol{x}) = n_0(1 - \nabla \cdot \mathcal{U}), \tag{3.4}$$

where $n_0 = \rho/m$ is the average background density. One of the central quantities of interest is the polarization function, $\Pi(q, \omega) = n_0^2 q^2 \, \Xi_L(q, \omega)$, which is related to the longitudinal susceptibility introduced earlier. This is the density-density response of the neutral system near the transition. Since the electronic liquid is charged and interacts via repulsive Coulomb interactions, $V(|\boldsymbol{x} - \boldsymbol{x}'|)$, we include it explicitly as

$$\Delta U = \frac{1}{2} \int_x \int_{x'} \delta n(x) V(|\boldsymbol{x} - \boldsymbol{x}'|) \delta n(x'), \tag{3.5}$$

where $\delta n(\boldsymbol{x}) = n(\boldsymbol{x}) - n_0 = -n_0 \nabla \cdot \mathcal{U}$. The experimentally measured density-

density response, $\chi(q,\omega)$, can be obtained from the polarizability after including the effects of Coulomb interactions,

$$\chi(q,\omega) = \frac{\Pi(q,\omega)}{1 - V(q)\Pi(q,\omega)}. \tag{3.6}$$

In the remainder of this study, we will calculate $\chi(q,\omega)$ near RP using the universal form of $\Xi_L(q,\omega)$, and highlighting both its similarities and differences when compared against the experimentally measured density response function in the cuprate strange metal. See Sec. II of the Supplementary Information [97] for more details.

To analyze the effect of the plasmon decay into the continuum, it is conceptually simpler to approach the transition from the rigid side. The imaginary part of the susceptibility, $\chi''(q,\omega)$, reveals a sharply dispersing plasmon for $\Delta q_\star \sim |\delta p|^{1/2}$ (up to logarithms), controlled by the distance to RP (δp), that broadens significantly as a result of decay into the low-energy vibrational states over a broad range of wavevectors and frequencies; see inset of Fig. 3.3(b). The effect of $V(q)$ on $\chi(q,\omega)$ is to renormalize the acoustic mode to the plasma frequency, $\omega_p = \sqrt{4\pi e^2 n_0/m}$, where we have assumed the three-dimensional form, $V(q) = 4\pi e^2/q^2$; see Fig. 3.3(c). The broadening of the plasmon due to decay into the unconventional continuum remains identical. The phenomenology described here is exactly what we set out to achieve theoretically inspired by the M-EELS experiments in strange metals—a plasmon that is damped beyond small momenta $q \gtrsim \Delta q_\star$ into a featureless, low-energy continuum. The close similarity that we demonstrate between the unconventional decay of the phonon into the vibrational continuum near RP and of the plasmon into the measured particle-hole continuum in strange metals is one of the central results of this paper.

Let us next turn to studying the detailed $q, \omega-$dependence of $\chi(q, \omega)$ near RP in order to make further comparisons with the measured charge response functions. For the smallest values of q, there is a sharp plasmon that appears at the plasma frequency, ω_p. For $q \gtrsim \Delta q_\star \sim |\delta p|^{1/2}$, the plasmon broadens rapidly, and $\chi(q, \omega)$ becomes nearly q-independent with a broad feature centered near $\Delta\omega_\star$. Increasing q further serves only to adjust the crossover frequency beyond which there is a crossover to a $1/\omega^3$ falloff, in accordance with the f-sum rule (see Figure 3.4(a)). The q-independent shape of $\chi''(q, \omega)$ is also shown as the dashed blue curve in Figure 3.3(d)-(e). This broad feature is tied to the same boson peak that was discussed above in the context of the onset of the enhancement of the low-energy modes in $\mathcal{D}(\omega)$.

Although our form of $\chi''(q, \omega)$ near the transition reproduces the strongly overdamped plasmon and the q-independent shape of the response over the measured frequency range, the response at the lowest frequencies does not have the characteristic plateau of the experiment. To address the possible origin of this feature, we can appeal to the inherent inhomogeneity that is present in these materials. There is experimental evidence for nanoscale electronic inhomogeneity across multiple families of cuprate single crystals (including, e.g. BSCCO) [98, 99]. For a given sample at a fixed nominal doping, the experiments probe the density response averaged over all of the inhomogeneous regions of the sample. To replicate this feature in our theoretical analysis, we sample and smear our results for $\chi(q, \omega)$ over a distribution of δp. We thus assume that the variations in doping level change the distance to the onset of rigidity. Our averaging presumes the disorder does not couple to the translational Goldstone mode of the transition (by solely changing the density of bonds). The doping, however, breaks translational symmetry, and pinning on defects is also known

to lower the threshold of rigidity [100, 101, 102, 103]. Adding the effects of pinning to our analysis could be fruitful in future work. The qualitative effects of the above averaging procedure are similar for any smooth, symmetric distribution.

Near the boson peak, the disorder-averaged susceptibility is most drastically altered. When the mean deviation from criticality is comparable to the width of the disorder distribution, $|\delta p| \leq \sigma$, the spectrum becomes dispersionless as a function of ω for large $q > \Delta q_\star$; see Fig. 3.3(d). Within our framework, the frequency-independent plateau observed near optimal doping can be interpreted as the disorder-induced smearing of the boson peak near RP. Beyond this featureless region, there is a crossover into an anomalous power-law regime, $\chi''(q,\omega) \sim 1/\omega^\alpha$ with $\alpha < 3$. Both of these features are similar to the experiments [66]; see Fig. 3.3(d)-(g) for a comparison. At the largest frequencies, the asymptotic forms of the polarization with and without disorder-averaging are identical with $\alpha = 3$. The shape of the susceptibility is largely independent of q over a wide range of ω. This leads to a q-independent crossover frequency from the plateau to a power-law fall off at large ω. As we move away from the transition fixing the magnitude of the disorder σ, the plateau at low frequencies evolves into a bump; see Fig. 3.3(e). This bump can be interpreted as a severely overdamped plasmon, whose location becomes nearly q-independent at large q. The q-independence is tied to the decay into the particle-hole continuum, whose onset is at a fixed $\Delta\omega_\star$.

The power-law scaling behavior of the singular part of the susceptibility χ'' before and after the inclusion of disorder averaging is illustrated in Fig. 3.4. At the highest frequencies, the power-law scaling is unaffected by the specific

type of disorder considered here. At low frequencies, we see the emergence of a plateau region whose width is q-independent (and set by the amount of disorder σ) for $q \gtrsim \Delta q_\star$. For experimental measurements close to this critical point, all wavevectors except for those closest to the center of the BZ will probe the incoherent plateau rather than the collective mode. The most notable difference between this framework and the one observed in the experiments is in the wavevector dependence of the magnitude of the response. If the response has a q-independent shape at all frequencies, then one infers that it must scale as $\sim q^2$ to satisfy the f-sum rule. The singular responses computed in this paper also satisfy the appropriate sum rules, since q sets the frequency at which we cross over into the Drude-type scaling $\sim \omega^{-3}$. See Sec. III of the Supplementary Information [97] for more details. A recent complimentary theoretical work [73] finds a distinct high-frequency scaling $\sim 1/\omega^2 \log^2(\omega)$, which is also consistent with the f-sum rule and is in better qualitative agreement with the experiments.

Within the framework of rigidity percolation, we have pointed out an intriguing analogy between the large collection of low-energy vibrational modes and the particle-hole continuum of strange metals, into which collective modes can rapidly decay. The onset energy of this decay is set by the distance to the critical point. Although the details of the specific momentum-dependence for the polarizability are not in perfect agreement with the MEELS experiment, we can reproduce a q-independent shape for $q > \Delta q_\star$ that is set by the distance to the critical point. It is possible that a different, and yet to be understood, universality class of rigidity transition displays a power-law density response that agrees better with the experiments. A broad implication of our hypothesis is that over a range of intermediate energy scales over which the density correla-

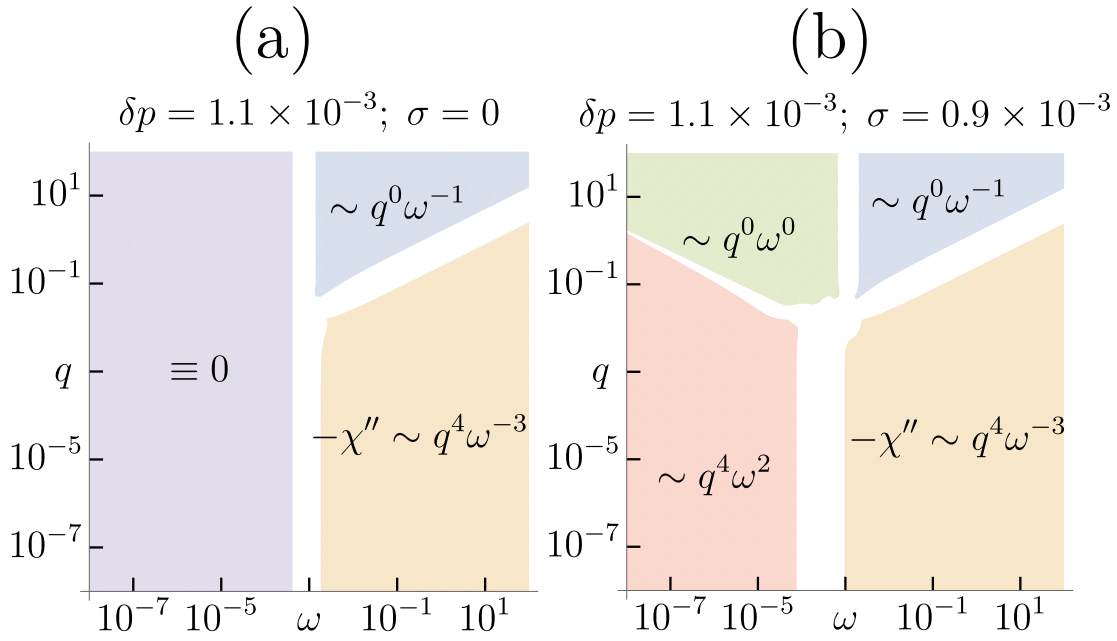

Figure 3.4: **Distinct spectroscopic regimes of the charge-density response.** Frequency and momentum dependence of χ'', (a) without ($\sigma = 0$) and (b) with ($\sigma = 0.9 \times 10^{-3}$) disorder averaging. Here $|\delta p| = 1.1 \times 10^{-3}$, $e = 10^{-4}$. In (a), the largest values of q lead to a bump in the susceptibility at a q-independent frequency $\Delta\omega_\star$, followed by a decay $\sim \omega^{-1}$ eventually crossing over into $\sim \omega^{-3}$ Drude-like behavior. In (b), a plateau in the response emerges at the lowest frequencies whose width is set by σ. The qualitative behavior is retained even after including corrections to the response that fix the scaling in the lowest frequency regime (see Fig. 3.3(d),(e)).

tions in strange metals appear to display features like jamming, the electronic fluid might also display interesting memory effects known to arise in glassy systems and near rigidity transitions. Finding new experimental ways to probe this physics remains an interesting future direction. Developing a microscopic quantum theory of interacting electrons whose effective theory reduces to an analogous rigidity transition is a challenging open problem [104, 94]. In this regard, exploring possible connections between the low-energy vibrational excitations near jamming and the low-energy non-quasiparticle-like excitations in the solvable quantum Sachdev-Ye-Kitaev models [81, 105] will be an interesting

theoretical exercise.

3.2.4 Methods

Universal scaling function

In three spatial dimensions and higher, the scaling function $\mathcal{L}(\widetilde{q},\widetilde{\omega})$ has the explicit form [9, 45]

$$\mathcal{L}(\widetilde{q},\widetilde{\omega}) = \left[a\,\widetilde{q}^2\,\mathcal{M}_{\pm}(\widetilde{\omega}) - \widetilde{\nu}(\widetilde{\omega})\right]^{-1}, \tag{3.7a}$$

$$\mathcal{M}_{\pm}(\widetilde{\omega}) = b\left[\sqrt{1 - c\,\widetilde{\nu}(\widetilde{\omega})} \pm 1\right], \tag{3.7b}$$

where a, b and c are constants, with $\widetilde{\nu}(\widetilde{\omega}) = \rho\,\widetilde{\omega}^2$ and $i\,\gamma\,\widetilde{\omega}$ for undamped and overdamped dynamics, respectively. Here ρ is a mass density and γ is a viscous drag coefficient. The plus and minus signs in $\mathcal{M}_{\pm}(...)$ correspond to the rigid and floppy states, respectively. We use the undamped form of the response exclusively.

Vibrational density of states

The vibrational density of states can be computed from

$$\mathcal{D}(\omega) = -\frac{\omega}{\pi}\int_{\mathrm{BZ}} d^2q\ \mathrm{Tr}\left(\mathrm{Im}\left[\mathcal{G}_{ij}\,(q,\omega)\right]\right), \tag{3.8a}$$

$$\mathcal{G}_{ij}\,(q,\omega) = \Xi_L\,(q,\omega)\,\hat{q}_i\hat{q}_j + \Xi_T\,(q,\omega)\left(\delta_{ij} - \hat{q}_i\hat{q}_j\right) \tag{3.8b}$$

The density of states has an additional ω prefactor as we are considering excitations in a classical disordered system.

Disorder averaging of charge-density response

We convolve our universal scaling function with a specific disorder distribution, such that the effective disorder-averaged polarization function takes the form (denoted '–')

$$\overline{\chi_{\delta p}(q,\omega)} = \int_{-\infty}^{\infty} d\,(\Delta p')\,\mathcal{P}_{\sigma}(\Delta p')\,\chi_{\delta p'}(q,\omega) \tag{3.9a}$$

$$\mathcal{P}_{\sigma}[\Delta p'] = \frac{1}{\sqrt{2\pi\sigma^2}} e^{-(\Delta p')^2/2\sigma^2}, \tag{3.9b}$$

where $\chi_{\delta p}(q,\omega)$ is the response at a fixed distance (δp) from RP, and we choose a Gaussian distribution, $\mathcal{P}_{\sigma}[\Delta p]$, with width σ and $\Delta p' \equiv \delta p' - \delta p$. For the forms of the response in Figures 3.3(d)-(e), the frequency is rescaled by $\overline{\omega}_{\star} = 10^{-3}$ in both figures, instead of the distinct δp. This is to make comparison to the experiment, where the dopant concentration is changed (moving the system further from a critical point in our framework), but not the frequency scale.

3.2.5 Acknowledgments

PA thanks Vincenzo Vitelli for suggesting a possible connection between jamming and the measured density response in Fig. 3.3. This work was supported in part by NSF DMR-1719490 (SJT and JPS). DC is supported by faculty startup funds at Cornell University. PA acknowledges support from the EPiQS program of the Gordon and Betty Moore Foundation, grant no. GBMF9452. DBL thanks financial support through FAPESP grants # 2016/01343-7 and # 2021/14285-3.

CHAPTER 4

UNIVERSAL SCALING OF VISCOELASTIC MATTER NEAR TWO DIMENSIONS

4.1 Renormalization group flows and normal form theory

The analysis that was performed in the manuscript in Chapter 2 was not completely satisfying to us. In the introductory section to Chapter 2, I show how two distinct (simplified) theories of the transition in the Ising model give identical predictions for certain quantities termed "universal:" critical exponents and scaling functions. Because these mean-field theories were so simple, I was able to cast them exactly into their scaling forms, with explicit formulas for the non-universal constants that need to be scaled away to put the asymptotic solution into universal form. In our original manuscript [9], we relied on numerical solutions, and previous analytic expansions, to cast solutions into their scaling form. However, the CPA is a closed set of self-consistent equations. Although they involve complicated integrals for any given choice of lattice Brillouin zone, the properties close to the phase transition, at low frequencies and long wavelengths, seemed to be independent of the choice of lattice. I very much wanted to find exact formulas for the right way to rescale the variables to match the numerical solutions.

Furthermore, there were a few quirks in the numerical solutions for the viscoelastic moduli close to the critical point. As these elastic networks approach the point where they lose their rigidity, the relevant frequency scales become very tiny (there are a huge number of low-energy modes that begin to appear, as evidenced by the density of states). The primary contribution to the integral

appearing in the CPA occurs at the phonon pole, which is placed very close to the origin and is sharply peaked. Often times, the true solution to the self-consistent equation would have a tiny negative imaginary part, but Mathematica required significant coaxing to return reasonable values for this imaginary part. On the liquid side of the transition for undamped dynamics, the imaginary part appeared to be zero for a range of frequencies that was much more numerically convincing than the numerical issues occurring on the solid side. The universal scaling form that we computed had this artifact on both sides of the transition, but there remained an open possibility that a singular correction to scaling could fix the low-frequency dissipation on the solid side.

Finally, as the dimension of space was reduced, the corrections to the scaling form seemed to become more and more significant in magnitude. In two dimensions especially, the collapse plots did not look very nice. Identifying relevant frequency scales (such as the scale at which the viscoelastic modulus' imaginary part was equal to its real part) and plotting them as a function of the distance to the critical point did not reveal anything seriously interesting; the critical exponents appeared identical to those seen in higher dimensions. All of these issues together led to a search for a closed-form expansion that would allow us to 1) describe the non-universal amplitudes of the scaling variables in terms of microscopic lattice parameters, 2) describe in an appropriate way the singular corrections to scaling necessary to describe low-frequency dissipation in the viscoelastic membrane close to the transition, and 3) give an explanation for the dimension-dependence of the amplitude of the corrections. The analytic structure that we found was much more interesting than what we expected.

Our first big breakthrough came in simplifying the integral term in the CPA.

As it is performed over a d-dimensional Brillouin zone, the integration region is generally a complicated polytope. However, close to the phase transition, the dominant contribution to the integral comes from the phonon pole at very low frequency. Quantities written for lattices like dynamical matrices and Green's functions greatly simplify in the limit of long wavelengths and low frequencies. For the rigidity transitions that we are focusing on, with linearly dispersing acoustic phonon modes and isotropy at the transition, the Green's function and dynamical matrix become isotropic tensors describing the dynamical modes of an isotropic elastic sheet, which has two independent stiffnesses (bulk and shear moduli). The integration region could then be replaced with a sphere without modifying the results of the expansion, with an upper wavevector cutoff given by q_{D} the Debye wavevector.

With this simplification in hand, the integrals could now easily be done analytically in integer dimensions. For $d = 3$, we could successfully compute the leading correction to scaling, which was a non-analytic $\sim \omega^{3/2}$ contribution to the self-consistent equation. The amplitude of this term could be folded into an invariant scaling combination U associated with a *dangerously* irrelevant variable: if one is interested in the scaling form very close to the transition, one can set $U = 0$. However, one then recovers the scaling functions derived in [2, 9], missing the low-frequency elastic dissipation. In $d = 2$, we found that the published scaling forms in [2, 9] are asymptotically *incorrect*: rather than a term like $\sim \omega^2$ appearing in the expansion, it was replaced with a term like $\sim \omega^2 \log(\omega)$. We first hinted at this kind of correction in the electron jamming manuscript [65], where the density fluctuations were occurring in pseudo-two-dimensional layered structures.

Our second breakthrough came in thinking deeply about the dimension dependence of the scaling of the self-consistent equation. For all integer dimensions $d \geq 3$, the leading-order scaling was identical. Suddenly, in $d = 2$, a logarithm has appeared. Why? Is two dimensions itself special, or does something happen in between two and three dimensions? These questions led us to attempt the expansion in arbitrary dimension d, rather than restricting to integer dimensions. This turned out to be a fruitful exercise: we unveiled that there is a completely new set of dimension-dependent critical exponents that governs the scale-invariance of the self-consistent equation below two dimensions. In this way, $d = 2$ represents the boundary between a set of exponents for the relevant variables that are dimension-independent ($d > 2$) and a set that are dimension-dependent ($d < 2$). This is a prediction for an "upper critical dimension" made by this particular theory.

With the complete analytical expansions at hand, the final step was to cast the scaling solutions into a form that was elegant and consistent with previous literature. The exercise in the upper critical dimension $d = 2$ proved especially difficult, since the invariant scaling combinations will inevitably involve logarithms of physical variables we care about, like ω. For this, we took inspiration from previous work on the analytic structure of renormalization group flows [49]. In a typical renormalization group procedure, one integrates out the high-frequency degrees of freedom and incorporates their effect into the low-energy modes. Commonly, this is done from the action, splitting the integral in momentum space into a high-energy sector and a low-energy sector and performing the integration over the high-energy sector. This can also be done in real space, such as in the decimation procedure for the Ising model: one groups small sets of neighboring Ising spins into a single degree of freedom, incorpo-

rating the fluctuations of the internal short-wavelength degrees of freedom into an effective interaction between the new spins and then rescaling the system to maintain the same microscopic length scale. In doing so, one reduces the correlation length by some factor related to the decimation procedure: if one integrates out every other spin but maintains the overall correlation structure, and then rescales the system by a factor of two to maintain the microscopic spin size, one transforms the correlation length as $\xi \to \xi/2$ in a single decimation step. Often, one abstracts to a continuous version of this decimation procedure, where the length scale changes by a factor of L/L_0 in each step. Then $\ell \equiv \log(L/L_0)$ tracks the number of decimation steps one performs, and one writes "flow equations" for parameters as a function of the single parameter ℓ, e.g.

$$\frac{\mathrm{d}\xi}{\mathrm{d}\ell} = -\xi. \tag{4.1}$$

This is an example of an equation giving a *renormalization group flow* – a prescription for how parameters in the model change with the decimation procedure.

Why does one apply this scale transformation in the first place? It helps to describe properties close to critical points. Note that the flow equation for the correlation length is only fixed if $\xi = 0$ or if "$\xi = \infty$," with the former being an attractive fixed point and the latter being a repulsive fixed point. In the Ising model, the correlation length is 0 for the $T = 0$ case (where the only possible configurations are the ground states of all +1 or all −1) and for the $T = \infty$ case (where all configurations occur with equal likelihood; the energy functional is irrelevant and all spins are independently randomly chosen to be ±1). The correlation length approaches infinity only at a critical point, where the system is correlated on all scales.[1] In this way, looking for sets of parameters that give

[1]The one-dimensional Ising model, where the spin decimation procedure can be performed

fixed points of renormalization group transformations can help one find critical points.

More importantly, perturbative analysis in the vicinity of the critical fixed point gives information about universal properties of the transition. For instance, one can often write a flow equation for the temperature T. If there is a critical renormalization group fixed point at T_c, one can transform this into a flow equation for the dimensionless variable $t \equiv (T - T_c)/T_c$ so that the critical fixed point is at $t = 0$ and is unstable. In the vicinity of the fixed point, the flows generically look like

$$\frac{\mathrm{d}\xi}{\mathrm{d}\ell} = -\xi, \qquad \frac{\mathrm{d}t}{\mathrm{d}\ell} = \lambda_t t \tag{4.2}$$

with $\lambda_t > 0$. Solving these flow equations starting at $(\ell = \ell_0, \xi = \xi_0, t = t_0)$ and eliminating $\ell - \ell_0$ gives

$$\xi = \xi_0 \left(\frac{t}{t_0}\right)^{-1/\lambda_t} \tag{4.3}$$

so that the eigenvalue appearing in the linearization of the flow at the fixed point characterizes the divergence of the correlation length with temperature near the fixed point. Typically this critical exponent is denoted $\nu \equiv 1/\lambda_t$. There are a wide variety of other critical exponents that commonly appear: β, for the magnetization, and δ, for an external field, appeared in the mean-field calculations in Chapter 2. There is also z, related to dynamics close to the critical point, α for specific heat, γ and η for correlation functions, and more. All of these exponents characterize the power-law relationships between parameters close to the critical point.

Now for a general piece of critical phenomena lore: phase transitions in

exactly, is a particularly unusual example. The correlation length $\xi = 0$ at $T = 0$, but $\xi \to \infty$ as $T \to 0^+$. One dimension is the lower critical dimension for the Ising model (so there is no phase transition at finite temperature). In $1 + \epsilon$ dimensions, there is a critical point at finite temperature that separates the high and low temperature phases.

high enough dimensions often take place with mean-field critical exponents.[2] The rough explanation for this is that ignoring fluctuations of certain degrees of freedom (a necessary step in deriving mean-field theories generally) can be justified in high dimensions. However, below some *upper critical dimension*, these fluctuations can no longer be ignored to capture the details close to the critical point accurately. In the Ising model, the upper critical dimension is well-known to be $d = 4$. In lower dimensions, the critical exponents can take strange values. For the $d = 2$ Ising model, the critical exponents are rational numbers (Onsager's exact solution gives many of them). In $d = 3$, the exponents can be computed to high precision using conformal field theory or non-perturbative methods (Chapter 6) and appear to be irrational numbers. Generically, the exponents change as a function of dimension once the dimension is lowered beneath the upper critical dimension.

We have seen that linearizations of the renormalization group flows about the critical fixed point give information about the critical exponents. How does changing the dimension change the exponents? We know that the exponents stay mean-field-like until an upper critical dimension, and then become dimension-dependent – what does this mean about the analytic structure of the renormalization group flows? A hint is provided by Wilson's ϵ expansion. In the ϵ expansion, one computes the critical exponents near the upper critical dimension $d = 4 - \epsilon$ by examining the renormalization group flow equations as a function of ϵ. Ignoring the detailed diagrammatic calculations, justifications of expansions, and so on, one finds flow equations of the type [107]

$$\frac{\mathrm{d}\xi}{\mathrm{d}\ell} = -\xi, \quad \frac{\mathrm{d}a}{\mathrm{d}\ell} = 2a + \frac{3}{2\pi^2}\frac{\Lambda^4}{\Lambda^2 + a}g, \quad \frac{\mathrm{d}g}{\mathrm{d}\ell} = \epsilon g - \frac{9}{2\pi^2}\frac{\Lambda^4}{(\Lambda^2 + a)^2}g^2 \tag{4.4}$$

[2] A counterexample to this is the Anderson transition, where there is good numerical evidence that the upper critical dimension is $d = \infty$ [106]. Even here, the critical exponents asymptotically approach their mean-field values as $d \to \infty$.

where a is the coefficient on the quadratic term in the free energy, g is a dimensionless version of the coefficient on the quartic term, and Λ is the upper cutoff on the momentum integral (these equations were derived using the momentum shell renormalization group). Typical lecture notes in this subject then point out that these flow equations have a pair of fixed points for $\epsilon > 0$:

$$\begin{aligned} a^* = g^* = 0 \text{ (Gaussian fixed point), and} \\ a^* = -\frac{1}{6}\Lambda^2\epsilon, g^* = \frac{2\pi^2}{9}\epsilon \text{ (Wilson-Fisher fixed point).} \end{aligned} \tag{4.5}$$

One can then linearize these flows in the vicinity of these fixed points to understand the topology of the renormalization group flows. The Gaussian fixed point has two relevant directions for $\epsilon > 0$, indicating that it is unstable. The Wilson-Fisher fixed point, on the other hand, has an attractive direction, meaning that flows starting at the critical point for a generic model in this universality class will flow to the Wilson-Fisher fixed point and have critical exponents governed by the linear stability analysis in its vicinity. These flows are illustrated in Figure 4.1. The critical exponents depend upon ϵ and can be used to understand the dimension-dependent critical exponents below $d = 4$. More interesting than the computation of the critical exponents, however, is the actual structure of the flows themselves: in the vicinity of $\epsilon = 0$, the flow for g undergoes a *transcritical bifurcation*. For $\epsilon < 0$, i.e. for $d > 4$, the attractive fixed point is the Gaussian one, even though the Wilson-Fisher fixed point formally exists. In 4 dimensions, the Gaussian and Wilson-Fisher fixed points cross and exchange their stability. This gives a general prescription for how one can get abruptly different behavior above and below the upper critical dimension: the renormalization group fixed points that govern the critical behavior above and below the upper critical dimension are different. This also gives a prescription for understanding the logarithmic corrections that ubiquitously appear in the

upper critical dimension: the assumption that the renormalization group flows can be linearized breaks down. Setting $\epsilon = 0$ in the flow for g means that g flows to 0 much more slowly than it does for any $\epsilon < 0$. This slow flow affects the invariant scaling combinations and means that relationships between parameters close to the critical point cannot be described purely by power laws.

Others in the group [49] have developed methods to classify *universality families* of critical points based on the analytic structure of the renormalization group flows. Normal form theory, borrowed from dynamical systems and bifurcation theory, allows us to cast differential equations into extraordinarily simple forms by restricting ourselves to certain classes of coordinate transformations. For the purposes of understanding universality and the renormalization group, it makes sense to restrict ourselves to analytic changes of variables, since the non-analyticities that arise close to phase transitions should be described by the structure of the renormalization group flow close to the fixed point, and allowing arbitrary non-analytic changes of variables could change the values of critical exponents or the structure of bifurcations. Once we have restricted to analytic changes of variables, we can then make a choice of the change of variables that makes the renormalization group flows as simple as possible, placing them into their normal form. For the Ising model in $d = 4$, most of the higher-order terms can be removed, leading to only quadratic and cubic terms in the flow for the marginally irrelevant variable g. The coefficient of the cubic term[3] is then just as universal as critical exponents are for fixed points that can be linearized.

Coming back to the CPA as an approximate theory governing the spacetime dynamics close to a rigidity transition – we can compute the critical exponents both above and below $d = 2$, and we find something resembling an upper

[3]The coefficient of the quadratic term can be set to 1 through a rescaling of g.

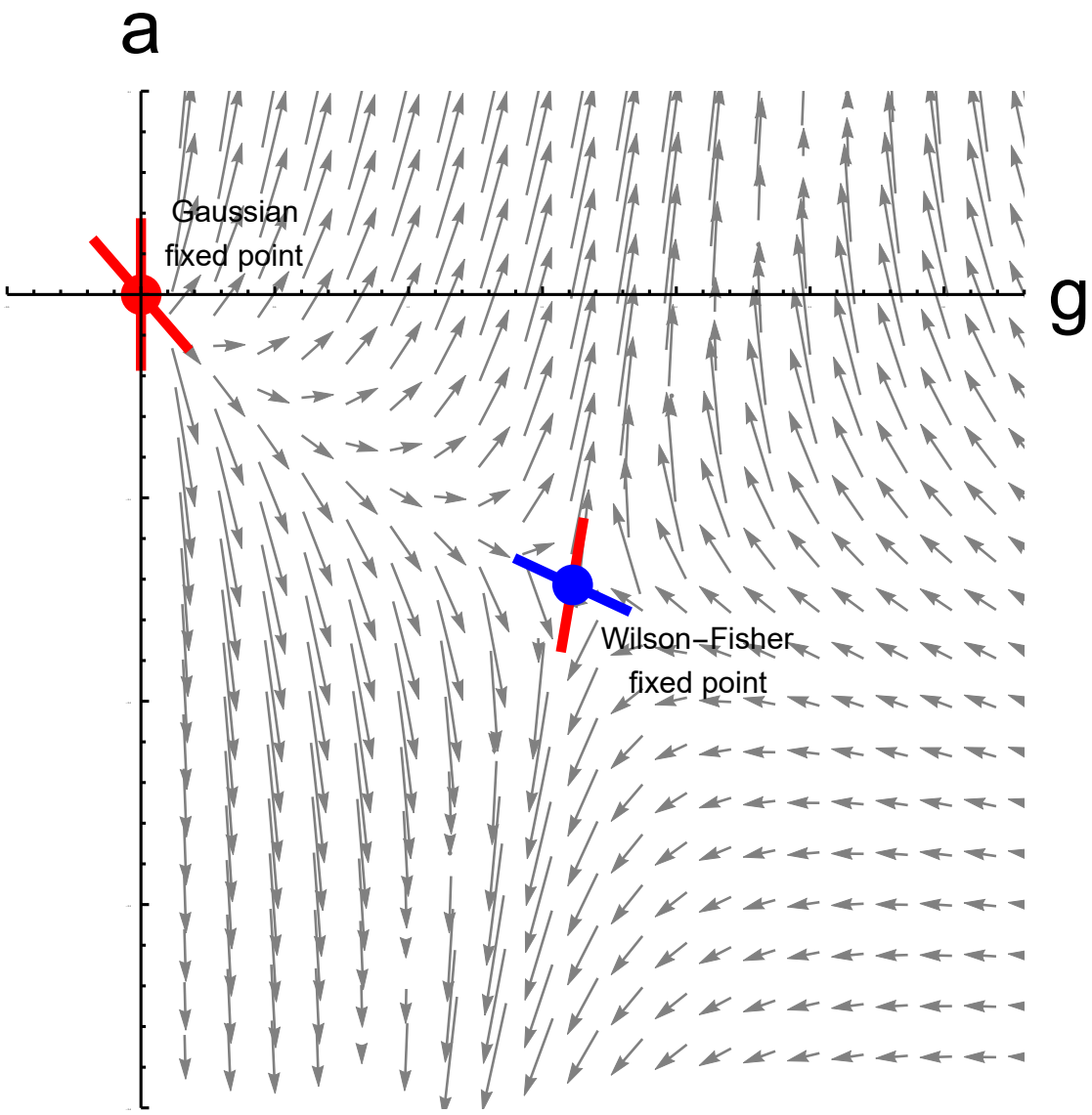

Figure 4.1: The flows of the parameters a and g as computed using momentum shell RG, setting $\epsilon = 1$. The vector field shows the direction of the flow. The red and blue line segments show unstable and stable eigendirections (respectively) at the two fixed points. The Gaussian fixed point is completely unstable in $d = 3$, while the Wilson-Fisher fixed point has a stable direction.

critical dimension from the structure of the critical exponents. We then make this correspondence precise by writing down renormalization group flows containing a transcritical bifurcation, where all coefficients of the universal terms in these flows are determined by the exact expansion of the CPA. The one-parameter family of flow equations are simply another way to express the scale-invariance that emerges from the self-consistent CPA equation near its bifurcation as a function of dimension d. We find that the logarithmic corrections in $d = 2$ are perfectly accounted for by these flows in 2 dimensions, which contain a variable that has become marginally irrelevant thanks to an exchange of stability of two fixed points. This variable above 2 dimensions is a dangerously irrelevant variable that incorporates the low-frequency elastic dissipation.

In the following manuscript, I discovered the logarithmic corrections in 2 dimensions (although later I found I was not the first to do so [44]), completed the full asymptotic analysis of the scaling of the response in all dimensions, and connected the logarithmic corrections to a transcritical bifurcation in renormalization group flows using normal form theory. Danilo Liarte and Jim Sethna again provided valuable inputs on the scaling forms and the extraction of universal predictions. Itai Cohen assisted in providing experimental insight and clarifying a large portion of the text.

4.2 Universal scaling solution for a rigidity transition: renormalization group flows near the upper critical dimension

This is a reformatted version of the manuscript appearing as Physical Review E 111, 045508 (2025) [108].

4.2.1 Abstract

Rigidity transitions induced by the formation of system-spanning disordered rigid clusters, like the jamming transition, can be well-described in most physically relevant dimensions by mean-field theories. A dynamical mean-field theory commonly used to study these transitions, the coherent potential approximation (CPA), shows logarithmic corrections in 2 dimensions. By solving the theory in arbitrary dimensions and extracting the universal scaling predictions, we show that these logarithmic corrections are a symptom of an upper critical dimension $d_{\text{upper}} = 2$, below which the critical exponents are modified. We recapitulate Ken Wilson's phenomenology of the $(4 - \epsilon)$-dimensional Ising model, but with the upper critical dimension reduced to 2. We interpret this using normal form theory as a transcritical bifurcation in the RG flows and extract the universal nonlinear coefficients to make explicit predictions for the behavior near 2 dimensions. This bifurcation is driven by a variable that is dangerously irrelevant in all dimensions $d > 2$ which incorporates the physics of long-wavelength phonons and low-frequency elastic dissipation. We derive universal scaling functions from the CPA sufficient to predict all linear response in randomly diluted isotropic elastic systems in all dimensions.

4.2.2 Introduction

We present here a complete analysis of a particular isotropic, homogeneous rigidity transition. Our solution provides universal scaling predictions for the linear responses of the system – viscosities, elastoplastic and viscoelastic functions, Green's functions, densities of states, etc. It also implies a renormalization

group flow which recapitulates the classic $(4-\epsilon)$-dimensional Ising critical point predictions with the upper critical dimension reduced to two.

There is a family of rigidity transitions of past and current interest, with many common features but not all sharing the same universality class. Most prominent is the recent focus on the jamming transition [14, 69], applied to glasses, colloidal and granular systems, and foams. In jamming, a replica solution in infinite dimensions [109, 110] makes quantitative predictions for microscopic power laws (universal contact force and gap size distributions) all the way down to two dimensions [111, 112, 46]. Other examples include rigidity transitions in tissues [25, 91] relevant to wound healing and embryonic organ formation, dislocation entanglement in crystals [92], and 'double descent' accuracy transitions in deep learning [26]. Several of these systems appear to share the same dimension-independent universal power laws above two dimensions, motivating the simplified model investigated here.

Our work is inspired by the discovery [2] of diluted networks in both two and three dimensions that show a jamming transition as an endpoint of a line of rigidity percolation transitions, studied through static simulations and via the coherent potential approximation. These networks have no linear elastic moduli in a floppy phase and show a jump in the bulk modulus and linear growth in the shear modulus at a jamming point of the phase boundary. With the inclusion of additional angular and bending forces, these models are also believed to be applicable to fiber networks, such as the ones found in cytoskeletal networks and extracellular matrices [113, 114]. Here, we present an analysis of this model for the rigidity percolation transition, where all static moduli grow linearly from zero.

Our model is an isotropic, continuum version of the coherent potential approximation (CPA) [1, 2, 9]. It replicates the CPA predictions for the dilution of a random, amorphous spring network studied by Düring et al. [44]. Both are outgrowths of what is termed rigidity percolation (RP) [115, 116, 59], where a network of springs connecting nodes with no angular forces is diluted, not until it becomes completely disconnected (percolation) but until its elastic moduli vanish. It is known that rigidity percolation on a two-dimensional triangular lattice has critical exponents that differ from those found for rigidity percolation on graphs generated from jammed packings of spheres, with a modulus that with a higher power with excess coordination number [5, 117]. We conjecture that lattice anisotropy [118], and/or undeformed springs in a line (forming *second-order constraints* [59, 119]) are relevant perturbations at the rigidity transition for spring networks, and that our theory is applicable to a randomly diluted isotropic network without these buckling transitions (Section 4.2.6). This continuum theory, when used to describe jamming [2, 120], matches most of the properties seen numerically, both directly and in spring network models generated from jammed configurations [121] and simulations of diluted amorphous spring networks [44]. The calculation presented here focuses on the case where the bulk modulus does not jump, which includes most of the rigidity transitions other than jamming. Nevertheless, this calculation captures the predicted scaling of the shear mode close to the jamming transition [120]. We leverage our exact solutions of the continuum theory to generate universal scaling forms for all linear response properties, and we use them to calculate new critical exponents below 2 dimensions described by nonlinear renormalization group flows. We identify a scaling variable which is dangerously irrelevant for $d > 2$ which is responsible for low-frequency dissipation, the phonon density of states, and

the logarithmic corrections in $d = 2$.

We conjecture that many qualitative features of our analysis are important predictions and tools that should apply more generally. (1) Many replica-theory and other mean-field methods yield self-consistent formulas that predict power-law scaling near transitions [122]. Our analysis is a guide to extracting universal predictions out of these self-consistent relations. For example, the Curie-Weiss law predicts the entire phase behavior of an Ising magnet above four dimensions [123], but only the power laws and the scaling function near the critical point are expected to be universal. (2) Much impressive work, especially in jamming, has focused on the microscopic behavior [124, 125, 126, 127, 128, 129, 130] (how jammed systems are *different* from regular systems [131]). Our previous work [40, 33, 9, 45, 65] has taken a different perspective by analyzing the emergent phase behavior in terms of Widom scaling theories (investigating how jamming may be *reduced* to regular system behavior). Our work here builds upon these by presenting a wonderful example of the rich phenomena that can be extracted by focusing on the macroscopic behaviors in space and time of this and other systems. (3) Our extraction of RG flows allows us to explain the quite non-trivial invariant scaling combinations in the upper critical dimension (as we found also in the 4D Ising model [49]); these variables should appear in a wide class of models that share this upper critical dimension. (4) Many higher-temperature features of glasses are missed in the infinite-dimensional replica theories (such as the continued relaxation below the mode-coupling transition) and are thought to be non-perturbative in the inverse dimension $1/d$. Our rigidity transition has a dangerously irrelevant variable above two dimensions that is needed to incorporate low-frequency vibrational modes and dissipation, which we show is indeed such a non-perturbative effect in the limit $d \to \infty$. The work

presented here provides a road map for dealing with such irrelevant variables.

Our work is similar in some aspects to that of a manuscript by Vogel et al. [132]. They form a self-consistent theory for the shear response of a nearly unjammed solid with similar structure to our continuum CPA. Their analysis incorporates nontrivial momentum dependence which is important in the disordered glassy phase studied by the authors of the article in previous work [133, 134] and by others [135]; this type of momentum-dependent modulus is ignored by the CPA. Our work, on the other hand, is focused on calculating the universal scaling functions for the transition, deducing nontrivial normal forms for renormalization group flows, and understanding specifically the singular behavior of the theory found in two dimensions.

The organizational structure of our paper is as follows: in Section 4.2.3, we briefly review the CPA as applied to weakened elastic media. We show that, under quite general assumptions, elastic moduli vanish linearly in deviations from the critical dilution fraction $\mu \sim \delta p \sim \delta\widetilde{z}$, where $\delta p \equiv p - p_c$ is the distance from the critical point in bond occupation probability and $\delta\widetilde{z} \equiv \widetilde{z} - \widetilde{z}_c$ is the distance from the critical point in coordination number. In Section 4.2.4, we evaluate the universal scaling functions for the space-time linear response of the theory near the critical point directly in $d = 3$ dimensions and in $d = 2$ dimensions, and show that the appropriate scaling for the dynamical behavior close to the critical point has log corrections in two dimensions, as was noticed in [44]. In Section 4.2.5 and Appendix C.1, we cast solutions close to the critical point into a scaling theory in general dimensions d, and show that $d = 2$ demarcates the boundary between two differing sets of critical exponents. We construct renormalization group flow equations that are consistent with the critical exponents

predicted by the theory (with more details located in Appendices C.2 and C.3), with an exchange of stability between two RG fixed points in $d = 2$. In this way, we interpret $d = 2$ as the upper critical dimension of the transition, and find the appropriate scaling variables in $d = 2$ analogously to those in the 4D Ising model. The logarithmic shifts that are one signature of the upper critical dimension are investigated in more detail in Appendix C.4 through a direct comparison to a lattice CPA calculation on the bond-diluted triangular lattice. Finally, in Section 4.2.6, we discuss the applicability of this model more broadly to a wide variety of different rigidity transitions in disordered elastic systems.

4.2.3 The CPA and critical exponents for static moduli

We examine a continuum version of the coherent potential approximation (CPA) inspired by the lattice CPA [1]. The lattice CPA can be used to describe a system comprised of purely harmonic springs of strength k_0 on some regular lattice that are independently randomly occupied with probability p. This is equivalent to placing a probability distribution on the strengths of bonds k'

$$k' \sim p\ \delta(k' - k_0) + (1 - p)\ \delta(k') \tag{4.6}$$

so that each bond of strength k_0 is independently randomly occupied with probability p. Other effective medium theories have placed more realistic distributions of bonds based on observations of stress and strain fluctuations from simulations of particular systems (soft spheres touching, gels near their gelation point, etc. [136]). One then tries to describe this disordered elastic system by a non-disordered *effective medium*, whose physical properties are renormalized by p. Finding the best effective value of stiffness k so that the disorder-averaged elastic Green's function $\langle \mathbf{G}(k', \omega) \rangle \approx \mathbf{G}(k(\omega), \omega)$, the elastic Green's

function for an effective medium with no disorder, amounts to solving a self-consistent equation for the stiffnesses. The effective moduli are allowed to become frequency-dependent and complex, transforming them into *visco*elastic moduli [1]. This CPA is related to the CPA used in other impurity scattering problems which makes a similar assumption that the self-energy is local $\Sigma(\omega, q) \approx \Sigma(\omega)$. The content of the approximation made by the CPA is twofold: first, the effective stiffnesses depend only on ω, and not on q. Second, this constraint is imposed by requiring that the *single-site* T-matrix for multiple scattering vanishes [137], as opposed to the *full* T-matrix (which is analytically intractable). The result of the approximation is a homogeneous effective medium that incorporates the effects of phonons scattering off of defects introduced by the disorder into a effective damping (Figure 4.2).

The self-consistent equation for the shear modulus of the effective medium under the assumptions of the lattice CPA [1, 2] is

$$\frac{p - \mu/\mu_{\mathrm{F}}}{1 - \mu/\mu_{\mathrm{F}}} = \frac{1}{\widetilde{z}} \fint_{\mathrm{BZ}} \mathrm{d}^d q \, \mathrm{Tr}\,(\mathbf{DG}), \tag{4.7}$$

where the integral is an average over the first Brillouin zone, $\widetilde{z}$ denotes the average number of constraints per microscopic unit in the undiluted system (in the lattice case, it is the number of bonds per node), μ_{F} is the shear modulus in the completely filled, non-disordered system, and $\mathbf{D}$ and $\mathbf{G}$ are the dynamical matrix and Green's function for the medium, respectively. This long-wavelength limit of the lattice problem reproduces the isotropic CPA for amorphous spring networks investigated by Düring et al. in [44]. This expression is self-consistently solved for $\mu(p, \omega)$, which is proportional to the best effective value of the microscopic stiffness k. Some definitions of important parameters that regularly appear are given in Table 4.1.

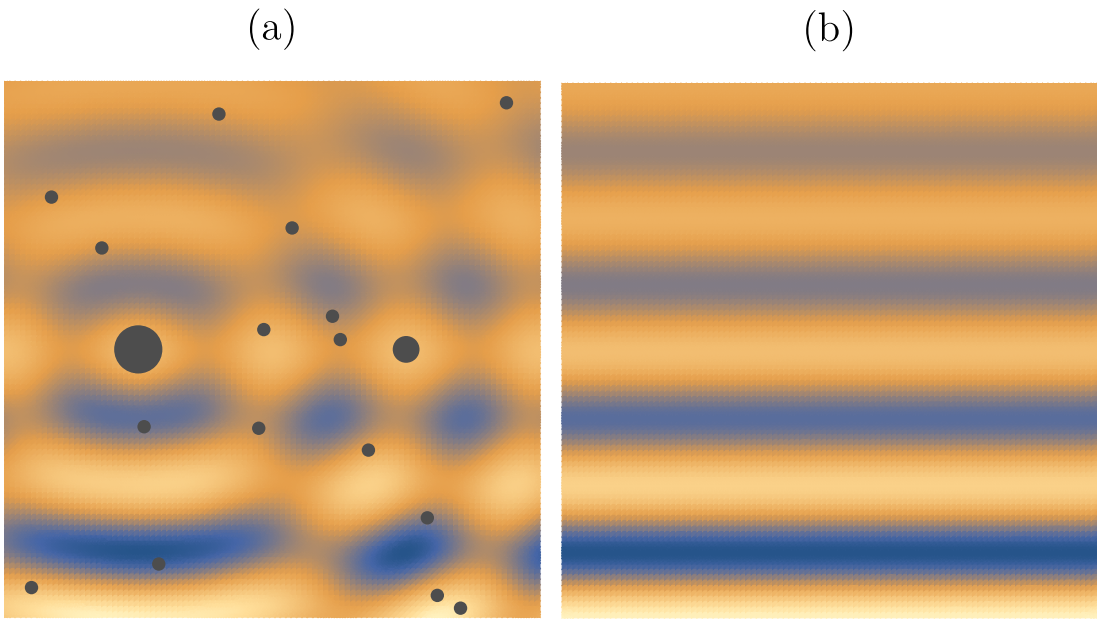

Figure 4.2: **Schematic of the approximation made by the CPA**. (a) A phonon traveling (upwards) into an elastic medium with randomly distributed defects scatters in complicated ways. The dark circles represent the isotropically scattering defects in our continuum CPA, while the colors represent the magnitude of the displacement field. (b) The same phonon traveling through the effective medium is damped as it propagates. The CPA gives renormalized elastic constants for a medium with no defects, which incorporates the strong scattering of shorter-wavelength phonons through a damping term in the effective moduli.

We are interested in properties of disordered rigidity transitions for systems that are statistically isotropic. To lose reference to any particular lattice, we pass to a continuum version of the CPA, where the Brillouin zone is replaced by a sphere of radius q_D (the Debye wavevector) and dynamical matrices and Green's functions are written for an isotropic continuum elastic sheet. We will see that this version of the CPA also describes the CPA scaling behavior of diluted lattices with a continuous rigidity transition that are isotropic at long wavelengths, as anisotropic terms enter as corrections to scaling. With only one independent microscopic stiffness, it suffices to track the behavior of the renormalized shear modulus μ as it deviates from its value in the unweakened system

μ_F, as all other stiffnesses are proportional to this modulus. We decompose the continuum dynamical matrix and Green's function into transverse and longitudinal parts to evaluate the integrand:

$$\begin{aligned}
\mathbf{D} &= D_L(q)\hat{q}_i\hat{q}_j + D_T(q)\left(\delta_{ij} - \hat{q}_i\hat{q}_j\right), \\
\mathbf{G} &= G_L(q,\omega)\hat{q}_i\hat{q}_j + G_T(q,\omega)\left(\delta_{ij} - \hat{q}_i\hat{q}_j\right), \\
\mathrm{Tr}\,(\mathbf{DG}) &= G_L(q,\omega)\,D_L(q) + (d-1)\,G_T(q,\omega)\,D_T(q).
\end{aligned} \tag{4.8}$$

At zero frequency, assuming the dynamical matrix of the effective medium is invertible (as it is on the solid side of the transition), $\mathbf{G}(q,0) = \mathbf{D}^{-1}$ (see the beginning of Appendix C.1 for details on the specific forms of $D_{L/T}$ and $G_{L/T}$), and so the integrand is the trace of a d-dimensional identity matrix and the self-consistent equation can be evaluated directly:

$$\frac{p - \mu/\mu_F}{1 - \mu/\mu_F} = \frac{d}{\widetilde{z}} \implies \frac{(p - d/\widetilde{z}) - (1 - d/\widetilde{z})\,\mu/\mu_F}{1 - \mu/\mu_F} = 0. \tag{4.9}$$

The constant $d/\widetilde{z}$ is identified as p_c. It is identical to the Maxwell counting constraint ignoring states of self-stress: each microscopic unit has on average $p\widetilde{z}$ constraints and d degrees of freedom, and so $p_c = d/\widetilde{z}$. Keeping $0 < p_c < 1$, and defining $\mu' = (1 - d/\widetilde{z})\,\mu/\mu_F$, one has

$$\frac{(p - p_c) - \mu'}{1 - \mu'/(1 - p_c)} = 0, \tag{4.10}$$

and so $\mu' \sim (p - p_c)^{f_{CPA}}$ with $f_{CPA} = 1$: the static shear modulus vanishes linearly with $p - p_c$ upon approaching the transition.

It is tempting, then, to declare the CPA a mean-field-like theory that gives dimension-independent critical exponents, as Landau theory does in magnets. This turns out not to be true; the dynamical scaling of the theory has much more interesting structure.

4.2.4 Two and three dimensions and a dangerously irrelevant variable

In this section, we expand the solution for the viscoelastic modulus $\mu(\omega)$ close to its continuous stiffness transition. We then cast the solution near the critical point in terms of scaling variables and identify universal scaling functions. In three dimensions (Section 4.2.4), we show that it is necessary to retain an invariant scaling combination associated with an irrelevant variable to capture the low-frequency dissipative part of the viscoelastic modulus in the case of microscopically undamped dynamics. This irrelevant variable also gives information about the low-frequency density of states. This suggests that the irrelevant variable is *dangerous*: it vanishes under a coarse-graining procedure, but it cannot be set to 0 directly without losing access to a description of important low-frequency vibrational modes.

In two dimensions (Section 4.2.4), we show that the scaling variables that were correct in three dimensions no longer capture the behavior near the critical point. There are large, logarithmic shifts in physically relevant frequencies. In Section 4.2.5, we will show that this modification of the scaling variables is a result of the leading irrelevant variable becoming marginal in $d = 2$, significantly altering the low-energy physics. This identifies $d = 2$ as the upper critical dimension, and we write new critical exponents and scaling functions below the upper critical dimension. We also construct renormalization group flows consistent with the analytic structure of the scaling variables.

Scaling in 3 dimensions

We first note that, at zero frequency, μ vanishes linearly with p as $p \to 3/\widetilde{z} \equiv p_c$. We subtract p_c from each side of Equation 4.7 (see Appendix C.1 from Eqn. C.3 to Eqn. C.11 for details) so that the self-consistent relation becomes

$$\frac{(p - p_c) - (1 - p_c)\,\mu/\mu_{\mathrm{F}}}{1 - \mu/\mu_{\mathrm{F}}} = \frac{3}{\widetilde{z} q_{\mathrm{D}}^3}\left(\int_0^{q_{\mathrm{D}}} \mathrm{d}q \frac{\mathrm{w}q^2}{(\lambda_{\mathrm{F}}/\mu_{\mathrm{F}} + 2)\,\mu q^2 - \mathrm{w}} + 2\int_0^{q_{\mathrm{D}}} \mathrm{d}q \frac{\mathrm{w}q^2}{\mu q^2 - \mathrm{w}}\right) \tag{4.11}$$

where the functional form of w depends upon the microscopic damping of the system. We focus on undamped dynamics, where $\mathrm{w} = \rho\omega^2$, but $\mathrm{w} = i\gamma\omega$ for overdamped dynamics has very similar scaling behavior. One could in principle also consider the case of Galilean-invariant Kelvin damping, where $\mathrm{w} = \rho\omega^2 + i\eta\omega q^2$, but the analysis of the asymptotic scaling in this manuscript assumes w is q-independent.[4] We write a scaling theory for small $\delta p \equiv p - p_c$, which is the distance to the critical point as measured in p. At $\mathrm{w} = 0$, the integral terms vanish. This suggests a definition for a scaling variable for the shear modulus:

$$\begin{aligned} M &\equiv \frac{\mu/\mu_0}{|\delta p|}, \\ \mu_0 &\equiv \frac{\mu_{\mathrm{F}}}{1 - p_c}. \end{aligned} \tag{4.12}$$

We use capital letters, such as M, to denote the corresponding scaling variable for a physical quantity like μ. The scaling variables are typically a physical quantity divided by a non-universal, dimensionful constant, such as μ_0, and some power of $|\delta p|$. We will use script letters, such as $\mathcal{M}$, to denote scaling functions, which take scaling variables as arguments.

[4]The function w relates the frequency of a mode to the corresponding eigenvalue of the dynamical matrix. In the case of a lattice with no damping, an eigenvector of the dynamical matrix with frequency ω_i would have a corresponding eigenvalue $m\omega_i^2 = \mathrm{w}'(\omega_i)$. In the continuum case, ρ replaces m (see Appendix C.1 from Eqn. C.3 to Eqn. C.7 for details).

The integrals in Equation 4.11 can be done directly; it is useful to substitute $\xi = (q/q_{\mathrm{D}})^2$ and rescale to $\mathrm{w_L} = \mathrm{w}/\left(\lambda_{\mathrm{F}}/\mu_{\mathrm{F}} + 2\right) q_{\mathrm{D}}^2$ and $\mathrm{w_T} \equiv \mathrm{w}/q_{\mathrm{D}}^2$ to find

$$\begin{aligned} &\frac{\delta p - |\delta p|\, M}{1 - |\delta p|\, M/\left(1 - p_c\right)} = \\ &-\frac{3}{2\widetilde{z}}\left(\int_0^1 \mathrm{d}\xi \frac{\xi^{1/2}}{1 - (\mu/\mathrm{w_L})\,\xi} + 2\int_0^1 \mathrm{d}\xi \frac{\xi^{1/2}}{1 - (\mu/\mathrm{w_T})\,\xi}\right). \end{aligned} \tag{4.13}$$

Assuming $\mathrm{Im}\,(\mu) < 0$ for $\mathrm{w} > 0$ (necessary for causality), we have

$$\begin{aligned} \frac{\delta p - |\delta p|\, M}{1 - |\delta p|\, M/\left(1 - p_c\right)} &= \frac{3}{\widetilde{z}}\left(\frac{\mathrm{w_L}}{\mu} + 2\frac{\mathrm{w_T}}{\mu}\right) - \\ -\frac{3}{\widetilde{z}}\left(\left(\frac{\mathrm{w_L}}{\mu}\right)^{3/2} \tanh^{-1}\left(\sqrt{\frac{\mu}{\mathrm{w_L}}}\right)\right.&+ \\ &\left.+2\left(\frac{\mathrm{w_T}}{\mu}\right)^{3/2} \tanh^{-1}\left(\sqrt{\frac{\mu}{\mathrm{w_T}}}\right)\right). \end{aligned} \tag{4.14}$$

We are interested in the low-frequency behavior. The terms proportional to w/μ dominate over the terms proportional to $(\mathrm{w}/\mu)^{3/2}$ at low frequencies. This suggests a scaling $\mathrm{w}/\mu \sim |\delta p|$, which suggests we should expand the functions $\tanh^{-1}(z)$ about their appropriate complex infinity. For undamped dynamics, we note that $\mathrm{Im}\,(\mu) \leq 0$ and hence $\mathrm{Im}\left(\sqrt{\mu}\right) \leq 0$ to respect causality. The function $\tanh^{-1}(z)$ can then be expanded to find

$$\begin{aligned} \frac{\delta p - |\delta p|\, M}{1 - |\delta p|\, M/\left(1 - p_c\right)} &\approx \frac{3}{\widetilde{z}}\left(\frac{\mathrm{w_L}}{\mu} + 2\frac{\mathrm{w_T}}{\mu}\right) + \\ &+ \frac{3}{\widetilde{z}}\frac{i\pi}{2}\left(\left(\frac{\mathrm{w_L}}{\mu}\right)^{3/2} + 2\left(\frac{\mathrm{w_T}}{\mu}\right)^{3/2}\right). \end{aligned} \tag{4.15}$$

One can check that since $\mathrm{Im}\,(\mu) \leq 0$, we can write

$$\begin{aligned} \frac{\delta p - |\delta p|\, M}{1 - |\delta p|\, M/\left(1 - p_c\right)} &\approx \frac{3}{\widetilde{z}}\left(\frac{\mathrm{w_L}}{\mu} + 2\frac{\mathrm{w_T}}{\mu}\right) + \\ &+ \frac{3\pi}{2\widetilde{z}}\left(\left(-\frac{\mathrm{w_L}}{\mu}\right)^{3/2} + 2\left(-\frac{\mathrm{w_T}}{\mu}\right)^{3/2}\right). \end{aligned} \tag{4.16}$$

This expansion is more general and also works for the overdamped case where $\mathrm{w} \sim i\gamma\omega$. This asymptotic analysis of the leading correction to the CPA result reproduces the calculation done in Appendix B of [52]. Now we are prepared to

define more invariant scaling variables and our first universal scaling function. We first insert the definition of M in for μ everywhere. Then, we define Ω^2 (named for the undamped case) as the scaling variable for w which makes the dominant term of the scaling for the frequency-dependent part $|\delta p|\,\Omega^2/M$. The definition of w in terms of Ω is then inserted in the higher-order frequency piece, and the remaining terms are all absorbed into a scaling combination U for an irrelevant variable. The result, after dividing both sides by $|\delta p|$ and throwing away the higher-order contribution from the denominator of the left-hand side, is

$$\begin{aligned} \pm 1 - M &= \frac{\Omega^2}{M} + U\left(-\frac{\Omega^2}{M}\right)^{3/2}, \\ \Omega^2 &\equiv \frac{\omega^2/\omega_0^2}{|\delta p|^2}, \quad U \equiv u/u_0\,|\delta p|^{1/2}. \end{aligned} \tag{4.17}$$

The sign $\pm 1 = \delta p/|\delta p|$ is for the rigid and floppy side of the transition, respectively; formulas for ω_0 and u/u_0 can be found in Appendix C.1. This is an implicit definition of a universal scaling function for $M = \mathcal{M}(\Omega, U)$.[5] Setting the leading irrelevant piece U to 0 allows us to solve a quadratic equation for M as $2\mathcal{M}(\Omega, 0) = \pm 1 - \sqrt{1 - 4\Omega^2}$, as found indirectly in [2] and directly in [9, 45]. However, this form of the universal scaling function (unphysically) has no scattering-induced dissipation on the rigid side of the transition until $\Omega = 1/2$, while the full solution retaining U has $\mathrm{Im}\,(\mathcal{M}) < 0$ for all $\Omega > 0$.[6] As mentioned in the introduction to this section, this identifies U as an invariant scaling combination associated with a *dangerously* irrelevant variable for the case of undamped microscopic dynamics, as the function $\mathcal{M}(\Omega, U)$ is not analytic in its second argument at zero. Retaining U is necessary to understand the details of the low-

[5] In a more complete self-consistent theory beyond the CPA such as [132], the shear modulus will also have a q-dependence, leading to a scaling form $\mathcal{M}(\Omega, Q, U)$.

[6] The effective medium theory misses the important contributions of quasilocalized modes to the low-frequency density of states, which give a characteristic scaling $D(\omega) \sim \omega^4$ [138].

frequency viscosity, susceptibility, and density of states.

For models with many soft modes, we can illustrate the excess number of soft modes by comparing the density of states with that of the Debye model, in which $D(\omega) \sim \omega^{d-1}$. We plot the predicted universal scaling forms for the density of states divided by the Debye form for different values of the dangerously irrelevant variable in Figure 4.3. The peak in the excess density of states is located near the frequency $\omega^* \sim |\delta p|$ where the density of states becomes nearly flat: a characteristic feature of all rigidity transitions in this family. The dangerous irrelevant variable U controls the continuum phonon density of states, which vanishes in the appropriate scaling limit.

We note in passing that the frequency scaling variable only appears in conjunction with the scaling variable for the modulus. Instead of defining a scaling for w, then, we could define a scaling variable for $f \equiv \mathrm{w}/\mu$. This turns out to be a particularly natural choice that eases the analysis in two dimensions. Written in terms of this scaling variable, the self-consistent equation reads

$$\begin{aligned} \pm 1 - M &= F + U(-F)^{3/2}, \\ F &\equiv \frac{f/f_0}{|\delta p|}. \end{aligned} \tag{4.18}$$

Scaling in 2 dimensions

We follow the steps above, and again evaluate the integral directly in $d = 2$, where now $2/\widetilde{z} = p_c$. We subtract p_c from each side of Equation 4.7 so that the self-consistent relation becomes

$$\begin{aligned} \frac{(p - p_c) - (1 - p_c)\,\mu/\mu_{\mathrm{F}}}{1 - \mu/\mu_{\mathrm{F}}} = \\ \frac{2}{\widetilde{z} q_{\mathrm{D}}^2}\left(\int_0^{q_{\mathrm{D}}} \mathrm{d}q \frac{\mathrm{w}q}{(\lambda_{\mathrm{F}}/\mu_{\mathrm{F}} + 2)\,\mu q^2 - \mathrm{w}} + \int_0^{q_{\mathrm{D}}} \mathrm{d}q \frac{\mathrm{w}q}{\mu q^2 - \mathrm{w}}\right) \end{aligned} \tag{4.19}$$

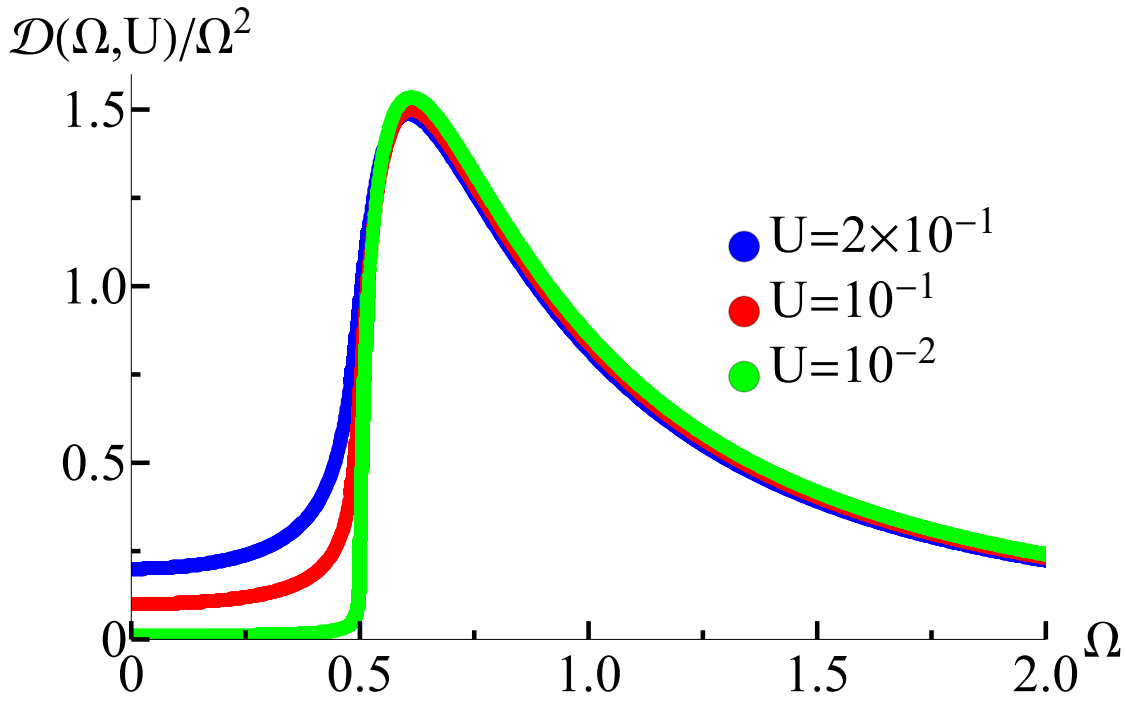

Figure 4.3: **Prediction for the shape of the excess density of states near the rigid-floppy transition in** $d = 3$ (see also Fig. C.1). We compare our density of states to the Debye result and find an excess of states that contribute to the *boson peak* that is often seen in disordered rigid systems. The dangerously irrelevant variable U must be retained to capture the Debye phonon contribution to the density of states below $\Omega = 1/2$. These long-wavelength phonons are of course important to the physics, but are swamped near the rigidity transition by the flat density of states above ω^*. Hence the phonon contribution is irrelevant in the RG sense, even though it is important to the physics.

We again write a scaling theory for small δp. The zero-frequency scaling for the modulus is the same as in Equation 4.12. We perform the same substitution as in $d = 3$ of $\xi = (q/q_D)^2$ and rescale to $w_L = w/(\lambda_F/\mu_F + 2)\, q_D^2$ and $w_T \equiv w/q_D^2$ to find

$$\frac{\delta p - |\delta p|\, M}{1 - |\delta p|\, M/(1 - p_c)} = -\frac{1}{\widetilde{z}}\left(\int_0^1 d\xi \frac{1}{1 - (\mu/w_L)\,\xi} + \int_0^1 d\xi \frac{1}{1 - (\mu/w_T)\,\xi}\right). \tag{4.20}$$

Assuming $\mathrm{Im}\,(\mu) < 0$ for $\mathrm{w} > 0$, we have

$$\begin{aligned} &\frac{\delta p - |\delta p|\, M}{1 - |\delta p|\, M/\,(1 - p_c)} = \\ &\frac{1}{\widetilde{z}}\left(\frac{\mathrm{w_L}}{\mu}\log\left(1 - \frac{\mu}{\mathrm{w_L}}\right) + \frac{\mathrm{w_T}}{\mu}\log\left(1 - \frac{\mu}{\mathrm{w_T}}\right)\right) \end{aligned} \tag{4.21}$$

We are interested in the low-frequency behavior. There is now quite clearly a logarithmic singularity at low frequencies, as discussed in [44][7]. Keeping only the leading-order low frequency terms, we have

$$\frac{\delta p - |\delta p|\, M}{1 - |\delta p|\, M/\,(1 - p_c)} \approx -c_1\frac{\mathrm{w}}{\mu}\log\left(-c_2\frac{\mathrm{w}}{\mu}\right). \tag{4.22}$$

One cannot define a scaling variable for frequency as a ratio of w and δp raised to some power as we did in $d = 3$, as extra factors of δp appear inside the logarithm when written in terms of the scaling variables. We instead implicitly define a scaling variable for $f \equiv \mathrm{w}/\mu$ as the right-hand side divided by $|\delta p|$:

$$\begin{aligned} \pm 1 - M &= F_2, \\ |\delta p|\, F_2 &\equiv -c_1 f \log\left(-c_2 f\right). \end{aligned} \tag{4.23}$$

The variable F_2 is the 2D quantity that corresponds to the right-hand side of Equation 4.18. Given that F_2 is an invariant scaling combination, we can investigate how this implies f depends upon $|\delta p|$ by inverting the definition of F_2:

$$f = -\frac{(F_2/c_1)\,|\delta p|}{W_{-1}\left((F_2 c_2/c_1)\,|\delta p|\right)}, \tag{4.24}$$

where $W_{-1}(z)$ is a particular branch of the Lambert W function satisfying $W(z)e^{W(z)} = z$. The appropriate branch of the W function has an expansion near $z = 0$ of the form $W_{-1}(z) \sim \log(z) - 2\pi i - \log\Big(\log(z - 2\pi i)\Big) + \ldots$ (see [139] for more details). This shows directly that the appropriate scaling variable for frequency has important logarithmic shifts close to the critical point in $d = 2$. These

[7] Their parameter ε is our $-\lim_{\omega\to 0} f$ on the floppy side of the transition with undamped dynamics.

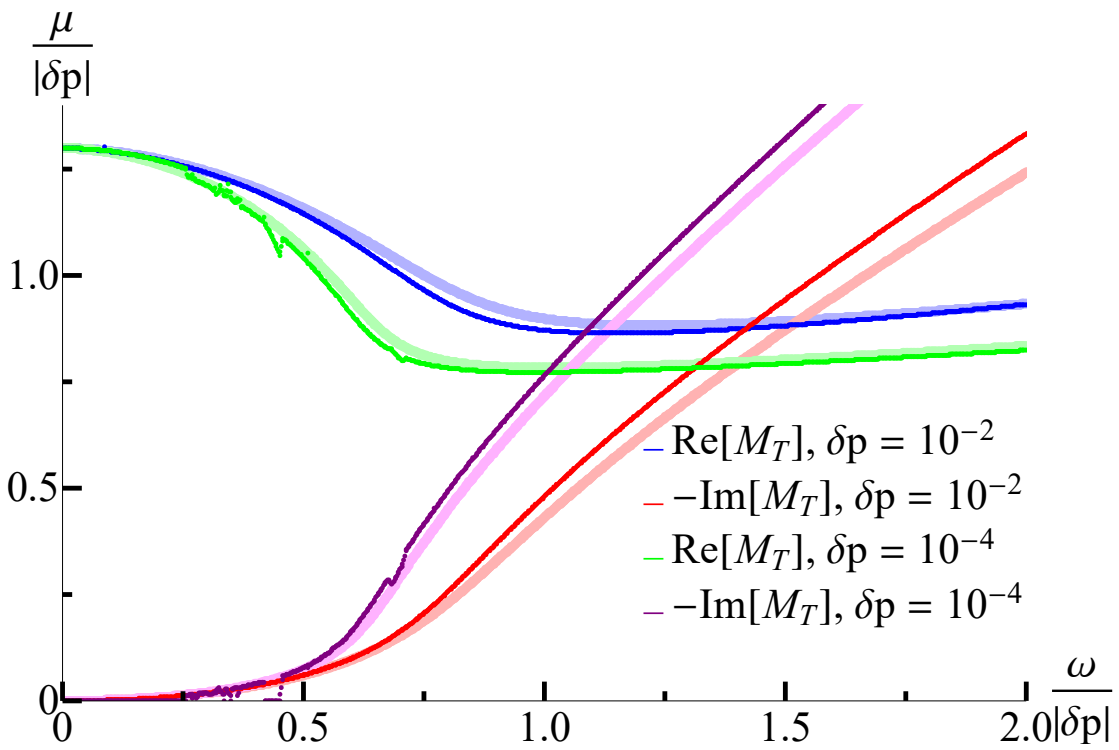

Figure 4.4: **Logarithmic frequency shifts in an effective medium theory for 2D rigidity percolation on the triangular lattice**. We plot numerical solutions of the lattice CPA (thin lines), rescaled shear modulus $M_T \equiv \mu/|\delta p|$ as a function of rescaled frequency $\Omega_T \equiv \omega/|\delta p|$, against our scaling solutions (thick lines, Equations 4.35 and C.86). This comparison is done at two distances from the critical point $\delta p = \left\{10^{-2}, 10^{-4}\right\}$, demonstrating nice agreement. All parameters in our scaling form are determined from the long-wavelength parameters of the triangular lattice (Appendix C.4), so there are no fitting parameters. The shift in the rescaled frequency Ω_T^* where $\mathrm{Re}\,(M_T) = -\mathrm{Im}\,(M_T)$ from ~ 1.4 to ~ 1.0 upon reducing δp from 10^{-2} to 10^{-4} is due to logarithmic corrections present in the upper critical dimension.

logarithmic shifts are confirmed in Figure 4.4, which compares our asymptotic scaling forms for the continuum CPA to a numerical solution of the CPA for the bond-diluted triangular lattice. More details of this comparison are located in Appendix C.4.

We believe that these logarithmic corrections to scaling can be detected in careful simulations of two-dimensional jammed packings. For instance, in [140],

the authors control the pressure of a nearly unjammed solid of soft spheres and examine the phonon transport properties. The authors examine several characteristic frequency scales and find a pure power law relating the pressure to each frequency scale: $\omega \sim p^{1/2}$ (their Figure 12(b)), consistent with the mean-field exponents and no logarithmic corrections. However, their collapse of physical features like the sound speed (their Figure 3(b)) is consistent with what would be seen with additional logarithmic corrections. In Figure 4.5, we plot predictions for the rescaled transverse sound speed c_{T} over identical ranges of frequency and comparable distances to the critical point. The residual shifts are comparable in magnitude and direction to what is seen in the simulation of compressed soft spheres in $d = 2$ after fitting the non-universal parameters, and in our case are explicitly due to logarithmic corrections to scaling.

We will now seek to unify these contrasting results for the scaling in 3D and 2D by passing to continuous spatial dimensions d and analyzing the transition as a function of spatial dimension, so that $d = 2$ and $d = 3$ appear as special cases.

4.2.5 General dimensions: RG flows and universal scaling functions

We now extend our analysis in the previous section to arbitrary continuous dimensions d. We show that new critical exponents arise for dimensions $d < 2$ (Section 4.2.5); we discuss their relevance and possible models to probe these new critical properties in Section 4.2.6. We use our predictions to deduce that the critical properties near two dimensions are described by a transcritical bifur-

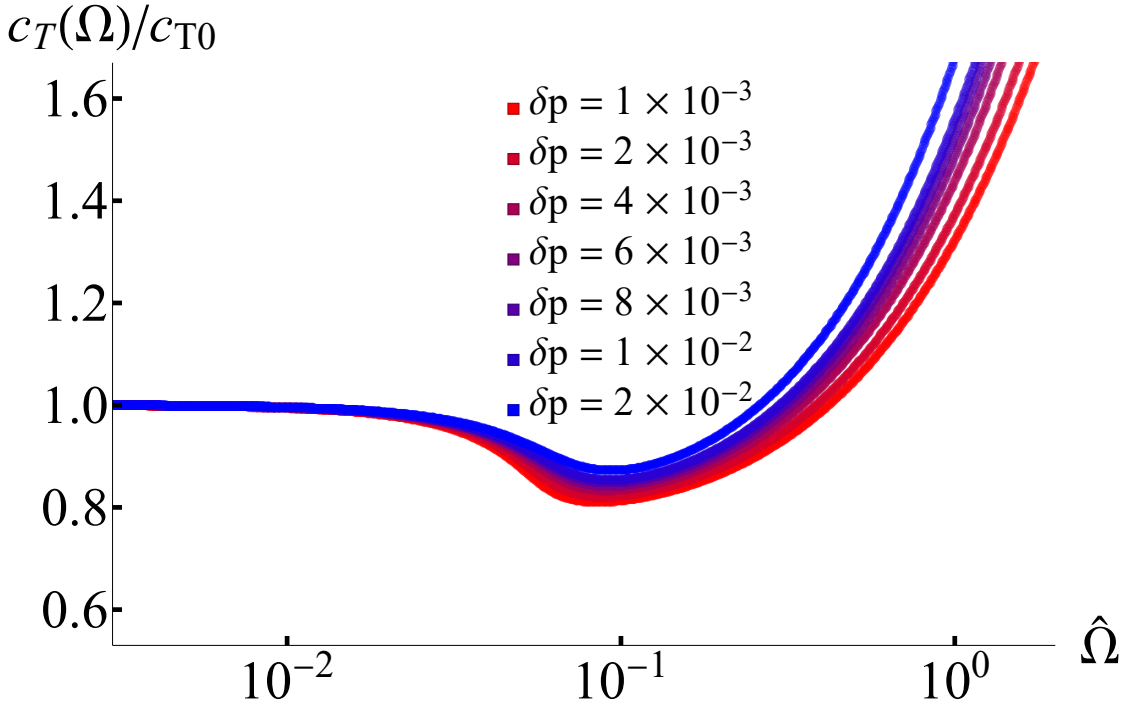

Figure 4.5: **Logarithmic shifts in the frequency-dependent transverse sound speed in two dimensions**. We plot our scaling solutions for the transverse sound speed $c_T \sim \sqrt{\mathrm{Re}\,[\mu]}$ against a rescaled frequency variable $\hat{\Omega} \equiv (\omega/\omega_0) \,/\, |\delta p|$ that ignores the logarithmic shifts. Just as in the 2D soft-sphere collapses in Figure 3(b) of [140], we see a broadening of the curves as we approach the critical point, which here is precisely due to logarithmic corrections.

cation in the renormalization group flows (as in the 4D Ising model, where the Gaussian and Wilson-Fisher fixed points exchange stability), use normal form theory [49] to predict the universal nonlinear terms needed in the RG, and use our exact solutions to deduce the CPA predictions for the values of these universal nonlinear terms (Section 4.2.5). We then investigate the fate of all invariant scaling combinations as we tune through $d = 2$ dimensions (Section 4.2.5) and write universal scaling functions for the viscoelastic shear modulus in terms of the appropriate scaling variables in each dimension. All details of the direct calculation from the CPA can be found in Appendix C.1; here we report the crucial parts necessary for the understanding of the invariant scaling combinations and

Variable	Description	Location
μ	viscoelastic shear modulus	—
δp	$p - p_c$: deviation from continuous rigidity transition p_c	—
w	$\rho\omega^2$: (undamped); $i\gamma\omega$: (overdamped)	—
f	w/μ: frequency measured relative to shear stiffness	—
M	$(\mu/\mu_0)\,/\,\lvert\delta p\rvert$: scaling variable formed between μ and δp	Eqn. 4.31, Eqn. 4.32, Eqn. C.9
F	$(f/f_0)\,/\,\lvert\delta p\rvert$: scaling variable formed between f and δp in $d > 2$	Eqn. 4.31, Eqn. C.19
F_2	scaling variable formed between f and δp in $d = 2$	Eqn. 4.35, Eqn. C.29
F_d	$(f/f_{0d})\,/\,\lvert\delta p\rvert^{2/d}$: scaling variable formed between f and δp in $d < 2$	Eqn. 4.32, Eqn. C.34
U	scaling variable for leading irrelevant correction to scaling in $d > 2$	Eqn. 4.31, Eqn. C.20
U_d	scaling variable for leading irrelevant correction to scaling in $d < 2$	Eqn. 4.32, Eqn. C.35
$\mathcal{M}$	universal scaling function for μ in $d > 2$	implicitly defined by Eqn. 4.31
$\mathcal{M}_2$	universal scaling function for μ in $d = 2$	implicitly defined by Eqn. 4.35
$\mathcal{M}_d$	universal scaling function for μ in $d < 2$	implicitly defined by Eqn. 4.32
$\mathcal{D}$	universal scaling function for the density of states in $d > 2$	Eqn. C.47
$\mathcal{D}_2$	universal scaling function for the density of states in $d = 2$	Eqn. C.49
$\mathcal{D}_d$	universal scaling function for the density of states in $d < 2$	Eqn. C.48
$\mathcal{G}$	universal scaling function for the Green's function in $d > 2$	Eqn. C.54
$\mathcal{G}_d$	universal scaling function for the Green's function in $d < 2$	Eqn. C.55

Table 4.1: **Descriptions of physical parameters and scaling variables.** The location within the manuscript of the definition of each variable is also included.

the calculation of scaling functions. Definitions of some variables that regularly appear can be found in Table 4.1, along with their location in the manuscript.

New exponents below $d = 2$

The CPA self-consistent equation (Equation 4.7) depends explicitly on the frequency only through **G** in the integral term, which splits naturally into a transverse and a longitudinal part, each of which can be evaluated separately. Following the derivation of the scaling in 3 and 2 dimensions, we first subtract p_c from each side of the equation, so that, to leading order in the scaling variables, each side of the equation $\sim |\delta p|^1$. Focusing arbitrarily on the longitudinal part, one can rescale the integration variable to $\xi = (q/q_{\mathrm{D}})^2$, to find integrals of the

form

$$-\frac{d}{2\widetilde{z}}\int_0^1 \mathrm{d}\xi\, \frac{\xi^{d/2-1}}{1-(\mu/\mathrm{w_L})\xi} = -\frac{1}{\widetilde{z}}\,{}_2\mathrm{F}_1\left(1, \frac{d}{2}; \frac{d}{2}+1; \frac{\mu}{\mathrm{w_L}}\right), \tag{4.25}$$

where $\mathrm{w_L}$ depends on the dynamics (overdamped, undamped) but is generally a frequency variable rescaled by longitudinal information; for undamped dynamics $\mathrm{w_L} = \rho\omega^2/(\lambda_\mathrm{F}/\mu_\mathrm{F} + 2)q_\mathrm{D}^2$. The function ${}_2\mathrm{F}_1\,(a, b; c; z)$ is the ordinary hypergeometric function. Note that μ is a complex number determined by the solution to the self-consistent equation. In this way, the analytic structure of the asymptotic scaling for μ is closely linked to the analytic structure of the hypergeometric function, which is convoluted enough to justify further investigation.

We now need to expand the hypergeometric function as $\mu/\mathrm{w_{L/T}}$ reaches its limiting value in the scaling limit. It is well-known in the field, and was found by us directly in Section 4.2.4, that this ratio diverges in the scaling limit in $d = 3$.[8] We will assume that this is true in all dimensions (without assuming any specific power laws) and self-consistently check it at the end. The hypergeometric function has a branch point at $z = \infty$ that we need to account for to do our expansion properly. There is a relation between the hypergeometric function's values inside the unit disk $|z| < 1$ and those outside that nicely elucidates the complex branch structure at ∞. Assuming d is not an even integer [141], we can

[8]Mean-field rigidity transitions have $\mu \sim |\delta p|$. In the the undamped case $\mathrm{w} = \rho\omega^2$ and it is well known that $\omega \sim |\delta p|$, so $\mu/\mathrm{w} \sim 1/|\delta p|$ diverges. In the overdamped case $\mathrm{w} = i\gamma\omega$, and we shall find $\omega \sim |\delta p|^2$, so again the ratio diverges as $1/|\delta p|$. In fact, our analysis is agnostic to the type of damping, so $\mathrm{w_{L/T}} \sim |\delta p|^2$ above $d = 2$ for all kinds of q-independent damping. This tells us the scaling of ω and hence that the ratio diverges.

separate our expression into two pieces

$$\frac{\Gamma\left(\frac{d}{2}\right)^2}{\Gamma\left(\frac{d}{2}+1\right)\Gamma\left(\frac{d}{2}-1\right)}{}_2\mathrm{F}_1\left(1,\frac{d}{2};\frac{d}{2}+1;\frac{\mu}{\mathrm{w_L}}\right)= \left(-\frac{\mathrm{w_L}}{\mu}\right){}_2\mathrm{F}_1\left(1,1-\frac{d}{2};2-\frac{d}{2};\frac{\mathrm{w_L}}{\mu}\right)+ +\Gamma\left(\frac{d}{2}\right)^2\frac{\Gamma\left(1-\frac{d}{2}\right)}{\Gamma\left(\frac{d}{2}-1\right)}\left(-\frac{\mathrm{w_L}}{\mu}\right)^{d/2}. \tag{4.26}$$

We will eventually recover the behavior in even dimensions d by carefully taking a limit. The hypergeometric function with $z = \mathrm{w_L}/\mu$ as an argument is 1 for $z = 0$ and can otherwise be expanded in a convergent power series in z. In other words, from our self-consistent equation, the longitudinal piece can be expanded in the scaling limit as

$$-\frac{1}{\widetilde{z}}{}_2\mathrm{F}_1\left(1,\frac{d}{2};\frac{d}{2}+1;\frac{\mu}{\mathrm{w_L}}\right)= C_1\left(\frac{\mathrm{w_L}}{\mu}\right)+C_2\left(-\frac{\mathrm{w_L}}{\mu}\right)^{d/2}+O\left(\left(\frac{\mathrm{w_L}}{\mu}\right)^2\right). \tag{4.27}$$

In the previously analyzed $d = 3$, for instance, this identifies the correction fixing the low-frequency imaginary part of the modulus as a non-analytic $(-\mathrm{w_L}/\mu)^{3/2}$ appearing in the self-consistent equation – related to our dangerously irrelevant variable.

One now tries to set the scaling of $\mathrm{w_L}/\mu$ by examining Equation 4.27. For $d > 2$, the term $(-\mathrm{w_L}/\mu)^{d/2}$ is subdominant at low frequencies to $\mathrm{w_L}/\mu$, and so $\mathrm{w_L}/\mu \sim |\delta p|$ so that either side of the self-consistent Equation 4.7 is balanced asymptotically as $\delta p \to 0$. On the other hand, for $d < 2$, $(-\mathrm{w_L}/\mu)^{d/2}$ sets the dominant contribution at low frequencies. In this scaling limit, $\mathrm{w_L}/\mu \sim |\delta p|^{2/d}$ so that $(-\mathrm{w_L}/\mu)^{d/2} \sim |\delta p|$ and either side of the self-consistent equation is balanced asymptotically as $\delta p \to 0$. We note that each of these scalings is consistent with $\mu/\mathrm{w_L} \to \infty$ in the scaling limit, justifying the expansion of the hypergeomet-

ric function around its branch point at ∞. This difference in scalings is reminiscent of a theory near its upper critical dimension: above $d = 2$, the critical exponents are dimension-independent and equal to their mean-field-like value. Below $d = 2$, the exponents are modified because the mean-field fixed point becomes unstable under the RG flow.

Deduced RG flow equations

In our case, we have access not to a principled set of renormalization group transformations for rigidity percolation or jamming, but only to previously studied scaling exponents and our explicit solutions. Here we posit RG flow equations that accurately reproduce the power-law invariant scaling combinations in our explicit solutions (see Appendix C.2). These flow equations are nonlinear functions of the system parameters that express the amount they change as the system is coarse-grained by a factor $1 + \mathrm{d}\ell$ and rescaled. We find from our explicit solution that we should measure w in units of μ (measuring frequency in units of stiffness). We also find there is an additional control variable u whose flow depends upon the dimension d: irrelevant for $d > 2$, becoming marginal in $d = 2$, and relevant at the original RG fixed point for $d < 2$.

The scale invariance near the critical point is characterized by properties (typically the eigenvalues) of the stable fixed point of the flows. We have seen that the scale invariance near the critical point changes completely as we pass through two dimensions. We can capture the scale invariance smoothly as a function of dimension by a set of coupled flow equations with a pair of fixed points that cross and exchange their stability as we pass through two dimensions.

Our group has developed [49] an understanding of how theories of critical phenomena behave in the vicinity of their upper and lower critical dimensions. Normal form theory, adapted from dynamical systems, gives a unifying description of renormalization group flows and special invariant scaling combinations. In particular, it gives us the language necessary to interpret flows near a bifurcation. In the Ising model near its upper critical dimension $d = 4$, for instance, a variable that can be identified with the quartic coupling u which was once irrelevant in $d > 4$ becomes marginal in $d = 4$ and relevant below (at the Gaussian fixed point), redirecting the flows to the new, stable Wilson-Fisher fixed point. In the normal form language, the RG flow of this parameter undergoes a transcritical bifurcation around $d = 4$. Through an analytic change of coordinates, the flow equations can be cast into their *normal form* in the vicinity of $d = 4$. In typical cases (such as in the three-dimensional Ising model), the normal form can completely linearize the flow at the fixed point, giving invariant scaling combinations that are ratios of powers of physical quantities, and hence power-law behavior that can be characterized by critical exponents. But precisely *at* the bifurcation in the upper critical dimension, one must keep specific nonlinear terms which cannot be removed by an analytic change of variables, and these nonlinear terms capture completely the well-known logarithmic corrections.

Based on our explicit solution, we thus posit the following RG flow equations[9], which accurately reproduce the power-law invariant scaling combina-

[9]Normal form theory [49] demands a cubic term Du^3 in the equation for $\mathrm{d}u/\mathrm{d}\ell$. We have checked that the constant $D = 0$ for our explicit solution.

tions in all dimensions $d \neq 2$:

$$\begin{aligned}
\frac{\mathrm{d}q}{\mathrm{d}\ell} &= q, \\
\frac{\mathrm{d}\delta p}{\mathrm{d}\ell} &= 2\delta p - u\,\delta p, \\
\frac{\mathrm{d}\mu}{\mathrm{d}\ell} &= 2\mu - u\,\mu, \\
\frac{\mathrm{d}f}{\mathrm{d}\ell} &= 2f, \\
\frac{\mathrm{d}u}{\mathrm{d}\ell} &= (2-d)u - u^2,
\end{aligned} \tag{4.28}$$

where the nonlinear terms can be removed in dimensions $d > 2$. Details of the determination of these flow equations can be found in Appendices C.2 and C.3. In the flow equations for parameters other than u, the terms involving products of flow parameters are higher-order and so the invariant scaling combinations in dimensions other than $d = 2$ can be accurately determined by setting u equal to its value at the stable RG fixed point, as we will do in the following section.

Scaling variables and scaling functions

We now use the flow equations deduced from the scaling behavior together with the asymptotic expansions of the CPA close to the critical point to write scaling variables and scaling functions for the viscoelastic moduli in arbitrary dimensions. Turning our focus to the flow equation for u, we find $u_c = 0$ for $d > 2$ and $u_c = 2 - d$ for $d < 2$: by construction, the flow equation for u undergoes a transcritical bifurcation in $d = 2$ (Figure 4.6).

To demonstrate that the scaling for f deduced from the flow equations is consistent with the direct CPA calculation both above and below $d = 2$, we combine the flow equations for δp and f to write

$$\frac{\mathrm{d}\log(f)}{\mathrm{d}\log(\delta p)} \approx \frac{2}{2-u_c} \implies f \sim \delta p^{2/(2-u_c)}. \tag{4.29}$$

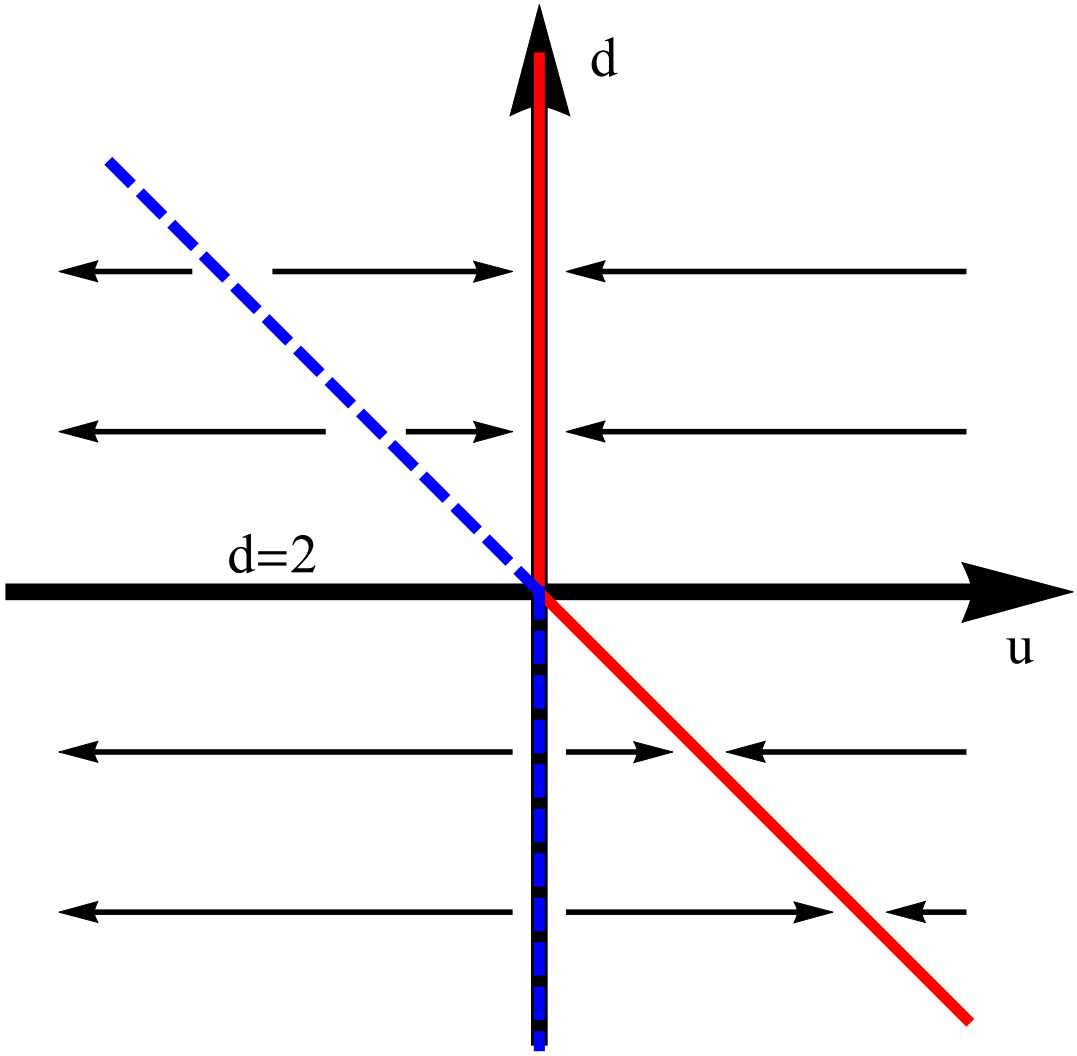

Figure 4.6: **Flows of the parameter u under the RG**. The solid, red lines indicate attractive fixed points. The dashed, blue lines indicate repulsive fixed points. For $d > 2$, u flows to 0. For $d < 2$, u flows to $u_c = 2 - d$, a different fixed point. This is a transcritical bifurcation; two fixed points cross and exchange their stability in $d = 2$. The dimension-dependent critical exponents for $d < 2$ are controlled by the new stable fixed point.

This is correct away from $d = 2$, as $u_c = 0$ makes the exponent $2/(2 - u_c) = 1$ and $u_c = 2 - d$ makes the exponent $2/(2 - u_c) = 2/d$. (We will explore $d = 2$ below, where the full flow equations including the nonlinear terms are needed to determine the complicated invariant scaling combinations.) For $d > 2$, we

must retain the flow equation for u despite its irrelevance; it is a dangerously irrelevant variable since the scaling function for M is not analytic at $U = 0$.

Is this interesting, given that we typically don't do simulations of colloidal gels or other disordered rigid systems *below* two dimensions? While we do not expect experiments to test our predictions in non-integer dimensions, in Section 4.2.6 we discuss applications to theoretical simulations in $d < 2$. In two dimensions, however, these predictions are in principle experimentally observable. This is a case where the upper critical dimension of a theory is physically relevant (at least as determined within the CPA). In the Ising model at its upper critical $d = 4$, there is a logarithmic singularity in the magnetization, which also has important (*very* slowly vanishing at the critical point) log-log corrections. Here, the situation is identical. Suppose one picks out a physically relevant piece of dynamical information at this rigidity transition, like the frequency ω^* where we cross over into being dominated by dissipation $\mathrm{Re}\,(\mu\,(\omega^*)) = -\mathrm{Im}\,(\mu\,(\omega^*))$. For all d away from 2, we can write how this physical frequency scales with our excess contact number: in the undamped case, $\omega^* \sim \delta p^{(4-u_c)/(4-2u_c)}$. But in 2 dimensions, there are detectable shifts in this frequency, and it turns out that for the undamped case $\omega^* \sim |\delta p| \left|\log |\delta p|\right|^{-1/2}$ with additional important log-log corrections.

This can be understood by writing the proper invariant scaling combinations in the upper critical dimension using the flow equations. In Appendix C.3, we show that the scaling of the frequency variable in 2 dimensions implied by the renormalization group flow equations is (making only the δp dependence explicit)

$$f \sim \frac{x(u)\delta p}{W\,(x(u)\,\delta p)}, \tag{4.30}$$

where W is again the Lambert W function and $x(u)$ is an explicit function of the (marginally) irrelevant scaling variable. This accurately reproduces the asymptotic behavior of the frequency scaling that was found by directly evaluating the CPA in $d = 2$ (Equation 4.24) and connects this result to scaling found in standard critical phenomena.

As investigated in the particular cases of $d = 3$ and $d = 2$ in previous sections, the CPA self-consistent equation also gives us predictions for the universal scaling *functions* determining the moduli; when written in the appropriate scaling variables for each dimension one can predict the shape of scaling collapse plots of measurements of viscoelastic moduli close to a rigidity transition. With this in mind, we seek to write the self-consistent equations in a form that is consistent with the posited renormalization group flow equations.

For dimensions $d > 2$ not even, retaining the lowest-order terms leads to a scaling function of the form

$$\begin{aligned} \pm 1 - M &= F + U\,(-F)^{d/2}\,, \\ F = \frac{f/f_0}{|\delta p|},\ M &= \frac{\mu/\mu_0}{|\delta p|},\ U = u/u_0\,|\delta p|^{d/2-1}\,, \end{aligned} \tag{4.31}$$

where the scaling variable F is the invariant scaling combination formed between f and δp and f_0, μ_0, and u/u_0 are complicated but explicit combinations of microscopic parameters (Appendix C.1). The sign $\pm 1 = \delta p/|\delta p|$ is for the rigid and floppy side of the transition, respectively. The scaling variable F can be adapted to deal with different microscopic dynamics. This is an implicit definition of a universal scaling function for $M = \mathcal{M}(F, U)$ for $d > 2$. Here we note that the scaling variable U varies with the correct power of δp to be identified as the invariant scaling combination formed between u and δp. Thus u is correctly identified as being irrelevant in dimension $d > 2$. As mentioned before in Sec-

tion 4.2.4, in previous work [9, 45], U is set to 0, making the eventual solution for $\mu(\omega)$ the solution to a quadratic equation, with a cuspy form not seen in the full numerical solution to the CPA. The variable u is dangerously irrelevant for microscopically undamped dynamics in all $d > 2$ and needs to be retained to understand the behavior of the low-frequency viscous part of the modulus. We also note that the effect of U is nonperturbative in the inverse spatial dimension: near $d = \infty$ perturbing in $\epsilon \equiv 1/d$, $U \sim |\delta p|^{1/(2\epsilon)}$. This effect is not specific to the CPA, since above the upper critical dimension the onset of the plateau in the density of states is $\omega^* \sim |\delta p|$ while a description of the phononic contribution to the low-frequency density of states gives Debye behavior $\sim \omega^{d-1}$ which is heavily suppressed in high dimensions.

Below dimension 2, we are forced to change our scaling variables to the ones relevant at the new attractive RG fixed point. We find

$$\begin{aligned} \pm 1 - M &= -(-F_d)^{d/2} - U_d F_d, \\ F_d &= \frac{f/f_{0d}}{|\delta p|^{2/d}},\ U_d = u_d/u_{0d}\,|\delta p|^{2/d-1}\,. \end{aligned} \tag{4.32}$$

This is an implicit definition of a universal scaling function for $M = \mathcal{M}_d(F_d, U_d)$ for $d < 2$. This scaling identifies U_d as the invariant scaling combination associated with u in the vicinity of the new attractive fixed point that has emerged below $d = 2$, with the correct exponent on δp (see Appendix C.2 and Appendix C.1 for details). We summarize the usual critical exponents in Table 4.2.

One can recover the scaling function in $d = 2$ by carefully taking a limit $d \to 2$. Reinstalling the definition of U above $d = 2$, and pulling out a factor of

	f_{CPA}	ν	z	$\theta \equiv \omega\nu$	γ
$d > 2$	1	$1/2$	2	$d/2 - 1$	2
$d < 2$	1	$1/d$	$1 + d/2$	$2/d - 1$	$1 + 2/d$

Table 4.2: **Critical exponents as predicted by the CPA** in the undamped case, away from the upper critical dimension $d_{\text{upper}} = 2$. The invariant scaling combinations in d_{upper} capture the logarithmic corrections typical of an upper critical dimension.

$\Gamma(d/2 - 1)$ that was previously absorbed into a definition of f_0, one finds

$$\begin{aligned} &\pm 1 - M = \\ &\quad -F' \left(\left(-(u/u_0)' \tfrac{2}{d-2} F' \left| \delta p \right| \right)^{d/2-1} - 1 \right) \Gamma\left(\frac{d}{2} - 1 \right). \end{aligned} \tag{4.33}$$

As $d \to 2^+$, this reproduces a limit similar to those seen in the replica trick $(x^n - 1)/n \to \log(x)$ as $n \to 0$ (elaborated upon in Appendix C.1). The resulting expression

$$\pm 1 - M = -F' \log\left(-(u_2/u_{02}) F' \left| \delta p \right| \right) \tag{4.34}$$

gives the right asymptotic behavior predicted by the RG flows *at* the transcritical bifurcation, but is not written in the appropriate scaling variables for $d = 2$; if one fixes these scaling variables but takes the scaling limit $\delta p \to 0$, one side of the self-consistent equation diverges. If one inserts the proper frequency variable, the equation is asymptotically

$$\begin{aligned} &\pm 1 - M = F_2, \\ &\quad F_2 = -\frac{f/f_{02}}{|\delta p|} \log\left(-(u_2/u_{02}) f/f_{02} \right). \end{aligned} \tag{4.35}$$

This is a definition of a universal scaling function for $M = \mathcal{M}_2(F_2)$ for $d = 2$. Explicit formulas for all quantities in terms of the microscopic parameters of the isotropic elastic sheet are also derived in Appendix C.1. In Figure 4.4, we numerically solve the CPA self-consistent equations for the triangular lattice in the undamped case, which is not microscopically isotropic and which has a hexagonal Brillouin zone. Nonetheless, because there is an emergent long-wavelength

isotropy, the scaling behavior of its modulus near the critical point is well-described by our forms of the scaling function for the isotropic elastic sheet. Performing the naïve rescalings $M_T = \mu/|\delta p|$ and $\Omega_T = \omega/|\delta p|$, one sees a slow but systematic shift of the crossing point Ω_T^* where $\mathrm{Re}\left(M_T(\Omega_T^*)\right) = -\mathrm{Im}\left(M_T(\Omega_T^*)\right)$. If Ω_T were the correct scaling variable to use, as it is in all $d > 2$, this crossing point would have small corrections away from $p = p_c$ but would otherwise be constant in Ω_T. Our form of the universal scaling function in $d = 2$ perfectly accounts for these logarithmic shifts.

4.2.6 Applicability of the transition to physical systems

To what systems do we expect the behavior to be quantitatively described by our universal scaling predictions? What features of our predictions do we expect to apply more broadly to rigidity transitions? Here we discuss clearly where our universal predictions do not apply, and speculate about where they may provide qualitative or quantitative guidance.

As noted in the introduction and in Appendix C.4, our continuum CPA does not correctly describe the diluted triangular spring lattice, which exhibits non mean-field critical exponents in its static properties in two dimensions rather than the predicted log-corrections to mean-field theory [5, 117]. Generalized to describe the abrupt jump in the bulk modulus, the continuum CPA applies qualitatively to simulations of spring network geometries generated from jammed packings [142]. The generalized continuum CPA reproduces the numerically observed jamming mean-field exponents in three dimensions, and both this calculation and the simulation find mean-field exponents with log corrections to

scaling in two dimensions (however, see below). Indeed, based partly on a discussion years ago with Carl Goodrich, we conjecture that randomly diluting a spring network generated from a jammed packing starting in the rigid phase will undergo a transition where both bulk and shear moduli grow continuously, described quantitatively by the version of our continuum CPA analyzed here [143].

Why is the triangular lattice (and, by implication, many other spring lattices) not behaving according to our theory? While the triangular lattice is statistically isotropic in its elastic moduli, many critical points are more sensitive than elastic theory to breaking of rotational invariance. The XY model is unstable to breaking of triangular and square symmetries [144, 145], and diffusion-limited aggregation is famous for breaking rotational invariance in a way that revealed itself only in (then) large simulations [118]. Statistically isotropic lattices might show mean-field behavior. Another likely culprit are the straight lines between bonds in the triangular lattice, which are shared with the Mikado networks [146] formed by random long fibers cross-linked at their intersections. A node connecting two parallel bonds cannot move freely under tensile stress, while at any non-zero angle it needs a third constraint to fix it in place: such *second-order constraints* are expected to change critical properties [59, 119]. A generic lattice with the same connectivity structure as a regular triangular lattice, as suggested by Jacobs [59], could be enough to show mean-field behavior. Diluted, statistically isotropic spring networks with random node positions show mean-field exponents, but it appears necessary to include the effects of pre-stress to capture information about additional frequency scales that arise close to the transition [52]. This can be done in an effective medium framework, and we expect similar logarithmic corrections in $d = 2$ to the ones investigated in this

manuscript. However, effective medium theories generally incorrectly predict the amplitudes of response properties such as sound attenuation, and a better starting theory is likely needed to understand this discrepancy [140].

As noted above, this continuum analysis has a natural extension to describe a jamming transition, inspired again by [2, 9, 45]. There the upper critical dimension is believed to be two, and our model (and the lattice CPA models) does agree with known critical exponents. However, our calculation for jamming shows logarithmic corrections to scaling that only arise in frequency-dependent quantities, as we have seen in this manuscript, while convincing numerical work shows logarithmic corrections to the finite-size scaling of zero-frequency elastic moduli in jamming simulations [142]. We suspect that the lack of logarithmic corrections to the finite-size effects in our 2D jamming variant is related to the CPA assumption that the moduli are independent of wavevector. One notes that the Green's function and other wavevector-dependent properties have a wavevector scale in 2D that does have logarithmic corrections to scaling $q^* \sim |\delta p|^{1/2} \left|\log |\delta p|\right|^{-1/2}$ (similar to the frequency scaling). Our current theory replaces the system near its rigidity transition with a uniform but frequency dependent modulus, ignoring the important effects of spatial fluctuations. A more sophisticated self-consistent approach allowing for more general forms of response functions, such as the manuscript of Vogel et al. [132] mentioned in the Introduction, could be analyzed to extract a universal scaling theory that not only correctly describes the finite-size effects in two-dimensional jamming, but also describes the 2D and 3D crossovers to the elastic-dipole induced correlations of glasses [133, 134, 147] and Rayleigh scattering. However, the detailed simulations of [44] do appear to reproduce the logarithmic shifts in the density of states and $\ell_c^{-1} \sim q^*$ explained in this work.

Will our predictions of new critical behavior for $d < 2$ in Section 4.2.5 have any chance of being tested? Jamming has been studied for hard disks in a one-dimensional channel [148], exhibiting different critical exponents for the distribution of small gaps than in higher dimensions. We suspect our predicted critical exponents for linear response properties may be only qualitatively predictive in $d = 1$. While our theory predicts exact new values for critical exponents for all $d < d_{\text{upper}} = 2$, we trust our predictions quantitatively only near the upper critical dimension. Indeed, other approximate methods such as mode-coupling theories [149, 150] give correct critical exponents in $d_{\text{upper}} - \epsilon$ only to order ϵ^1, where higher-order corrections demand further diagrammatic calculations.

The calculation presented here could, however, quantitatively describe a rigidity transition in a one-dimensional model with long-range bonds. For instance, the one-dimensional Ising model [151] with bond strengths that decay with a power law $J(r) \sim r^{-(1+\sigma)}$ has an ordering transition for $\sigma < \sigma_{\text{L}} = 1$ and has nontrivial critical exponents for $1/2 < \sigma < 1$. The situation is similar in ordinary percolation with long-range bonds [152], where having a bond length distribution $P(r) \sim r^{-(1+\sigma)}$ leads to a percolation transition at a threshold $0 < p_c < 1$ for $0 < \sigma < 1$, and nontrivial critical exponents for $1/3 < \sigma < 1$ with additional logarithmic corrections to scaling at $\sigma = 1/3$. This could be extended to an elastic rigidity transition by replacing the connecting bonds by elastic springs and measuring the elastic modulus. Additionally, the long-range random-bond Ising model in one dimension has a spin glass phase [153]. These are all cases where tuning the exponent associated with the range of the interaction can be used to continuously tune the effective dimension of the critical properties of the transition, allowing us to access the continuous predictions of critical exponents in the vicinity of the upper critical dimension.

Finally, additional extensions to this scaling theory can in principle be added by hand. Exactly *at* the rigidity transition, there is no linear response regime, which has attracted much interest in the jamming community. Tiny deformations induce both microscopic topology changes and avalanches of all sizes. Scaling theories have been developed to describe, for instance, power-law relationships between friction coefficients and shear rate in granular matter close to its flowing instability [134, 154]. Analytical predictions for the universal scaling functions may not be as simple to determine, but once a suitable scaling theory is established, adding new phenomena (such as rheological responses beyond the linear regime) should be possible.

4.2.7 Summary & Conclusions

In summary, we take seriously a dynamical version of the CPA, a frequently used effective medium theory. We examine its predictions close to the critical point, casting solutions into scaling forms to identify universal pieces. We first examine its predictions for the universal scaling functions for effective viscoelastic moduli close to the critical point in $d = 3$ and identify a dangerously irrelevant variable that controls low-frequency dissipation in the case of microscopically undamped dynamics. We then investigate $d = 2$, and we find that the appropriate invariant scaling combinations are not ratios of powers of parameters, as we would expect close to a hyperbolic RG fixed point. To our surprise, although the exponents with which the *static* moduli vanish with δp are unchanged with dimension, the critical exponents associated with relevant length and time scales in the system change quantitatively as we pass below $d = 2$. This identifies $d = 2$ as the upper critical dimension of the theory. From the ex-

act solution, we deduce from normal form theory [49] a set of renormalization group flow equations which have a transcritical bifurcation in two dimensions. These are constructed to match the forms of the scaling variables above, below, and in the upper critical dimension $d = 2$. These forms are self-consistently checked against numerical solutions of the lattice CPA for a bond-diluted triangular lattice, verifying these important corrections in this physically relevant dimension.

4.2.8 Acknowledgments

The authors thank Gilles Tarjus for recommending deeper analysis of the connection with the $4 - \epsilon$ expansion of the Ising model. SJT thanks Bulbul Chakraborty for interesting discussions about logarithmic corrections in the upper critical dimension. SJT, IC, and JPS are supported by NSF DMR-2327094. DBL is supported by FAPESP through grants # 2021/14285-3 and # 2022/09615-7.

CHAPTER 5

SIMULATIONS OF RIGIDITY TRANSITIONS IN ANISOTROPIC RANDOM LATTICES

5.1 Anisotropy in real biological materials

There has been recent interest in understanding real biological materials starting from extreme points in their phase diagram. When a wound heals, for instance, cells around the injury appear to liquify to fill the gap, indicating that an external stimulus has driven them to change their phase to perform a function [155]. By understanding properties of the phase transition that they undergo, we can understand properties related to cell operations within their phase under normal, non-healing conditions.

Similar phase transitions from (more) floppy to (more) rigid states occur in cartilage. When a sample of cartilage is isolated and highly strained, its stiffness can increase by several orders of magnitude over changes of a few percent in strain (a highly nonlinear elastic effect). These kinds of crossovers can be captured using models that incorporate chains made of stiff rods (mimicking the collagen fibers in the cartilage) that straighten out under large strains, leading to engagement of the stiff fibers' stretching modes. Understanding the response of real cartilage then entails incorporating corrections to this transition when background gels, bending stiffnesses, or secondary networks are added [6, 7, 8]. Importantly, this behavior in cartilage is highly anisotropic, as the stretching modes of long fibers are engaged preferentially along the maximum extensive axis for the applied strain.

Even isotropic networks become anisotropic under the finite strains that are necessary to induce strain stiffening. But the collagen networks that are believed to be involved in strain stiffening are intrinsically anisotropic: near the surface of cartilage, the fibers are oriented preferentially parallel to the surface before gradually rotating into other configurations within the bulk. This anisotropy that is baked into the structure of the collagen network can affect the response even at infinitesimal strains, where we probe the linear elastic regime. A generic theory of linear elasticity incorporates the different strains in different directions into a 4-index elasticity tensor $C_{ijk\ell}$:

$$E = \frac{1}{2}\epsilon_{ij}C_{ijk\ell}\epsilon_{k\ell}. \tag{5.1}$$

where ϵ_{ij} is the linearized symmetric strain tensor, expressed in terms of derivatives of the local displacement field u_i:

$$\epsilon_{ij} = \frac{1}{2}\left(\nabla_i u_j + \nabla_j u_i\right). \tag{5.2}$$

The elasticity tensor is symmetric under the interchange of dummy indices $ij \leftrightarrow k\ell$ because the energy density is quadratic in the strain tensor (this is called the *major symmetry*). It is independently symmetric under the interchange $i \leftrightarrow j$ and $k \leftrightarrow \ell$ thanks to the symmetry of the stress and strain tensors (these are called *minor symmetries*).

The stress that is felt under a particular strain can then be straightforwardly computed:

$$\sigma_{ij} = \frac{\partial E}{\partial \epsilon_{ij}} = C_{ijk\ell}\epsilon_{k\ell} \tag{5.3}$$

which is a generalization of Hooke's law for linear springs to a linear elastic medium in arbitrary dimensions. We can count how many independent components of $C_{ijk\ell}$ are possible under different symmetries in d dimensions. In the

least symmetric case, each index can be in the set $\{1, \ldots, d\}$. This gives d^4 components before taking into account the major and minor symmetries. This can be done by forming a matrix out of the independent (taking into account the minor symmetries) pairs of components ij and $k\ell$. In dimension $d \geq 2$, there are $n = d + d!/2!(d-2)!$ of these pairs (in $d = 3$, the $n = 6$ independent pairs are $\{xx, yy, zz, xy, yz, zx\}$, for instance). We imagine forming an $n \times n$ matrix of these elastic coefficients. The major symmetry is then simply the statement that this matrix is symmetric. An $n \times n$ symmetric matrix has $n(n+1)/2$ independent components. This means that the most anisotropic linear elastic material possible in d dimensions has

$$\frac{1}{2}\left(d + \frac{d!}{2(d-2)!}\right)\left(d + \frac{d!}{2(d-2)!} + 1\right) = \frac{1}{8}d\,(d+1)\left(d^2 + d + 2\right) \tag{5.4}$$

independent stiffnesses that can be measured to characterize the response properties. In $d = 2$, this number is 6, while in $d = 3$, this number is 21. Additional symmetries of the material can then be used to further reduce the number of independent elastic components.

This reduction generally goes as follows: the uniform material is typically invariant in its properties under some group of transformations from $O(d)$: reflections and rotations in d dimensions. This invariance could come, for instance, from its microstructure (like having a crystal with a cubic unit cell). Suppose $R_{ij} \in O(d)$ is a symmetry of the material. Then we can rotate the coordinates within our shear and recover the same energetic cost of deformation. Under a rotation, a shear transforms as

$$\epsilon_{ij} \to \epsilon'_{ij} = R_{ik}\epsilon_{k\ell}R_{j\ell} \tag{5.5}$$

This means that we find further relationships amongst the different components

of the elastic tensor:

$$\frac{1}{2}\epsilon_{ij}C_{ijk\ell}\epsilon_{k\ell} = \frac{1}{2}\epsilon'_{ij}C_{ijk\ell}\epsilon'_{k\ell} = \frac{1}{2}R_{im}\epsilon_{mn}R_{jn}C_{ijk\ell}R_{ko}\epsilon_{op}R_{\ell p}. \tag{5.6}$$

Reindexing $i \leftrightarrow m, j \leftrightarrow n, k \leftrightarrow o, \ell \leftrightarrow p$ gives

$$\frac{1}{2}\epsilon_{ij}C_{ijk\ell}\epsilon_{k\ell} = \frac{1}{2}\epsilon_{ij}\left(R_{mi}R_{nj}C_{mnop}R_{ok}R_{p\ell}\right)\epsilon_{k\ell} \tag{5.7}$$

or, since the strain is arbitrary,

$$C_{ijk\ell} = R_{mi}R_{nj}R_{ok}R_{p\ell}C_{mnop}. \tag{5.8}$$

When we construct our 4-index tensor, we have our scalar "moduli." To get the 4-index orientation of the material correct, we can write a basis for all 4-index tensors from outer products of four orthonormal basis vectors à la $\hat{x}_i\hat{x}_j\hat{x}_k\hat{x}_\ell$.[1] Once again, the major and minor symmetries of the elasticity tensor, together with the additional symmetries imposed by the material, restrict the number of independent coefficients we are allowed to have. Let's focus on two dimensions for now. We only have six independent components of the elasticity tensor. We can represent the invariance given by the major and minor symmetries by grouping terms that transform into each other under these symmetries with the same coefficient:[2]

$$\begin{aligned} C_{ijk\ell} = {} & C_{11}\hat{x}\hat{x}\hat{x}\hat{x} + C_{22}\hat{y}\hat{y}\hat{y}\hat{y} + C_{33}\left(\hat{x}\hat{y}\hat{x}\hat{y} + \hat{x}\hat{y}\hat{y}\hat{x} + \hat{y}\hat{x}\hat{x}\hat{y} + \hat{y}\hat{x}\hat{y}\hat{x}\right) + \\ & + C_{12}\left(\hat{x}\hat{x}\hat{y}\hat{y} + \hat{y}\hat{y}\hat{x}\hat{x}\right) + C_{13}\left(\hat{x}\hat{x}\hat{x}\hat{y} + \hat{x}\hat{x}\hat{y}\hat{x} + \hat{x}\hat{y}\hat{x}\hat{x} + \hat{y}\hat{x}\hat{x}\hat{x}\right) + \\ & + C_{23}\left(\hat{y}\hat{y}\hat{x}\hat{y} + \hat{y}\hat{y}\hat{y}\hat{x} + \hat{x}\hat{y}\hat{y}\hat{y} + \hat{y}\hat{x}\hat{y}\hat{y}\right). \end{aligned} \tag{5.9}$$

[1] This is just like how a vector v_i can be expanded in an orthonormal basis $\hat{x}_i$. These basis tensors for the four-index case can be thought of as $d \times d$ matrices of $d \times d$ matrices with a single entry 1 and all other entries 0.

[2] Here I use the common matrix naming convention for the components of the elasticity tensor, where $\{xx, yy, xy\} \leftrightarrow \{1, 2, 3\}$ for the indices.

Now let's suppose that our material is symmetric independently under x and y reflections.[3] These flip the signs of terms with an odd number of $\hat{x}$ and $\hat{y}$, so $C_{13} = C_{23} = 0$, and we have only four independent moduli:

$$C_{ijk\ell} = C_{11}\hat{x}\hat{x}\hat{x}\hat{x} + C_{22}\hat{y}\hat{y}\hat{y}\hat{y} + C_{33}\left(\hat{x}\hat{y}\hat{x}\hat{y} + \hat{x}\hat{y}\hat{y}\hat{x} + \hat{y}\hat{x}\hat{x}\hat{y} + \hat{y}\hat{x}\hat{y}\hat{x}\right) + C_{12}\left(\hat{x}\hat{x}\hat{y}\hat{y} + \hat{y}\hat{y}\hat{x}\hat{x}\right). \tag{5.10}$$

Suppose additionally that the material is invariant under rotations by 90°. This transforms $\hat{x}$ into $\hat{y}$ and $\hat{y}$ into $-\hat{x}$, which maps $\hat{x}\hat{x}\hat{x}\hat{x} \to \hat{y}\hat{y}\hat{y}\hat{y}$ and the other terms grouped in parentheses into themselves (since each term has the same number of $\hat{x}$'s and $\hat{y}$'s). This means that $C_{11} = C_{22}$, and so we have three independent elastic moduli:

$$C_{ijk\ell} = C_{11}\left(\hat{x}\hat{x}\hat{x}\hat{x} + \hat{y}\hat{y}\hat{y}\hat{y}\right) + C_{33}\left(\hat{x}\hat{y}\hat{x}\hat{y} + \hat{x}\hat{y}\hat{y}\hat{x} + \hat{y}\hat{x}\hat{x}\hat{y} + \hat{y}\hat{x}\hat{y}\hat{x}\right) + C_{12}\left(\hat{x}\hat{x}\hat{y}\hat{y} + \hat{y}\hat{y}\hat{x}\hat{x}\right). \tag{5.11}$$

Finally, let's assume that the material is additionally invariant under rotations by 60°. This transforms $\hat{x}$ into $\hat{x}/2 + \sqrt{3}\hat{y}/2$ and $\hat{y}$ into $-\sqrt{3}\hat{x}/2 + \hat{y}/2$. The 4-index basis objects get mapped into monstrously long expressions, but we can use Mathematica to check their coefficients. For instance, before the transformation, the coefficient of $\hat{x}\hat{x}\hat{x}\hat{x}$ is C_{11}. After the transformation, it is $\left(C_{11} + 9C_{11} + 3C_{33} + 3C_{33} + 3C_{33} + 3C_{33} + 3C_{12} + 3C_{12}\right)/16$. Because the coefficients before and after the transformation must be equal to respect the symmetry, one has

$$C_{11} = \frac{5}{8}C_{11} + \frac{3}{4}C_{33} + \frac{3}{8}C_{12} \implies C_{11} = C_{12} + 2C_{33}, \tag{5.12}$$

eliminating another independent modulus. We can check the coefficients of other terms, like $\hat{x}\hat{x}\hat{y}\hat{y}$, but these turn out to give the same equation for C_{11} in

[3] This is the situation with the anisotropic triangular lattice that we will study in detail in the manuscript of this section.

terms of C_{12} and C_{33}. Hence we have only two independent moduli:

$$\begin{aligned} C_{ijk\ell} = (C_{12} + 2C_{33})\,(\hat{x}\hat{x}\hat{x}\hat{x} + \hat{y}\hat{y}\hat{y}\hat{y} + \hat{x}\hat{x}\hat{y}\hat{y} + \hat{y}\hat{y}\hat{x}\hat{x}) + \\ + C_{33}\,(\hat{x}\hat{y}\hat{x}\hat{y} + \hat{x}\hat{y}\hat{y}\hat{x} + \hat{y}\hat{x}\hat{x}\hat{y} + \hat{y}\hat{x}\hat{y}\hat{x} - 2\hat{x}\hat{x}\hat{y}\hat{y} - 2\hat{y}\hat{y}\hat{x}\hat{x})\,. \end{aligned} \tag{5.13}$$

Is this as simple as it gets? The first of these collections of basis tensors in parentheses is 1 if the first two *and* the last two indices are equal, and zero otherwise. This is the tensor $\delta_{ij}\delta_{k\ell}$. The second term in parentheses is 1 if the first and third *and* second and fourth indices agree but are different from each other *or* if the first and fourth *and* second and third indices agree but are different from each other. It is also -2 if the first two and last two indices agree individually as pairs but are different from each other. These conditions can be written all together as $\delta_{ik}\delta_{j\ell} + \delta_{i\ell}\delta_{jk} - 2\delta_{ij}\delta_{k\ell}$.[4] Hence the above expression reduces to

$$C_{ijk\ell} = C_{12}\delta_{ij}\delta_{k\ell} + C_{33}\left(\delta_{ik}\delta_{j\ell} + \delta_{i\ell}\delta_{jk}\right). \tag{5.14}$$

One can check easily that this tensor is in fact invariant under any rotation, even though we have only imposed a few discrete symmetries. In arbitrary dimension d, $\delta_{ij}\delta_{k\ell}$ and $\left(\delta_{ik}\delta_{j\ell} + \delta_{i\ell}\delta_{jk}\right)$ are the only 4-index isotropic tensors that one can construct obeying the major and minor symmetries of the elasticity tensor [36]. This is general enough to justify giving names to the coefficients; these coefficients are called the *Lamé parameters* $C_{12} \equiv \lambda$ and $C_{33} \equiv \mu$. The two independent moduli can also be decomposed into a shear modulus G (the energetic cost for a shear ϵ_{xy} (for instance) is $G\epsilon^2/2$) and a bulk modulus B (the energetic cost for a dilation $\epsilon_{ij} = (\epsilon_{kk}/d)\,\delta_{ij}$ is $B\epsilon^2/2$). Using the expression for the isotropic elastic medium, one can find these moduli in terms of the Lamé parameters:

$$G = \mu, \qquad B = \lambda + \frac{2}{d}\mu. \tag{5.15}$$

[4] It is worth checking the cases $\hat{x}\hat{x}\hat{x}\hat{x}$ and $\hat{y}\hat{y}\hat{y}\hat{y}$ – they are 0 thanks to a convenient cancellation.

As an inhomogeneous anisotropic three-dimensional material, cartilage is sufficiently complicated that completely characterizing even its linear elastic properties is a hard job. We are interested in understanding the behavior of cartilage and more general anisotropic rigid networks close to a rigidity transition. Because the number of independent elastic constants for a homogeneous maximally anisotropic material grows very quickly with dimension $\sim d^4/8$, we restrict our computational analysis to a simpler, two-dimensional case and focus on qualitative aspects of the transition (since many of the critical exponents seen in rigidity percolation are not mean-field-like, we do not expect the exponents to match an analysis performed for the corresponding three-dimensional problem).

For a model that undergoes a rigidity transition, we choose a central force bond percolation model on a triangular lattice. At long wavelengths, the triangular lattice is isotropic.[5] When we randomly dilute the triangular lattice, its long-wavelength elastic properties remain statistically isotropic, and we can talk about average values for the two independent moduli as a function of bond occupation fraction. We investigate an anisotropic version of this dilution problem by preferring bonds in the horizontal direction by some multiplicative factor r. This breaks the 60° rotation symmetry of the randomly diluted triangular lattice down to a network that is symmetric under independent reflections across any horizontal or vertical axis. Specifically, we study the average response proper-

[5] A calculation similar to the ones performed above shows that imposing a 60° rotation symmetry in a two-dimensional linear elastic medium immediately reduces the number of independent elastic constants to two.

ties of the system with quenched disorder in the Hamiltonian

$$
\begin{aligned}
H &= \frac{1}{2}\sum_{\langle ij\rangle} k_{ij}\left|\mathbf{u}_i - \mathbf{u}_j\right|^2, \\
k_{ij} &\sim p\ \delta\left(k_{ij}-k\right) + (1-p)\ \delta\left(k_{ij}\right) \quad \text{(isotropic)}, \\
k_{ij} &\sim \frac{3pr}{2+r}\left(1+\frac{4}{3}\left(\frac{1}{r}-1\right)\left(1-\cos^2\left(\theta_{ij}\right)\right)\right)\ \delta\left(k_{ij}-k\right) + \\
&\quad + \left(1-\frac{3pr}{2+r}\left(1+\frac{4}{3}\left(\frac{1}{r}-1\right)\left(1-\cos^2\left(\theta_{ij}\right)\right)\right)\right)\ \delta\left(k_{ij}\right) \quad \text{(anisotropic)}
\end{aligned}
\tag{5.16}
$$

as we tune p and r, which are parameters governing the probability distribution of disorder.[6] The more complicated expression in the anisotropic case can be understood as follows: for bonds along the horizontal direction, we independently randomly fill each with probability $p_1 = 3pr/(2+r)$. For bonds along the other two directions, we independently randomly fill each with probability $p_2 = p_3 = 3p/(2+r)$. This guarantees that $p_1/p_2 = p_1/p_3 = r$, so that bonds in the horizontal direction are a factor of r more likely to be filled, and $(p_1+p_2+p_3)/3 = p$, so that we have filled a fraction p of the total available slots on average. Several filling configurations of the lattice are shown in Figure 5.1.

From the calculation regarding the elasticity tensor above, we expect to have four independent elastic moduli for $r > 1$. These can be written as a bulk modulus + three shear moduli, or as four independent components of the elasticity tensor sufficient to reconstruct the full linear elastic theory for the material $C_{11} = C_{xxxx}$, $C_{22} = C_{yyyy}$, $C_{12} = C_{xxyy}$, and $C_{33} = C_{xyxy}$. C_{11}, C_{22}, and C_{33} can be measured directly by applying small strains ϵ_{xx}, ϵ_{yy}, and ϵ_{xy} and measuring $2E/\epsilon^2$. The final modulus can be measured through a bulk dilation of the material $\epsilon_{ij} = \left(\epsilon_{xx}+\epsilon_{yy}\right)/2\ \delta_{ij}$ as the bulk modulus is $\left(C_{xxxx}+2C_{xxyy}+C_{yyyy}\right)/4$ and C_{xxxx} and C_{yyyy} can be independently measured. We study finite systems and

[6] Here θ_{ij} is the angle that the bond connecting nearest neighbor nodes $\langle ij\rangle$ makes with the horizontal axis, so the probability distribution governing the filling of the bonds depends upon the bond orientation.

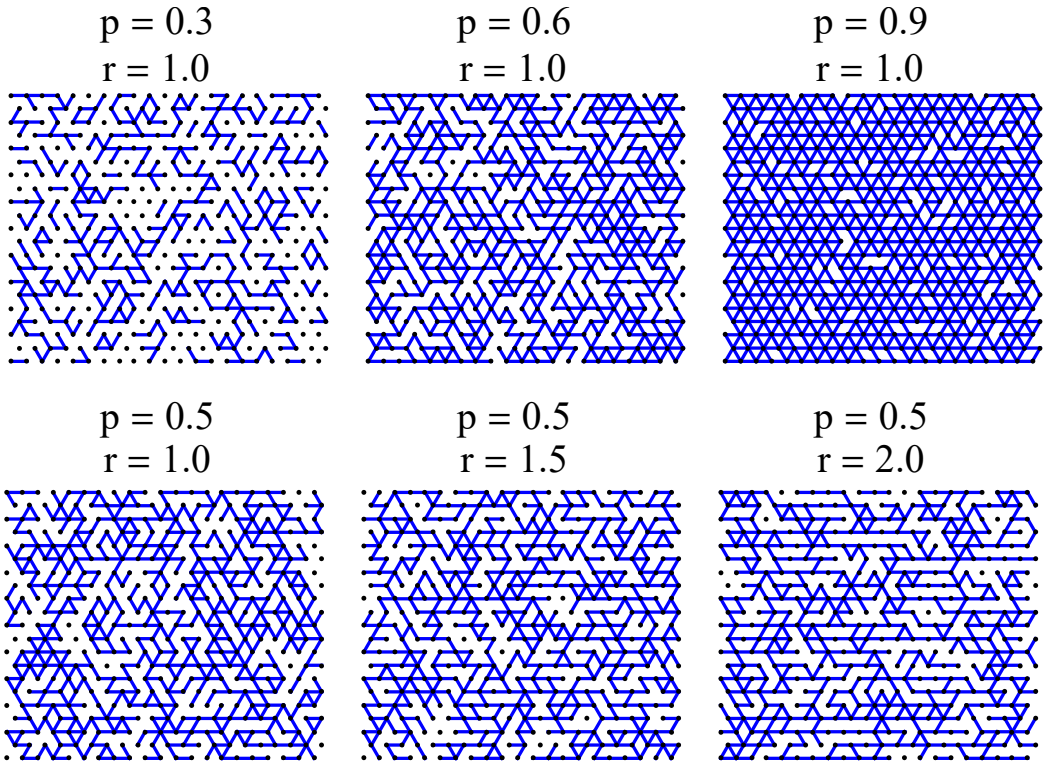

Figure 5.1: The anisotropically diluted triangular lattice for various values of p and r. A fraction p of the total bonds is filled on average. The horizontal bonds are r times more likely to be filled than the bonds along the other directions.

apply strains by adjusting the boundary conditions in an appropriate way. For instance, an ϵ_{xx} strain can be simulated as follows: take a finite rectangle of the relaxed system with periodic boundary conditions; say that the periodic domain has dimensions L_x and L_y. An application of a tiny ϵ_{xx} transforms L_x into $L_x(1 + \epsilon)$. The lattice is then allowed to relax to reduce the potential energy until force balance is achieved at every node. For a regular triangular lattice, the nodes move affinely and the modulus can be easily computed in terms of the microscopic spring stiffnesses k. For a given disorder realization where a random set of bonds are removed, the nodal displacements are non-affine.

Once enough bonds are removed, eventually the lattice can completely re-

lax under an infinitesimal strain. We detect this by tracking the linear elastic moduli $\left\langle C_{ijk\ell} \right\rangle$ averaged over the distribution of bond disorder. In practice, we set a small strain of $\epsilon = 10^{-3}$. One of the challenges of these simulations is that the strain above which one sees nonlinear elastic behavior vanishes close to the transition. Hence, for fixed strain, one inevitably crosses over into a regime where the elastic energy is not quadratic in the applied strain very close to the transition, which is not what we want if we are measuring the linear elastic moduli. This can be avoided by setting the strain to be very small, and also by confirming in the simulation that the energy is still quadratic in the strain for a range of strains above 10^{-3}.

In the isotropic case $r = 1$, the linear elastic moduli generally vanish as power laws in deviations $\delta p \equiv p - p_c$ to a single critical filling fraction p_c. We perform a finite-size scaling analysis to extract critical exponents for finite size effects ν and the vanishing of moduli f_{iso} and find good agreement with previous results in the literature [6, 3]:

$$C_{ijk\ell} \sim L^{-f_{\text{iso}}/\nu} C_{ijk\ell}\left(\delta p \; L^{1/\nu}\right) \tag{5.17}$$

with $f_{\text{iso}} = 2.2 \pm 0.3$ and $\nu = 1.3 \pm 0.2$. In the anisotropic case, the moduli appear to vanish at different locations on the phase diagram, leading to an intermediate phase where only one of the moduli (C_{xxxx}) remains nonzero. We confirm these phase boundaries are different in the thermodynamic limit by tracking their location as a function of L^{-1} and extrapolating to $L^{-1} = 0$. Furthermore, the exponent with which C_{xxxx} appears to vanish is much larger than the other moduli, with $f^{\text{aniso}}_{xxxx} = 4.0 \pm 1.0$ and the others $f^{\text{aniso}}_{ijk\ell \neq xxxx} = 2.2 \pm 1.0$ indistinguishable from the isotropic case. For C_{xxxx}, then, there appears to be a pair of universality classes that describe the critical behavior in the vicinity of $r = 1$. We can analyze the data in this vicinity using crossover scaling: in addition to the usual two

relevant variables L^{-1} and δp, there is a third important variable $r-1$ controlling the degree of anisotropy. We manage to collapse the data in the vicinity of the $r = 1$, $p = p_c$ isotropic critical point through the form

$$C_{xxxx} \sim L^{-f_{\rm iso}/\nu} C_{xxxx}\left(\delta p\, L^{1/\nu},\ (r-1)\, L^{\zeta/\nu}\right). \tag{5.18}$$

This collapse is quite challenging even having estimates for ν, $f_{\rm iso}$, and p_c from the isotropic collapse. This is because one needs to generate data at the same values of the invariant scaling combinations to verify the collapse. It is much harder to densely sample the two-dimensional manifold of the universal scaling function. By sampling many values of p and r near the critical point, one can get an estimate for ζ based on a collapse where points are not very close to each other. One can then try to generate data at a constant value of $(r-1)L^{\zeta/\nu}$ to see if the collapse works. ζ then gets fiddled with and the procedure repeated until the collapse is acceptable. Our result is that $\zeta = 0.25 \pm 0.1$, a rather small number.

To bring the discussion back to real biological systems, what implications do our results have for cartilage and other biological systems sitting near rigidity transitions? First of all, we have shown that by tuning the degree of anisotropy, rigid systems can greatly change the sensitivity of the linear response to external perturbations. The rigidity transitions in anisotropic elastic systems appear to exhibit their own classes of critical exponents, so in order to have a quantitative theory of the long-wavelength elastic properties of these networks close to these phase transitions, one needs to include anisotropy as a relevant tuning knob.

In the following manuscript, I spearheaded the analysis of the simulation results (finite-size scaling in the isotropic case; two-variable scaling when anisotropy is added) performed by William Wang (previously a CS undergrad

here at Cornell) and assisted in comprehensive edits to the manuscript. William Wang wrote the code necessary to strain the disordered elastic networks and measure their response, performed the simulations, generated all figures and wrote the first draft of the manuscript. Jim Sethna, Bulbul Chakraborty, and Moumita Das provided theoretical guidance in crossover phenomena and the connection of relevant experimental control knobs to renormalization group eigendirections. Itai Cohen came up with the idea of more deeply investigating networks that are microscopically anisotropic inspired by real biological systems like cellular cytoskeletons and cartilage fibers. Anna Barth, Navneet Singh, Japheth Omonira, and Jonathan Michel provided their own perspectives based upon their experimental and simulation results that guided the direction of the manuscript.

5.2 Rigidity transitions in anisotropic networks: a crossover scaling analysis

This is a reformatted version of the manuscript appearing in Soft Matter, ***2025****, 21, 3278-3289 [117].*

5.2.1 Abstract

We study how the rigidity transition in a triangular lattice changes as a function of anisotropy by preferentially filling bonds on the lattice in one direction. We discover that the onset of rigidity in anisotropic spring networks on a regular triangular lattice arises in at least two steps, reminiscent of the two-step melting

transition in two dimensional crystals. In particular, our simulations demonstrate that the percolation of stress-supporting bonds happens at different critical volume fractions along different directions. By examining each independent component of the elasticity tensor, we determine universal exponents and develop universal scaling functions to analyze isotropic rigidity percolation as a multicritical point. Our crossover scaling approach is applicable to anisotropic biological materials (e.g. cellular cytoskeletons, extracellular networks of tissues like tendons), and extensions to this analysis are important for the strain stiffening of these materials.

5.2.2 Introduction

Rigidity percolation in central-force lattice models has emerged as an important tool for modeling structural networks in cells and cellular tissues [156, 3, 4, 157]. Such central-force lattices consist of harmonic springs connecting nodes. The network is randomly filled by introducing springs between nodes to achieve a density p, which denotes the fraction of occupied bonds in the network. At low bond occupation, the bond network does not span the entire system. As p increases, the network undergoes a percolation transition where a cluster of bonds can now span the entire network. This tenuous cluster can only support stresses if there are angular forces between bonds [158]. In many practical scenarios, such bond bending forces are small compared with bond stretching. In such cases, the contribution to rigidity from bond bending is ignored. In this scenario, the network remains floppy until p reaches the so-called rigidity percolation threshold where bond stretching is activated under infinitesimal deformation of the network.

Rigidity percolation has been well studied in isotropic networks under different bending and stretching constraints [5, 159, 160]. However, less is understood about anisotropic networks. Anisotropic networks occur naturally in many biological tissues, such as bone [161, 162] and tendon [163, 164], both of which are composed of collagen fibrils oriented strongly in some direction. Anisotropy is expected to alter the onset of rigidity percolation, which is known to be sensitive to details of the bond distributions. For example, previous work has shown that including structural correlation within isotropic networks can result in significant changes in the critical bond occupation threshold for rigidity percolation [20, 165]. Furthermore, studies have shown that straining a percolated but floppy network, such as by shearing it in one direction, can drive a rigidity transition [166]. For example, straining the network preferentially along the maximum extension axis activates bond stretching, which rigidifies the network. Finally, previous computational studies have also modeled anisotropic networks through an anisotropically diluted triangular lattice and found that the onset of rigidity agrees well with a simple Maxwell constraint counting argument and that the system can be approximated using an effective medium theory (see [3]). Missing from these analyses, however, are detailed investigations of whether the critical exponents and scaling functions characterizing the rigidity transitions depend on these details of the bond distributions. Measuring the critical exponents and how they depend on the bond distributions is critical for determining whether such mechanical phase transitions are in the same universality class, which informs the relevant physics governing these transitions. Understanding this physics is an important step for learning how to control these transitions in materials ranging from biological tissues to synthetic fiber networks.

Here, we will examine the critical exponents and locations of phase boundaries in anisotropic networks. Though our model is quite similar to ones previously investigated [3], we find slightly different critical exponents for the isotropic rigidity percolation transition. Remarkably, we also discover that when we tune away from isotropy, the network exhibits *two rigidity transitions*. The first is associated with the component of the strain tensor for stretching along the preferential filling direction. The second rigidity transition is associated with the remaining components of the strain tensor. As such we find that the isotropic rigidity transition is a multi-critical point from which anisotropic rigidity transitions emanate (Fig. A.2). It is unclear whether this intermediate, infinite anisotropy elastic phase will be present for *generic* lattices (see Section 5.2.5), but similar infinite anisotropy mechanical responses should arise in strain-stiffened networks (see Fig. 5.5).

5.2.3 Methods

Model for anisotropic rigidity percolation

We generate triangular lattices (coordination number $z = 6$) of L^2 sites and periodic boundary conditions in both directions. Bonds are diluted based on their orientation, where p denotes the fraction of occupied bonds in the network. Anisotropy is introduced during lattice generation by filling bonds preferentially based on their orientation. We define the ratio r as the probability of bond occupation along the horizontal direction divided by the probability of bond occupation in the other two independent directions. We then build lattices using methods similar to those previously developed (see Appendix D.1 for details)

and investigate the regime where $r \geq 1$. Importantly, we are able to adjust r without changing p, which allows us to shuffle bonds and investigate how long-wavelength anisotropy affects the scaling of moduli in equally dense networks. In these coordinates, $r = 1$ represents a completely randomly diluted triangular lattice and $r = \infty$ a lattice which has bonds only in the horizontal direction. Our choice of anisotropy for generic r results in four independent long-wavelength components of the elasticity tensor, $\{C_{xxxx},\ C_{yyyy},\ C_{xyxy},\ C_{xxyy}\}$, each of which can be extracted for the various lattices.

Simulation details

We measure the components of the elasticity tensor for each random lattice realization at different values of filling fraction p, anisotropy r, and linear system size L. To measure these components, we first apply a small external strain ε_{ij} of magnitude 10^{-3} to ensure we probe the linear response. In the regime of linear elasticity, the energetic cost of such a deformation is quadratic in the strain:

$$E = \frac{1}{2}\varepsilon_{ij}C_{ijkl}\varepsilon_{kl}. \tag{5.19}$$

We apply strains ε_{xx}, ε_{yy}, and ε_{xy} to measure the elastic coefficients C_{xxxx}, C_{yyyy}, and C_{xyxy} directly. To measure C_{xxyy}, we perform a bulk compression and subtract out the energetic contributions from the independently measured C_{xxxx} and C_{yyyy} moduli. We introduce strains to the lattice by applying the proper transformation matrix to the positions of each of the nodes. For example, to stretch the network in the horizontal direction (to apply strain ε_{xx}), the following matrix is

applied:

$$T = \begin{bmatrix} 1+\gamma & 0 \\ 0 & 1 \end{bmatrix}, \tag{5.20}$$

where we set γ to 10^{-3}. Since we implement periodic boundary conditions in both directions, all nodes are transformed in the same manner.

In order to measure the energetic costs of our imposed strains in the disordered lattices, we minimize the central-force energy functional over the positions of the nodes. To capture the linear response, we truncate to leading order in the displacement of vertices:

$$E = \frac{1}{2} \sum_{\langle ij \rangle} k_{ij} \left(\mathbf{u}_{ij} \cdot \hat{\mathbf{r}}_{ij} \right)^2 \tag{5.21}$$

where $\mathbf{u}_{ij}$ is the difference between the displacement vectors for vertices i and j, and $\hat{\mathbf{r}}_{ij}$ is defined as the unit vector between vertices i and j in the initial configuration. The spring constant k_{ij} connecting sites i and j is either 0 or 1, according to the random number seed, p, and r. For each type of imposed fixed-amplitude strain, we minimize Equation (5.21) and use the resulting energy and Equation (5.19) to extract the values of the independent moduli. To improve convergence rates, a Cholesky factorization is computed [167] and used as a preconditioner for a conjugate gradient method [168] (see Appendix D.2 for details). It is worth noting that Equation (5.21) is valid only in the regime of linear response, which may be violated at higher strains. We verify that our choice of strain, 10^{-3}, is sufficiently small by computing the full untruncated energy for a network size of 50x50 with p=0.645 and r=1.5. These parameters place this network near both rigidity transitions (see Figure A.2) and therefore this network would be most strongly expected to violate linear response. We find that this lattice obeys linear response, with an energy scaling quadratically in strain, up

to strains of 10^{-2}. This indicates that nonlinearities in strain are negligible and Equation (5.21) is valid in the parameter space we explore here.

We then individually perform scaling analyses for each independent component of the elasticity tensor. Starting with a rigid network, we repeatedly remove bonds and minimize the energy for each strain until the network becomes sufficiently "floppy" in all directions; here, a network is considered floppy in a particular direction if the corresponding modulus falls below a threshold of $G_{\min} \equiv 10^{-8}$, which is the simulation tolerance. The moduli as a function of p were averaged for each system size and orientation strength pair (L, r), sampled over 10^2–10^4 random seeds. This procedure allows us to perform a scaling analysis of each component of the elasticity tensor separately.

5.2.4 Results

Isotropic Networks

We begin by focusing on the long-wavelength isotropic case, where bonds are removed without regard to their orientation ($r = 1$). We determine the value of p where each lattice becomes able to support a stress, defined to be p_c. To extrapolate our results to infinite lattices, we conduct a finite-size scaling analysis (Appendix D.3). For a given system size, we find the rigidity threshold for many different lattices and create a histogram of these p_c values. We find that for increasing lattice sizes, L, the width of the histogram for the threshold values p_c decreases as $L^{-1/\nu}$. We also find that the mean value of the histogram, $\langle p_c \rangle_L$, approaches a value p_c^∞, the threshold in the infinite system, with the same

power law:

$$\langle p_c \rangle_L - p_c^\infty \sim L^{-1/\nu}. \tag{5.22}$$

Our analysis determines that $p_c^\infty = 0.645 \pm 0.002$, depicted by the black dot along the horizontal axis of Fig. A.2, and $\nu = 1.3 \pm 0.2$. The location of the threshold at p_c^∞ indicates a small deviation from the naïve Maxwell constraint counting, which states that the 2D triangular lattice to have 2 constraints per site, $p = 2/3$ of the lattice must be occupied. The deviation from this prediction in our measured value of p_c^∞ is similar to what is found in other works [5]. Importantly, we find that in the isotropic system ($r = 1$) all the moduli share the same threshold value p_c^∞.

Next, we perform a finite-size scaling analysis of each component of the elasticity tensor, which admits a scaling

$$\begin{aligned} C_{ijkl}(p, L) &= L^{-f_{ijkl}^{\text{iso}}/\nu} C_{ijkl}^{\text{iso}}(X) \\ X &\equiv (\delta p) L^{1/\nu}, \end{aligned} \tag{5.23}$$

where $\delta p \equiv p - p_c^\infty$. Thus, in principle each modulus component could have a different scaling exponent, f_{ijkl}^{iso}, and shape, C_{ijkl}^{iso}. The universal function $C_{xxxx}^{\text{iso}}(X)$ is plotted along with the appropriately rescaled data for C_{xxxx} in Fig. 5.3. We find excellent scaling for the different system sizes. In the inset of Fig. 5.3, we plot the collapsed data against the equivalent scaling variable $|X|^{-\nu}$, which is a more common choice of variables in the literature, but leads to two branches of the scaling function. We find similarly excellent collapses for all the modulus data (see Fig. D.5 for the collapse of other components of the elasticity tensor). For all of these analyses we use the threshold $p_c^\infty = 0.646$, the critical exponent $\nu = 1.3$, and obtain $f_{ijkl}^{\text{iso}} = f^{\text{iso}} = 2.2 \pm 0.3$. Thus, every independent component of the linear elasticity tensor appears to vanish as $|\delta p|^{f^{\text{iso}}}$ (see Appendix D.4).

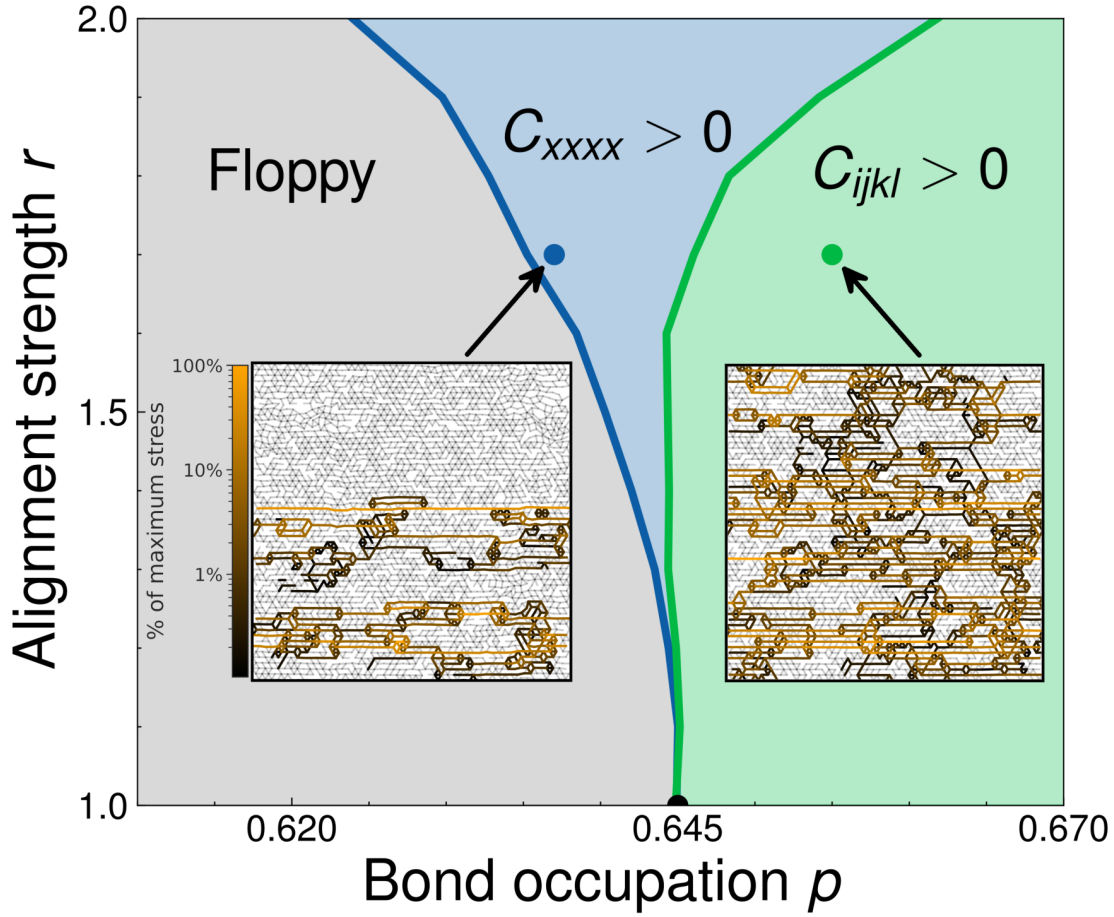

Figure 5.2: **Rigidity percolation phase diagram and rigid clusters.** The location of the phase boundaries are found in the thermodynamic limit using a finite-size scaling analysis. The insets show an anisotropic network close to its rigidity percolation point for the C_{xxxx} modulus (left) and $C_{ijkl} \neq C_{xxxx}$ moduli (right). The shading corresponds to the energy contributed by each bond after a strain in the x direction (gray indicating little to no stress and brighter indicating higher stress.

Anisotropic Networks

We extend our analysis in the previous section to lattices with long-wavelength anisotropy ($r > 1$), where we preferentially fill bonds in the x direction. We begin with the determination of the phase boundary. For each value of r, we perform a finite-size scaling analysis similar to the one we conducted for the isotropic case: we create histograms of the values of p where C_{ijkl} vanishes, $p_c^{ijkl}(r)$, and

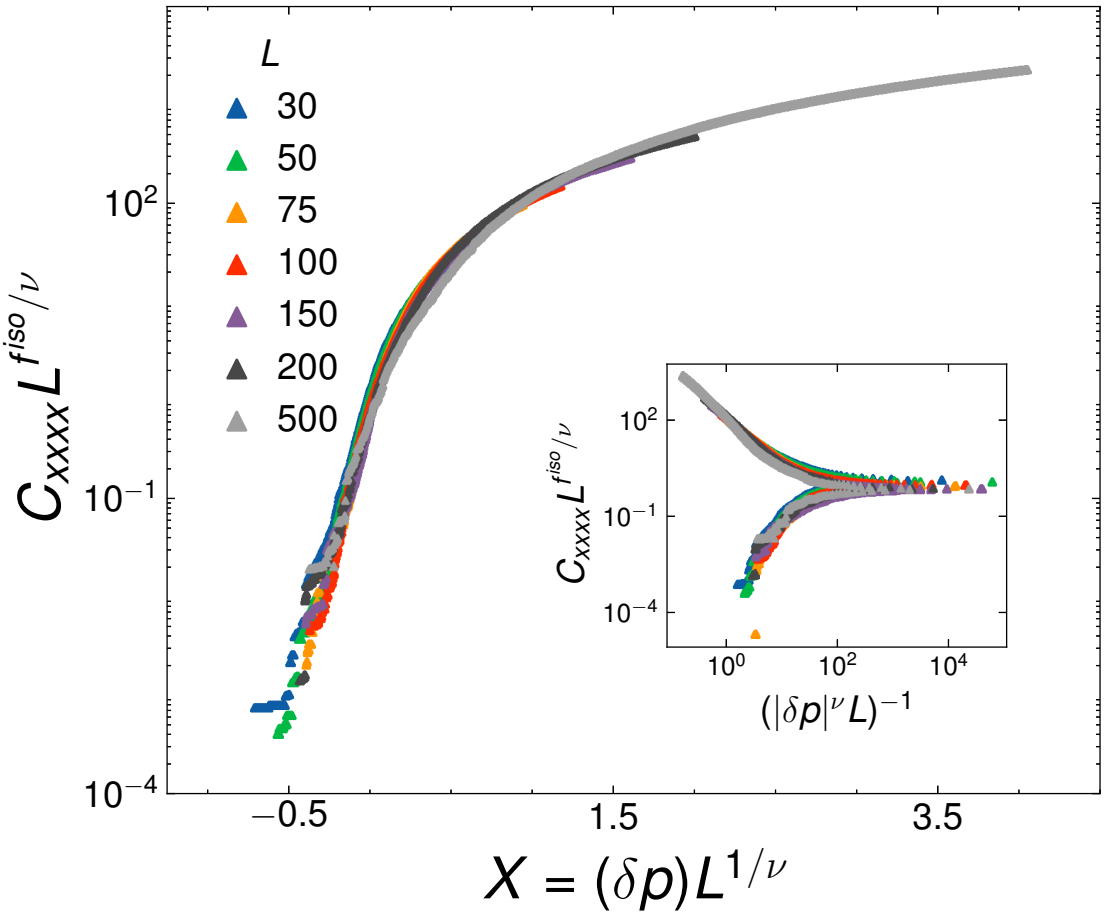

Figure 5.3: **Universal scaling function for the C_{xxxx} component of the elasticity tensor at isotropy** ($r = 1$)**.** All data for this component of the elasticity tensor collapse onto a single curve C^{iso}_{xxxx} when plotted against the finite-size scaling variable $X \equiv (\delta p) L^{1/\nu}$. The inset shows the same collapse against the scaling variable $(|\delta p|^\nu L)^{-1}$ (on a log-log scale). See Appendix D.4 for a similar analysis of the other components of the elasticity tensor. We use $p_c^\infty = 0.646$, $\nu = 1.3$, and $f^{\text{iso}} = 2.2$ to obtain excellent collapse for all the components of the elasticity tensor.

determine how their mean values extrapolate to the infinite system. For each value of r we find that the mean location of the critical point is well described by:

$$\langle p_c^{ijkl}(r) \rangle_L - p_c^{\infty,ijkl}(r) \sim L^{-1/\nu'}. \tag{5.24}$$

Remarkably, we find that for $r > 1$, the transition for the C_{xxxx} modulus is

distinct from the threshold values for the other components of the elasticity tensor. We find that the phase boundary for C_{xxxx} bends towards lower values of p with increasing r (Fig. A.2). The transition curves for the other moduli appear nearly identical for each system size and bend towards higher values of p with increasing r. This separation indicates a region for which the network is only rigid when strained along the preferred bond orientation direction. We verify these phase boundaries are the same at isotropy but distinct for $r > 1$ by measuring the separations between the histograms of p_c values for different components of the elasticity tensor as a function of system size (see Appendix D.5). Thus, the transition from a floppy to a rigid phase occurs in two stages when the system is anisotropic.

We note that for finite system sizes, C_{ijkl} never truly vanishes on average because if there are enough bonds remaining to create a rigid system-spanning truss ($p > O(1/L)$), this configuration occurs with finite probability. However, we still expect that in the intermediate regime between $\langle p_c^{xxxx}(r)\rangle_L$ and $\langle p_c^{ijkl}(r)\rangle_L$, finite systems will have an elasticity tensor with a principal axis in the x-direction due to our formulation of anisotropy.

Next, we test the scaling behavior of the elasticity tensor components near the critical points. In principle, including anisotropy could introduce corrections to scaling that bend the phase boundary in a trivial way, leaving all critical exponents the same as in the isotropic system. We tested this scenario, by fixing $r > 1$ and attempting to collapse the data near the relevant $p_c(r)$ values for each component of the elasticity tensor, keeping $f^{\text{aniso}} = f^{\text{iso}}$ and $\nu' = \nu$, but found very poor collapse. This poor collapse suggests that the anisotropic phase transition is in an entirely different universality class, with different values for the

critical exponents. We thus conjecture that the vicinity of $r = 1$ should be analyzed as a crossover scaling between two distinct critical points.

Inspired by renormalization group approaches, we analyze our data using crossover scaling functions expected to be valid in the vicinity of the isotropic critical point:

$$\begin{aligned} C_{ijkl}(p, r, L) &= L^{-f^{\text{iso}}/\nu} C_{ijkl}(X, Y) \\ X \equiv (\delta p) L^{1/\nu},\ & Y \equiv (r - r_c) L^{\zeta/\nu} \end{aligned} \tag{5.25}$$

with $r_c \equiv 1$. Note that $C_{ijkl}(X, 0)$ is equal to the previously defined $C^{\text{iso}}_{ijkl}(X)$ in Equation (5.23). Based on the form of this crossover scaling function, we expect that the moduli depend upon the anisotropy r only through a second scaling variable, Y; that is, we expect a scaling collapse of all of our data when plotted against X and Y with a single undetermined exponent $\zeta > 0$.

We first estimate ζ by examining the shape of the phase boundaries in the infinite system away from isotropy. Specifically, as shown in Appendix D.6, because the arguments of the universal scaling function are invariant scaling combinations, this phase boundary must occur at a fixed value of $X/Y^{1/\zeta} = \delta p/(r - r_c)^{1/\zeta}$ (with corrections to scaling), so that the separation between the two phase boundaries in Fig. A.2 scales as $(r - r_c)^{1/\zeta}$. From this estimate based on the shape of the phase boundaries, we find $\zeta = 0.25 \pm 0.1$.

Many other quantities share this crossover scaling ansatz and allow for independent estimates of ζ. The widths of the histograms of p_c values as we tune away from isotropy are also amenable to a crossover scaling analysis, with the variable Y collapsing these widths (Appendix D.6). From this scaling collapse, we similarly estimate $\zeta = 0.25 \pm 0.1$ and find nice collapse (Fig. D.9).

This estimate for ζ and the scaling ansatz in Equation (5.25) can be used to collapse the elasticity tensor components for 250,000 simulations consisting of anisotropy values ranging between $1.0 \leq r \leq 2.0$, bond occupation values ranging between $0.6 \leq p \leq 0.68$, and system sizes L ranging between $30 \leq L \leq 500$. We show a two variable scaling collapse for the C_{xxxx} and C_{yyyy} moduli in Fig. 5.5. We find excellent collapse of each independent modulus onto a two dimensional sheet. The overlaid data points consist of a portion of the data used to produce the sheet and indicate various slices of constant Y: $Y = 0$, $Y = 0.66$, and $Y = 1.65$. The $Y = 0$ curve (black) shows the finite-size scaling for isotropic systems and is identical to that shown in Fig. 5.3. We observe similarly excellent collapse at the two higher values of Y (Figs. D.11–D.12). For ease of visualization, we also include height contours projected onto the X-Y plane. The height contours for C_{xxxx} curve toward lower values of X as the scaling variable Y increases, reflecting the fact that the corresponding phase transition curves toward lower values of p as r increases. The other moduli, such as C_{yyyy}, show the opposite systematic behavior, tending towards higher values of X for increasing Y.

The critical exponents determined thus far, including ζ, are properties of the *isotropic* rigidity percolation critical point. We are also interested in the *anisotropic* critical exponents, such as the critical exponent with which each modulus vanishes with p in an infinite anisotropic system (f^{aniso}_{ijkl}). The universal scaling function $C_{ijkl}(X, Y)$ for the crossover between the isotropic and anisotropic critical points in principle contains all of these anisotropic critical exponents in its singularities in various asymptotic regimes. However, it is quite difficult to get reliable high-precision fits to generic two-variable scaling functions that include precise information about their singularities. We instead independently estimate f^{aniso}_{ijkl} by examining the largest system sizes of simulations performed

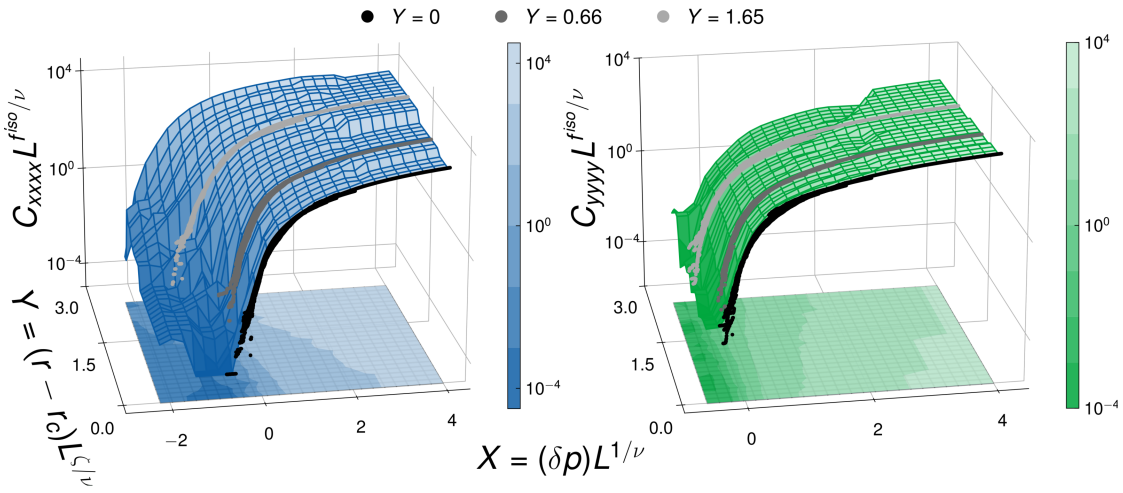

Figure 5.4: **Crossover scaling of anisotropic rigidity percolation.** Each independent elastic modulus, a function of the variables (p, r, L), collapses onto a two dimensional sheet when plotted against scaling variables $X \equiv (\delta p)L^{1/\nu}$ and $Y \equiv (r - r_c)\, L^{\zeta/\nu}$. (left) The scaling function $C_{xxxx}(X, Y)$ and (right) the scaling function $C_{yyyy}(X, Y)$. The isotropic data ($Y = 0$, Fig. 5.3) is scattered in black, and constant values of $Y = 0.66$ and $Y = 1.65$ are scattered in gray (Figs. D.11–D.14). The height contours are projected onto the X-Y plane.

at $r = 1.2, 1.5$. In addition, we analyze the data for $Y = 0.66, 1.65$.

We find that the critical exponents for C_{xxxx} are distinct from those found for the isotropic system while those for the other elasticity tensor components cannot be distinguished from those found for the isotropic system:

$$\begin{aligned} f^{\text{aniso}}_{xxxx} &\neq f^{\text{iso}}_{xxxx} \\ f^{\text{aniso}}_{ijkl} &\approx f^{\text{iso}}_{ijkl} \quad (ijkl \neq xxxx) \end{aligned} \tag{5.26}$$

with $f^{\text{aniso}}_{xxxx} = 4.0 \pm 1.0$, compared to our estimate of $f^{\text{iso}} = 2.2 \pm 0.3$. As usual in crossover scaling, the multicritical point governs short length scales and regions far from the critical lines emanating from it. We thus expect to find a crossover from f^{aniso}_{xxxx} to f^{iso}_{xxxx} as networks move away from the anisotropic critical point, as demonstrated in Fig. D.10. We also attempt to independently estimate ν^{aniso}, the finite-size scaling exponent away from isotropy, using the collapse plots shown in Fig. D.9 (Appendix D.6), but our estimates span a wide range of values 1.2 –

Exponent	Estimate
ν	1.3 ± 0.2
f^{iso}	2.2 ± 0.3
ζ	0.25 ± 0.1
ν^{aniso}	$1.2 - 3.2$
f^{aniso}_{xxxx}	4.0 ± 1.0
f^{aniso}_{ijkl} $(ijkl \neq xxxx)$	2.2 ± 1.0

Table 5.1: **Numerical estimates of critical exponents.**

3.2. Our estimates for all scaling exponents are shown in Table 5.1.

5.2.5 Conclusions

We find that rigidity percolation in our model anisotropic system occurs in at least two steps, with the modulus in the direction of alignment becoming nonzero at lower volume fractions. Our estimate of at least one of the critical exponents of the anisotropic transition, f^{aniso}_{xxxx}, appears distinct from the corresponding exponent for the isotropic transition f^{iso}, which suggests that these anisotropically diluted networks feature two distinct universality classes.

It was a surprise to us that the rigidity percolation transition for the isotropic lattice broke up into several transitions when it became anisotropic. First, obtaining multiple transitions is contrary to the naïve usage of Maxwell counting to determine the location of the rigidity transition. As shown in the insets of Fig. A.2, the rigid modes become anisotropic, and span horizontally before they span vertically.

Second, our results are fundamentally different from connectivity percolation, where regardless of the value of r there can only be one transition. The left inset in Fig. A.2 shows several horizontal stress-supporting chains spanning the

network. The critical point at which C_{xxxx} first becomes non-zero presumably separates a phase where there are no stress-supporting chains from one where there are a finite density of such chains. In regular percolation, two such paths connecting the system horizontally that are separated by any finite distance will have a finite probability per unit length of being connected by bonds extending in the vertical direction. Hence, for ordinary percolation, as soon as one crosses the horizontal percolation point in an anisotropic system, it must percolate in the other directions as well. This argument suggests that lattices with bending stiffnesses and angular springs, which are believed to become rigid at the connectivity percolation threshold [158], lack this intermediate phase. However, in typical situations where bending stiffnesses are much weaker than stretching stiffnesses, a remnant of this intermediate phase should be measurable even when bending is included.

In retrospect, we should have expected separate transitions in central force rigidity percolation on regular lattices. Maxwell counting tells us when the number of zero modes can vanish in the absence of states of self stress, but does not tell us whether the zero modes couple to a given mode of deformation [119, 169]. Straight lines of bonds supporting stress in a large system, when connected vertically, may only contain contributions to the stress that grow quadratically (i.e. non-linearly) in the strain: the length of a beam connecting (x, y) to $(x', y + \epsilon)$ grows as ϵ^2, suggesting the corresponding linear elastic modulus is 0. A similar nonlinear response to infinitesimal strains is found to stabilize hypostatic jammed packings of ellipsoidal particles [170], in violation of simple constraint-counting arguments. The perfect square lattice has no C_{xyxy} shear modulus, and the perfect hexagonal lattice has no non-zero moduli except the bulk modulus – why should anisotropic random lattices not possess

separate transitions?

Since generic lattices have no straight lines of bonds, it is not clear to us whether they will have intermediate phases with infinite anisotropy in linear response. (Indeed, a non-generic lattice which supports horizontal strain under tension has straight lines of bonds that buckle under compression making the effective modulus under compression still zero). Even in this case, we expect crossover scaling to be an important component of the analysis of anisotropic generic lattice networks. Our analysis suggests that the scaling of anisotropic generic networks could exhibit a crossover between distinct rigidity transition universality classes.

The difference between generic and non-generic lattices is no longer crucial after finite deformations; under tension a node connecting only two bonds will naturally straighten out to 180° and not support perpendicular stresses to linear order. Along these lines it might be interesting to investigate whether separate rigidity transitions arise in floppy isotropic random lattices under finite deformation. Preliminary results suggest strain stiffening leads to rigidity along the extension axis without rigidity under some of the other modes of deformation (see Fig. 5.5).

What kind of rigidity critical points do we expect? The C_{xxxx} transition where horizontal stress-bearing chains first arise could be self-similar (with a single diverging correlation length), but could also be self-affine (with the vertical spacing between chains diverging with a different power on the stress-supporting side than the rigid cluster lengths diverge on the floppy side, akin to directed percolation, where connectedness lengths are controlled by different critical exponents parallel and perpendicular to the preferred direction [171, 172, 173]).

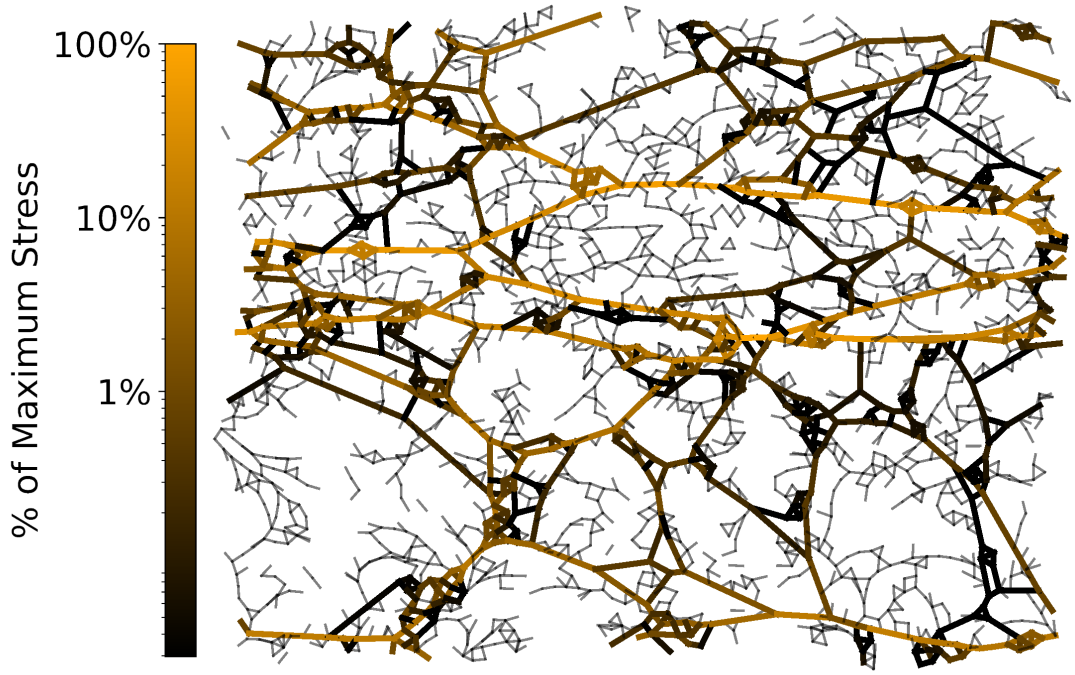

Figure 5.5: **Generic, isotropic triangular lattice strained in the horizontal direction until it becomes rigid, forming straight lines of bonds important for rigidity. The bonds are shaded corresponding to the energy contributed.** Preliminary results suggest that one of the four tangent moduli (C_{xyxy}) remains zero for a range of strains above the strain stiffening threshold, with C_{xxxx} being the dominant modulus.

Whether the three other moduli become non-zero simultaneously or separately in this model is not numerically resolved yet, but one expects that more complicated anisotropies (say a 3D model with brick-like symmetry) will allow for separate transitions for those moduli as well.

Finally, it would be interesting to consider whether the results presented here have any bearing on biological networks. Many biological tissues, including bone, tendon, muscle, and blood vessels, have an extracellular matrix that exhibits preferential alignment, giving rise to anisotropic elastic moduli. It may be possible to understand the extracellular matrices of these tissues as anisotropic

networks which have crossed the rigidity percolation transition in the stiff direction, but not the other directions. A quantitative description of these tissues may require analyzing the effects of second-order constraints, changing the contact number distribution, and exploring the crossover between this pair of zero-bending stiffness transitions and a bending-dominated regime. Moreover, cells are able to control how matrix elements are generated. Cells may generate networks with many different rigidity transitions to tune between, where the particular way matrix elements are laid down biases the thresholds of the different components of the elasticity tensor. As such, the results presented here could have profound implications for understanding more complicated networks in many biological systems.

5.2.6 Conflicts of interest

There are no conflicts to declare.

5.2.7 Data availability

The data used in this study are available at doi.org/10.5281/zenodo.13910625.
The code for the network simulations can be found at doi.org/10.5281/zenodo.13894006.

5.2.8 Acknowledgements

The authors acknowledge Thomas Wyse Jackson for critical discussions in the early phases of the project. WYW, IC, NS, SJT, and JPS are supported by NSF

DMR 2327094. JO was supported in part by the NSF MRSEC DMR-1719875. BC was supported by NSF CBET award number 2228681 and NSF DMR award number 2026834. AB is supported by NSF DGE 2139899. JAM and MD are supported by NSF EF 1935277.

CHAPTER 6

UNIVERSAL SCALING FUNCTIONS FROM THE NON-PERTURBATIVE FUNCTIONAL RENORMALIZATION GROUP

6.1 An exact renormalization group for the Ising model in one dimension

The renormalization group has been one of the great success stories in physics over the past fifty years. Many techniques exist to implement the general procedure that is usually presented in a mysterious way: "integrate out" (somehow) the short-wavelength degrees of freedom, and then rescale the fields to recover a new theory defined on the same length scales as the old. Real-space methods are simple to visualize: one can explicitly remove certain degrees of freedom and incorporate their fluctuations into fluctuations of other degrees of freedom. Kadanoff's block-spin renormalization group can be used to identify the (lack of) phase transition in the one-dimensional Ising model. In fact, one can get almost all the way to an exact result for the correlation length in the model using purely renormalization-group arguments.

With N spins, the partition function for the one-dimensional Ising model is

$$Z_N = \sum_{\{s_i\}} \exp\left(-\beta H_N\left(\{s_i\}\right)\right), \quad H_N = -J\sum_{i=1}^{N-1} s_i s_{i+1}, \quad s_i = \pm 1. \tag{6.1}$$

All thermodynamic quantities (specific heat, magnetization, etc.) can be derived in the thermodynamic ($N \to \infty$) limit by computing the free energy per spin

$$f = \lim_{N\to\infty}\left(-\frac{1}{N\beta}\log\left(Z_N\right)\right) \tag{6.2}$$

and then taking suitable derivatives. Does the system magnetize? At what temperature does this happen? We will start with a crude real-space renormalization group to answer these questions. The renormalization group describes how system parameters change if we view the system on a larger length scale. For instance, if we measure a length L with a ruler, and then increase the spacing between our ruler increments by a factor of 3, the new length we measure is $L/3$. The same thing happens with other scales of the system, like the temperature: when viewed on longer length scales, the effective temperature of the system will also change.

What does it mean if parameters don't change under a change of length scale; that is, what if we are at a fixed point of the RG operation? Because coarse-graining does not affect the physics on the scale of the correlation length, but the length scales are rescaled by some factor a, the correlation length after a single renormalization group step satisfies

$$\xi \to \xi' = \xi/a \text{ and } \xi = \xi' \implies \xi = \xi/a \implies \xi = 0 \text{ or } \xi = \infty. \tag{6.3}$$

The first of these cases ($\xi = 0$) is typical of an infinite- or zero-temperature state, where a spin value at a site tells you nothing about any other spin, even nearest-neighbors: the spins are totally uncorrelated.[1] The other is characteristic of a system at its phase transition: there is no typical length scale, there are fractal structures and fluctuations on all scales, etc. So fixed points of RG transformations can be used to find critical points, but not all fixed points of RG transformations are critical points.

We will now coarse-grain the one-dimensional Ising model through decimation. There is only one parameter in the model, since the inverse temperature

[1] When the system has a magnetized phase, the overall magnetization is subtracted and we look at the correlations between spin *flips*.

β and energy scale J appear in the partition function only in the combination $\beta J \equiv K$. Suppose we do a coarse-graining of our system, transforming our old partition function into a new one with only 1/3 as many spins. We do so by grouping our spins together in sets of 3, and then replacing these groups with a *single* spin according to the undemocratic rule that $s_{3i} = s'_i$ (that is, we simply ignore 2/3 of the spins, but we will perfectly account for the fluctuations of the spins we have thrown away). Note that the length scale is already rescaled by the new choice of index. The question is: can we figure out the new K describing our system after performing this decimation?

If we write out Z, the exponential of the sum turns into the product of many exponentials.

$$Z = \sum_{\{s_i\}} \dots e^{K s_0 s_1} e^{K s_1 s_2} e^{K s_2 s_3} \dots \tag{6.4}$$

We would like to write this in the new system, in terms of the new spin variables s'_i and a new inverse temperature K'. The sum over the unprimed variables can be split into the sum over the primed variables and a sum over the unprimed spins with indices not multiples of three (the spins that are ignored). We now seek to perform the sum over the ignored spins.

$$Z = \sum_{\{s'_i\}} \sum_{s_i,\, i \neq 3k} \dots e^{K s'_0 s_1} e^{K s_1 s_2} e^{K s_2 s'_1} \dots \tag{6.5}$$

Now come some steps that will appear to be magic. The fact that this is a "trick" is a hint that, for more complicated models, this procedure cannot be done explicitly. Write

$$e^{K s_1 s_2} = (1 + s_1 s_2 \tanh(K)) \cosh(K) . \tag{6.6}$$

Note that this is obviously not true in general (no s_i appear in exponentials!), but it is true for both possible allowed values of $s_1 s_2 = \pm 1$. Then inside the

summand of the partition function,

$$\cdots \sum_{s_1,s_2} e^{Ks_0's_1} e^{Ks_1s_2} e^{Ks_2s_1'} \ldots =$$

$$\sum_{s_1,s_2} \ldots \cosh^3(K) \left(1 + s_0' s_1 \tanh(K)\right) \left(1 + s_1 s_2 \tanh(K)\right) \left(1 + s_2 s_1' \tanh(K)\right) \ldots = \quad (6.7)$$

$$= \ldots 4\cosh(K)^3 \left(1 + (\tanh(K))^3 s_0' s_1'\right) \ldots$$

since after expanding and summing, only terms even in s_1 and s_2 survive. We now want to put this back into the usual form of the partition function. The term in the parentheses looks like the original one. Define

$$\tanh(K') \equiv (\tanh(K))^3 . \quad (6.8)$$

Then the above term in the partition function is

$$\begin{aligned} &= 4\cosh(K)^3 \left(1 + \tanh(K')\, s_0' s_1'\right) = \left[4\frac{\cosh(K)^3}{\cosh(K')}\right] \left(1 + \tanh(K')\, s_0' s_1'\right) \cosh(K') \\ &= \left[4\frac{\cosh\left(\tanh^{-1}\left((\tanh(K'))^{1/3}\right)\right)^3}{\cosh(K')}\right] e^{K' s_0' s_1'} \equiv e^{-g(K') + K' s_0' s_1'} \end{aligned} \quad (6.9)$$

Then the full partition function is exactly

$$Z = \sum_{\{s_i'\}} \exp\left(-H'(\{s_i'\})\right), \quad H' = Ng(K') - K' \sum_i s_i' s_{i+1}'. \quad (6.10)$$

Apart from the shift that is independent of the spin configuration and hence does not affect the distribution of states, we have gotten back a nearest-neighbor Ising model. Equation 6.8 tells us how the inverse temperature rescales after a single decimation step. We can imagine repeatedly applying the function

$$K_n \to K_{n+1} = \tanh^{-1}\left(\tanh(K_n)^3\right) \quad (6.11)$$

and seeing how the inverse temperature flows. This recursion relation has only two fixed points: when $K = 0$, it is mapped to 0, and when $K = \infty$, $\tanh(K) = 1$

and is hence mapped to $K = \infty$. Now note that, away from the fixed points, $\tanh(K_n) < 1$ and $\tanh^{-1}(x)$ is monotonic so $K_{n+1} < K_n$. This means that, away from the fixed points, we always flow to the stable fixed point $K_\infty = 0$ (infinite temperature). The other fixed point, $K = \infty$ (zero temperature), is unstable. In many sets of lecture notes, this completes the analysis of the decimation RG for the 1D Ising model: there is no phase transition at finite temperature.

However, we can actually do much better than this. The exponent 3 that appears in the recursion relation of Equation 6.8 is specific to the fact that we have transformed groups of 3 spins into a single spin. One can repeat the calculations above, grouping any integer number of spins $\kappa + 1 \geq 2$, and find an incremental flow equation for K

$$\tanh(K') = (\tanh(K))^{1+\kappa} \tag{6.12}$$

In the example where we group 3 spins together, $\kappa = 2$. Here, κ counts the number of spins that are thrown away at each step per group. Note that this transformation is exactly true at every integer, including $\kappa = 0$. Let's assume that we can analytically extend this transformation to non-integer values of κ and write this as a continuous flow equation for K taking $\kappa = \mathrm{d}\ell$. Then

$$\mathrm{d}K = K' - K = \tanh^{-1}\left((\tanh(K))^{1+\mathrm{d}\ell}\right) - K \implies \frac{\mathrm{d}K}{\mathrm{d}\ell} = \lim_{\mathrm{d}\ell \to 0}\left(\frac{\tanh^{-1}\left((\tanh(K))^{1+\mathrm{d}\ell}\right) - K}{\mathrm{d}\ell}\right). \tag{6.13}$$

Write

$$(\tanh(K))^{1+\mathrm{d}\ell} \approx \tanh(K) + \mathrm{d}\ell \tanh(K)\log(\tanh(K)) = \tanh(K)(1 + \mathrm{d}\ell \log(\tanh(K))) \tag{6.14}$$

and

$$\tanh^{-1}(x(1-\epsilon)) = \tanh^{-1}(x) + \frac{x}{x^2 - 1}\epsilon \tag{6.15}$$

with $x = \tanh(K)$ (and hence $x/(x^2-1) = -\cosh(K)\sinh(K)$) to see

$$\lim_{\mathrm{d}\ell\to 0}\left(\frac{\tanh^{-1}\left((\tanh(K))^{1+\mathrm{d}\ell}\right)-K}{\mathrm{d}\ell}\right) = \lim_{\mathrm{d}\ell\to 0}\left(\frac{\tanh^{-1}(\tanh(K))+\mathrm{d}\ell\sinh(K)\cosh(K)\log(\tanh(K))-K+O\left(\mathrm{d}\ell^2\right)}{\mathrm{d}\ell}\right) \tag{6.16}$$

giving

$$\frac{\mathrm{d}K}{\mathrm{d}\ell} = \cosh(K)\sinh(K)\log(\tanh(K)) = \frac{1}{2}\sinh(2K)\log(\tanh(K)). \tag{6.17}$$

This is negative for any K positive, verifying the result from the incremental decimation. Written in terms of dimensionless temperature $T \equiv 1/K$, one has

$$\frac{\mathrm{d}T}{\mathrm{d}\ell} = -\frac{T^2}{2}\sinh\left(\frac{2}{T}\right)\log\left(\tanh\left(\frac{1}{T}\right)\right). \tag{6.18}$$

The right-hand side is a well-defined power series in $p = e^{-1/T}$ near $T = 0$, but it is not analytic in T. The first few terms are

$$\frac{\mathrm{d}T}{\mathrm{d}\ell} = \frac{T^2}{2} - \frac{T^2}{3}e^{-4/T} - \frac{T^2}{15}e^{-8/T} - \ldots \tag{6.19}$$

where p enters in powers that are multiples of 4 and the prefactors (other than the first one) are $1/n(n+2)$ where n is the n^{th} odd number. This behavior, particularly the vanishing of the linear term, is understood in the context of bifurcation theory. Generically (that is, excluding very special cases), one can linearize flow equations in the vicinity of a fixed point (see Chapter 4). These linearized flow equations give eigenvalues of the flow that are related to critical exponents. The fact that the flow cannot be linearized in the 1D Ising model is related to the fact that we are at its lower critical dimension.

Because we have made no serious approximations at this stage, we can take this analysis one step further. The correlation length transforms simply under the renormalization group transformation:

$$\frac{\mathrm{d}\xi}{\mathrm{d}\ell} = -\xi. \tag{6.20}$$

This can be combined with the flow equation for the temperature to generate a differential equation that describes the correlation length as a function of temperature everywhere in the phase diagram:

$$\frac{\mathrm{d}\xi}{\mathrm{d}T} = \frac{2\xi}{T^2 \sinh\left(\frac{2}{T}\right) \log\left(\tanh\left(\frac{1}{T}\right)\right)}. \tag{6.21}$$

This can be directly integrated, giving

$$\xi = -\frac{c}{\log\left(\tanh\left(1/T\right)\right)}. \tag{6.22}$$

with an undetermined c. Here we have used the renormalization group to learn something quantitative about correlations in the model *without* computing anything about the correlation function $\left\langle s_i s_j \right\rangle$! We can go another step further. Because our expression for the correlation length is exact at all temperatures, we can write the correlation function at all temperatures[2] as well:

$$\left\langle s_i s_j \right\rangle = \exp\left(-\frac{|i-j|}{\xi}\right) = \left(\tanh\left(\frac{1}{T}\right)\right)^{\frac{|i-j|}{c}}. \tag{6.23}$$

From an exact transfer matrix solution to the 1D Ising model, it is known that $c = 1$. The renormalization group is quantitative! But in practice, it cannot be implemented in such an exact form for the vast majority of problems of interest.

6.2 Non-perturbative methods in the RG

In addition to this explicit real-space renormalization group, there is also the more generalizable momentum shell renormalization group, where one can perform the upper sections of momentum integrals and incorporate their results into scalings of fields and generation of new interactions. Momentum shell

[2]Here we must also use our knowledge that $\eta = 1$ for the 1D Ising model.

renormalization group is usually done perturbatively in some small parameter; the interaction strength, number of vector components, disorder strength, distance to $d = 4$, etc. could control which Feynman diagrams one chooses to evaluate or resum. In this sense, this technique is perturbative. There are other techniques for performing the renormalization group procedure that are "non-perturbative" in that they do not rely upon a small parameter to evaluate the theory. However, there are of course still approximations that are made.

In the functional renormalization group, one chooses to work directly with the free energy functional.[3] We start with the partition function written as a functional integral [174]

$$\mathcal{Z}[J] = \int \mathcal{D}[\phi]\ e^{-S[\phi]+\int \mathrm{d}^d r\, J\phi} \tag{6.24}$$

with the action $S = \beta H$ given by

$$S[\phi] = \int \mathrm{d}^d r \left\{ \frac{1}{2}(\nabla\phi)^2 + \frac{r_0}{2}\phi^2 + \frac{u_0}{4!}\phi^4 \right\}. \tag{6.25}$$

To implement the renormalization group, we would like to start from a static model whose thermodynamic properties are given by a Landau free energy, and gradually incorporate more and more of the fluctuations until we reach a static model whose thermodynamic properties fully capture the fluctuations relevant to the problem at hand. This is done by modifying the action, introducing a shift

$$\Delta S_k[\phi] = \frac{1}{2}\int \frac{\mathrm{d}^d p}{(2\pi)^d}\phi(-p) R_k(p)\phi(p) = \frac{1}{2}\int \mathrm{d}^d r \int \mathrm{d}^d r'\ \phi(r) R_k(r-r')\phi(r') \tag{6.26}$$

where $R_k(p)$ is the *regulator function* that plays the role of a cutoff in Wilson's formulation of the renormalization group. The idea behind it is that $R_k(p)$ crosses

[3] In the following, I will write expressions mostly focusing on the scalar ϕ^4 model since we are interested in the manuscript in demonstrating our methods for the Ising model.

over from being $\sim k^2$ in magnitude at small p to rapidly decaying to 0 at large p, with a crossover between these two behaviors occurring at the scale k. We begin our analysis at $k_{\text{in}} \ll \Lambda$, the scale at which the microscopic theory is defined, but k_{in} should be large.[4] The regulator then has the effect of giving all of the fluctuating modes up to scale k_{in} a huge "mass" term, freezing all of their fluctuations. As we decrease k to 0, we incorporate the effects of lower and lower energy fluctuations. We will track the behavior of thermodynamic quantities as we vary k from k_{in} to 0.

We first add this regulator term to the action, giving

$$\mathcal{Z}_k[J] = \int \mathcal{D}[\phi]\ e^{-S[\phi]-\Delta S_k[\phi]+\int \mathrm{d}^d r\, J\phi}. \tag{6.27}$$

We then define a scale-dependent effective action $\Gamma_k[\phi]$ via a modified Legendre transformation:

$$\Gamma_k[\phi] = -\log\left(\mathcal{Z}_k[J]\right) + \int \mathrm{d}^d r J\phi - \Delta S_k[\phi], \tag{6.28}$$

where the second term would be the usual way the Legendre transformation would be implemented (note that the effective action is a function of ϕ rather than J, so $J = J[\phi]$ is the external field that minimizes the free energy given the field configuration ϕ). The additional, and unusual, $\Delta S_k[\phi]$ that is included in the definition of $\Gamma_k[\phi]$ is 0 when $k = 0$, and so it has no effect on the thermodynamic quantities of the system with all fluctuations included. It is added to simplify the flow equation for $\Gamma_k[\phi]$, which we will now seek to derive by taking a partial derivative with respect to k.

What terms are held fixed when the derivative with respect to k is taken? The field ϕ is an internal coordinate of the functional $\Gamma_k[\phi]$, so it must be held fixed.

[4] In practice, it is usually fine to start at $k_{\text{in}} = \Lambda$ [174].

The external field J, however, must be considered as k-dependent to satisfy the relation $\phi = \delta/\delta J\left(\log\left(\mathcal{Z}_k\right)\right)$, since $\mathcal{Z}_k$ is k-dependent. This can be done in two steps: first, take the derivative of $\log\left(\mathcal{Z}_k\right)$ with respect to k while holding J fixed. Then, add back in a correction that results when we allow J_k to vary with k. We will first take the derivative with respect to k holding J fixed. For the first term, we find

$$\begin{aligned}
-\partial_k \log\left(\mathcal{Z}_k\right) &= \frac{1}{\mathcal{Z}_k}\int \mathcal{D}\left[\phi\right]\ \left(\partial_k \Delta S_k\left[\phi\right]\right) e^{-S\left[\phi\right]-\Delta S_k\left[\phi\right]+\int \mathrm{d}^d r\, J\phi} \\
&= \frac{1}{2}\int \mathrm{d}^d r \int \mathrm{d}^d r'\ \partial_k R_k\left(r-r'\right)\left[\frac{1}{\mathcal{Z}_k}\int \mathcal{D}\left[\phi\right]\ \phi\left(r\right)\phi\left(r'\right) e^{-S\left[\phi\right]-\Delta S_k\left[\phi\right]+\int \mathrm{d}^d r\, J\phi}\right].
\end{aligned} \tag{6.29}$$

The term in square brackets looks like a correlation function of some kind, and so it can likely be written in terms of functional derivatives of $W_k \equiv \log\left(\mathcal{Z}_k\right)$ with respect to the external field J. Without repeating the tedious algebra, we know some things about connected correlation functions:[5]

$$\begin{aligned}
\langle\phi(r)\rangle &= \frac{\delta W_k}{\delta J(r)}, \\
\langle\phi(r)\phi(r')\rangle - \langle\phi(r)\rangle\langle\phi(r')\rangle &= \frac{\delta^2 W_k}{\delta J(r)\delta J(r')}, \\
\implies \langle\phi(r)\phi(r')\rangle &= \frac{\delta^2 W_k}{\delta J(r)\delta J(r')} + \frac{\delta W_k}{\delta J(r)}\frac{\delta W_k}{\delta J(r')}.
\end{aligned} \tag{6.30}$$

Hence,

$$-\partial_k \log\left(\mathcal{Z}_k\right) = \frac{1}{2}\int \mathrm{d}^d r \int \mathrm{d}^d r'\ \partial_k R_k\left(r-r'\right)\left[\frac{\delta^2 W_k}{\delta J(r)\delta J(r')} + \frac{\delta W_k}{\delta J(r)}\frac{\delta W_k}{\delta J(r')}\right]. \tag{6.31}$$

Now we want to compute this derivative allowing J to vary with k. We have

$$\partial_k W_k\Big|_\phi = \partial_k W_k\Big|_J + \int \mathrm{d}^d r\ \frac{\delta W_k}{\delta J_k(r)}\partial_k J_k(r)\Big|_\phi = \partial_k W_k\Big|_J + \int \mathrm{d}^d r\ \phi(r)\partial_k J_k(r)\Big|_\phi. \tag{6.32}$$

Unsurprisingly, this additional term that is generated is exactly cancelled by the k derivative of the Legendre transformation term $\int \mathrm{d}^d r\, J\phi$. The derivative of the

[5] Some of these formulas can be confusing because ϕ represents both the internal variable of the field in the functional and its own expectation value.

additional $-\Delta S_k$ that was added cancels the paired product of single functional derivatives of W_k that appear. In summary, taking the derivative at constant ϕ, we have

$$\begin{aligned}
\partial_k \Gamma_k [\phi] &= -\partial_k W_k + \partial_k \int \mathrm{d}^d r J_k \phi - \partial_k \Delta S_k [\phi] \\
&= -\partial_k W_k \Big|_J - \int \mathrm{d}^d r \, \phi(r) \partial_k J_k(r) + \int \mathrm{d}^d r \, \phi(r) \partial_k J_k(r) - \partial_k \Delta S_k [\phi] \\
&= -\partial_k W_k \Big|_J - \partial_k \Delta S_k [\phi] \\
&= \frac{1}{2} \int \mathrm{d}^d r \int \mathrm{d}^d r' \, \partial_k R_k (r - r') \left[\frac{\delta^2 W_k}{\delta J(r) \delta J(r')} + \frac{\delta W_k}{\delta J(r)} \frac{\delta W_k}{\delta J(r')} \right] - \\
&\qquad - \frac{1}{2} \int \mathrm{d}^d r \int \mathrm{d}^d r' \, \partial_k R_k (r - r') \, \phi(r) \, \phi(r') \\
&= \frac{1}{2} \int \mathrm{d}^d r \int \mathrm{d}^d r' \, \partial_k R_k (r - r') \left[\frac{\delta^2 W_k}{\delta J(r) \delta J(r')} + \frac{\delta W_k}{\delta J(r)} \frac{\delta W_k}{\delta J(r')} \right] - \\
&\qquad - \frac{1}{2} \int \mathrm{d}^d r \int \mathrm{d}^d r' \, \partial_k R_k (r - r') \frac{\delta W_k}{\delta J(r)} \frac{\delta W_k}{\delta J(r')} \\
&= \frac{1}{2} \int \mathrm{d}^d r \int \mathrm{d}^d r' \, \partial_k R_k (r - r') \left[\frac{\delta^2 W_k}{\delta J(r) \delta J(r')} \right].
\end{aligned} \tag{6.33}$$

This double functional derivative of W_k is the propagator, which can also be written as $\left(\Gamma_k^{(2)} [\phi] + R_k \right)^{-1}$. (The additional R_k that appears is due to the additional ΔS_k in the definition of Γ_k). Hence, we have the exact result which is known as Wetterich's equation:[6]

$$\partial_t \Gamma_k [\phi] = \frac{1}{2} \mathrm{Tr} \left[\partial_t R_k \left(\Gamma_k^{(2)} [\phi] + R_k \right)^{-1} \right] \tag{6.34}$$

where the trace in this case is integration over both spatial variables. This is occasionally written in diagrammatic form, which is more nontrivial and useful for expressing the exact flow equations for the higher-order n-point 1PI vertices $\Gamma_k^{(n)}$ (Figure 6.1).

[6]Note that the partial derivative with respect to k on each side of Wetterich's equation can be replaced by the partial derivative with respect to any function of k and the above derivation will still hold. Often, works in the NPRG literature will flow with respect to an RG time $t \equiv \log(k/\Lambda)$ which is 0 when $k = \Lambda$ and goes to $-\infty$ as $k \to 0$. This is the opposite of typical real space procedures, which might run a parameter $\ell = \log(\Lambda/k)$ from 0 to ∞ to incorporate the fluctuations on all scales.

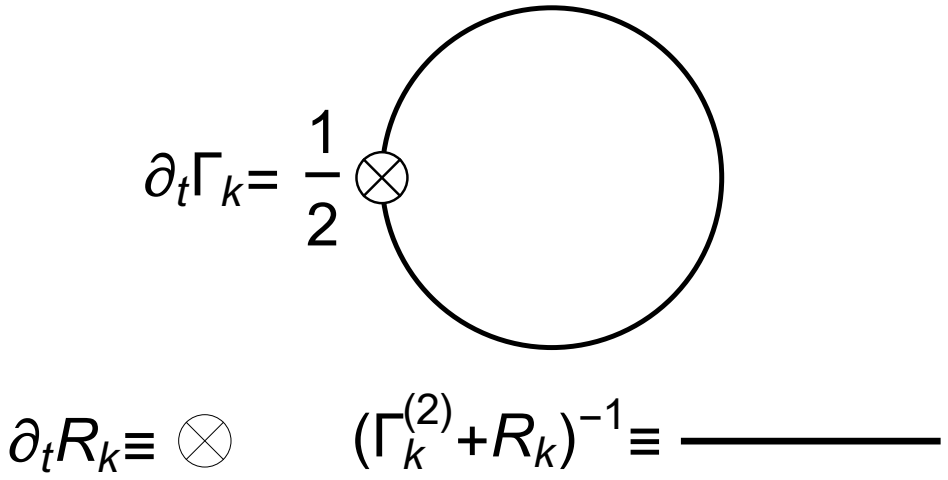

Figure 6.1: The diagrammatic expression of Wetterich's equation; see also Equation 6.34.

This is still an impossible-to-solve functional equation.[7] The simplifying assumptions that are usually made to find approximate solutions are done at the level of the effective action, keeping terms up to a certain number of spatial derivatives. The simplest approximation, known as the local potential approximation (LPA), assumes that the effective action can be written entirely in terms of an effective potential $U_k(\phi)$:

$$\Gamma_k^{\mathrm{LPA}}[\phi] = \int \mathrm{d}^d r \left\{ \frac{1}{2} (\nabla\phi)^2 + U_k\left(\phi^2\right) \right\}. \tag{6.35}$$

Within this approximation scheme, the propagator can be easily calculated in momentum space:

$$\left(\Gamma_k^{(2)}[\phi] + R_k\right)^{-1} = \frac{1}{p^2 + 2U_k'(\phi^2) + 4\phi^2 U_k''(\phi^2) + R_k(p)} \tag{6.36}$$

where the $'$ denotes derivatives of the function $U_k\left(\phi^2\right)$ with respect to its argument. To recover an equation that one can proceed to solve numerically, one

[7] It is, for instance, equivalent to an infinite set of coupled partial differential equations for the coefficients of each term in the derivative expansion.

typically now makes a choice of regulator. There is a vast literature comprised of methods of choosing the regulator. For instance, one can choose a family of regulators that satisfies the asymptotic conditions of the regulator with a variational parameter, and set the variational parameter using some optimization condition.[8] Another technique is to choose a regulator that allows one to carry through the calculations explicitly as easily as possible, a so-called "optimized regulator" [174, 175]

$$R_k(p) = \left(k^2 - p^2\right)\Theta\left(k^2 - p^2\right) \implies \partial_t R_k(p) = 2k^2\Theta\left(k^2 - p^2\right). \tag{6.37}$$

Then Wetterich's equation becomes (dividing by $V \equiv \int \mathrm{d}^d r$ on each side and translating the trace over the spatial variables into momentum space)

$$\partial_t U_k = \frac{1}{2}\int \frac{\mathrm{d}^d p}{(2\pi)^d} \frac{\partial_t R_k(p)}{p^2 + 2U_k'\left(\phi^2\right) + 4\phi^2 U_k''\left(\phi^2\right) + R_k(p)}. \tag{6.38}$$

The form of the regulator cuts off the momentum integral above k and makes everything spherically symmetric, allowing us to evaluate the angular part of the integral followed by the trivial radial part

$$\begin{aligned}\partial_t U_k &= \frac{1}{2}\frac{1}{(2\pi)^d}\frac{2\pi^{d/2}}{\Gamma\left(\frac{d}{2}\right)}\frac{2k^2}{k^2 + 2U_k'\left(\phi^2\right) + 4\phi^2 U_k''\left(\phi^2\right)}\int_0^k \mathrm{d}p\; p^{d-1} \\ &= \frac{1}{d}\frac{1}{2^d\pi^{d/2}}\frac{1}{\Gamma\left(\frac{d}{2}\right)}\frac{2k^{d+2}}{k^2 + 2U_k'\left(\phi^2\right) + 4\phi^2 U_k''\left(\phi^2\right)}.\end{aligned} \tag{6.39}$$

This is now a single PDE, which was obtained essentially by truncating the action to the order of the effective potential depending on static field configurations. This can be integrated starting from an initial condition given by a Landau free energy, such as $U_\Lambda(x) = f_0 + (a_0/2)\,x + (g_0/4)\,x^2$, to give the effective potential including all fluctuations.[9]

[8] Some aspects of the flow depend upon the regulator, like the locations of fixed points. The flows derived here differ from those used in the manuscript by multiplicative scale factors (see just before Equation 6.47). The universal properties are independent of these scale factors, and they are mostly (but not entirely) independent of the choice of regulator.

[9] Note that the internal variable of U is ϕ^2 already to respect the $\mathbb{Z}_2$ symmetry.

There are yet more simplifications that one can perform to treat the critical properties of the problem exactly. First, one rescales the fields and the parameters inside of the potential by their so-called "engineering dimensions" to eliminate explicit references to the cutoff scale k. Because the physical system becomes (approximately) scale-invariant at the critical point, the only length scale is k^{-1}, and so we expect quantities written in units of k^{-1} to flow to a fixed point. By matching powers of k either at the outset before integrations have been performed or in the current PDE, one finds $U_k = k^d \tilde{U}_k$ and $\phi^2 = k^{d-2}\tilde{\phi}^2$.

When writing the flow for the rescaled effective potential in terms of the rescaled field, there are two wacky additional terms that appear thanks to the chain rule. One comes from ∂_t currently being taken at constant ϕ^2, while we would like to write a flow that occurs at constant $\tilde{\phi}^2$. This can be amended by noting that

$$\partial_t\Big|_{\tilde{\phi}^2} = \partial_t\Big|_{\phi^2} + \partial_t\phi^2\Big|_{\tilde{\phi}^2}\partial_{\phi^2} = \partial_t\Big|_{\phi^2} + (d-2)\,\phi^2\partial_{\phi^2} = \partial_t\Big|_{\phi^2} + (d-2)\,\tilde{\phi}^2\partial_{\tilde{\phi}^2}. \tag{6.40}$$

The other term comes from the fact that the flow for $\tilde{U}_k$ can be written as

$$\partial_t\tilde{U}_k = \partial_t\left(k^{-d}U_k\right) = -d\tilde{U}_k + k^{-d}\partial_t U_k. \tag{6.41}$$

Putting this all together, leaving $'$ to mean the derivative of the function with respect to its field-like argument, we have

$$\partial_t\tilde{U}_k = -d\tilde{U}_k + (d-2)\,\tilde{\phi}^2\tilde{U}_k' + \frac{1}{d}\frac{1}{2^d\pi^{d/2}}\frac{1}{\Gamma\left(\frac{d}{2}\right)}\frac{2}{1+2\tilde{U}_k'+4\tilde{\phi}^2\tilde{U}_k''}. \tag{6.42}$$

Now all explicit references to k have been eliminated. Next, instead of allowing the effective potential to flow from its mean-field form and become an arbitrary function, we can try to get an approximate solution by projecting it back onto the space of functions of the form $\tilde{U}_k(\tilde{\phi}^2) = \tilde{f}_t + (\tilde{a}_t/2)\,\tilde{\phi}^2 + (\tilde{g}_t/4)\,\tilde{\phi}^4$. This transforms the PDE for $\tilde{U}_k$ into a set of coupled ordinary differential equations for only the

first three coefficients of the expansion of $\tilde{U}_k$ – we simply expand the PDE to the appropriate order in $\tilde{\phi}^2$ and match coefficients. Doing so gives

$$\begin{aligned}\frac{\mathrm{d}\tilde{f}_t}{\mathrm{d}t}+\frac{1}{2}\frac{\mathrm{d}\tilde{a}_t}{\mathrm{d}t}\tilde{\phi}^2+\frac{1}{4}\frac{\mathrm{d}\tilde{g}_t}{\mathrm{d}t}\tilde{\phi}^4 &= -d\tilde{f}_t-\tilde{a}_t\tilde{\phi}^2+\left(\frac{d}{4}-1\right)\tilde{g}_t\tilde{\phi}^4+\\ &\quad+\frac{2}{d}\frac{1}{2^d\pi^{d/2}}\frac{1}{\Gamma\left(\frac{d}{2}\right)}\frac{1}{1+\tilde{a}_t+\tilde{g}_t\tilde{\phi}^2+2\tilde{g}_t\tilde{\phi}^2}.\end{aligned} \tag{6.43}$$

The final term gets expanded as a series in $\tilde{\phi}^2$:

$$\begin{aligned}\frac{1}{1+\tilde{a}_t+\tilde{g}_t\tilde{\phi}^2+2\tilde{g}_t\tilde{\phi}^2} &= \frac{1}{1+\tilde{a}_t}\frac{1}{1+\frac{3\tilde{g}_t}{1+\tilde{a}_t}\tilde{\phi}^2}\\ &= \frac{1}{1+\tilde{a}_t}-\frac{3\tilde{g}_t}{(1+\tilde{a}_t)^2}\tilde{\phi}^2+\frac{9\tilde{g}_t^2}{(1+\tilde{a}_t)^3}\tilde{\phi}^4+O\left(\tilde{\phi}^6\right).\end{aligned} \tag{6.44}$$

Hence we have the following:

$$\begin{aligned}\frac{\mathrm{d}\tilde{f}_t}{\mathrm{d}t} &= -d\tilde{f}_t+\frac{2}{d}\frac{1}{2^d\pi^{d/2}}\frac{1}{\Gamma\left(\frac{d}{2}\right)}\frac{1}{1+\tilde{a}_t},\\ \frac{\mathrm{d}\tilde{a}_t}{\mathrm{d}t} &= -2\tilde{a}_t-2\frac{2}{d}\frac{1}{2^d\pi^{d/2}}\frac{1}{\Gamma\left(\frac{d}{2}\right)}\frac{3\tilde{g}_t}{(1+\tilde{a}_t)^2},\\ \frac{\mathrm{d}\tilde{g}_t}{\mathrm{d}t} &= (d-4)\,\tilde{g}_t+4\frac{2}{d}\frac{1}{2^d\pi^{d/2}}\frac{1}{\Gamma\left(\frac{d}{2}\right)}\frac{9\tilde{g}_t^2}{(1+\tilde{a}_t)^3}.\end{aligned} \tag{6.45}$$

In the special case $d = 3$, these become

$$\begin{aligned}\frac{\mathrm{d}\tilde{f}_t}{\mathrm{d}t} &= -3\tilde{f}_t+\frac{1}{6\pi^2}\frac{1}{1+\tilde{a}_t},\\ \frac{\mathrm{d}\tilde{a}_t}{\mathrm{d}t} &= -2\tilde{a}_t-\frac{1}{\pi^2}\frac{\tilde{g}_t}{(1+\tilde{a}_t)^2},\\ \frac{\mathrm{d}\tilde{g}_t}{\mathrm{d}t} &= -\tilde{g}_t+\frac{1}{\pi^2}\frac{6\tilde{g}_t^2}{(1+\tilde{a}_t)^3}.\end{aligned} \tag{6.46}$$

Many aspects of these flow equations are non-universal, and some coefficients can be changed through simple redefinitions of $\tilde{f}_t$, $\tilde{a}_t$, and $\tilde{g}_t$ that do not modify e.g. the universal linearizations of the flows near fixed points. For instance,

choosing $f = 6\pi^2 \tilde{f}_t$, $a = \tilde{a}_t$, and $g = \tilde{g}_t / \left(3\pi^2\right)$, one finds the slightly simpler

$$\begin{aligned} \frac{\mathrm{d}f}{\mathrm{d}t} &= -3f + \frac{1}{1+a}, \\ \frac{\mathrm{d}a}{\mathrm{d}t} &= -2a - \frac{3g}{(1+a)^2}, \\ \frac{\mathrm{d}g}{\mathrm{d}t} &= -g + \frac{18g^2}{(1+a)^3}, \end{aligned} \tag{6.47}$$

which are the forms of the flows that will be used throughout the manuscript.

The more general expression can be used in the usual way to locate the Gaussian and Wilson-Fisher fixed points, linearize and find relevant and irrelevant eigenvalues, etc.[10] The relevant eigenvalue for $d < 4$ is

$$-\lambda_t = \frac{1}{3}\left(2d - 5 + \sqrt{121 + \frac{d}{2}(11d - 100)}\right). \tag{6.48}$$

For $d = 3$, this gives an estimate for ν:

$$\nu_{\mathrm{LPA}}^{\mathrm{trunc}} = -\frac{1}{\lambda_t} = \frac{6}{2 + \sqrt{82}} = 0.542721934\ldots \tag{6.49}$$

This is not the most incredible estimate in the world. The ϵ expansion to linear order predicts $\nu_{\epsilon^1} = 1/2 + \epsilon/12 = 0.58333\ldots$, closer to the CFT value of $\nu_{\mathrm{CFT}} = 0.629971(4)$. However, most of the error in this version of the LPA comes from the truncation of the potential to quartic order in the field. If one works directly with the PDE for $\tilde{U}_k$, one finds an estimate $\nu_{\mathrm{LPA}} = 0.650$, much closer to the CFT value [174]. Thanks to several exponent relations true for the Ising model below the upper critical dimension, there are only two independent critical exponents related to relevant variables (e.g. ν and η). The magnetization exponent can be written in terms of them as $2\beta = \nu(d - 2 + \eta)$. In three dimensions, then, a nonzero η is needed to predict anything other than $\beta = \nu/2$. However, the LPA

[10] Because t flows backwards to implement the renormalization group, relevant eigenvalues are negative and irrelevant ones are positive.

always predicts $\eta = 0$ due to a lack of wave function renormalization. The next-simplest theory, LPA'[11], modifies the coefficient attached to $(\nabla\phi)^2$ from $1/2$ to $Z_k/2$, incorporates Z_k into the flows of the effective potential, and gives nonzero predictions for η.

There have been decades of study focused on applications of the functional RG to classical and quantum field theories, the BKT transition, gravity, and nuclear physics. Most of the focus has been on examining the implied phases and critical exponents near phase transitions. For the Ising model, the derivative expansion (for which the LPA is the zeroth-order term) has been pushed up to 6^{th} order, giving exponents indistinguishable from the conformal bootstrap predictions $\nu_{\text{DE}_6} = 0.63012(16)$. We have been interested in the shapes of the universal *scaling functions* that emerge near the critical point. As discussed in Chapter 4, we have also been interested in the incorporation of universal corrections to the leading singular behavior of response properties. We can use normal form theory to extend the domain in parameter space over which the renormalization group flow equations appear linear. The LPA within the NPRG gives a very nice testing ground for some of these principles, since in computing the trajectories of $\tilde{U}_k$ (either directly or through the truncation scheme) one fully computes the shape of the free energy functional through $\Gamma_k[\phi]$. Derivatives of the free energy with respect to various fields give response functions, susceptibilities, and specific heats, which all have universal forms close to the transition.

In the following manuscript, I performed many detailed numerical tests of theoretically derived scaling results. Itay Griniasty wrote the package that performs the change of variables perturbatively in the vicinity of the matched fixed points and did many other numerical and analytical checks. He also created the

[11] Pronounced "ell pee ay prime."

algorithm that propagates the partial derivatives along the critical and unstable manifolds, which we will also turn into a package. Jim Sethna suggested the idea of using the powerful techniques from the NPRG to extract universal scaling functions, as much of the focus in the past had been on the universal critical exponents alone. He has also been deeply involved in the analysis of the analytical and numerical work performed so far.

6.3 Extracting universal scaling functions from the NPRG

This section is a reformatted version of a manuscript to be submitted to Physical Review B or E.

6.3.1 Introduction

The power of the nonperturbative functional renormalization group (NPRG) is that it can explicitly coarse-grain a microscopic free energy to extract the universal behavior near the critical point for a particular system in a particular dimension. The NPRG literature has focused on honing their tools, measuring progress using the convergence to well measured properties at the critical point – universal exponents, amplitude ratios, ...Our mission is to extract two types of predictions implicitly calculated in high-precision NPRG implementations that are not readily available in conformal bootstrap or other methods. (1) We want numerically accessible approximations of the universal scaling *functions* for the Gibbs and Helmholtz free energies. In the future, we envision universal scaling for higher correlation functions and for multivariable scaling functions

including singular corrections to scaling, crossover scaling functions and multicritical points, and functions that continuously vary in dimension (perhaps allowing faster convergence leveraging the normal-form bifurcation theories at the upper and lower critical dimensions). (2) The NPRG explicitly calculates the nonuniversal properties of the surrounding phases, which are often lacking any other perturbatively solvable limiting description (i.e., the theory of liquids [176], and the QCD phase diagram [177, 178]). All properties of these phases are in principle given by the same analytic coordinate transformation we will use to extract the universal scaling functions. Rather than referring to the original NPRG calculations for predictions, we can summarize them using the universal scaling functions and the coordinate transformations.

In this work, we first review the basic concepts underpinning the implementation of the NPRG (Section 6.3.2). We use the NPRG to write down the parameter flows in the simplest case of the LPA applied to the 3D Ising model. We then review the application of normal form theory to the renormalization group. We show that the explicit nonlinear equations given by NPRGs lead to situations where we can explicitly evaluate the map from the bare coordinates to the nonlinear scaling fields of normal form theory. We implement this change of coordinates, both perturbatively around the fixed point and via numerical integration of exact ODEs for partial derivatives (Section 6.3.3). This allows us to predict standardized universal scaling functions to numerical precision within a given NPRG. We give an example of this evaluation for the susceptibility of the 3D Ising model including the leading irrelevant correction (Section 6.3.4). We end with speculations about extending the radius of the nonlinear coordinate transformations using neural networks and implications for predicting phase behavior in real experiments (Section 6.3.5).

	This work	NPRG [174, 176]	Cardy [34, Sec. 3.3]	Raju et al. [49]
Gibbs free energy	$V = F + A\Phi^2 + G\Phi^4$	$U = f + a\phi^2 + g\phi^4$	$\mathcal{H}(t,h) - mh$	$\mathcal{H}(t,h) - mh$
Variables	A, G, F, Φ	a, g, f, ϕ	$\mathbf{K} = \{t, u, f, m\}$	$\theta = \{t, u, f, m\}$
Rescaled variables	$\{a, g, f, \phi\}$	$\{\widetilde{a}, \widetilde{g}, \widetilde{f}, \widetilde{\phi}\}$	…	…
Nonlinear scaling fields	$\{t, u, v\}$	…	$\mathbf{u}(\mathbf{K}) = \{u_t, u_u, u_f, u_m\}$	$\widetilde{\theta}(\theta) = \{\widetilde{t}, \widetilde{u}, \widetilde{f}, \widetilde{m}\}$
Cutoff and log factor	$\ell, k = \Lambda \exp(-\ell)$	$-t, k = \Lambda \exp(t)$	$\ell, \xi = \xi_0 \exp(-\ell)$	$\ell, \xi = \xi_0 \exp(-\ell)$

Table 6.1: Conventions on variable names. We use rather different conventions in this manuscript from those traditional in the statistical mechanics literature [34], or our previous work [49] to conform to those in the NPRG literature [174]. Our work [49] emphasizes the analytic change of variables to nonlinear scaling fields, so we originally used tildes to represent this, while the NPRG literature uses tildes to represent the rescaled Gibbs free energy and field. Particularly confusing is the NPRG log coarse-graining factor t, which is *not* the reduced temperature and is *minus* the traditional variable ℓ. In this context, under coarse-graining the relevant variables have negative eigenvalues at the fixed point and the irrelevant variable have positive eigenvalues. Also, one coarse-grains from the microscopic free energy to the macroscopic free energy by integrating t backward from t_0 to $-\infty$.

6.3.2 Using normal forms to extract scaling functions

Our attempt here is to develop and test the machinery for extracting the universal scaling functions and the predictions for the surrounding phases in the least complicated and most mainstream case: NPRG for the 3D Ising model, within the LPA (without "field renormalization" or gradient corrections) in a three-parameter approximation which truncates the potential to a quartic, giving a Gibbs free energy

$$\begin{aligned} \Gamma^{\mathrm{LPA}}[\Phi] &= \int \mathrm{d}^3 r \left[\frac{1}{2} (\nabla\Phi)^2 + V(\Phi) \right] \\ V(\Phi | A, G, F) &= F + A\Phi^2 + G\Phi^4. \end{aligned} \tag{6.50}$$

In this approximation, the NPRG provides ordinary differential equations for the three parameters A, G, and F as the short wavelengths are coarse-grained from a microscopic wavevector Λ to a wavevector or momentum scale $k = \Lambda \exp(-\ell)$, $\ell = \ln(\Lambda/k)$. (Note that ℓ conventionally flows to *larger* values as

the NPRG coarse-grains, see Table 6.1). We henceforth measure k in units of Λ. As usual in the renormalization group (RG), one needs to rescale the fields and the free energy in order for the system at its critical point to flow to a fixed point; here

$$\begin{aligned}
\mathcal{V} &= k^{-D}V = k^{-3}V = e^{3\ell}V = f + a\phi^2 + g\phi^4 \\
\phi &= k^{-(D-2)/2}\Phi = k^{-1/2}\Phi = e^{\ell/2}\Phi \\
a &= k^{-2}A = e^{2\ell}A \\
g &= k^{D-4}G = k^{-1}G = e^{\ell}G \\
f &= k^{-D}F = k^{-3}F = e^{3\ell}F.
\end{aligned} \tag{6.51}$$

and the nonlinear RG equations take the general form

$$\begin{aligned}
\frac{\mathrm{d}a}{\mathrm{d}\ell} &= 2a + \sum_{i,j=0}^{\infty} A_{ij}a^i g^j = 2a + \frac{3g}{(1+a)^2} \\
\frac{\mathrm{d}g}{\mathrm{d}\ell} &= (4-D)g + \sum_{i,j=0}^{\infty} G_{ij}a^i g^j = g - \frac{18g^2}{(1+a)^3} \\
\frac{\mathrm{d}f}{\mathrm{d}\ell} &= df + \sum_{i,j=0}^{\infty} F_{ij}a^i g^j = 3f - \frac{1}{1+a}.
\end{aligned} \tag{6.52}$$

We note at the outset that the flows for a and g are coupled to each other but do not depend upon f. If we work in the projected space of (a, g), as we will commonly do, we can ignore the effects of f, which acts as a shift in the overall free energy as a function of Φ. The point $a = g = 0$ here is the mean-field fixed point, so the linear terms in Equation 6.52 reflect the mean-field 3D critical exponents, where a and g both are relevant. The other fixed point, which has an attractive direction in (a, g), is the Wilson-Fisher fixed point, located at $(a_{\mathrm{WF}}, g_{\mathrm{WF}}) = (-1/13, 96/2197)$. Table 6.1 provides a dictionary translating the notation we use here and in previous work [49] to that used in the NPRG [176, 174] and statistical physics [34] communities.

The traditional RG procedure is to start by linearizing the flow equations at

the fixed point $(a_{\mathrm{WF}}, g_{\mathrm{WF}}) = (-1/13, 96/2197)$ and using the linear flows to derive the universal critical exponents (like β in $M(T) \sim (T_c - T)^{\beta}$) between pairs of properties near the critical point and the forms of universal scaling functions (like $\mathcal{M}$ in $M(T, H) = (T_c - T)^{\beta}\mathcal{M}(H/(T_c - T)^{\beta\delta})$) relating three or more quantities. This procedure must be supplemented in cases like the 2D Ising model (where the exact solution has a logarithmic divergence in the specific heat due to a *resonance* that demands special attention) and the 4D Ising model (where both a resonance and the marginal variable give logarithms). Recent work [49] systematizes and generalizes this approach by applying a version of bifurcation normal form theory to the nonlinear RG flow equations. For *hyperbolic* flows (like the 3D Ising model we study here), one can linearize the RG flows order by order by a polynomial change of variables. In Section 6.3.3, encouraged by normal form theory, we shall explore methods to analytically or numerically change variables from $\{a, g, f\}$ to linearized variables $\{t(a, g, f), u(a, g, f), v(a, g, f)\}$, such that

$$\begin{aligned} \frac{\mathrm{d}t}{\mathrm{d}\ell} &= \lambda_t t = \frac{1}{\nu} t, \\ \frac{\mathrm{d}u}{\mathrm{d}\ell} &= \lambda_u u = -\omega u, \\ \frac{\mathrm{d}v}{\mathrm{d}\ell} &= Dv. \end{aligned} \tag{6.53}$$

where $\lambda_t > 0$ and $\lambda_u < 0$ are the nontrivial eigenvalues at the fixed point, t is the relevant, temperature-like direction, u introduces the leading correction to scaling due to the slowest-decaying irrelevant operator, and v tracks the coarse-graining of the shift of the free energy. One can solve these equations and use $k = e^{-\ell}$ to show that

$$t = t_0 k^{-1/\nu}, \quad u = u_0 k^{\omega}, \quad \text{and} \quad v = v_0 k^{-D}. \tag{6.54}$$

What do we expect the universal scaling form to look like? We expect that this free energy will depend on the linearized variables t, u, and v in invari-

ant scaling combinations. It is usual to write these invariant combinations by pulling out powers of the temperature t: $Vt^{-D\nu}$, $\phi t^{-\beta}$, $ut^{\omega\nu}$, $vt^{-D\nu}$, and kt^{ν} (in cases where we do not coarse-grain all the way to $k = 0$). The form of the free energy can then be written as

$$V = t^{D\nu}\mathcal{V}(\phi t^{-\beta}, ut^{\omega\nu}, vt^{-D\nu}, kt^{\nu}). \tag{6.55}$$

How do we extract the NPRG LPA universal scaling function for the Gibbs free energy V? As discussed before, we will solve for the change of variables $t(a, g, f)$, $u(a, g, f)$, $v(a, g, f)$ and their inverses $a(t, u, v)$, $g(t, u, v)$, $f(t, u, v)$. We then know

$$V(\phi|a, g, f, k) = k^D\left(f + a\phi^2 + g\phi^4\right). \tag{6.56}$$

But this is k^D times a function of $t = t_0k^{-\lambda_t}$, $u = u_0k^{-\lambda_u}$, and $v = v_0k^{-D}$. Hence in our approximation we find

$$V(\phi|a, g, f, k) = k^D\widehat{\mathcal{V}}(\phi k^{1/2}, tk^{\lambda_t}, uk^{\lambda_u}, vk^D) \tag{6.57}$$

with

$$\widehat{\mathcal{V}}(\phi, t, u, v) = f(t, u, v) + a(t, u, v)\phi^2 + g(t, u, v)\phi^4, \tag{6.58}$$

and $\nu = 1/\lambda_t$, $\omega = -\lambda_u$, and $\beta = \nu/2$.

Clearly, this last result $\beta = \nu/2$ is due to our approximations; in general, the relevant exponent relation gives $\beta = (D - 2 + \eta)\nu/2 = (1 + \eta)\nu/2$. Indeed, LPA without a field renormalization is known to predict $\eta = 0$ [174, p. 9]. This is fixed in what is termed LPA', where the free energy has an extra term Z which is incorporated into the flows, changing from $(1/2)(\nabla\Phi)^2 + V(\Phi)$ to $(Z/2)(\nabla\Phi)^2 + V(\Phi)$.

6.3.3 Changing coordinates to the normal form

First, we find a change of coordinates locally near the fixed point that has an attractive direction. The change of coordinates matches the nonlinear LPA coordinates, in which the flows are distorted, to a set of coordinates in which the flows are perfectly linear everywhere (in this case). This leads to several interesting singularities. In the original LPA coordinates (a, g), the flows have two fixed points, (Gaussian and Wilson-Fisher), while the normal form coordinates have only one fixed point with the eigenvalues of the more attractive Wilson-Fisher fixed point. In the normal form coordinates, $t = 0$ defines the critical manifold $a_c(g)$, which is the separatrix of the LPA flows. One only approaches the Gaussian fixed point asymptotically as $t = 0$, $u \to -\infty$, leading to a bunching of contour lines[12].

Another interesting singularity occurs in the inverse direction of the map. When one computes the change of coordinates $(t, u) \to (a, g)$ along the critical manifold by numerically integrating explicit equations of motion for the partial derivatives, one finds a blowup in finite ℓ corresponding to a particular value of u along the critical manifold. However, upon approaching this blowup, arbitrarily large values of g are sampled, suggesting that the contour lines of the map $(a, g) \to (t, u)$ are bunched at a finite value of u, similar to the situation near $g = 0$ in the inverse map which was due to the Gaussian fixed point. Each of these singularities appears to be an artifact of the change of coordinates and the choice of form of analytic corrections to scaling, and hence they do not seem to have physical significance. However, one may describe the crossover from

[12]This can be fixed by applying these methods to a normal form that incorporates both fixed points, such as the normal form of the transcritical bifurcation for the $(4 - \epsilon)$-dimensional Ising model with $\epsilon = 1$.

3D Ising to mean-field behavior using a normal form that captures both fixed points.

To find a polynomial change of variables $(a, g) \leftrightarrow (t, u)$ order by order we employ the following strategy:

1. Map both flows to the normal form to first order following Wiggins [179].
2. The flow of (t, u) can also be written as $\mathcal{L}_{\text{LPA}} \cdot \frac{\partial(t,u)}{\partial(a,g)}$, and so we can write a system of first order ODEs for $(t, u)[a, g]$:
$$\mathcal{L}_{t,u} = \mathcal{L}_{\text{LPA}} \cdot \frac{\partial(t, u)}{\partial(a, g)} \tag{6.59}$$
where $\mathcal{L}$ are the normal form flows derived above.
3. We then iteratively solve for $\partial_a^i \partial_g^j (t, u)$, iterating on $n = i + j$. For $n = 1$ the eigenvectors of the linearized normal form flows from (a, g) are mapped to those in (t, u) up to rescaling:
$$\left.\frac{\partial(t, u)}{\partial(a, g)}\right|_{\text{WF}} = \begin{pmatrix} c_1 & 0 \\ 0 & c_2 \end{pmatrix}. \tag{6.60}$$

This final statement represents a pair of degrees of freedom in the mapping to the normal form coordinates, since if the (linear) normal form flows for t and u are satisfied, then they are also satisfied for $t' = c_1 t$ and $u' = c_2 u$. There is in principle another free parameter associated with the linear normal form flow for v. In practice, shifting (c_1, c_2) rescales invariant scaling combinations in easily identifiable ways. These free parameters can then be used to set the scale of the universal scaling function, e.g., one can choose to make $M = (-t)^\beta$ exactly true for the Ising model with $h = 0$ via a suitable redefinition of the scale of t.

Alternatively, one can set the scale of (c_1, c_2) by examining the region of convergence of the series expansion of the coordinate transformation $(a, g) \leftrightarrow (t, u)$.

We can select $c_1 = 1$ and choose c_2 so that the scale of the convergence region is similar in all directions. This is achieved by selecting $c_2 \approx 10.1284$. These are the values we will take to report future numbers in this preliminary manuscript, with the understanding that many of these numbers depend upon the choice of (c_1, c_2). Another option would be to examine Table 6.2 and select c_1 to set the first entry to 1 and c_2 to set the second entry to 1. Then all higher derivatives of this function are standardized, universal numbers.

The implementation of this perturbative change of variables is general enough that we implement it through a Mathematica package cov.wl, which takes as input two (potentially nonlinear) flow equations, the fixed points to match, the order of the expansion, and the names of variables, and outputs the numerically computed expansion to that order. The routine automatically ensures that the eigenvalues at the fixed points match, which is a necessary condition for the normal forms to work. Later, when we propagate partial derivatives of the coordinate transformation along the critical and unstable manifolds beyond the radius of convergence of the series expansion, we will use these perturbative solutions as initial conditions for the partial derivatives to arbitrary order.

6.3.4 Extracting useful implementations of the universal scaling functions

When an experimentalist adjusts their tuning knobs (a, g) to send their system through a critical point, the critical manifold is crossed in a way that involves both of the normal form coordinates t and u in general. The crossing of the

critical manifold generically occurs far from the fixed point of any RG trajectory. The many irrelevant variables involved guarantee that the critical behavior of the system is set by the attractive fixed point of an RG transformation. Because the normal form coordinates describe the behavior of the system arbitrarily far from the fixed point[13], one can translate between the experimentalist's findings and the universal predictions from normal form theory. This is what we seek to do in this section.

Suppose an experimentalist measures the susceptibility of an experimental system in the "LPA Ising" class, so that the flows for a and g perfectly describe some appropriate RG procedure. Parameters intrinsic to the experimental system that are not easily changed by the experimentalist set $g = g_{\text{exp}}$, and the experimentalist reduces their knob a until the susceptibility diverges. We denote $\Delta a \equiv a - a_c(g_{\text{exp}})$. Alongside the pure power-law divergence

$$\chi(a, g) \sim \Delta a^{-\gamma}, \tag{6.61}$$

the experimentalist also notices deviations from the pure power law as Δa grows from 0. To emphasize these deviations, the experimentalist can plot $\Delta a^{\gamma}\chi(a, g)$ against Δa and admire its deviations from a flat line. Some of these deviations are associated with analytic corrections to scaling, while others are due to the singular corrections to scaling coming from the least irrelevant variable. The expansion of $\Delta a^{\gamma}\chi(a, g)$ at constant g near this point in ascending powers of Δa

[13]There may be convergence issues if the RG transformation has multiple fixed points and is matched to a normal form that describes only one of them, as is the case in this section. These issues can be fixed by using a nonlinear normal form [49], but one must then deal with much more complicated invariant scaling combinations.

is

$$\begin{aligned}
\Delta a^{\gamma}\chi = \Delta a^{\gamma} t^{-\gamma}\mathcal{X}\left(ut^{\omega\nu}\right) &= \left(\frac{\partial t}{\partial a}\right)^{-\gamma}\mathcal{X}(0) \\
&+ \Delta a^{\omega\nu} u\left(\frac{\partial t}{\partial a}\right)^{-\gamma+\omega\nu}\mathcal{X}'(0) \\
&- \Delta a \frac{\gamma}{2}\left(\frac{\partial t}{\partial a}\right)^{-\gamma-1}\left(\frac{\partial^2 t}{\partial a^2}\right)\mathcal{X}(0) \\
&+ \Delta a^{2\omega\nu}\frac{u^2}{2}\left(\frac{\partial t}{\partial a}\right)^{-\gamma+2\omega\nu}\mathcal{X}''(0) \\
&+ \Delta a^{1+\omega\nu}\Bigg[\left(\frac{\partial t}{\partial a}\right)^{-\gamma+\omega\nu}\left(\frac{\partial u}{\partial a}\right)\mathcal{X}'(0) \\
&+ \frac{u}{2}\left(-\gamma+\omega\nu\right)\left(\frac{\partial t}{\partial a}\right)^{-\gamma+\omega\nu-1}\left(\frac{\partial^2 t}{\partial a^2}\right)\mathcal{X}'(0)\Bigg] \\
&+ O\left(\Delta a^{3\omega\nu}\right).
\end{aligned} \tag{6.62}$$

Here the terms in the expansion involving t and u and their partial derivatives are evaluated at the point $a = a_c(g_{\text{exp}})$, $g = g_{\text{exp}}$. We can make numerical predictions for all of these corrections and then implement the experiment to check the results.

Finding an expansion of the universal scaling function

We first use the normal form coordinates to determine a good expansion of the universal scaling function. This can be done using the expansion of the susceptibility, for instance, around the fixed point of the RG transformation in the normal form coordinates:

$$\begin{aligned}
\chi(t,u) &= \\
t^{-\gamma}\mathcal{X}\left(ut^{\omega\nu}\right) &= t^{-\gamma}\mathcal{X}(0) + t^{-\gamma+\omega\nu}u\mathcal{X}'(0) \\
&\quad + \frac{1}{2}t^{-\gamma+2\omega\nu}u^2\mathcal{X}''(0) + O\left(u^3\right)
\end{aligned} \tag{6.63}$$

The experimentalist measures the inverse of the second derivative of their free energy, which is the thermodynamic value of A^{-1}, where A is the coefficient on

the quadratic term in the expansion of the free energy as a function of ϕ. Performing the expansion of a^{-1} and comparing to the series for the scaling function gives relationships between the derivatives of the scaling function and the values that certain combinations of parameters reach as $t \to \infty$ up the unstable manifold:

$$\begin{aligned}
\mathcal{X}(0) &= \lim_{t\to\infty} \frac{t^{\gamma}}{a} \\
\mathcal{X}'(0) &= -\lim_{t\to\infty} \frac{t^{\gamma-\omega\nu}}{a^2}\left(\frac{\partial a}{\partial u}\right) \\
\mathcal{X}''(0) &= \lim_{t\to\infty} \frac{t^{\gamma-2\omega\nu}}{a^3}\left(2\left(\frac{\partial a}{\partial u}\right)^2 - a\left(\frac{\partial^2 a}{\partial u^2}\right)\right) \\
&\vdots
\end{aligned} \tag{6.64}$$

where all quantities are evaluated at $u = 0$.

To compute both these values and the remainder of the terms that appear in the experimentalist's expansion, we need a way to find all derivatives of the map from $(a, g) \leftrightarrow (t, u)$ along the critical and unstable manifolds. In both cases, these derivatives are needed outside the radius of convergence of the multivariable series solution near the attractive fixed point.

Finding derivatives of the map along flow trajectories

To find derivatives of the map from $(a, g) \leftrightarrow (t, u)$ far from the fixed point, we resort to numerical integration schemes. The initial conditions for flows of the derivatives can be set at the fixed point by the multivariable series expansions. We can find how these partial derivatives flow along invariant curves of the RG. We will report the derivation for flows of $\partial_t^i \partial_u^j a$ along the unstable manifold which are necessary for the computation of the expansion of the universal scaling function. The derivation of the flows for $\partial_t^i \partial_u^j a$ along the critical manifold, or

for the flows of $\partial_t^i \partial_u^j g$, $\partial_a^i \partial_g^j t$, or $\partial_a^i \partial_g^j u$ along either manifold, follow similarly.

We will track $\partial_t^i \partial_u^j a$ as a function of t along $u = 0$. We subtract and add a term from the flow for this partial derivative:

$$\frac{\mathrm{d}}{\mathrm{d}t} \partial_t^i \partial_u^j a = \frac{\mathrm{d}}{\mathrm{d}t} \partial_t^i \partial_u^j a - \partial_t^i \partial_u^j \frac{\mathrm{d}}{\mathrm{d}t} a + \partial_t^i \partial_u^j \frac{\mathrm{d}}{\mathrm{d}t} a \tag{6.65}$$

On the right-hand side, we can write the first two total derivatives with respect to t using the chain rule:

$$\frac{\mathrm{d}}{\mathrm{d}t} = \partial_t + \frac{\mathrm{d}u}{\mathrm{d}t} \partial_u = \partial_t + \frac{\mathcal{L}_u}{\mathcal{L}_t} \partial_u. \tag{6.66}$$

The final place where the total derivative occurs can be written as

$$\frac{\mathrm{d}a}{\mathrm{d}t} = \frac{\mathcal{L}_a}{\mathcal{L}_t}, \tag{6.67}$$

leading to

$$\begin{aligned} \frac{\mathrm{d}}{\mathrm{d}t} \partial_t^i \partial_u^j a = &\left(\partial_t + \frac{\mathcal{L}_u}{\mathcal{L}_t} \partial_u \right) \partial_t^i \partial_u^j a \\ &- \partial_t^i \partial_u^j \left(\partial_t + \frac{\mathcal{L}_u}{\mathcal{L}_t} \partial_u \right) a + \partial_t^i \partial_u^j \left(\frac{\mathcal{L}_a}{\mathcal{L}_t} \right) \end{aligned} \tag{6.68}$$

Although it appears that partial derivatives of higher order appear on the right-hand side, the highest-order partials cancel out, leading to an ordinary differential equation for $\partial_t^i \partial_u^j a$ depending only on the mixed partial derivatives of a and g of order at most i in t and of order at most j in u. One can then simultaneously solve all of the ODEs for $\partial_t^i \partial_u^j a$ and $\partial_t^i \partial_u^j g$ and all lower-order partials using the initial conditions from the series expansion. These give the partial derivatives along flow trajectories, i.e. $\partial_t^i \partial_u^j a\,(t, u(t))$, of which the critical and unstable manifolds are special cases.

Equipped with this scheme, we can use Eqn. 6.64 to compute numerical values for these coefficients. The result of the first 5 of these terms are tabulated in Table 6.2. The other partials required for the evaluation of the series in Eqn. 6.62

Quantity	Value
$\mathcal{X}(0)$	1.0059874(5)
$\mathcal{X}'(0)$	0.286943(2)
$\mathcal{X}''(0)$	−0.19938(2)
$\mathcal{X}^{(3)}(0)$	57.4782(2)
$\mathcal{X}^{(4)}(0)$	250.127(4)

Table 6.2: Some estimates for the Taylor series of $\mathcal{X}(ut^{\omega\nu})$.

can also be computed in this way and propagated out to the value of g at which the experiment occurs.

Comparison of expansion prediction with a numerical experiment

With estimates for the expansion of the universal scaling function and other partial derivatives of the map $(a, g) \leftrightarrow (t, u)$ along the critical manifold, we can now perform an experiment. The experimentalist fixes values of (a, g_{exp}) and varies a until they hit the critical manifold, measuring the thermodynamic susceptibility. Their measurements can be found using the flow for a, tracking $\chi = \lim_{\ell\to\infty} A_\ell^{-1} = \lim_{\ell\to\infty} e^{-2\ell} a_\ell$. To emphasize the deviations from a pure power-law divergence, we plot $\Delta a^\gamma \chi$ against Δa. The values for the critical exponents within the LPA can be found by linearizing the flows for a and g in the vicinity of the attractive fixed point, leading to

$$\begin{aligned} \gamma &= \frac{12}{\sqrt{82}+2} = 1.08544\ldots, \\ \omega\nu &= \frac{\sqrt{82}-2}{\sqrt{82}+2} = 0.638185\ldots \end{aligned} \tag{6.69}$$

We suppose that the experiment is performed at $g_{\text{exp}} = g_{\text{WF}} + 0.01$ and $g_{\text{exp}} = g_{\text{WF}} + 0.05$ and that the experimentalist begins their excursion towards the critical point at $\Delta a_{\text{start}} = 0.1$. A to-scale illustration of this experiment in (a, g) coordinates is shown in Fig. 6.2.

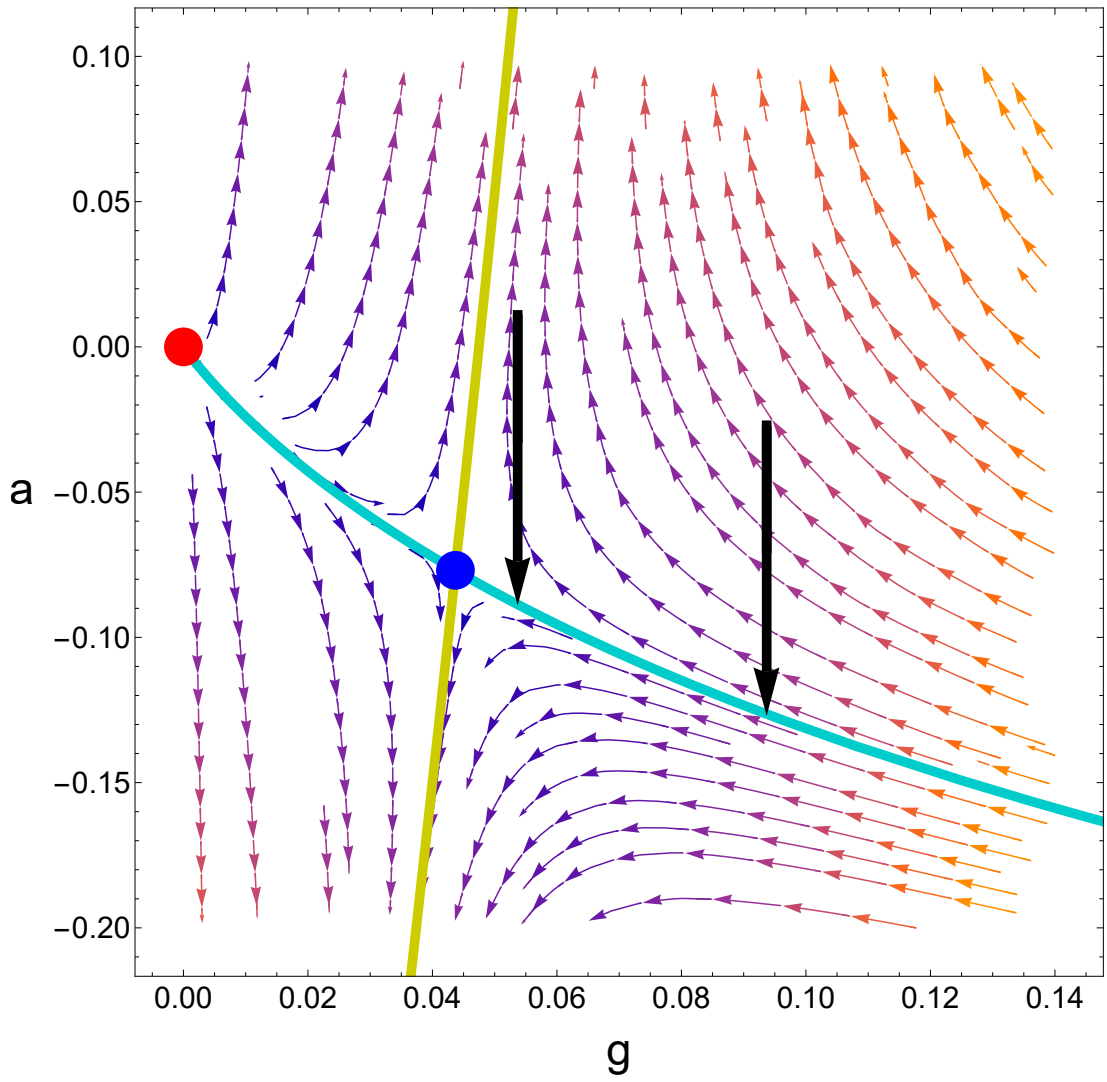

Figure 6.2: An experimentalist tunes their a knob at fixed g_{exp}, reaching the critical manifold. Shown are the cases where $g_{\text{exp}} = g_{\text{WF}} + 0.01$ and $g_{\text{exp}} = g_{\text{WF}} + 0.05$ with $\Delta a_{\text{start}} = 0.1$.

We report the first several partial derivatives needed to evaluate Eqn. 6.62 at this location along the critical manifold in Table 6.3. Inserting these values, together with the values for the universal scaling function from Table 6.2, leads to a prediction for what the experimentalist should measure upon approaching

	$g_{\text{exp}} = g_{\text{WF}} + 0.01$	$g_{\text{exp}} = g_{\text{WF}} + 0.05$
u	0.127792	0.343426
$\partial_a t$	0.930383	0.910144
$\partial_a u$	–0.761318	–0.765994
$\partial_a^2 t$	0.109251	0.043786

Table 6.3: Some estimates for the partial derivatives of the coordinate transformation $(a, g) \leftrightarrow (t, u)$ needed to evaluate Eqn. 6.62 at the point $a = a_c(g_{\text{exp}})$, for two values of g_{exp}.

the critical manifold; for instance, when $g_{\text{exp}} = g_{\text{WF}} + 0.05$, we find:

$$\begin{aligned} \Delta a^{\gamma}\chi = 1.11423 \\ + 0.102782\,\Delta a^{\omega\nu} \\ - 0.029092\,\Delta a \\ - 0.011548\,\Delta a^{2\omega\nu} \\ - 0.230356\,\Delta a^{1+\omega\nu} + \ldots \end{aligned} \tag{6.70}$$

The comparison between two experiments and two expansions to $O(\Delta a^{1+\omega\nu})$ is shown in Fig. 6.3, demonstrating excellent agreement.

We can track the error that the expansion in powers of Δa makes as we increase the order of the expansion in Equation 6.62. These contour plots are shown in Appendix E.1 and demonstrate improved accuracy everywhere in (a, g) except near the Gaussian fixed point, which is not captured in our change of coordinates to the linear normal form.

6.3.5 Discussion and outlook

Our coordinate transformation to the normal form can be implemented in a number of ways. In this work, we performed a perturbative expansion that

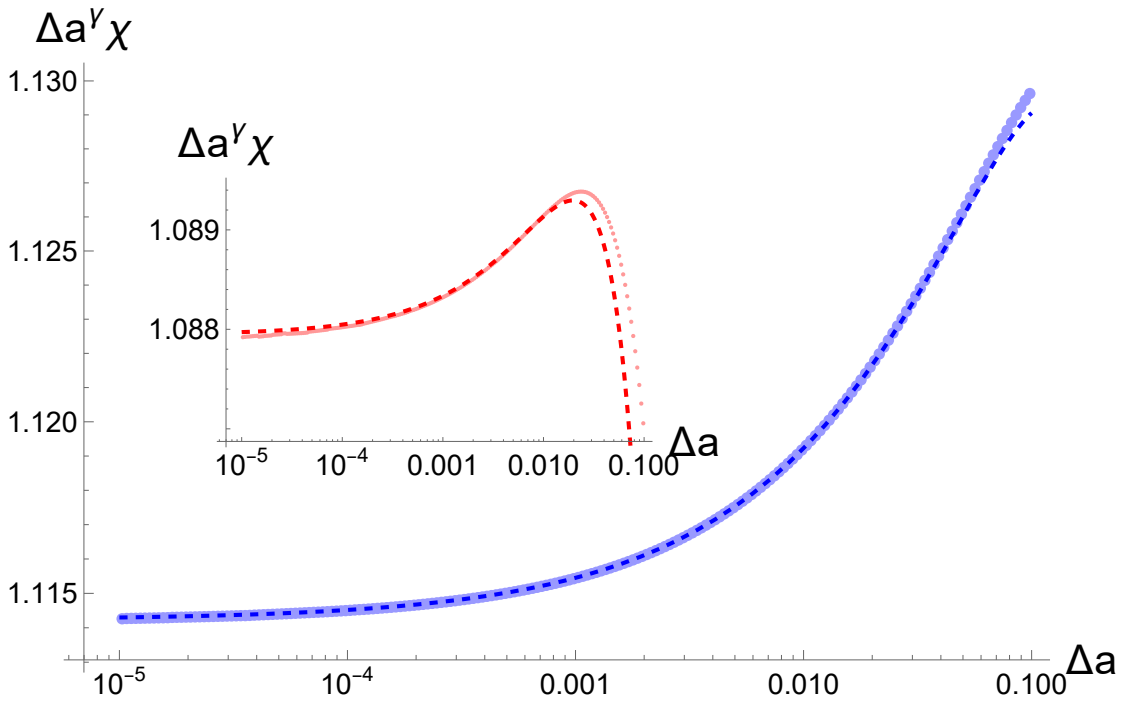

Figure 6.3: Deviations from the pure power-law divergence in an experiment can be attributed to a combination of singular and analytic corrections to scaling. In addition to information about the universal scaling function, information about the analytic transformation from $(a, g) \leftrightarrow (t, u)$ is needed to make direct comparison to an experiment. Given an explicit set of RG equations and a normal form, all information about this transformation can be computed. This allows an experiment performed near the critical manifold in the (a, g) variables (points) to be described completely in an expansion in Δa with no fitting parameters (dashed lines). The blue curves are for $g_{\text{exp}} = g_{\text{WF}} + 0.05$, while the red curves in the inset correspond to $g_{\text{exp}} = g_{\text{WF}} + 0.01$.

matched the flows of the nonlinear LPA equations for the 3D Ising model near the Wilson-Fisher fixed point to normal form flow equations that are linear everywhere. This perturbative solution has a limited region of convergence. However, we can propagate the change of coordinates outside of the region of convergence using numerical integration schemes, giving us reliable coordinate transformations along the critical and unstable manifolds.

We can in principle determine the coordinate transformations between $(a, g) \leftrightarrow (t, u)$ far from the critical and unstable manifolds numerically. This

can be effectively implemented using a neural network to learn the mapping $(a, g) \to (t, u)$, using the desired linear flows in (t, u) to write a loss function. This determines the mapping over an array of points that can be placed far from the critical and unstable manifolds. Ultimately, this allows one to fold the analytic corrections into a numerically determined function that can be reported in a .dat file as the weights associated with a particular neural network architecture. Once this analytic change of coordinates is determined in a large region, the form of the universal scaling function (which can be determined without reference to the points far from the unstable manifold) will describe the physics in this larger region.

We also hope, in the future, to investigate how the change of coordinates operates when we work with more complicated, nonlinear normal forms. We expect better convergence properties for the change of variables when we have a normal form that captures all of the fixed points present in the original nonlinear flows. This may allow us to capture the crossover between the 3D Ising behavior near the Wilson-Fisher fixed point and the tricritical Ising model near the $g = 0$ fixed point in 3D.

Finally, we hope to extend this work by standardizing the normal forms of a variety of universality classes as in [49] and combining them with predictions from much more sophisticated NPRGs (like DE_6 [**?**]). The high-precision universal scaling functions extracted using the procedures demonstrated in this work can then be made publicly available in repositories for experimentalists to access, leading to information about universality classes that goes far beyond the usual tabulation of critical exponents.

6.3.6 Acknowledgments

SJT thanks Anna Barth, Archishman Raju, Jason Kim, and Matthieu Tissier for useful conversations.

CHAPTER 7

TOPOLOGICAL DEFECTS IN BENT-CORE LIQUID CRYSTALS: FUSION AND BRAIDING

7.1 Classifying topological defects and characterizing their combination rules in ordered media

Topological defects constitute a beautiful meeting of physics (free energies, order parameters, symmetries) and mathematics (homotopy and group theory). Most of the mathematics involved in the other projects discussed in this thesis comes from analytic function theory, differential equations, and bifurcation theory. In contrast, the mathematics necessary to understand topological defects deal primarily with homotopy theory and group theory. The results in this chapter are also best understood through pictures, and I like drawing pictures. The topological defects that I will focus on are those that occur in liquid crystals.

What is a liquid crystal? A liquid crystal is a material comprised of microscopic units that has less long-ranged translational order than a crystal (so it is not a crystal, and can often flow like a liquid) but that has long-ranged orientational order (molecules that are separated by long distances still prefer to align in ordered phases). In this way, it has a type of order that is intermediate between that of a liquid and that of a crystal. Some common ordered phases of liquid crystals include nematic (no translational order), smectic (translational order in one direction, 2D liquid-like translational order in the others), and cholesteric (layer-like structure with a regular twist angle between layers). I will focus on the nematic phases, where there is no translational order and the

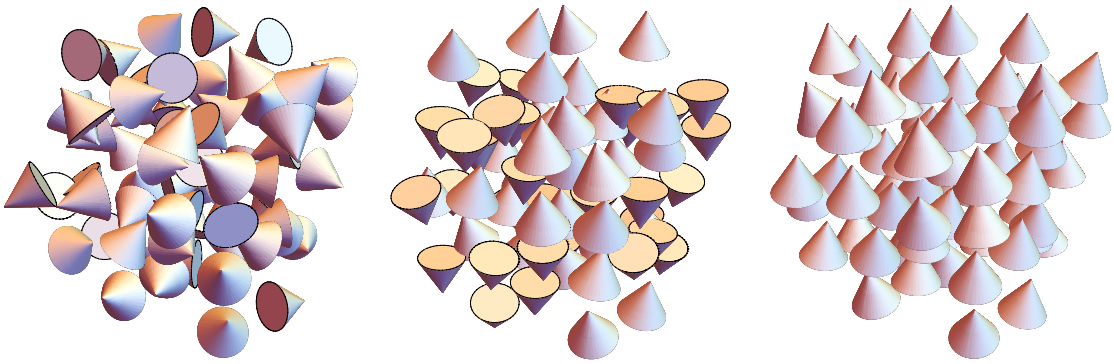

Figure 7.1: Speculative nematic phases formed in a liquid crystal made of cone-shaped molecules upon lowering the temperature (from left to right). Intermediate phases which break the symmetry in intermediate ways are possible.

free energy can be written for an order parameter involving local directors only.

Even specializing to nematic phases, there are a bewildering variety of symmetries that can be broken. The usual caricature of a nematic liquid crystal involves smooth rod-like molecules that have symmetry group $D_{\infty h}$. However, one must draw a distinction between the symmetries of the molecular components of the nematic liquid crystal and the symmetries of the nematic phase that is formed. For instance, we can imagine a nematic comprised of cone-like molecules (Figure 7.1), so that the most orientationally ordered phase has a vector-like symmetry (points in some direction). One can then imagine a free energy functional that allows for three phases: a randomly oriented phase (at the highest temperatures), a vector-ordered phase (at the lowest temperatures), and a uniaxial nematic phase (at intermediate temperatures) where the cones point along a particular direction, but randomly are aligned or antialigned. In the intermediate phase, the symmetry of the *phase* is that of a uniaxial nematic, and so to analyze elastic properties within the phase it is sufficient to work with a field theory that involves a uniaxial nematic order parameter.

Once we have characterized the symmetry of the phase, we can think about the topological space in which the "zero temperature" order parameter lives. For a Heisenberg magnet, for instance, the order parameter space is topologically S^2, since the magnetization can point in any direction in 3 dimensions, and all of the spins are aligned (so the magnitude of the ordering is fixed). This is in contrast to a "soft-spin" order parameter, where we imagine averaging the direction of a collection of Heisenberg spins in some finite region. The soft spin order parameter can detect the transition from the paramagnetic to the ferromagnetic phase: it is on average $0 \in \mathbb{R}^3$ in the paramagnetic phase.

Let us classify the topological order parameter in the ordered phases of the cone-shaped molecule. In the lowest-temperature phase, all of the cones are aligned, and the order is vector-like since rotation about an axis passing through the point of the cone and the center of the flat face is a symmetry. To find the topological order parameter, we want to find a topological space where (1) each point in the topological space corresponds to one and only one ordered state, and (2) the topological space is "connected properly." For vector order, S^2 does the job, since each point on S^2 represents a direction that a vector can point, and continuous rotations by π in any direction are smoothly connected to rotations by $-\pi$. However, to prepare ourselves for more complicated examples, it is useful to follow a workflow that works for any liquid crystal nematic phase. Instead of trying to "guess" a topological space that is properly connected, we can start with the very "large" order parameter space of SO(3). Each point in SO(3) corresponds to a configuration of a phase: one takes a proper rotation matrix from the usual representation of SO(3) and applies it to an object with the symmetry of the phase. However, the mapping from points in SO(3) to configurations is not one-to-one: if one applies an element of SO(3) that corresponds to a sym-

metry P of the phase, then one gets an equivalent configuration. To ensure that each point in the order parameter space corresponds to a unique configuration, we can take as our topological order parameter space the topological quotient space SO(3)/P. This keeps the connectivity properties of SO(3) while ensuring the mapping is one-to-one [180].

As an aside: why do we not take O(3) as a starting point? Mirror symmetries can be interesting. We will see that bent-core nematics, despite being achiral on average, can organize themselves into chiral phases which break mirror symmetries. These mirror symmetries split the order parameter space into disconnected components. When we go to classify the topological defects, the disconnected components of the order parameter space are counted by π_0, which allows for the identification of domain walls but does not have any interesting group structure. For the chiral phases of these nematics, then, if the mirror symmetry is spontaneously broken, the phase can organize into bubbles of a particular chirality, separated by domain walls that represent a flip in the chirality (similar to the Ising model domain walls). Once this organization is complete, it is sufficient to complete the characterization of the topological defects *within* each of the chiral bubbles, each of which lives within just one connected component of the order parameter space. Staying away from domain walls allows us to remain in a single connected component of the order parameter space and classify the defects starting from the connected space SO(3) rather than O(3).

For the (speculative) most ordered phase of the conical molecules, the phase is invariant under rotations about an axis pointing in the direction of the average ordering. This space of rotations can be thought of as the topological space SO(2). The order parameter space corresponding to this phase, then, is

SO(3)/SO(2) $\cong S^2$. This procedure allows us to also understand the order parameter space of the intermediate phase: in addition to rotations about a preferred axis being a symmetry, the phase is also invariant under a 180° rotation about any axis perpendicular to the continuous symmetry axis. These transformations together are sometimes called $D_{\infty h}$ (as in, an infinite dihedral group with a horizontal mirror plane). The order parameter space is then SO(3)/$D_{\infty h} \cong S^2/\mathbb{Z}_2 \cong \mathbb{RP}^2$ (the real projective plane). For completeness, the completely disordered phase looks the same under any transformation in SO(3), so its topological order parameter space is the trivial topological space SO(3)/SO(3) $\cong e$ with only one element. This situation, where molecules of a certain symmetry can form nematic phases of a wide variety of intermediate symmetries, is taken to its extreme in nematics that are formed of bent-core molecules. Because the molecules are not very symmetric at all, it is possible for them to form many phases of various intermediate symmetries in their quest to break the order parameter space all the way down to O(3).

Why is characterizing the topological order parameter space of liquid crystals a useful endeavor? It will help us to understand the *topological defects* that arise in the phase. Roughly speaking, a topological defect is a discontinuity in the order parameter field of a material that cannot be removed by local deformations of the order parameter field. These defects are highly stable, since they require a large-scale rearrangement (which constitutes a high energy barrier) or combination with another defect to remove. Perhaps the most well-known defects are vortices in the XY model. I will use this system to illustrate how topological order parameter spaces and homotopy theory are the right tools to describe the existence of and combination rules for topological defects.

The XY model involves vectors of fixed length that are confined to rotate along a single axis. There is an energy functional that prefers local alignment of these vectors, similar to the Ising model. When one performs a dynamical simulation of a finite-size XY model based on the Metropolis algorithm, for low temperature quenches, one does not immediately settle into an ordered phase. First, one sees an intermediate dynamical regime where vortices form, before some of the vortices move together and annihilate due to energetic effects.[1] These vortices are point-like objects where the order parameter field performs a complete twist (or more generally, some integer number of twists). Because the order parameter changes rapidly near the defect "core," these defects have much higher energy than a uniform configuration of the order parameter. However, in order to achieve a uniform configuration from an isolated defect, the system must surmount an even higher energy barrier. In practice, the order parameter field will smooth out under low-temperature quench dynamics by bringing together defects with opposite "twists" that allow the order parameter field to smooth out without creating system-spanning "rifts."

How do we understand what kinds of defects are even possible in the XY model or in more general systems? Abstracting the problem is useful here in generalizing the results to other systems with different kinds of order. Let us start with a two dimensional XY model. We may draw a loop somewhere in the material and track how the order parameter varies as we travel along the loop counter-clockwise. The topological order parameter space in the XY model is the circle S^1. As we traverse the loop in real space, the order parameter changes, and we can follow the path that is being traced out in the topological order

[1]The XY model in two spatial dimensions has no long-ranged order due to the Mermin-Wagner theorem. There is a vortex unbinding BKT transition that separates a phase with exponentially decaying order from a phase with algebraically decaying order. I am not focused on the phase transitions in liquid crystals and other orientationally ordered materials in this thesis.

parameter space S^1. Because we end at the same place we began (it is a loop in real space), the order parameter takes the same value at the beginning and end of the loop, and so the path that is traced out in order parameter space is also a closed loop. We will now focus on the properties of the loops that are induced in order parameter space.

If we have surrounded a portion of the material that is mostly ordered, the order parameter may wiggle slightly on S^1 as we travel along the loop in real space. However, the loop in order parameter space will be mostly localized to a particular portion of the circle $\theta \in [\theta_c - \Delta\theta, \theta_c + \Delta\theta]$ with $\Delta\theta \ll \pi$. In real space, we can imagine smoothing out this configuration into a perfectly ordered configuration in a continuous way by making all of the vectors align to point at θ_c. This procedure also alters the loop that is induced in order parameter space in a continuous way: we contract the loop on S^1 to a single point at θ_c (Figure 7.2). Without thinking about the actual order parameter configuration, then, we see that we can approach complete order in a continuous way for some section of the material when the loop in order parameter space can be smoothly contracted to a point.

In contrast, let's consider the situation where we surround a vortex in real space with our loop (say, one where the vector completes a full rotation counter-clockwise as we traverse the loop counter-clockwise). The loop in the order parameter space now wraps around S^1 once counterclockwise. Unlike in the case of the mostly ordered section of the material, we cannot smoothly contract the loop that wraps around S^1 once counterclockwise to a point, since a point does not wrap around S^1 at all. The number of times this loop winds around S^1 is precisely the *winding number*, and it is topological in the sense that continuous

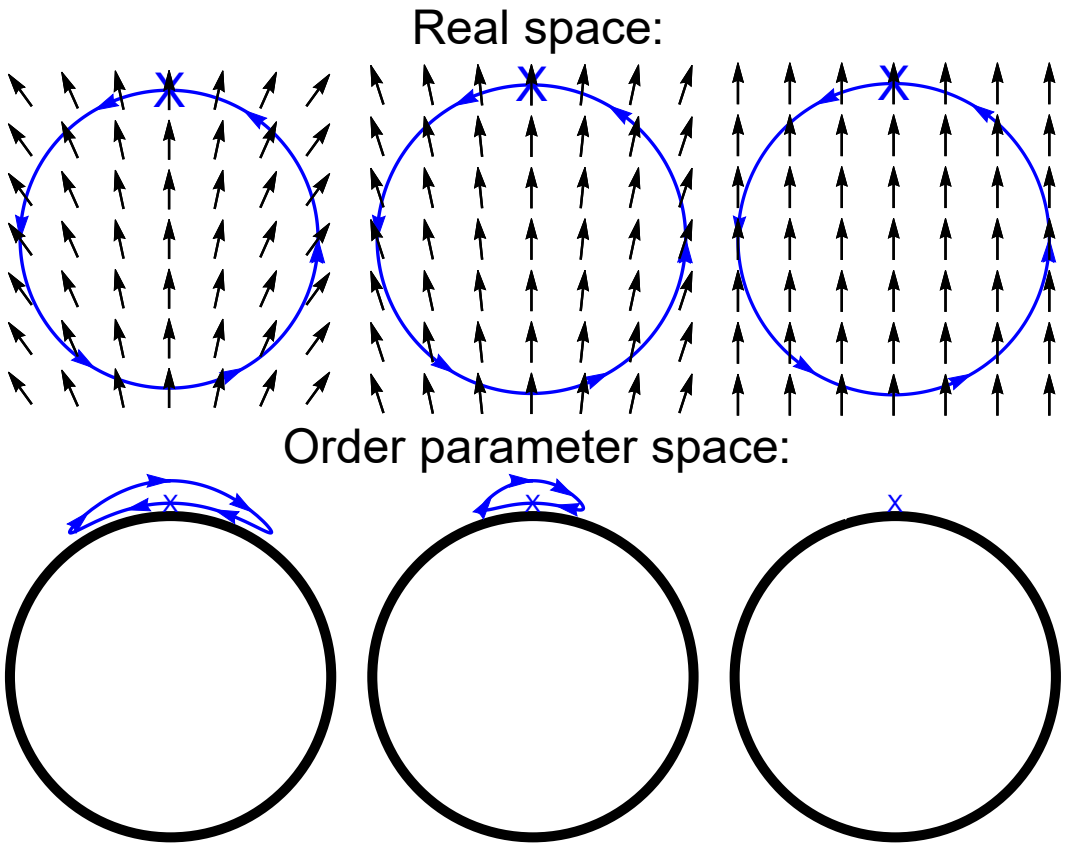

Figure 7.2: In a region with no topological defects, one can smoothly deform the order parameter field to the uniform configuration. In order parameter space, the image of a (real space) labelling loop is smoothly contracted to a point. The curve in order parameter space is offset from S^1 for visualization purposes.

deformations of the loop in S^1 cannot change this number. Any value in $\mathbb{Z}$ is a winding number that gives a label to an isolated vortex defect.[2] The positive values (WLOG) correspond to the number of counter-clockwise rotations of the order parameter field, while the negative values correspond to the number of clockwise rotations of the order parameter field.

[2]In this and other cases, energetics place additional restrictions on conformations that are actually observed. For instance, an isolated defect with winding number +2 may spontaneously split into a pair of +1 defects that are repelled from each other. In this way, it is often the case that only ±1 defects are seen because the system reduces its energy by relieving gradients in the order parameter field near the core by performing these topologically allowed processes. In the absence of these energetic considerations, the fully topological classification scheme is sufficient to classify all defects and their combination rules.

The labelling by winding number has an additional feature: if two loops in order parameter space have the same winding number, then one can deform the loops in order parameter space to be *identical*. This is somewhat hard to visualize in the case of the order parameter space S^1. Imagine we have an isolated defect configuration where the order parameter makes a single counter-clockwise twist in a steady way, with the angle θ of the order parameter being equal to the angle θ_p of a polar coordinate system in real space. This has winding number +1. Next, imagine another isolated defect configuration with angle $\theta = 2\theta_p$ for $0 < \theta_p < \pi$ and angle $\theta = 0$ for $\pi \leq \theta_p \leq 2\pi$. This defect also has winding number +1. One can deform the second configuration to look identical to the first through a smooth deformation of the loop in order parameter space. These two loops are then called *homotopic*. The study of these loops (and generalizations thereof) in topological spaces is called homotopy theory. The machinery of homotopy theory allows us to classify loops in other, more general order parameter spaces. In this case, the fundamental group $\pi_1\left(S^1\right)$ encodes information about loops on S^1. Unsurprisingly, $\pi_1\left(S^1\right) \cong \mathbb{Z}$, so loops are labelled by an integer that represents the number of times they wind around S^1. Loops that share this number are homotopic to each other.

To understand what happens when two topological defects come together, it is useful to imagine the following picture: once the defects are separated by some distance $\sim a$ the lattice spacing, we can no longer practically distinguish one defect from a pair of defects. So let us draw two defects near each other, and surround both of them with a single loop: this is the way we would classify the defect after the pair of defects is brought together. Now deform the loop continuously in real space so that it first surrounds the right defect counter-clockwise, returning to its original position, and then surrounds the left defect

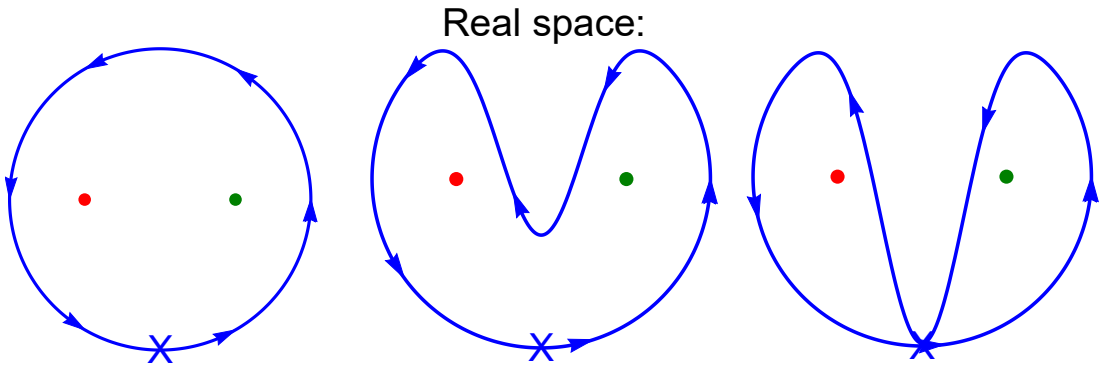

Figure 7.3: A deformation of a labelling loop in real space surrounding a pair of defects. The deformed labelling loop maps to a pair of loops in order parameter space which are traversed in order. The labelling of loops in order parameter space has a group structure under the operation of loop concatenation; this group structure is described by π_1 (OP).

counterclockwise, returning to its original position (Figure 7.3). The combined loop still registers the same topological invariant, since it was continuously deformed and did not pass through any of the defects. But now the loop in order parameter space can be thought as two loops traversed in order: first, a labelling loop for the right defect; next, a labelling loop for the left defect. The two loops in order parameter space can be concatenated since they each begin and end at the same point. For the case of the XY model, if the first loop has a winding number n_1, while the second loop has a winding number n_2, the net loop has winding number $n_1 + n_2$. In addition to the labelling of vortices by $\mathbb{Z}$, the vortices also have combination rules that are given by the group structure $(\mathbb{Z}, +)$.

This is not a coincidence: for a general topological space OP, the fundamental group π_1 (OP) is a *group*, with elements and a rule for combining them. The elements in the group are given by the different classes of homotopically distinct loops emanating from a single point[3] in the order parameter space. The group

[3]This point is arbitrary but must be the same starting and ending point for all loops in the classification procedure.

operation is given by the labelling of a loop formed by sequential concatenation of a pair of loops. In the case where the fundamental group of the order parameter space is non-abelian, the labelling and description of combinations of defects is significantly more complicated. Already one can foresee problems with the generalization of the procedure in the XY model: if I bring together a defect labelled by g_1 and a defect labelled by g_2, do I recover an element $g_1 g_2$ or an element $g_2 g_1$? In fact, the unambiguous labelling of topological defects by elements of the fundamental group does not extend to the case where the fundamental group is non-abelian.

The first step to resolving this issue is in identifying a deficiency in the labelling procedure for loops in topological spaces. We call two topological defects identical if we can smoothly deform one into the other (in real space). If we surround a defect with a loop and perform this deformation, the induced loop in order parameter space can continuously wiggle around any way it likes, and it is not necessary for any part of the loop to remain fixed in order parameter space. This is called a *free* homotopy of loops. In contrast, the labelling that the fundamental group describes is for a *based* homotopy of loops. In order to define the operation of loop concatenation that gives rise to the group structure, all loops must start and end at the same point. This based homotopy can miss the fact that two loops can be freely homotopic to each other. Two loops may be freely deformed into each other, but this deformation may require the base point to be detached. This distinction only occurs in spaces that have a non-abelian homotopy group.[4]

Before we look at the specifics, note two facts: (1) A loop traced backwards is assigned the inverse group element of a loop traced forwards, since the net

[4] A great example is for the figure-eight space, which is the plane with two holes.

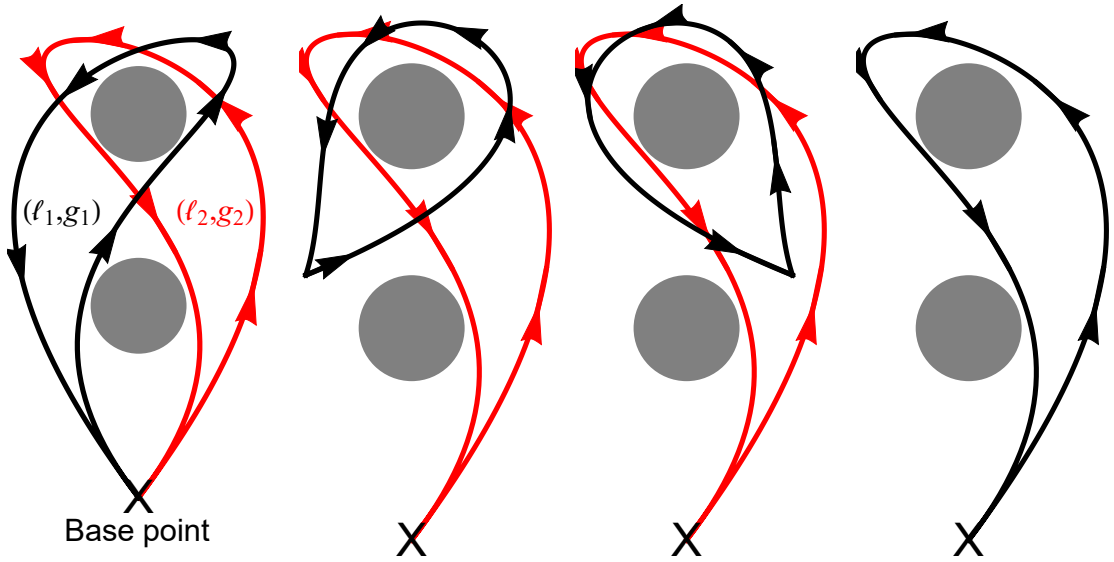

Figure 7.4: In the so-called figure-eight space (the plane with two holes), loops can be freely homotopic but not homotopic based at X. Shown is a free homotopy that transforms loop ℓ_1 into loop ℓ_2. There is no continuous way to make these loops equivalent without detaching them from their base point. This is an indicator that π_1 of this space is non-abelian.

loop formed by tracing these loops in succession can be contracted to a point. (2) Loop concatenation at the base point gives a product structure. One must be consistent with the choice of right or left multiplication in the group. We will take consecutive loop concatenations to represent right multiplication in the group, so that tracing out (ℓ_1, g_1) followed by (ℓ_2, g_2) gives the loop $(\ell_1\ell_2, g_1g_2)$.

So how do we label topological defects when the fundamental group of the order parameter space is non-abelian? In some sense, the labelling by elements of the fundamental group is too restrictive, since loops that are freely homotopic may be assigned different elements of the fundamental group. However, they do still share a feature, which I will now illustrate. Suppose we have two loops (ℓ_1, g_1) and (ℓ_2, g_2) that are freely homotopic to each other. This means that we can make ℓ_1 look identical to ℓ_2 if we allow for arbitrary continuous deformation of ℓ_1 (see Figure 7.4).

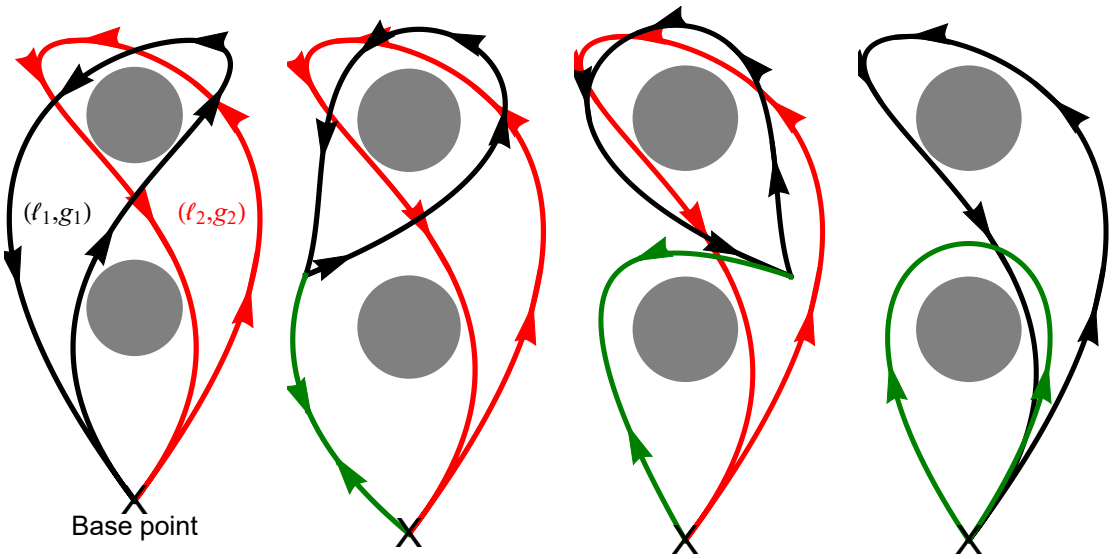

Figure 7.5: The free homotopy illustrated in Figure 7.4 is easily converted to a based homotopy. We imagine first leaving the base point along the dark green curve, then traversing the black loop, and then travelling backwards along the dark green curve. Once the free homotopy is complete, the dark green curve becomes a pair of loops that start and end at the base point that have tracked the motion of the base point under the free homotopy.

After this deformation is performed, we can inspect what happened to the base point. Because ℓ_2 starts and ends at the base point, we can draw a continuous path for the base point that starts and ends at the original location of the base point (so that it is a loop – call it (ℓ_3, g_3)) (see Figure 7.5).

If ℓ_1 and ℓ_2 could be deformed into each other without moving the base point, then ℓ_3 is contractable to a point, and $g_1 = g_2$ since ℓ_1 and ℓ_2 are equivalent under based homotopy. In contrast, if ℓ_3 is homotopically nontrivial, then ℓ_1 and ℓ_2 are assigned different elements of the fundamental group even though they are freely homotopic. However, if we first "undo" the tangling of the base point (trace out ℓ_3), then trace out ℓ_2, and then "redo" the tangling of the base point (trace out ℓ_3 backwards), we recover a loop that is in the same *based* homotopy

class as ℓ_1. From the multiplication structure of the group, this means that

$$g_3 g_2 g_3^{-1} = g_1 \tag{7.1}$$

where g_1 and g_2 represent the group elements assigned to the loops that are freely homotopic and g_3 is the group element assigned to the loop representing the trajectory of the base point in the path that deforms ℓ_1 into ℓ_2. The element g_3 can be any element of π_1 (OP). Two elements of a group g_1 and g_2 that are related in this way are said to be in the same *conjugacy class*. Hence, conjugacy classes of the fundamental group label topologically distinct defects.[5] Conjugacy classes partition groups. To understand how two defects combine, we must define an operation on conjugacy classes. The natural way this is done is as follows: for two conjugacy classes C_1 and C_2, generate the multiset $C_1 * C_2$ of all pairwise products $g_1 g_2$ where $g_1 \in C_1$ and $g_2 \in C_2$, including duplicate group elements. If C_1 has N_1 elements and C_2 has N_2 elements, then $C_1 * C_2$ will always have $N_1 \times N_2$ elements.

The elements in $C_1 * C_2$ can always be written as a combination of several conjugacy classes from the original group. Why? Suppose $g_1 g_2$ is in the set $C_1 * C_2$. We want to be sure that an arbitrary conjugate group element g_c is also in $C_1 * C_2$. Because g_c is conjugate to $g_1 g_2$, there is an element g_3 such that $g_3 g_1 g_2 g_3^{-1} = g_c$. Because C_1 is a conjugacy class, $g_3 g_1 g_3^{-1} \in C_1$. Because C_2 is a conjugacy class, $g_3 g_2 g_3^{-1} \in C_2$. Taking the product of these elements gives g_c, so $g_c \in C_1 * C_2$. This procedure further shows that $C_1 * C_2$ as a multiset can be partitioned into conjugacy classes, with the possibility of complete conjugacy class appearing multiple times. Hence one can write operations like $C_1 * C_2 = 4C_3 + C_4$. Note that a requirement for this statement to be true is that $N_1 \times N_2 = 4N_3 + N_4$ – this gives

[5] For an abelian group, each element represents its own conjugacy class, so it is sufficient to label defects by elements of the group itself.

a simple sanity check for the tedious group theoretic calculations performed by simply counting the number of elements in each conjugacy class. Finally, one can show that $C_1 * C_2 = C_2 * C_1$ so that this operation is commutative: if $g_1 g_2 \in C_1 * C_2$, then it is also in $C_2 * C_1$ since $g_1 g_2 = \left(g_1 g_2 g_1^{-1}\right) g_1 \in C_2 * C_1$.

This operation has physical relevance. When multiple conjugacy classes appear on the right-hand side of the operation, such as in $C_1 * C_2 = 4C_3 + C_4$, this means that upon bringing a defect of type 1 and type 2 together, the resulting defect depends upon the specifics of the way in which the defects are brought together. We may end up with a defect of type 3 or of type 4, depending upon the other defects living in the local environment that the defects are being dragged through. A classic example of this arises in orthorhombic biaxial nematics, which can be thought of as the most ordered phase of right rectangular prism molecules with three nonequal side lengths. A defect can be formed by a π rotation about an axis passing through one of the faces (call the normal to this face $\hat{x}$). A topologically equivalent defect is formed by a $-\pi$ rotation about the same axis.[6] If one brings together defects registering locally as π and $-\pi$ rotations about the same axis, they will annihilate and give the completely ordered configuration. However, if one brings together two defects locally registering as $+\pi$, one gets a defect that represents a complete 2π swirl of the order parameter field which cannot be untangled. The order parameter space for this phase is $\mathrm{SO}(3)/D_2$, and $\pi_1(\mathrm{SO}(3)/D_2) \cong \mathbb{H}$, the quaternions. The conjugacy classes of $\mathbb{H}$ are (using the Pauli matrix representation):

$$C_0 = \{1\}, \quad \overline{C_0} = \{-1\}, \quad C_x = \{\pm i\sigma_x\}, \quad C_y = \left\{\pm i\sigma_y\right\}, \quad C_z = \{\pm i\sigma_z\}. \tag{7.2}$$

The conjugacy class multiplication table is shown in Table 7.1.

[6] The deformation that takes these two defects into each other is the classic "escape into the third dimension."

	C_0	$\overline{C_0}$	C_x	C_y	C_z
C_0	C_0	$\overline{C_0}$	C_x	C_y	C_z
$\overline{C_0}$	$\overline{C_0}$	C_0	C_x	C_y	C_z
C_x	C_x	C_x	$2C_0 + 2\overline{C_0}$	$2C_z$	$2C_y$
C_y	C_y	C_y	$2C_z$	$2C_0 + 2\overline{C_0}$	$2C_x$
C_z	C_z	C_z	$2C_y$	$2C_x$	$2C_0 + 2\overline{C_0}$

Table 7.1: The conjugacy class multiplication table for an orthorhombic biaxial nematic phase.

The relevant entry for bringing together two C_x defects is $C_x * C_x = 2C_0 + 2\overline{C_0}$. This means that, depending upon the way these defects are brought together, we may end up with a trivial configuration C_0 or a full twist $\overline{C_0}$. More details on how braiding of defects is related to conjugation by certain group elements is contained in the manuscript for the case of phases with trihedral symmetry.

In the following manuscript, I wrote all parts except for the beginning of the Introduction. I performed the group-theoretic calculations necessary to understand the braiding and fusion rules in the different symmetry-allowed phases. I also generated all figures, and came up with general ways to draw defects in liquid crystals whose symmetries form a point group of SO(3). Leo Radzihovsky assisted in writing the Introduction giving broader context to the classification and its relevance and taught me about the exotic Landau theories needed to understand interesting orientational order. This project came into existence after a conversation that we had at the Boulder School 2022: Hydrodynamics Across Scales.

7.2 Topological defects in nematic phases of bent-core liquid crystals

This section is a reformatted version of a manuscript to be submitted to Physical Review E.

7.2.1 Abstract

Motivated by a growing family of bent-core liquid crystals – "bananas" and twist-bent heliconical nematics – that require higher orientational order parameters to characterize their spontaneous chiral and other novel fluid phases, we systematically classify and study their topological defects utilizing the machinery of homotopy theory. In addition to the exhaustive classification, focusing on the optically isotropic tetrahedratic phase characterized by a third rank tensor, we demonstrate that it exhibits non-abelian topological defects that may help to identify this otherwise elusive order. Our defect classification complements the earlier Landau order-parameter, symmetry breaking characterization of banana fluid phases [181].

7.2.2 Introduction

Driven predominately by competing entropic effects, liquid crystals exhibit a rich variety of phases that spontaneously break spatial symmetries that are intermediate between a fully disordered homogeneous and isotropic fluid and a three-dimensional crystal. Studies of spontaneously anisotropic fluid phases of

conventional calamitics and discotics were launched by Reinitzer's 1890s discovery of cholesterics and are well-characterized by a rank-2 traceless symmetric tensor capturing their dielectric tensor and associated optical anisotropy. Synthesis of new molecular materials has driven a steady discovery of novel liquid crystalline phases. These include a rich variety of spontaneously chiral ferroelectric states of bent-core "banana" [182, 183, 184, 185, 186, 187, 188, 189, 190, 191] and heliconical (twist-bend) nematics [192, 193, 194, 195, 196, 197], a holy grail of basic scientific exploration and crucial to liquid crystal display technology.

Such bent-core liquid-crystalline fluids have been extensively studied by Lubensky and Radzihovsky [181, 198] who exhaustively characterized them by Landau symmetry breaking and associated tensor order parameters, summarized in Fig. 7.7. In addition to reproducing conventional uniaxial and orthorhombic biaxial nematics, they also discovered a variety of novel fluid phases, such as the optically isotropic tetrahedratic T phase, characterized by a nonzero symmetric third-rank tensor (angular momentum $\ell = 3$) order parameter and its nematically ordered N_T (neither uniaxial nor biaxial, but rather exhibiting a 4-fold improper S_4 rotational symmetry about its nematic axis) and spontaneously chiral $(N_T + 2)^*$ cousins.

Such a Landau order-parameter classification from the disordered high-temperature side is a powerful approach that is a starting point for treatment of the associated phase transitions into the ordered phases. Complementarily, states and phase transitions can also be characterized from the ordered low-temperature side in terms of the associated Goldstone modes and corresponding topological defects. This is the quest we undertake in the current work.

Namely, utilizing the powerful machinery of homotopy theory, we fully classify the topological defects in the nematic phases of bent-core molecules summarized in Fig. 7.7. One of the most interesting findings of our work is new non-abelian defects and fusion rules that appear in the tetrahedratic T and trihedral $N + 3$ phases.

Following this Introduction, in Section 7.2.3, we review the symmetry-allowed phases for the bent-core liquid crystals. In Sections 7.2.4 and 7.2.5, we review the non-abelian defect classification procedure in orthorhombic biaxial nematics, along with our methods for drawing representative defects for systems with orientational order. Several of the allowed phases of a liquid crystal formed of banana molecules have the same symmetries (and hence the same topological defects) as the fully ordered phase of orthorhombic biaxial nematics. In Section 7.2.6, we identify the defects in all nematic phases of the bent-core liquid crystal, focusing on the triadic and tetrahedratic phases, and write out their combination rules. Exhaustive classification of defects and combination rules in all phases is confined to the supplemental information.

7.2.3 Phases and their symmetries

Table 7.2 lists the phases we consider, their symmetries, and the nonvanishing order parameters that characterize them, with notation inherited from [181]. This list includes phases with all symmetries that can be constructed from the order parameters p^i, Q^{ij}, and T^{ijk} except for the lowest-symmetry phase with C_1 symmetry, which we do not consider (but this phase would have the same topological line and point defects as the $N + V$ phase). All other point-group

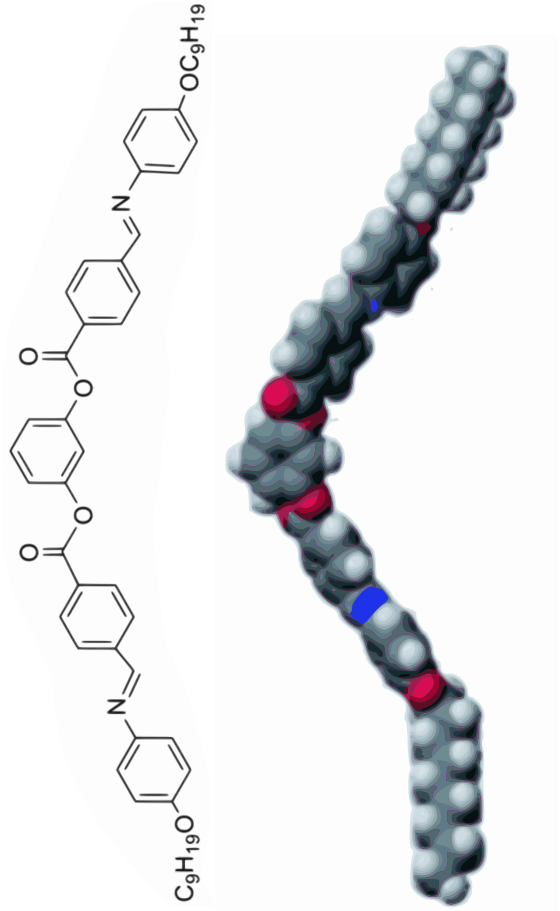

Figure 7.6: **Image of a bent-core NOBOW molecule.** Instantaneously, a molecule can be found in a chiral nonplanar configuration (as shown on the right), but it fluctuates equally between chiralities. On average it is planar and therefore achiral. The condensed phases of these planar bent-core molecules can break a wide variety of symmetries unrelated to the symmetries of the constituent molecules.

symmetries including cubic, icosahedral, simple tetrahedral (T), and even lower symmetries such as S_2, C_3, and C_{2h} cannot be characterized without the introduction of 4th- or higher-rank tensor order parameters. As is customary, we denote the Isotropic phase by I and the Nematic phase by N. The N phase has $D_{\infty h}$ symmetry, and it is completely characterized within the space of p^i, Q^{ij}, and T^{ijk} by the single uniaxial order parameter S. In general, the N phase will also have nonvanishing components of all even rank tensors (explicitly induced

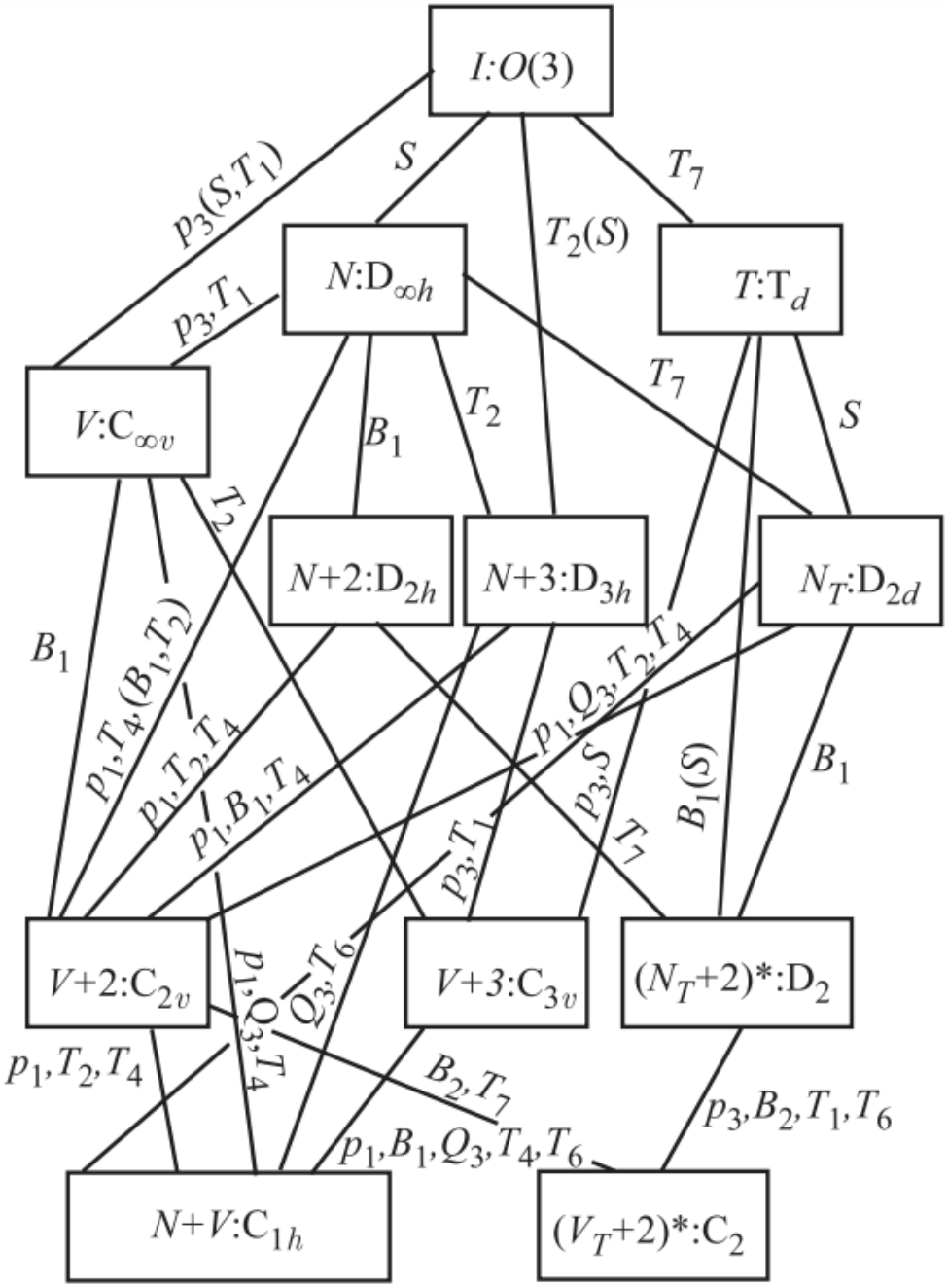

Figure 7.7: **A flowchart capturing phases and phase transitions** between liquid crystal phases of banana molecules, reproduced from [181]. Order parameters which become nonzero at each of the transitions are indicated, as well as the symmetry groups of each phase. Order parameters in parentheses also become nonzero due to nonlinear couplings.

Phase	Symmetry	Order Parameter	Connected OP Space	π_1	π_2
V	$C_{\infty v}$	p_3, S, T_1	$SO(3)/C_\infty \cong S^2$	0	$\mathbb{Z}$
N	$D_{\infty h}$	S	$SO(3)/D_\infty \cong \mathbb{R}P^2$	$\mathbb{Z}_2$	$\mathbb{Z}$
$N+2$	D_{2h}	S, $\boldsymbol{B}_{1,2}$	$SO(3)/D_2$	$\mathbb{H}$	0
$N+3$	D_{3h}	S, $\boldsymbol{T}_{2,3}$	$SO(3)/D_3$	Dic_3	0
T	T_d	$\boldsymbol{T}_{6,7}$	$SO(3)/T$	$2T$	0
N_T	D_{2d}	S, $\boldsymbol{T}_{6,7}$	$SO(3)/D_2$	$\mathbb{H}$	0
$(N_T+2)^*$	D_2	S, B_1, T_6, T_7	$SO(3)/D_2$	$\mathbb{H}$	0
$V+2$	C_{2v}	p_3, S, B_1, T_1, T_6; or p_1, S, B_1, T_2, T_4	$SO(3)/C_2$	$\mathbb{Z}_4$	0
$V+3$	C_{3v}	p_3, S, T_1, $\boldsymbol{T}_{2,3}$	$SO(3)/C_3$	$\mathbb{Z}_6$	0
$(V_T+2)^*$	C_2	p_3, S, B_1, T_1, T_6, T_7; or p_1, S, B_1, T_2, T_4, T_5	$SO(3)/C_2$	$\mathbb{Z}_4$	0
$N+V$	C_{1h}	p_1, p_3, S, B_1, Q_3, T_1, T_2, T_4, T_6	$SO(3)$	$\mathbb{Z}_2$	0

Table 7.2: Anisotropic liquid phases of banana-shaped molecules, their symmetries in the Schoenflies notation, and their nonvanishing order parameters. The notation for the order parameters ($\boldsymbol{B}_{1,2}$, etc.) is inherited from [181] as the amplitude in a basis expansion of the tensors that enter the Landau free energy. Some of the phases, such as the $N+V$ phase, can be characterized by other sets of symmetry-equivalent order parameters, involving, for example, linear combinations of p_1 and p_2 rather than p_1 alone. For the enumeration of the order parameter space, we work directly with the connected component SO(3) so domain walls that are allowed between chiral phases are ignored. The first and second homotopy groups, π_1 and π_2, are related to the labelling of and combination rules for line and point defects in three dimensions, respectively.

through $\mathrm{Tr}(Q^n T_{2n})$ coupling), but we will ignore them, focusing on the nontrivial order parameters of rank 3 or less that actually drive the ordering transitions. There is a phase with vector or, equivalently, $C_{\infty v}$ symmetry, which we denote by V. The predominant order parameter of this phase is the vector $\mathbf{p}$, which we take to be along $\mathbf{n}$ (i.e., nonzero p_3). Once p_3 orders, it explicitly induces S and T_1 order parameters, through the $p^i p^j p^k T^{ijk}$ and $p^i p^j Q^{ij}$ couplings, respectively.

One crucial point, relevant for the Goldstone modes in each of the phases, is that only the vector-ordered V phase and the uniaxial nematic N phase have a continuous part of their symmetry group. The Goldstone modes in these cases

are well-known as spin waves as they differ from each other only by an additional broken discrete symmetry. A hydrodynamic theory of general biaxial nematics with all three rotational symmetries broken [199] describes the dynamics of the Goldstone modes of each of the other liquid phases retaining only discrete symmetry subgroups of SO(3).

7.2.4 Homotopy theory of defects

The homotopy theory of topological defects has been successful in describing classes of nonequivalent defects and how they combine in systems that have exotic order parameter spaces. By surrounding a discontinuity in the order parameter field with two points (for π_0), a curve (for π_1), or a surface (for π_2), one finds a mapping to the corresponding hypersurface in the order parameter space. If the hypersurface induced in the order parameter space can be contracted to a single point, then the configuration in real space can be smoothly patched without tearing the order parameter field. Otherwise, the labelling (for π_0) or the assigned group element (for $\pi_{n\geq 1}$) is related to the character of the defect and indicates how it interacts with other defects.

Focusing on the fundamental group, π_1, we are able to label point defects in two spatial dimensions or line defects in three spatial dimensions. When the fundamental group is abelian, one can label the defects by elements of the fundamental group and find addition rules for bringing defects together. For the XY model in two spatial dimensions, the point defects are vortices. The order parameter space of the set of two-dimensional vectors of unit length is S^1, and $\pi_1\left(S^1\right) = \mathbb{Z}$, which is abelian. This means that vortices are measured by their

"charge," and add as the integers do. If π_1 is non-abelian, however, the defects are labelled and interact in a more complicated way [180]. The abiguity of multiplication order is fixed by a labelling of defects according to the *conjugacy classes* of the fundamental group, and the defect resulting from the combination of two defects depends upon the path by which they are brought together. Perhaps the best-known example of this occurs in orthorhombic biaxial nematics, where π rotational defects about the three nonequivalent perpendicular axes interact in interesting ways.

The labelling by conjugacy classes of the fundamental group arises from the differences between *based* and *free* homotopies of loops. If we privilege a point in the order parameter space (a *reference configuration* of our liquid crystal molecule), and ask whether loops are homotopic keeping the reference configuration fixed, we find the based homotopy group, which is isomorphic to the fundamental group of the space independent of which point we choose to privilege. Physical topological defects are considered equivalent if one can be smoothly deformed into the other, *without* the restriciton of keeping a particular point with fixed orientation; this deformation corresponds to a *free* homotopy of loops in the order parameter space. Two loops in order parameter space are *freely* homotopic (and hence correspond to the same type of physical topological defect) if their fundamental group elements lie in the same conjugacy class [180]. In the special case of an abelian fundamental group, the conjugacy classes are the group elements themselves, and so we can label defects with group elements.

To identify the order parameter space of a liquid crystal allowed to rotate in three dimensions, one typically begins with the full space group of distance-

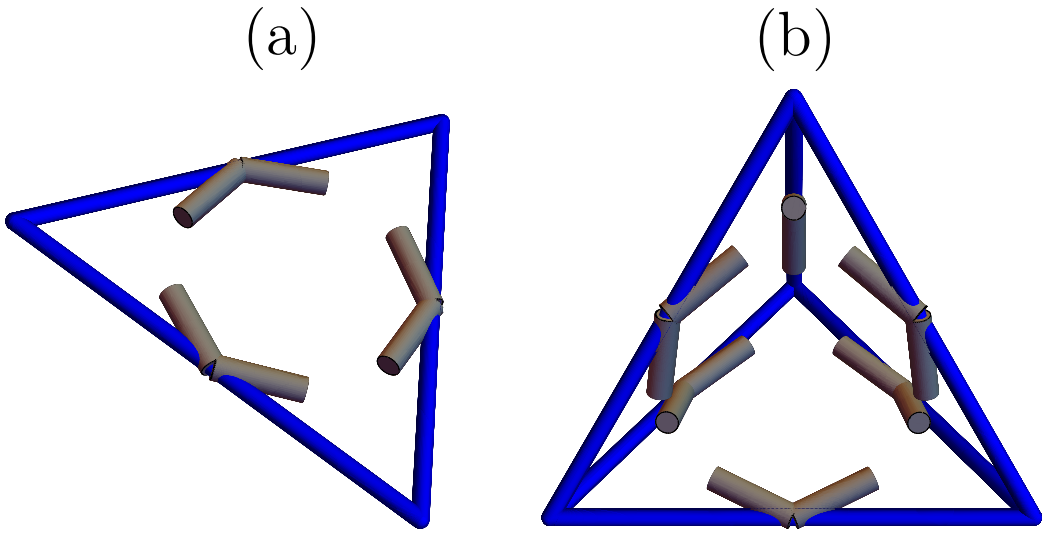

Figure 7.8: **A visualization of banana molecules condensing** into (a) the $N + 3$ phase and (b) the T phase. Each of these phases has a non-abelian first homotopy group characterizing the line defects, which leads to path-dependence in the combination rules.

preserving transformations in three dimensions, O(3). O(3) has two disconnected components. These are relevant for π_0, which is used to classify domain walls in chiral liquid crystals. After identifying domain walls, it suffices to work with a single connected component (SO(3)) as one can parameterize continuous paths around other types of isolated defect. The order parameter space of the liquid crystal can be written as the quotient space SO(3)/M, where M is the group of rotational symmetries of the liquid crystal phase in question. In the continuum theory, each point in the space corresponds to a unique orientation of an object with symmetry group M, given a reference configuration (the identity in SO(3)/M). In the case of the banana molecules, different types of ordering can arise that break spatial symmetries, characterized by the invariant space M. For example, in the Tetrahedratic T-phase, the bent-core molecules order to lie on the edges of tetrahedra (as illustrated in Fig. 7.8(b)), and so this phase has a symmetry that is the full tetrahedral point group T_d.

Computing the homotopy groups of defects whose symmetry group is a point subgroup of SO(3) is straightforward. Following [180], one lifts SO(3) to its universal cover SU(2), and the point subgroup P to its corresponding *double group* $2P$. Then, using the fundamental theorem on the fundamental group, the fundamental group is the double group itself:

$$\pi_1\left(\mathrm{SO}(3)/P\right) \cong \pi_1\left(\mathrm{SU}(2)/2P\right) \cong 2P. \tag{7.3}$$

When the fundamental group is discrete, the higher homotopy group π_2 is trivial [180], and there are no topologically stable point defects in three dimensions. This is the case for all nematic phases of the banana liquid crystal except for the vector phase and the uniaxial nematic phase, both of which have well-understood point and line defects. A more complete elaboration of this procedure will be laid out for the orthorhombic biaxial nematic phase in the next section.

Taking inspiration from the labelling of loops in based homotopy classes, one can draw representatives of each type of defect in real space by parameterizing a smooth path in SU(2) from the identity to the element in $2P$ representing the defect label, and then applying the corresponding element in SO(3) (via the two-to-one homomorphism identifying $u\left(\hat{n},\theta\right) = \exp\left(i\left(\theta/2\right)\hat{n}\cdot\sigma\right) \in \mathrm{SU}(2)$ with the rotation matrix $R\left(\hat{n},\theta\right) \in \mathrm{SO}(3)$) to the reference configuration along a closed path in real space surrounding the defect. Specifically, suppose we would like to draw a point defect in two dimensions labeled by an element $p = u\left(\hat{n}_p,\theta_p\right) \in 2P$. Using polar coordinates in real space, we can create an order parameter field that is continuous everywhere except for the origin by applying the rotation matrix $R\left(\hat{n}_p,\theta_p \times \left(\theta/2\pi\right)\right)$ to each molecule located at a point (r,θ) in real space. Then loops surrounding the origin starting and ending at the reference configuration would measure a defect of value p.

For liquid crystals that have order parameter spaces with a non-abelian fundamental group, defects can change their character (the homotopy group element which they are assigned) as they are braided around other defects if one does not keep the labelling loop consistent. A visual description of this can be seen in Figure 7.9. As one braids one defect around another, the measurement path with respect to the reference configuration is smoothly deformed to wind around one of the defects. Specific examples of this will be shown in the biaxial phases, the tetrahedratic T-phase, and the triadic $N + 3$ phase.

7.2.5 Warmup: orthorhombic biaxial nematics

Perhaps the most well-known example of a liquid crystalline molecule that has non-abelian topological defects is the orthorhombic biaxial nematic. Because this is also a symmetry of several of the phases of the liquid crystal comprised of bent-core molecules ($N + 2$, N_T, $(N_T + 2)^*$), it is instructive to enumerate and illustrate these topological defects in a way that extends naturally to the defects in the phases with more interesting broken discrete symmetry groups.

Isolated defect classification and drawing representatives

One can represent these molecules as rectangular prisms with three nonequal sides. The symmetry group of this molecule, considered as a subgroup of SO(3), is the dihedral point group D_2. This group is abelian and has the following group presentation:

$$D_2 = \left\langle \alpha,\ \beta \middle| \alpha^2 = \beta^2 = (\alpha\beta)^2 = 1 \right\rangle. \tag{7.4}$$

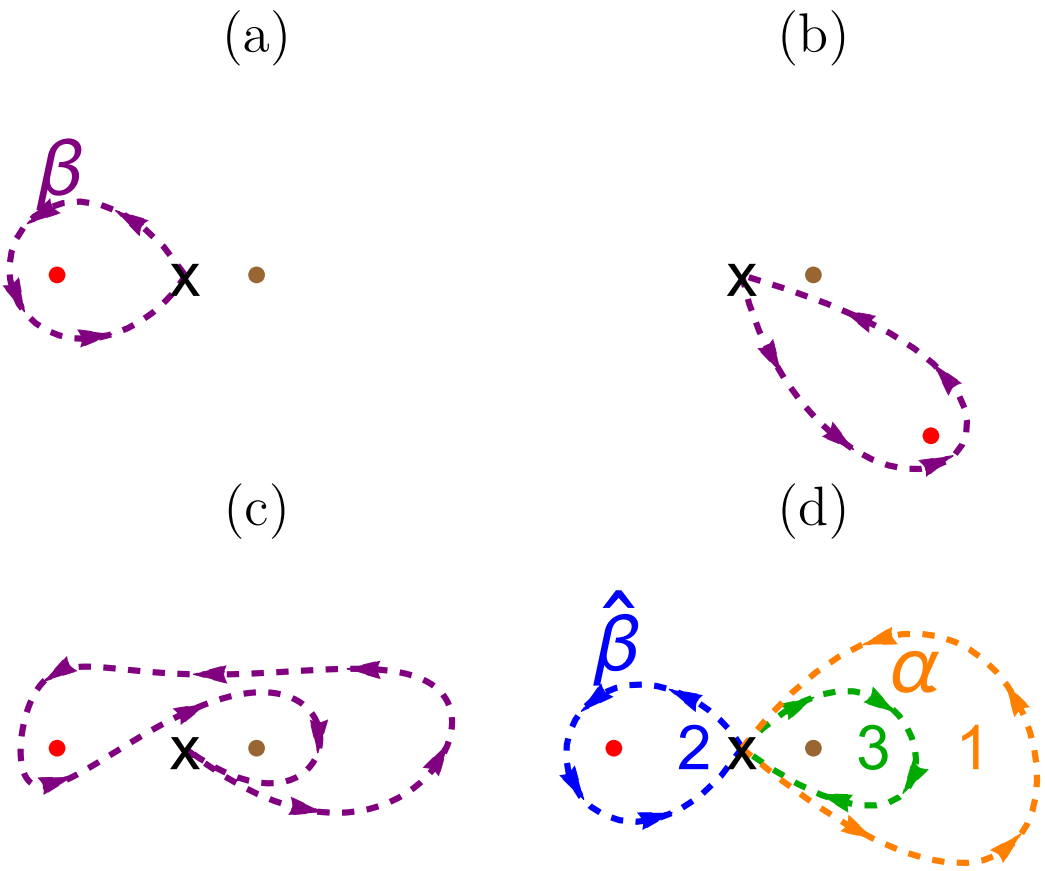

Figure 7.9: **A demonstration of the result of braiding** two defects that is valid in systems with abelian or non-abelian fundamental groups. A red point defect is wound around a brown point defect in two dimensions while the order parameter field at the base point **X** is kept fixed as a reference configuration. (a) The purple path winding counterclockwise around the red defect measures a defect with group element $\beta \in \pi_1$ (OP), where OP is the order parameter space. (b – c) As the red defect is looped around the brown one, all changes in the order parameter field are continuous. The loop is assigned group element β at all times. (d) the purple path is deformed into three paths that all start and end at the base point **X**, traversed in order $1 \to 2 \to 3$. Since the full path is assigned homotopy group element β, we have that $\beta = \alpha\widehat{\beta}\alpha^{-1} \implies \widehat{\beta} = \alpha^{-1}\beta\alpha$, where $\alpha \in \pi_1$ (OP) is the group element measured for the brown defect. $\widehat{\beta}$ and β are hence in the same conjugacy class, but may be different group elements in a non-abelian group.

The order parameter space of the liquid crystal is then $\mathrm{SO}(3)/D_2$. To compute the first homotopy group using the fundamental theorem on the fundamental group, we first lift the point group $D_2 \subset \mathrm{SO}(3)$ to its corresponding *double* group $2D_2 \subset \mathrm{SU}(2)$. This is done in a straightforward way from the perspective of the group presentation:

$$2D_2 = \left\langle \alpha,\, \beta \middle| \alpha^2 = \beta^2 = (\alpha\beta)^2 = -1 \right\rangle. \tag{7.5}$$

We now see immediately that, making the identifications $\alpha \to -i\sigma_x$ and $\beta \to -i\sigma_y$, $2D_2 \cong \mathbb{H}$, the quaternions. Completing the calculation, one has

$$\pi_1\left(\mathrm{SO}(3)/D_2\right) \cong \pi_1\left(\mathrm{SU}(2)/\mathbb{H}\right) \cong \mathbb{H}. \tag{7.6}$$

Because the fundamental group π_1 is discrete, $\pi_2\left(\mathrm{SO}(3)/D_2\right) = 0$ and there are no nontrivial point defects allowed in three dimensions for the orthorhombic biaxial nematic phases [180]. Because $\pi_1\left(\mathrm{SO}(3)/D_2\right)$ is non-abelian, the physical defects are labelled by conjugacy classes of the fundamental group to keep the labelling consistent for arbitrary labelling loops (see Figure 7.9). The conjugacy classes of $\mathbb{H}$ are

$$\begin{aligned} &C_0 = \{1\}, \quad \overline{C_0} = \{-1\}, \\ &C_x = \{\pm i\sigma_x\}, \quad C_y = \left\{\pm i\sigma_y\right\}, \quad C_z = \{\pm i\sigma_z\}. \end{aligned} \tag{7.7}$$

Although these conjugacy classes have been suggestively labelled, it can often be difficult to visualize these defects when the fundamental groups are more exotic. The following procedure (illustrated in Figure 7.10) for drawing representative defects will work for any point subgroup of SU(2). First, choose a reference configuration of a liquid crystal molecule. In this case, we choose a rectangular prism to have the $\hat{x}$, $\hat{y}$, and $\hat{z}$ axes normal to the small, medium, and large faces by surface area, respectively (Figure 7.10(c)). Then, choose a defect label

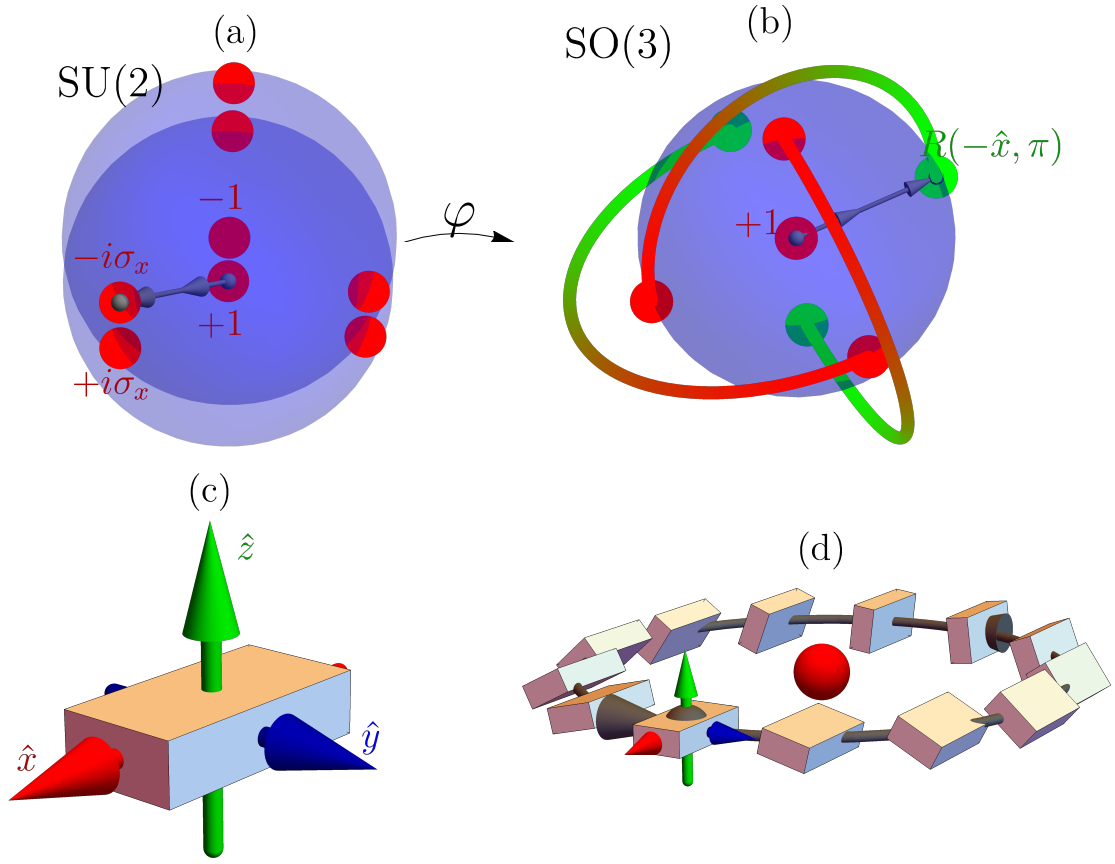

Figure 7.10: **A procedure for drawing defects** labelled by elements in SU(2), for the particular example of orthorhombic biaxial nematics. (a) SU(2) with the eight points in $2D_2 \cong \mathbb{H}$ labelled in red. A path is parameterized in SU(2) connecting the identity to $-i\sigma_x$. Because $-i\sigma_x \in \mathbb{H}$, this is a closed loop in SU(2)/$\mathbb{H}$. (b) SO(3) with the four points in D_2 labelled in red and green. The red and green points that are connected by a red-green curve are the same transformation in SO(3). Under the two-to-one homomorphism φ, the parameterized path in SU(2) is mapped to a path in SO(3). Because $-i\sigma_x \in 2D_2$, $\varphi(-i\sigma_x) \in D_2$. This means that the path is also a closed loop in SO(3)/D_2, the order parameter space. (c) The chosen reference configuration for the orthorhombic biaxial nematic has the unit normals for the small, medium, and large sides parallel to the $\hat{x}$, $\hat{y}$, and $\hat{z}$ axes, respectively. (d) The defect is drawn by applying the rotations along the curve in (b) to the reference configuration in (c) as we wind around a closed loop in real space. This could be thought of as a loop encircling a point defect in two dimensions or a line defect core in three dimensions.

in the fundamental group: we will choose $-i\sigma_x \in \pi_1(\mathrm{SO}(3)/D_2)$ for this demonstration. We parameterize a path in SU(2) from the identity element 1 to $-i\sigma_x$. Because each element in SU(2) can be written as $u(\hat{n}, \theta_{\mathrm{OP}}) = \exp(i(\theta_{\mathrm{OP}}/2)\,\hat{n}\cdot\sigma)$, a natural choice of path is to fix $\hat{n}$ and vary θ_{OP} from 0 to $\theta_{\mathrm{OP}}^{\max} > 0$. Here the subscript OP means that this angle refers to rotation angles in the order parameter space. In this case, we can take $\hat{n} = -\hat{x}$ and $\theta_{\mathrm{OP}} \in [0, \pi]$ (Figure 7.10(a)).

This path in SU(2) can be projected down to a distinct path in SO(3) using the two-to-one homomorphism φ from SU(2) to SO(3) that identifies $u(\hat{n}, \theta_{\mathrm{OP}})$ with the rotation $R(\hat{n}, \theta_{\mathrm{OP}})$ about the axis $\hat{n}$ counterclockwise by an angle θ_{OP}. By construction, the projected path will begin at the identity element of SO(3) and end at an element of D_2, which must also be the identity in the quotient space $\mathrm{OP} = \mathrm{SO}(3)/D_2$. In this way, elements of $\pi_1(\mathrm{OP})$ can be used to draw loops of certain homotopy classes in OP (Figure 7.10(b)).

Finally, one can draw a point defect corresponding to $-i\sigma_x$ in real space as follows: take the closed loop in $\mathrm{SO}(3)/D_2$ and dilate the "time" coordinate θ_{OP} so that it varies from 0 to 2π while tracing out the same path in $\mathrm{SO}(3)/D_2$. One now has a continuous mapping from $\theta \in [0, 2\pi]$ to rotation matrices. Draw a field of molecules that begin all in the reference configuration. Then to each molecule at physical space polar coordinate (r, θ), $\theta \in [0, 2\pi]$, apply the rotation matrices that are parameterized along the loop in $\mathrm{SO}(3)/D_2$. In this example, this means applying the rotation matrix $R(-\hat{x}, \theta/2)$ to each molecule at physical space polar coordinate (r, θ). The result of this is the expected 180° swirl clockwise about $\hat{x}$ (Figure 7.10(d)).

Because the fundamental group is non-abelian, this drawn defect should be labelled a C_x defect. If one follows the same procedure, starting with $+i\sigma_x$, then

one would get a defect that swirls about the same axis but in the opposite direction. The fact that $\pm i\sigma_x$ both belong to the conjugacy class C_x tells us directly that these defects can be smoothly deformed to look like each other (via "escape into the third dimension," rotating every molecule about e.g. the $\hat{y}$ axis by π). This deformation in real space would correspond to a free homotopy of loops in the order parameter space. We have included a video of such a smooth deformation, together with the corresponding free homotopy of loops in $\mathrm{SO}(3)/D_2$. At each frame of the video, the path shown in SO(3) is a closed loop in the OP space (which can be seen by the fact that the configuration of the physical molecules varies continuously in real space around the loop). At the end of the video, the loop starts and ends at an element of D_2, which are elements of the symmetry group of the molecule.

Defect combination and braiding

When the fundamental group of the OP space is abelian, the unique group product of the two group elements of the combining defects determines the label of the net defect. The label of the defect also depends on the choice of reference configuration: a π swirl of the orthorhombic biaxial nematic, for instance, can be thought of as a clockwise or counterclockwise swirl of any of the $\hat{x}$, $\hat{y}$, and $\hat{z}$ axes, depending on the choice of reference configuration. After a reference configuration is chosen with coordinate axes fixed, the label of a particular defect can depend on the path chosen to encircle it, if it is in the vicinity of additional defects. To see this, consider Fig. 7.9(a) and Fig. 7.9(c). One can label the red defect via the loop starting at the reference configuration **X** in Fig. 7.9(a), and one would record an element $\beta \in \pi_1$ (OP). One could just as well label the defect

using the loop in Fig. 7.9(c), and one would record an element $\widehat{\beta} = \alpha^{-1}\beta\alpha$. This is relevant for defect combination in the group.

In the following sections, we will not go into such detail. We will enumerate the homotopy groups and conjugacy classes, and we will show some representatives of each type of defect for phases where the symmetries are particularly interesting. In the supplemental material, examples of each kind of defect in many more of the phases are shown.

7.2.6 Defect enumeration and combination in bent-core liquid crystal phases

The first and second homotopy groups of all of the possible symmetry-allowed phases of the banana molecules are shown in the final two columns of Table 7.2. The only phases with nontrivial point defects in three dimensions ($\pi_2 \neq 0$) are V (vector) and N (uniaxial nematic). There are no stable line defects in the V phase, and the point defects are labelled by and combine like integers (under addition). In the N phase, the point defects are not simply labelled by $\mathbb{Z}$, since the point defects can change their sign by winding around a line defect, and hence there is a path dependence in the way point defect addition occurs [180]. Because these phases are well-understood, and the fundamental groups of all other phases are discrete, there are no further interesting topological point defects to discuss in three dimensions.

There are four other phases whose fundamental groups are abelian and whose defects can hence be labelled by group elements. These are the $V + 2$,

$V + 3$, $(V_T + 2)^*$, and $N + V$ phases. All of these have a finite number of defect types that add as in the cyclic group $\mathbb{Z}_n$. For instance, in the $V+2$ phase, there are three types of defect that could be labelled 1_+, 2_+, and 3_+, and whose combination is governed by addition modulo 4 (with 0_+ representing the topologically trivial configuration).

There are three phases ($N + 2$, N_T, and $(N_T + 2)^*$) whose fundamental group is the quaternions $\mathbb{H}$, and whose defects are labelled by conjugacy classes of $\mathbb{H}$ (of which there are 4 + the trivial field configuration). This is the same defect classification as for orthorhombic biaxial nematics, whose defects are also well-understood and fully classified in e.g. [180] and the previous section.

This leaves just two phases whose topological defects we need to enumerate: the tetrahedratic T-phase and the triadic $N + 3$ phase. As we show next, each of these has a non-abelian fundamental group and hence can display braiding statistics, entanglement of line defects, and path dependence in defect addition. We seek to fully enumerate and illustrate the types of defect in each of these phases and connect them to experimental observables of the bent-core molecule liquid crystal system.

Tetrahedratic T-phase

Within the tetrahedratic T-phase, the orientationally-ordered units are clusters of six bent-core molecules lying on the edges of tetrahedra. The fundamental group of the order parameter space of a liquid crystal comprised of such ordered clusters is the binary tetrahedral group $2T$, which is a non-abelian group with 24 elements. These elements are most simply written in terms of Pauli

	$\mathbf{C_0}$	$\overline{\mathbf{C_0}}$	$\mathbf{C_Q}$	$\mathbf{C_{w_1}}$	$\mathbf{C_{-w_1}}$	$\mathbf{C_{w_2}}$	$\mathbf{C_{-w_2}}$
$\mathbf{C_0}$	C_0	$\overline{C_0}$	C_Q	C_{w_1}	C_{-w_1}	C_{w_2}	C_{-w_2}
$\overline{\mathbf{C_0}}$	$\overline{C_0}$	C_0	C_Q	C_{-w_1}	C_{w_1}	C_{-w_2}	C_{w_2}
$\mathbf{C_Q}$	C_Q	C_Q	$6C_0 + 6\overline{C_0} + 4C_Q$	$3C_{w_1} + 3C_{-w_1}$	$3C_{w_1} + 3C_{-w_1}$	$3C_{w_2} + 3C_{-w_2}$	$3C_{w_2} + 3C_{-w_2}$
$\mathbf{C_{w_1}}$	C_{w_1}	C_{-w_1}	$3C_{w_1} + 3C_{-w_1}$	$3C_{w_2} + C_{-w_2}$	$C_{w_2} + 3C_{-w_2}$	$4C_0 + 2C_Q$	$4\overline{C_0} + 2C_Q$
$\mathbf{C_{-w_1}}$	C_{-w_1}	C_{w_1}	$3C_{w_1} + 3C_{-w_1}$	$C_{w_2} + 3C_{-w_2}$	$3C_{w_2} + C_{-w_2}$	$4\overline{C_0} + 2C_Q$	$4C_0 + 2C_Q$
$\mathbf{C_{w_2}}$	C_{w_2}	C_{-w_2}	$3C_{w_2} + 3C_{-w_2}$	$4C_0 + 2C_Q$	$4\overline{C_0} + 2C_Q$	$3C_{w_1} + C_{-w_1}$	$C_{w_1} + 3C_{-w_1}$
$\mathbf{C_{-w_2}}$	C_{-w_2}	C_{w_2}	$3C_{w_2} + 3C_{-w_2}$	$4\overline{C_0} + 2C_Q$	$4C_0 + 2C_Q$	$C_{w_1} + 3C_{-w_1}$	$3C_{w_1} + C_{-w_1}$

Table 7.3: Combination rules for defects in the tetrahedratic T-phase. When there are multiple classes resulting from the product of two conjugacy classes, then the resulting defect depends upon the path along which two defects are brought together.

matrices. The 24 elements include the 8 elements of $\mathbb{H} = \left\{\pm 1, \pm i\sigma_x, \pm i\sigma_y, \pm i\sigma_z\right\}$ as a subgroup, together with the 16 additional elements of the form $w_{\pm\pm\pm\pm} \equiv \left(\pm 1 \pm i\sigma_x \pm i\sigma_y \pm i\sigma_z\right)/2$:

$$2T = \mathbb{H} \cup \left\{\frac{1}{2}\left(\pm 1 \pm i\sigma_x \pm i\sigma_y \pm i\sigma_z\right)\right\} \tag{7.8}$$

with the usual multiplication rules in SU(2). There are 7 conjugacy classes of the binary tetrahedral group, and hence 6 distinct types of defect:

$$\begin{aligned} C_0 &= \{1\}, \quad \overline{C_0} = \{-1\}, \quad C_Q = \left\{\pm i\sigma_x, \pm i\sigma_y, \pm i\sigma_z\right\}, \\ C_{w_1} &= \{w_{++++}, w_{++--}, w_{+-+-}, w_{+--+}\}, \\ C_{w_2} &= \{w_{+++-}, w_{++-+}, w_{+-++}, w_{+---}\}, \\ C_{-w_1} &= -C_{w_1}, \quad C_{-w_2} = -C_{w_2}. \end{aligned} \tag{7.9}$$

The conjugacy class multiplication table, which shows how defects of different classes combine, is shown as Table 7.3.

Understanding and visualizing the configuration of the banana molecules lying on the edges of the tetrahedral clusters around these defects is again

done through the two-to-one homomorphism between SU(2) and SO(3). Take, for instance, a defect represented by $w_{++++} = \exp\left(i\frac{\pi}{3}(1,1,1)/\sqrt{3}\cdot\sigma\right)$. A smooth path in SU(2) from 1 to w_{++++} is traced out when the rotation matrix $R\left(\left(1/\sqrt{3}, 1/\sqrt{3}, 1/\sqrt{3}\right), \frac{2\pi}{3}\left(\frac{\theta}{2\pi}\right)\right)$ is applied to each point (r,θ) in real space. This defect, together with a reference configuration of the tetrahedron, is illustrated in Figure 7.11. It corresponds to a $2\pi/3$ vortex, where the tetrahedral clusters are rotated by $2\pi/3$ around one of their 3-fold axes as the defect is encircled. The defect may change its appearance upon braiding around other kinds of defect (or equivalently, choosing a different measurement loop), but it will always be measured to lie in the C_{w_1} conjugacy class of $2T$.

Triadic $N+3$ phase

Within the triadic $N+3$ phase, the bent-core molecules organize into planar triangular clusters, lying on the edges of an equilateral triangle that is free to rotate in three dimensions (Fig. 7.8(a)). The fundamental group of the order parameter space of a liquid crystal comprised of this molecule is the 12-element non-abelian dicyclic group Dic_3 (which is the double group of the 6-element dihedral group D_3). Once again, these elements can be written in terms of Pauli matrices. There are 6 conjugacy classes of the dicyclic group Dic_3, and hence 5 types of defect:

$$\begin{aligned} C_0 &= \{1\}, \quad \overline{C_0} = \{-1\}, \\ C_1 &= \left\{\exp\left(\pm i\frac{\pi}{3}\sigma_z\right)\right\}, \quad C_2 = -C_1, \\ C_{\mathrm{even}} &= \left\{i\sigma_x, i\sigma_x\exp\left(\pm i\frac{2\pi}{3}\sigma_z\right)\right\}, \quad C_{\mathrm{odd}} = -C_{\mathrm{even}}. \end{aligned} \tag{7.10}$$

The conjugacy class multiplication table, which shows how defects of different classes combine, is shown as Table 7.4.

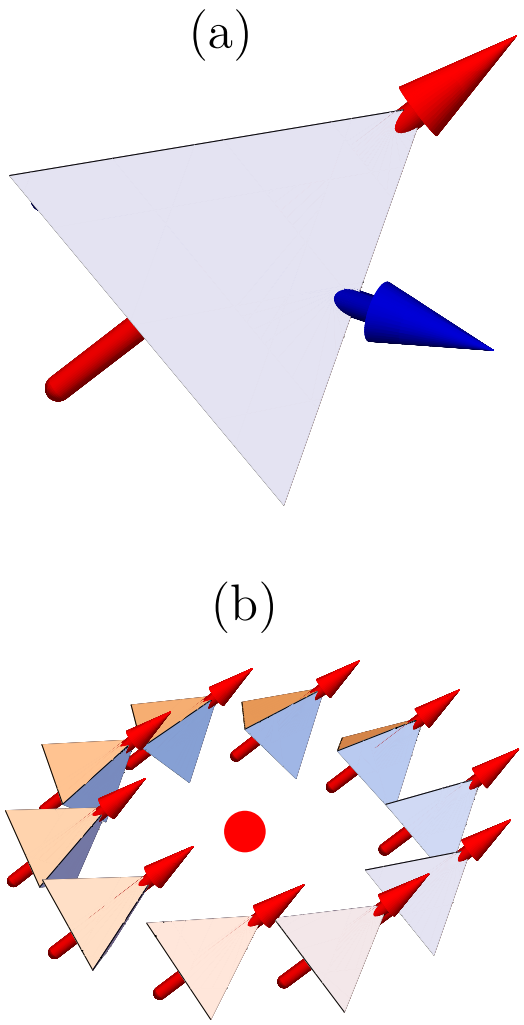

Figure 7.11: **A tetrahedratic defect.** (a) A reference configuration of the tetrahedron is shown; the blue axis is $\hat{x}$, which passes through the center of two edges. The red axis is $(\hat{x} + \hat{y} + \hat{z})/\sqrt{3}$, which passes through a vertex and the center of a face. (b) For a defect labelled w_{++++} (the red point), the tetrahedron originally in the reference configuration executes a rotation counterclockwise by $2\pi/3$ about the red axis as the defect is traversed counterclockwise in real space. It can be smoothly deformed into any other defect in the C_{w_1} class.

	$\mathbf{C_0}$	$\overline{\mathbf{C_0}}$	$\mathbf{C_1}$	$\mathbf{C_2}$	$\mathbf{C}_{\text{even}}$	$\mathbf{C}_{\text{odd}}$
$\mathbf{C_0}$	C_0	$\overline{C_0}$	C_1	C_2	C_{even}	C_{odd}
$\overline{\mathbf{C_0}}$	$\overline{C_0}$	C_0	C_2	C_1	C_{odd}	C_{even}
$\mathbf{C_1}$	C_1	C_2	$2C_0 + C_2$	$2\overline{C_0} + C_1$	$2C_{\text{odd}}$	$2C_{\text{even}}$
$\mathbf{C_2}$	C_2	C_1	$2\overline{C_0} + C_1$	$2C_0 + C_2$	$2C_{\text{even}}$	$2C_{\text{odd}}$
$\mathbf{C}_{\text{even}}$	C_{even}	C_{odd}	$2C_{\text{odd}}$	$2C_{\text{even}}$	$3\overline{C_0} + 3C_1$	$3C_0 + 3C_2$
$\mathbf{C}_{\text{odd}}$	C_{odd}	C_{even}	$2C_{\text{even}}$	$2C_{\text{odd}}$	$3C_0 + 3C_2$	$3\overline{C_0} + 3C_1$

Table 7.4: Combination rules for defects in the triadic $N + 3$ phase.

The path dependence of defect addition in this non-abelian group, together with the braiding statistics, can be best demonstrated through a sequence of snapshots (or a video). Suppose we begin with a +2/3 defect (labelled by element $\beta_2 = \exp\left(i\frac{2\pi}{3}\sigma_z\right) \in C_2$) next to a flip defect (labelled by element $\alpha = i\sigma_x \in C_{\text{even}}$). The +2/3 defect β_2 can be split into two +1/3 defects (labelled by $\beta_1 = \exp\left(i\frac{\pi}{3}\sigma_z\right) \in C_1$. This is the meaning of $C_1 * C_1 = 2C_0 + C_2$ in the class multiplication table for the triadic phase: one way of bringing together two C_1 defects gives us a C_2 defect. Next, we take one of the defects labelled β_1 and wind it around defect α, a process identical to what is shown in Figure 7.9. This gives us a defect labelled by $\widehat{\beta_1} = (i\sigma_x)^{-1} \exp\left(i\frac{\pi}{3}\sigma_z\right)(i\sigma_x) = \exp\left(-i\frac{\pi}{3}\sigma_z\right) \in C_1$. Our +1/3 defect has transformed into a −1/3 defect! However, the labelling by the conjugacy class C_1 has remained consistent. Now we bring together the +1/3 and the −1/3 defects and use one to annihilate the other, giving us the C_0 trivial configuration. This procedure illustrates the path dependence of the combination of two C_1 defects when in the vicinity of other defects.

7.2.7 Summary

Motivated by a large class of newly synthesized and experimentally extensively studied bent-core "banana" liquid crystals [200], in this manuscript we presented an exhaustive characterization of bent-core fluid phases in terms of their topological defects. Our study thus complements an earlier Landau order-parameter approach [181] that predicted a web of phases and associated phase transitions. Focusing on the most exotic tetrahedratic fluid [7] with tetrahedral T_d symmetry, using homotopy machinery we demonstrated that its vortex line defects are non-abelian and have fully characterized their braiding and fusion properties. We expect our prediction to be a useful experimental diagnostic of this (linear-)optically isotropic tetrahedral fluid. We also complete this analysis for all other symmetry-allowed nematic phases.

7.2.8 Acknowledgments

SJT would like to acknowledge James P. Sethna for useful discussions. This work was supported in part by NSF DMR-1719490 (SJT) and by the Simons Investigator Award from the James Simons Foundation (LR).

[7] The tetrahedratic fluid remains to be experimentally discovered.

APPENDIX A

APPENDIX OF CHAPTER 2

This Appendix is a reformatted version of a manuscript appearing on the arXiv as "Universal scaling for disordered viscoelastic matter II: Collapses, global behavior and spatio-temporal properties." This was later reformatted into the S.I. of [9].

A.1 Abstract

Disordered viscoelastic materials are ubiquitous and exhibit fascinating invariant scaling properties. In a companion article [9], we have presented comprehensive new results for the critical behavior of the dynamic susceptibility of disordered elastic systems near the onset of rigidity. Here we provide additional details of the derivation of the singular scaling forms of the longitudinal response near both jamming and rigidity percolation. We then discuss global aspects associated with these forms, and make scaling collapse plots for both undamped and overdamped dynamics in both the rigid and floppy phases. We also derive critical exponents, invariant scaling combinations and analytical formulas for universal scaling functions of several quantities such as transverse and density responses, elastic moduli, viscosities, and correlation functions. Finally, we discuss tentative experimental protocols to measure these behaviors in colloidal suspensions.

A.2 Introduction

Disordered elastic systems encompass a wide range of materials, from amorphous solids [201] and network glasses [15] to biopolymer fiber networks [5], articular cartilage [4], confluent cell tissues [202, 25] and even machine learning [26]. Their theoretical development has not only led to a much deeper understanding of traditionally difficult problems as the glass transition; it has also pushed the boundaries of science to incorporate new frameworks such as topological mechanics [203, 204], non-reciprocal phase transitions [205] and novel mechanical metamaterials [206, 207, 208, 21]. In a companion article [9], we have employed a systematic analysis of the invariant scaling of the dynamic susceptibility to determine the universal critical behavior of several classes of disordered viscoelastic materials near the onset of rigidity. Here we present a derivation of the theoretical results shown in [9], and discuss additional details for scaling collapses, the global behavior of universal scaling functions, and general scaling forms for diverse spatio-temporal properties such as moduli, viscosities and correlation functions.

Jamming [14] and Rigidity Percolation (RP) [15] provide two of the most suitable approaches to characterize the fascinating scaling behavior that is exhibited by several classes of disordered viscoelastic materials near the onset of rigidity [16]. Both are often modeled by elastic networks close to Maxwell's threshold for mechanical stability [17], and represent transitions from a rigid phase to a floppy one when the average coordination number becomes smaller than the isostatic value. RP is usually described in terms of networks in which bonds between sites are randomly removed, and is characterized by a second-order transition for all elastic moduli [1, 23]. In turn, jamming is usually described

in terms of disordered arrangements of spheres that exhibit an unusual critical behavior, with a first-order transition for the bulk modulus and a second-order transition for the shear modulus.

Whereas effective-medium theories have been routinely employed in the derivation of the critical behavior associated with RP [1, 22, 23], a genuine finite-dimensional effective-medium theory for jamming had remained elusive until recently [2]. Incidentally, a phenomenological theory providing a synthesis of available numerical work on the universal critical scaling of jamming has also been proposed recently [40]. Here we show how to combine these two developments [2, 40] to derive the scaling behavior of a large class of disordered elastic materials near jamming and rigidity percolation. Our results are based on a scaling Ansatz for the longitudinal response that is akin to the one considered in Ref. [40]. They go beyond the results of [40] by incorporating rigidity percolation in addition to jamming, as well as wavelength and frequency dependencies in addition to static results. We use the effective-medium theory of Ref. [2] to both validate our scaling forms and to extract analytical formulas for the universal scaling functions. Our results go beyond the results of [2] by incorporating the analysis of a wide variety of physical quantities, particularly spatio-temporal properties such as dynamic response and correlation functions.

The remainder of this article is organized as follows. In Sec. A.3, we present a brief review of key results of Ref. [2] (Sec. A.3.1), and a derivation of the critical exponents and universal scaling functions for the longitudinal response (Sec. A.3.2). To validate the theory of Sec. A.3.2, we present in Sec. A.4 scaling collapse plots near both jamming and rigidity percolation, for undamped and overdamped dynamics, in the rigid and floppy phases, and discuss the global

behavior of the longitudinal response. We then use results from Sec. A.3.2 to derive the universal scaling behavior of several additional quantities in Sec. A.5 — the transverse dynamic response, moduli and viscosities, density response and correlation functions. Finally, we end with an outlook in Sec. A.7.

A.3 Theory

Here we present a brief review of key results from Ref. [2], which we use in the derivation of critical exponents and universal scaling functions for the longitudinal response (Sec. A.3.2) and other quantities (Sec. A.5).

A.3.1 Effective-medium theory for jamming and rigidity percolation

We use the honeycomb-triangular lattice (HTL) model [2] to describe both static and dynamical properties of jamming and rigidity percolation (RP) near the threshold of mechanical stability. The HTL model combines suitable properties of two periodic lattices: The honeycomb lattice (solid lines in Fig. A.1) with finite bulk modulus $B > 0$ and zero shear modulus $G = 0$, and two triangular lattices (dashed and dotted lines) with finite $B, G > 0$. In simulations, bonds (harmonic elastic interactions) of the honeycomb lattice and the triangular lattices have unit spring constant and are populated [1] with probability p_{B} and p_{N}, respectively. In the effective-medium theory, the honeycomb and triangular lat-

[1] This is a special case of the more general model in which the bond occupation probability can be different for the two triangular lattices.

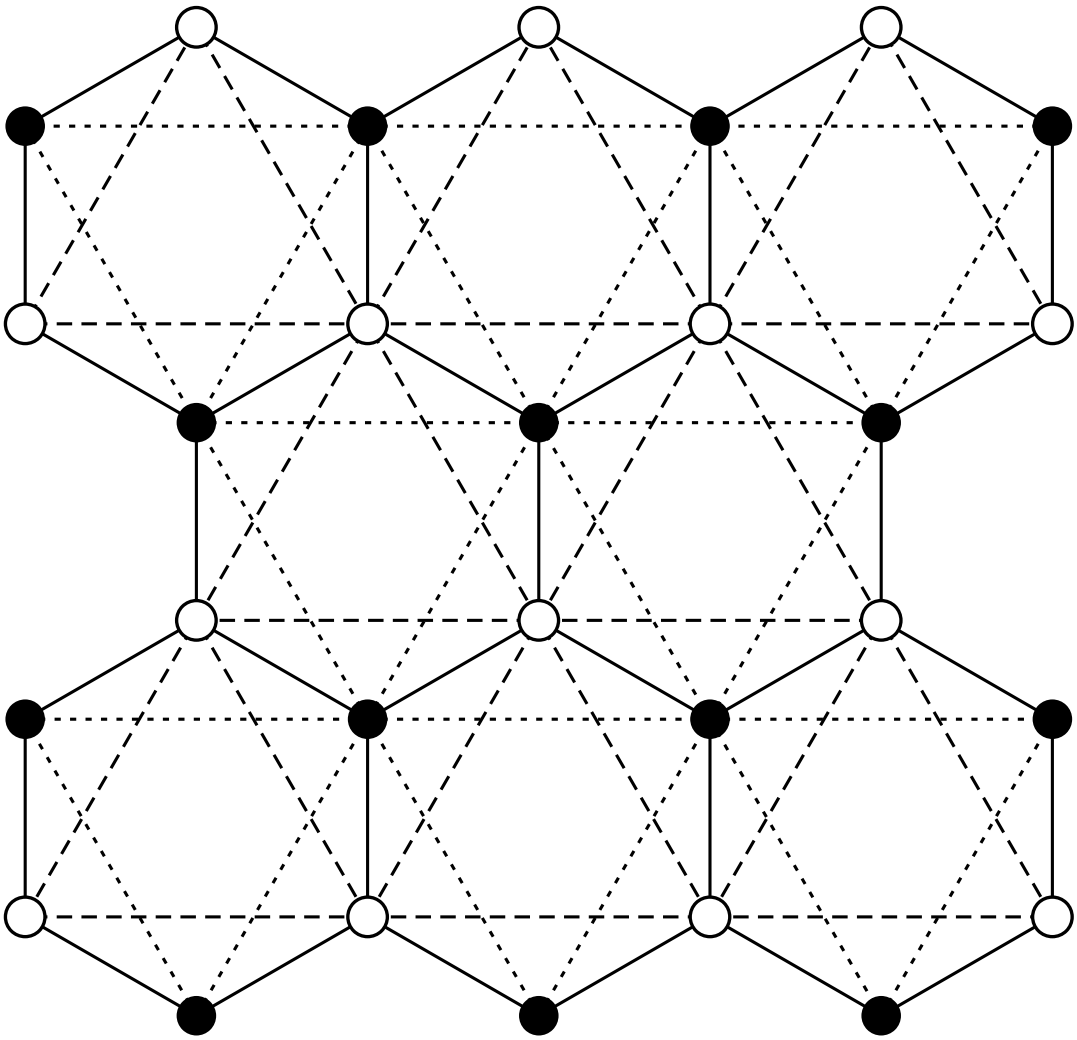

Figure A.1: Illustration of the honeycomb-triangular lattice model. In simulations, bonds of the honeycomb lattice (solid lines) and the two triangular lattices (dashed and dotted lines) are populated with probability p_{B} and p_{N}, respectively. In the effective medium theory, the fully-occupied honeycomb and triangular sub-lattices have frequency-dependent effective spring constants $k_{\mathrm{B}}(\omega)$ and $k_{\mathrm{N}}(\omega)$, respectively, satisfying a set of self-consistent equations.

tices are fully populated with bonds with complex frequency-dependent effective spring constant $k_{\mathrm{B}}(\omega)$ and $k_{\mathrm{N}}(\omega)$, respectively.

We use the Coherent Potential Approximation [41, 1, 22] (CPA) to derive a set of self-consistent equations for $k_{\mathrm{B}}(\omega)$ and $k_{\mathrm{N}}(\omega)$, and then describe elastic and

phonon properties of the HTL model near jamming and RP. The derivation of the CPA self-consistent equations is standard, and we do not include it here. Here the randomly-diluted lattice is modeled by homogeneous lattices with effective spring constants satisfying the set of equations [2]:

$$k_\alpha = \frac{p_\alpha - h_\alpha}{1 - h_\alpha}, \tag{A.1}$$

where p_α and k_α are the occupancy probability of each bond and the effective spring constant for sub-lattice $\alpha \in \{B, N\}$, respectively. The functions $h_\alpha = h_\alpha(p_\mathrm{B}, p_\mathrm{N}, \omega)$ are defined by

$$h_\alpha = \frac{1}{\tilde{z}_\alpha N_c} \sum_{\mathbf{q}} \mathrm{Tr}\left[D_\alpha(\mathbf{q}) \cdot \mathcal{G}(\mathbf{q}, \omega)\right], \tag{A.2}$$

where N_c is the total number of cells, ω is the frequency, q is the wavevector, and $D_\alpha(\mathbf{q})$ and $\tilde{z}_\alpha$ are the dynamical matrix and the number of bonds per unit cell for sub-lattice α, respectively. The trace is taken over an mD-dimensional space, where m is the number of sites per unit cell and D is the spatial dimension. The Green's function $\mathcal{G}$ is defined by

$$\mathcal{G}(\mathbf{q}, \omega) = \left[\sum_\alpha D_\alpha(\mathbf{q}) - \omega^2 \mathbb{I}\right]^{-1}, \tag{A.3}$$

where $\mathbb{I}$ is an identity matrix. Note that $\sum_\alpha D_\alpha$ depends on all effective spring constants k_α, so that Eq. A.1 self-consistently determines the values of all k_α for given p_B, p_N and ω.

Elastic moduli can be expressed in terms of the effective springs constants by taking the long-wavelength limit of the dynamical matrix while ensuring that internal degrees of freedom are relaxed before the limit of small wavevector is taken. The HTL has isotropic elasticity, with bulk and shear moduli given by

$$B = \frac{3}{4} k_\mathrm{B} + \frac{9}{2} k_\mathrm{N}, \quad G = \frac{9}{4} k_\mathrm{N}, \tag{A.4}$$

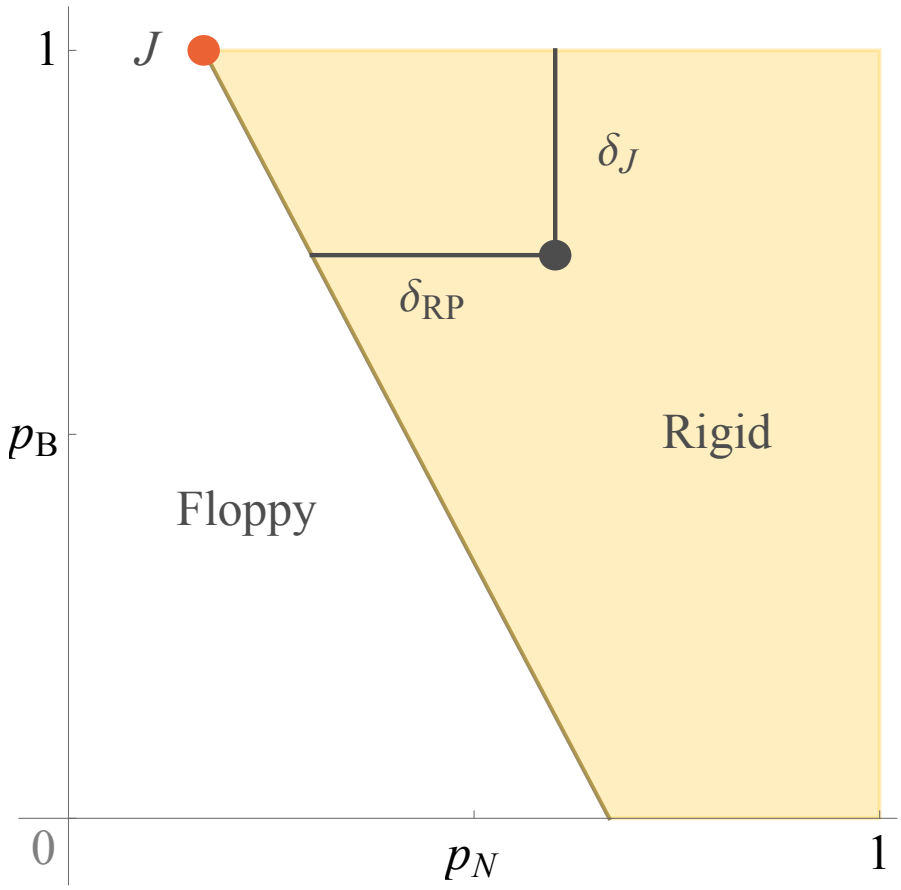

Figure A.2: Phase diagram of the HTL model in terms of bond occupation probabilities for the honeycomb (p_B) and triangular (p_N) lattices. The gray line is an RP line that terminates at a multicritical jamming point J (red disk). The diagram also shows the pair of scaling variables δp_B and δp.

respectively. These definitions along with solutions of the CPA equations allow us to draw the zero-frequency phase diagram shown in Fig. A.2.

Using a perturbation analysis, one can write the asymptotic equations for the low-frequency behavior of k_B and k_N near the jamming point J [2]:

$$k_B \approx \frac{k_N}{k_N + \delta p_B / b_1}, \tag{A.5}$$

$$k_N \approx b_2 \, |\delta p| \left(\sqrt{1 - c \, \frac{\tilde{\omega}(\omega)}{|\delta p|^2}} \pm 1 \right), \tag{A.6}$$

where b_1, b_2 and c are constants, the plus and minus signs on the second equa-

tion correspond to the rigid and floppy phases, respectively, and

$$\tilde{\omega}(\omega) \equiv \begin{cases} \rho\,\omega^2, \text{ for undamped dynamics,} \\ i\,\gamma\,\omega, \text{ for overdamped dynamics,} \end{cases} \tag{A.7}$$

where ρ and γ represent the mass density and a drag coefficient, respectively. Using Eqs. (A.5) and (A.6), we can write,

$$k_{\mathrm{B}} \approx \left[1 + \frac{\delta p_{\mathrm{B}}}{b\,|\delta p|\left(\sqrt{1 - c\,\tilde{\omega}(\omega)/|\delta p|^2} \pm 1\right)}\right]^{-1}, \tag{A.8}$$

where $b \equiv b_1 \cdot b_2$ is constant. From Eq. (A.8), we can derive the scaling behavior of the frequency-dependent bulk modulus:

$$B(\omega) \approx a\left[1 + \frac{\delta p_{\mathrm{B}}/|\delta p|^{\varphi}}{\mathcal{M}_{\pm}(\omega/|\delta p|^{z\nu})}\right]^{-1}, \tag{A.9}$$

where a is a constant corresponding to the bulk modulus of the fully-populated honeycomb lattice in our model. The exponent $\varphi = 1$, and the product $z\,\nu = 1$ and 2 for undamped and overdamped dynamics, respectively. The universal scaling function $\mathcal{M}$ is given by

$$\mathcal{M}_{\pm}(v) \equiv b \times \begin{cases} \sqrt{1 - c\,\rho\,v^2} \pm 1, & \text{(undamped),} \\ \sqrt{1 - i\,c\,\gamma\,v} \pm 1, & \text{(overdamped).} \end{cases} \tag{A.10}$$

where b and c are constants, and the plus and minus correspond to solutions in the elastic and floppy states, respectively. In Sec. A.3.2, we use Eq. (A.9) to derive the scaling behavior of the longitudinal response.

In turn, the scaling behavior for the shear modulus G follows directly from the asymptotic behavior of k_{N} in Eq. (A.6):

$$G(\omega) \approx g\,|\delta p|^{\beta_{\mathrm{G}}}\,\mathcal{M}_{\pm}(\omega/|\delta p|^{z\nu}), \tag{A.11}$$

where $\beta_{\mathrm{G}} = 1$ and g is a constant.

Note that these scaling forms were obtained using an approximation that is valid near the multicritical point J. Some of the nonuniversal constants change as one moves away from the J point towards larger values of δp_{B} (see e.g. the slope of the shear modulus in Ref. [2]). Though these constants depend on model details, we expect the functional forms to be universal.

A.3.2 Critical exponents and universal scaling function for longitudinal response

Now we use the results presented in Sec. A.3.1 to derive the critical exponents and universal scaling functions for the longitudinal response near both jamming and RP, for undamped and overdamped dynamics in the solid and fluid phases.

In the long wavelength limit, the longitudinal component of the dynamic response function χ_{L} of an isotropic viscoelastic material is given by [36, 209]

$$\chi_{\mathrm{L}} = \left\{ -\rho\,\omega^2 - i\,\gamma\,\omega + q^2 \left[B(\omega) + 2\,\frac{D-1}{D} G(\omega) \right] \right\}^{-1} . \tag{A.12}$$

The complex elastic moduli $B(\omega) = B' + iB''$ and $G(\omega) = G' + iG''$ can be decomposed into storage (B' and G') and loss (B'' and G'') components. Interestingly, we observe a nonzero loss modulus in our effective-medium results even if there is no dissipation term in the dynamics (i.e. if $\gamma = 0$.) This happens because the dynamical CPA involves an average over disorder that maps simple springs into Kelvin-Voigt elements (combinations of springs and dashpots [209]), which lead to nonzero imaginary parts if the frequency is sufficiently high. Physically, this is the way CPA incorporates scattering of long-wavelength phonons off the disordered lattice.

For $G/B \ll 1$ (near jamming) we can write

$$\begin{aligned}\chi_{\mathrm{L}} &\approx \left[-\rho\,\omega^2 - i\,\gamma\,\omega + q^2\,B(\omega)\right]^{-1} \\ &\approx \Big\{-\rho\,\omega^2 - i\,\gamma\,\omega + a\,q^2 \\ &\quad \times\left[1 + \frac{\delta p_{\mathrm{B}}/|\delta p|^{\varphi}}{\mathcal{M}_{\pm}(\omega/|\delta p|^{z\nu})}\right]^{-1}\Big\}^{-1}\end{aligned} \tag{A.13}$$

where $\varphi = 1$, $z\,\nu = 1$ and 2 for undamped and overdamped dynamics, respectively, and we have used the asymptotic form for the bulk modulus [Eq. (A.9)]. Now we multiply both sides of (A.13) by $|\delta p|^2$ to write

$$\begin{aligned}|\delta p|^2\chi_{\mathrm{L}} \approx \Bigg\{&-\rho\left(\frac{\omega}{|\delta p|}\right)^2 - i\,\gamma\frac{\omega}{|\delta p|^2} \\ &+a\left(\frac{q}{|\delta p|}\right)^2\left[1 + \frac{\delta p_{\mathrm{B}}/|\delta p|^{\varphi}}{\mathcal{M}_{\pm}(\omega/|\delta p|^{z\nu})}\right]^{-1}\Bigg\}^{-1}.\end{aligned} \tag{A.14}$$

Let us define the nonuniversal scaling factors [34],

$$\chi_0 \equiv c, \quad q_0 \equiv \frac{1}{\sqrt{ac}}, \quad \delta_0 \equiv b, \tag{A.15}$$

$$\omega_0 \equiv \begin{cases} 1/\sqrt{\rho\,c}, & \text{for the undamped case,} \\ 1/(\gamma\,c), & \text{for the overdamped case,}\end{cases} \tag{A.16}$$

which lead to the scaling form:

$$\frac{\chi_{\mathrm{L}}}{\chi_0} \approx |\delta p|^{-\gamma}\mathcal{L}\left(\frac{q/q_0}{|\delta p|^{\nu}}, \frac{\omega/\omega_0}{|\delta p|^{z\nu}}, \frac{\delta p_{\mathrm{B}}/\delta_0}{|\delta p|^{\varphi}}\right), \tag{A.17}$$

with

$$\mathcal{L}(u, v, w) = \left[\frac{u^2}{1 + w/\left(\sqrt{1 - \tilde{v}(v)} \pm 1\right)} - \tilde{v}(v)\right]^{-1}, \tag{A.18}$$

where $\mathcal{L}$ is a universal scaling function, the exponents $\gamma = 2$ and $\nu = 1$ for jamming, and

$$\tilde{v}(v) = \begin{cases} v^2, & \text{for the undamped case,} \\ i\,v, & \text{for the overdamped case.}\end{cases} \tag{A.19}$$

The exponents γ, z and ϕ are associated with the susceptibility, correlation time, and crossover behavior, respectively [34, 37]. As we show in Sec. A.5, our exponent ν for the correlation length is associated with traditional definitions for diverging length scales ℓ^* and ℓ_c (see e.g. [38]), and should not be confused with exponents for the finite-size scaling of the probability density $\Delta \sim L^{1/\nu}$, as reported in calculations based on the pebble game [59].

At fixed δp_{B}, the limit $\delta p \to 0$ leads to RP criticality (cf. Fig. A.2). Thus, we can study the crossover to rigidity percolation by considering the invariant scaling combination $\delta p_{\mathrm{B}}/|\delta p|^{\varphi} \gg 1$, so that, from Eq. (A.14):

$$|\delta p|^2 \chi_{\mathrm{L}} \approx \left[-\rho \left(\frac{\omega}{|\delta p|} \right)^2 - i\,\gamma \frac{\omega}{|\delta p|^2} + a \left(\frac{q}{|\delta p|} \right)^2 \frac{|\delta p|^{\varphi}}{\delta p_{\mathrm{B}}} \mathcal{M}_{\pm} \left(\frac{\omega}{|\delta p|^{z\nu}} \right) \right]^{-1} . \tag{A.20}$$

Since δp_{B} is an irrelevant variable for rigidity percolation, we define $q_0 \equiv \sqrt{\delta p_{\mathrm{B}}/(a\,c)}$. Now the term $|\delta p|^{\varphi}$ has to be incorporated into the invariant scaling combination for q, leading to $\nu = 1/2$ for RP. Since the product $z\,\nu$ depends only on the type of dynamics (undamped or overdamped,) the exponent z must also change for rigidity percolation. The longitudinal response then behaves as:

$$\frac{\chi_{\mathrm{L}}}{\chi_0} \approx |\delta p|^{-\gamma} \bar{\mathcal{L}} \left(\frac{q/q_0}{|\delta p|^{\nu}}, \frac{\omega/\omega_0}{|\delta p|^{z\nu}} \right), \tag{A.21}$$

where

$$\bar{\mathcal{L}}(u, v) = \left[u^2 \left(\sqrt{1 - \tilde{v}(v)} \pm 1 \right) - \tilde{v}(v) \right]^{-1} . \tag{A.22}$$

Table A.1 lists the values of the critical exponents γ, z, ν, φ, β_{B} and γ_{B} for both jamming and RP, and for both undamped and overdamped (between parentheses, if different from undamped) dynamics. The exponents for the bulk modulus β_{B} and bulk viscosity γ_{G} are defined by equations (A.34) and (A.43), respec-

	γ	z	ν	φ	β_{B}	γ_{B}
Jamming	2	1 (2)	1	1	0	1 (2)
Rigidity Percolation	2	2 (4)	1/2	-	1	0 (1)

Table A.1: Critical exponents (cf. Eqs. (A.17), (A.21), (A.33) and (A.41)) extracted from the longitudinal response function near jamming and rigidity percolation for undamped and overdamped (between parentheses, if different from undamped) dynamics.

tively, in Sec. A.5. Note that previous studies [38, 39] of the response of frictionless jammed spheres to a sinusoidal perturbation report exponents ν that are in-between the ones presented here.

Our formulation of Eqs. (A.17) and (A.21) represents a deliberate effort to emphasize model-independent (universal) features. Note e.g. that our model definition of the non-universal scaling factor q_0 is different for jamming and RP; the latter involves a term that increases as one moves away from the jamming multicritical point. Besides, our formulation allows for the suitable incorporation of analytic corrections to scaling [47, 48, 34, 49], which can be added in a case-by-case basis. In general, we expect these corrections to appear through the introduction of nonlinear scaling fields,

$$u_q(q, \omega, \delta_{\mathrm{J}}) = \frac{q}{q_0} + \dots \tag{A.23}$$

$$u_\omega(q, \omega, \delta_{\mathrm{J}}) = \frac{\omega}{\omega_0} + \dots \tag{A.24}$$

$$u_{\mathrm{J}}(q, \omega, \delta_{\mathrm{J}}) = \frac{\delta_{\mathrm{J}}}{\delta_0} + \dots \tag{A.25}$$

which would replace q/q_0, ω/ω_0 and $\delta_{\mathrm{J}}/\delta_0$ in Eqs. (A.17) and (A.21). Here the dots represent higher-order terms and perhaps linear terms in the other variables (rotating the axes). These nonlinear scaling fields can be viewed as the difference between the lab parameters and Nature's natural variables, or as the coordinate transformation removing the (hypothetical) nonlinear terms in the

renormalization group to their hyperbolic normal form [49]. In order to use our scaling predictions to describe behavior far from the critical point, one must first determine the appropriate scaling fields u_q, u_ω and $u_\jmath$ for the particular system.

A.4 Scaling and global asymptotic behavior for longitudinal response

Our universal scaling forms for the longitudinal response provide a valuable tool both to investigate invariant critical behavior and to quickly assess the overall global behavior of $\chi_{\rm L}$. In this section, we employ full EMT solutions to validate the universal scaling functions $\mathcal{L}$ and $\bar{\mathcal{L}}$ [see Eqs. (A.18) and (A.22)], by means of scaling collapse plots for both overdamped (Sec. A.4.1) and undamped (Sec. A.4.2) dynamics. We then show how to use our solutions to quickly explore the invariant global behavior exhibited by $\chi_{\rm L}$.

A.4.1 Overdamped dynamics

Equations (A.17) and (A.21) imply that solutions for $|\delta p|^\gamma \chi_{\rm L}$ as a function of one of the three invariant scaling combinations (the other two kept constant) should lie on the curves given by Eqs. (A.18) and (A.22), respectively. Hence, plots for different values of $|\delta p|$ should collapse for several paths approaching jamming or RP. Figure A.3 shows an example of a scaling collapse plot of the rescaled longitudinal response as a function of rescaled frequency for overdamped dynamics at fixed $q/|\delta p|^\nu$ and $\delta_\jmath/|\delta p|^\varphi$, and for paths approaching jamming (first row) and RP (second row) from both the rigid and floppy phases (see inset in

each panel). Although there are model-specific predictions for the nonuniversal scaling factors, we choose them to best fit the collapsed data.

In the elastic phase [(a) and (c)], one observes a crossover to a regime dominated by dissipation (the imaginary part of χ_{L} in red) as the frequency increases. Note that $\mathcal{L}'$ plateaus at low frequency, but decays to zero at high frequency. In turn, $\mathcal{L}''$ decays to zero both at low and high frequencies, though it decays slower than $\mathcal{L}'$ at large v, except in the limit of very large u and v, where both $\mathcal{L}'$ and $\mathcal{L}''$ decay as $v^{-1/2}$. Thus, there is a frequency scale in which $\mathcal{L}' \sim \mathcal{L}''$, characterizing a crossover to a regime where the imaginary dissipative part dominates the dynamic response. From Eq. (A.18), we find that $\omega \sim D^* q^2$ in this regime, leading to the definition of an effective diffusion constant

$$D^* \sim |\delta p|^{(z-2)\nu}. \tag{A.26}$$

Using the exponents shown in Table A.1, we find that $D^* \sim O(1)$ and $\sim |\delta p|$ for jamming and RP, respectively. In terms of rescaled variables, this crossover happens at $v \sim u^2$ (see Fig. 2(b) and (d) of our companion manuscript [**?**]). In the liquid phase [(b) and (d)], $\mathcal{L}'$ behaves as in the elastic phase, but $\mathcal{L}''$ diverges rather than vanishing at low v due to the predominant viscous response of the fluid state.

Equations (A.18) and (A.22) also imply that our universal functions for the longitudinal response $\mathcal{L}(u, v, w)$ and $\bar{\mathcal{L}}(u, v)$ generally behave as $u^\alpha v^\beta$ with the exponents α and β depending on the region in the u (rescaled wavector) $\times$ v (rescaled frequency) plane. To illustrate and map this global behavior, we show in Fig. A.4 the power-law regions for which $\mathcal{L}(u, v, w) \propto u^\alpha v^\beta$ and $\bar{\mathcal{L}}(u, v) \propto u^\alpha v^\beta$, with (α, β) very close to their asymptotic values. The first and second rows correspond to our scaling forms for jamming and RP, respectively. To generate

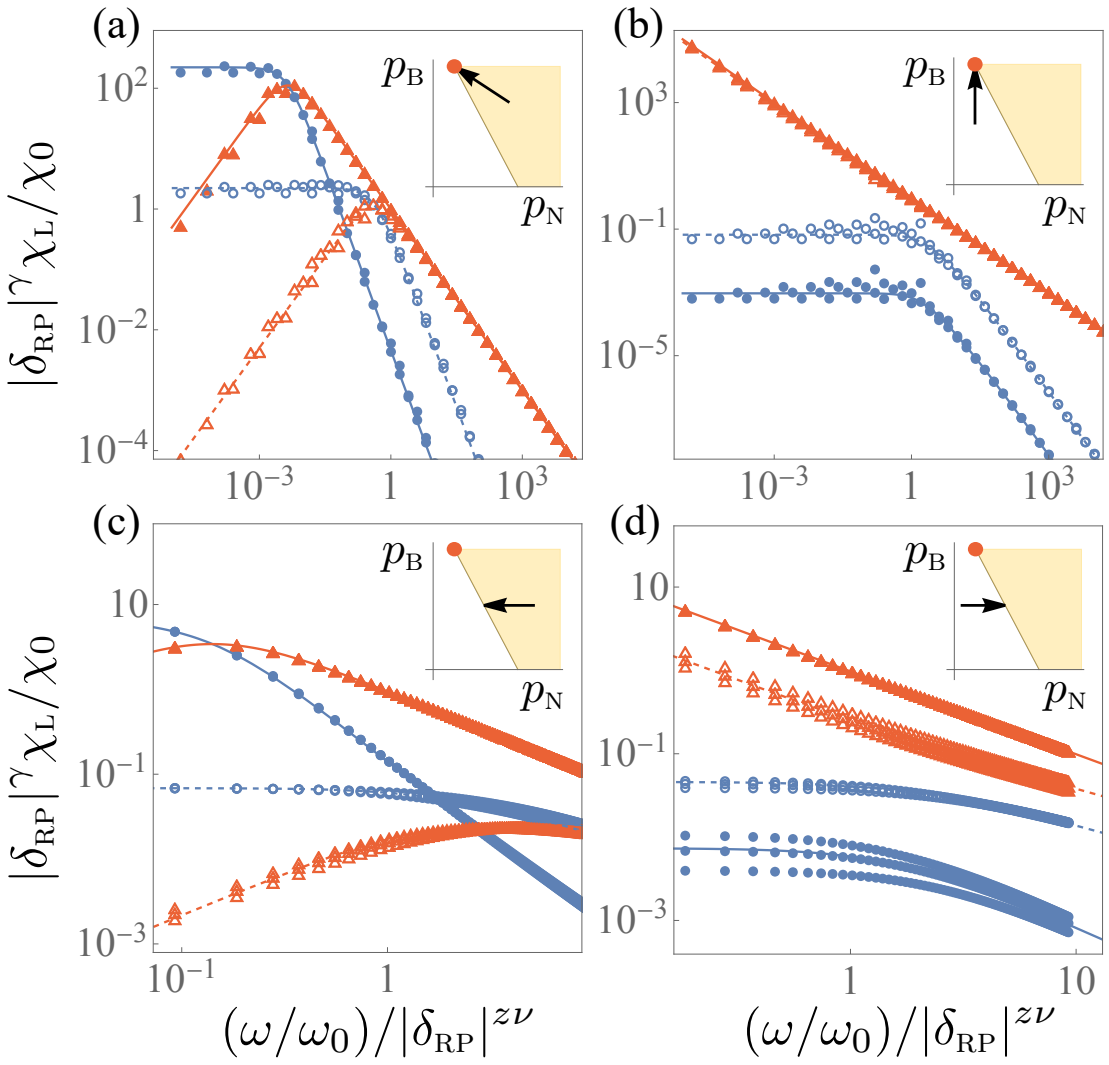

Figure A.3: Scaling collapse plots showing the universal behavior of the longitudinal response as a function of rescaled frequency near jamming (first row) and RP (second row), for overdamped dynamics. Blue disks and red triangles are full solutions of the EMT equations for the real and imaginary parts of $|\delta p|^\gamma \chi_L/\chi_0$, respectively. Solid and dashed curves are the universal scaling predictions of Eqs. (A.18) and (A.22). We consider points approaching jamming and RP along the paths indicated in the inset graphs of each panel. We use $q/|\delta p|^\nu = 0.1$ (closed symbols) and 1 (open symbols) in all panels, and $\delta p_B/|\delta p|^\varphi$ equal to $\sqrt{5}/4$ from the rigid side (a), and equal to 2 from the floppy side (b). Full solutions run at $|\delta p| = 10^{-2}$, 10^{-3}, and 10^{-4} for RP and a range $|\delta p| \in [5\times10^{-2}, 5\times10^{-6}]$ for jamming show convergence to our universal asymptotic predictions.

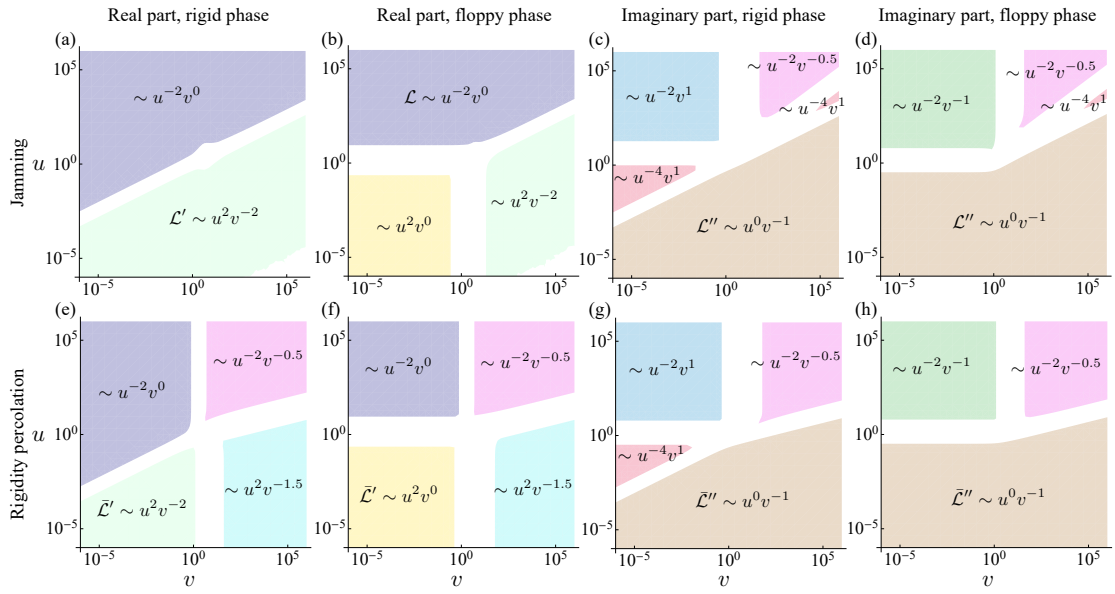

Figure A.4: **Overdamped asymptotic exponents for universal longitudinal response.** Diagram in the u (rescaled wavevector) $\times v$ (rescaled frequency) plane, showing regions of distinct power-law behavior of the jamming (first row) and RP (second row) universal scaling functions for overdamped dynamics in both the rigid and floppy phases. The first and second (third and fourth) columns correspond to the real (imaginary) parts of $\mathcal{L}$ and $\bar{\mathcal{L}}$. We use $w = 1$ for jamming.

each panel, we numerically calculate the exponents using $f_\alpha \equiv \partial \log \mathcal{L}/\partial \log u$ and $f_\beta \equiv \partial \log \mathcal{L}/\partial \log v$ for jamming and similar formulas for RP. We then plot the regions in which $|f_\alpha - \alpha| < 0.1$ and $|f_\beta - \beta| < 0.1$, for several values of α and β.

Figure A.4 offers a vivid pictorial view allowing an easier assessment of the global behavior associated with our universal forms for jamming and rigid percolation. By comparing the two rows, notice how the change in universality class is also reflected in the behavior of the universal scaling functions. For instance, although jamming and RP exhibit similar qualitative features for the imaginary part [(c), (d), (g) and (h)], RP shows additional regimes for the real part, which do not appear in jamming [compare e.g. (a) and (e) or (b) and (f)].

A.4.2 Undamped dynamics

Now we repeat the analysis of section A.4.1 using $\tilde{\omega}(\omega) = \rho\,\omega^2$ in Eq. (A.7), i.e. for the undamped case. Figure A.5 shows a scaling collapse plot for the rescaled longitudinal response as a function of rescaled frequency at fixed values of $q/|\delta p|^{\nu}$ for jamming and RP (first and second rows, respectively), and at fixed values of $\delta_{\mathrm{I}}/|\delta p|^{\varphi}$ for jamming. We consider several values of $|\delta p|$ corresponding to points approaching jamming and RP along the paths shown in the insets of Fig. A.3, so that e.g. the path for panel A.5(a) is the same as the one shown in the inset of panel A.3(a). The real part of $|\delta p|^{\gamma}\chi_{\mathrm{L}}/\chi_0$ can be negative; hence it is shown in linear scale in the insets of each panel of Fig. A.5. Note that the full solutions of our effective-medium theory equations converge to our universal scaling functions, except in the limit of very low frequencies, which we briefly discuss below.

The asymptotic solutions derived in [2] do not capture the small but nonzero imaginary parts of the effective spring constants at frequencies smaller than $\sim \omega^*$ (the characteristic crossover to isostaticity) when there is no damping. This feature has important consequences for energy dissipation in systems believed to exhibit behavior related to RP. The corrections to scaling appear as singular perturbations to the self-consistency equations and vanish as powers of $|\delta p|$ in dimensions larger than three. Moreover, the scaling variables contain logarithms in two dimensions. This analysis is beyond the scope of the present work, and will be presented in a separate manuscript.

Figure A.6 shows the global asymptotic behavior of our universal scaling functions for the longitudinal response near jamming (first row) and RP (second row). We use the same approach that we have used to make Fig. A.4, as

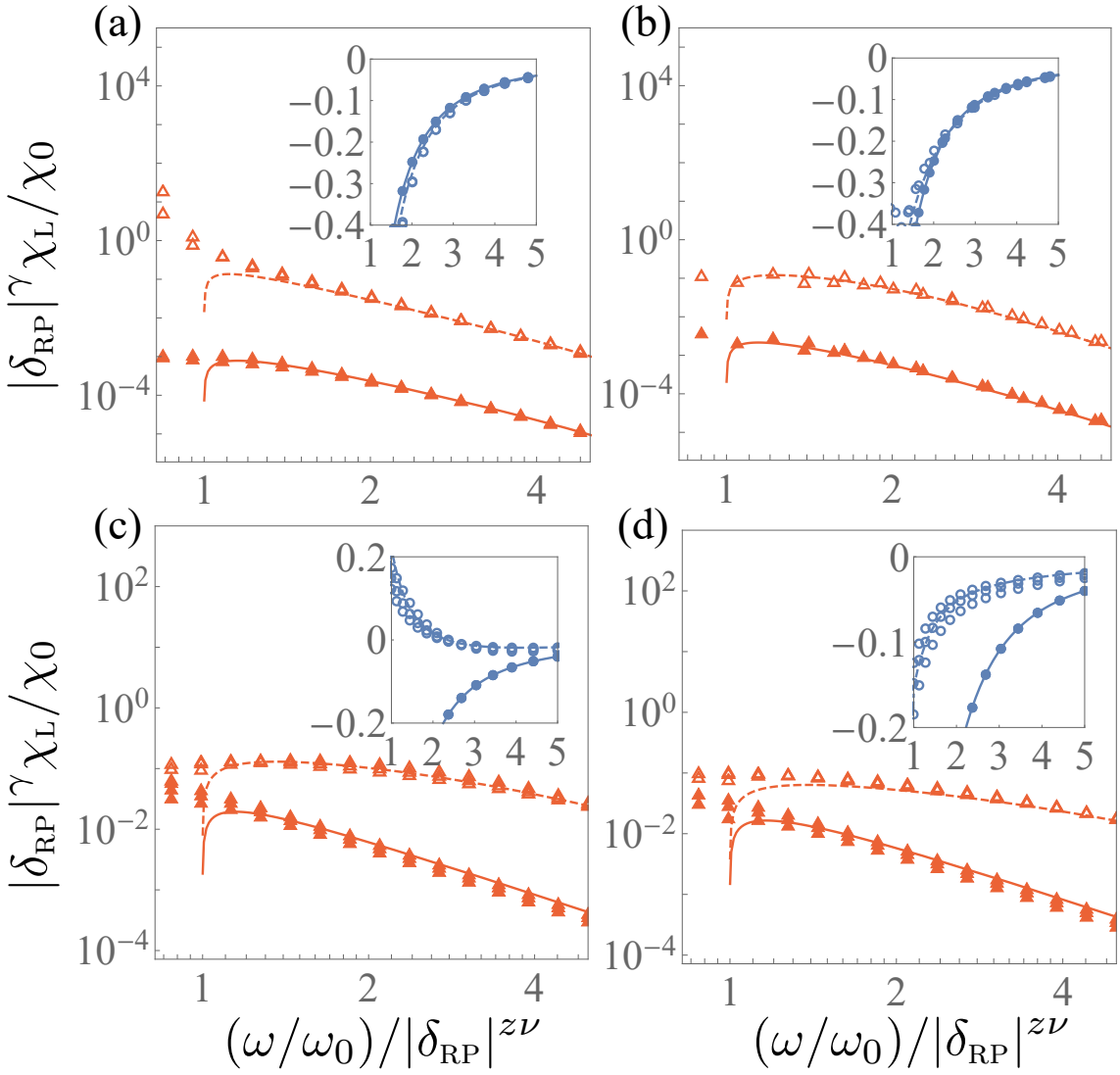

Figure A.5: Scaling collapse plots showing the universal behavior of the longitudinal response as a function of rescaled frequency near jamming (first row) and RP (second row), for undamped dynamics. Blue disks and red triangles are full solutions of the EMT equations for the real and imaginary parts of $|\delta p|^{\gamma}\chi_{\rm L}$, respectively. Solid and dashed curves are the universal scaling predictions of Eqs. (A.18) and (A.22). We consider points approaching jamming and RP along the same paths indicated in the inset graphs of each panel of Fig. A.3; for instance, the path for panel (a) is the same as the one shown in the inset of Fig. A.3(a), etc. We use $q/|\delta p|^{\gamma} = 0.1$ (closed symbols) and 1 (open symbols) in all panels, and $\delta p_{\rm B}/|\delta p|^{\varphi}$ equal to $\sqrt{5}/4$ from the rigid side (a), and equal to 2 from the floppy side (b). Full solutions run at $|\delta p| = 10^{-2}$, 10^{-3}, and 10^{-4} for both jamming and RP show convergence to our universal asymptotic predictions.

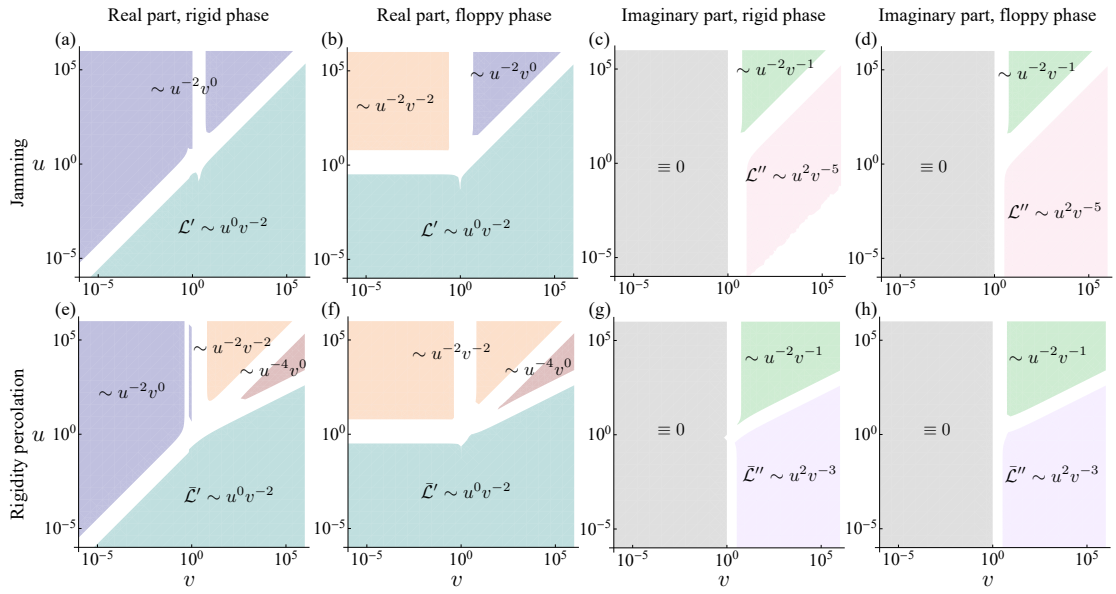

Figure A.6: **Undamped asymptotic exponents for universal longitudinal response.** Diagram in the u (rescaled wavevector) $\times v$ (rescaled frequency) plane, showing regions of distinct power-law behavior of the jamming (first row) and RP (second row) universal scaling functions for undamped dynamics in both the rigid and floppy phases. The first and second (third and fourth) columns correspond to the real (imaginary) parts of $\mathcal{L}$ and $\bar{\mathcal{L}}$. We use the crossover invariant scaling combination $w = 1$.

described in Sec. A.4.1. Notice that the lack of an imaginary part of our scaling functions at low frequency is indicated by gray regions on the left sides of panels (c), (d), (g) and (h). Again, it is straightforward to compare jamming and RP, or the behavior in the rigid and floppy phases. As in the overdamped case, the finite bulk modulus at jamming leads to a disparate global behavior of the scaling forms, in comparison with RP.

A.5 Derivation of the scaling behavior of other quantities

Our scaling Ansatz for the longitudinal response [Eqs. (A.17) and (A.21)], along with our explicit formulas for the universal functions [Eqs. (A.18) and (A.22)],

allow us to derive more general scaling forms for many quantities. Here we present a derivation of the universal scaling functions and critical exponents for the transverse dynamic response, bulk and shear moduli, bulk and shear viscosities, density response and correlation functions.

A.5.1 Transverse dynamic response

To extract the universal scaling functions and critical exponents associated with the transverse dynamic response, we follow the same steps that we used in Sec. A.3.2. We start with the long-wavelength limit of the transverse component of the dynamic response function χ_{T} of an isotropic viscoelastic material [209, 36, 210, 37]:

$$\chi_{\mathrm{T}} = \left\{-\rho\,\omega^2 - i\gamma\omega + q^2\,G(\omega)\right\}^{-1}. \tag{A.27}$$

Near jamming, the complex shear modulus $G(\omega)$ satisfies Eq. (A.11), so that

$$\chi_{\mathrm{T}} \approx \left\{-\rho\,\omega^2 - i\gamma\omega + q^2 g|\delta p|^{\beta_{\mathrm{G}}}\mathcal{M}_{\pm}\left(\frac{\omega}{|\delta p|^{z\nu}}\right)\right\}^{-1}, \tag{A.28}$$

where $z\nu = 1$ and 2 for undamped and overdamped dynamics, respectively. Multiplying both sides by $|\delta p|^2$, we obtain

$$|\delta p|^2\chi_{\mathrm{T}} \approx \left\{-\rho\left(\frac{\omega}{|\delta p|}\right)^2 - i\,\gamma\,\frac{\omega}{|\delta p|^2} + g\left(\frac{q}{|\delta p|^{1/2}}\right)\mathcal{M}_{\pm}\left(\frac{\omega}{|\delta p|^{z\nu}}\right)\right\}^{-1}, \tag{A.29}$$

which leads to

$$\frac{\chi_{\mathrm{T}}}{\chi_0} \approx |\delta p|^{-\gamma_{\mathrm{T}}}\bar{\mathcal{L}}\left(\frac{q/q_0}{|\delta p|^{\nu}}, \frac{\omega/\omega_0}{|\delta p|^{z\nu}}\right), \tag{A.30}$$

where $\bar{\mathcal{L}}$ is given by Eq. (A.22), and the nonuniversal scaling factors χ_0, q_0 and ω_0 are not necessarily the same as the ones used for the longitudinal response. The

critical behavior of χ_T does not change if one approaches RP instead of jamming. The exponent $\gamma_T = \gamma = 2$, and the exponents z and ν are the same as the ones for the longitudinal response near RP (see Table A.1).

A.5.2 Elastic moduli and viscosities

We have already reviewed the scaling behavior of the elastic moduli in Sec. A.3.1 [see Eqs. (A.9) and (A.11)]. Here we present an alternative approach that leverages the connection between the dynamic response and the moduli leading to critical exponents and universal scaling functions for B and G.

Near jamming, Eq. (A.12) leads to

$$B \approx \frac{1}{2\,q}\frac{\partial {\chi_L}^{-1}}{\partial q}. \tag{A.31}$$

Using Eq. (A.17), we then find,

$$\begin{aligned} B &\approx {\chi_0}^{-1}\frac{1}{2\,q}|\delta p|^{\gamma}\frac{\partial \mathcal{L}^{-1}}{\partial q} \\ &= \frac{({\chi_0\,q_0}^2)^{-1}}{2\,((q/q_0)/|\delta p|^{\nu})}|\delta p|^{\gamma-2\nu}\frac{\partial \mathcal{L}^{-1}}{\partial((q/q_0)/|\delta p|^{\nu})}, \end{aligned} \tag{A.32}$$

so that,

$$\frac{B}{B_0} \approx |\delta p|^{\beta_B}\mathcal{B}\left(\frac{q/q_0}{|\delta p|^{\nu}}, \frac{\omega/\omega_0}{|\delta p|^{z\nu}}, \frac{\delta p_B/\delta_0}{|\delta p|^{\varphi}}\right), \tag{A.33}$$

where B_0 is a a nonuniversal scaling factor,

$$\beta_B = \gamma - 2\,\nu, \tag{A.34}$$

and

$$\mathcal{B}(u,v,w) = \frac{1}{2\,u}\frac{\partial}{\partial u}\left[\frac{1}{\mathcal{L}(u,v,w)}\right]. \tag{A.35}$$

Near rigidity percolation, the universal function $\mathcal{B}(u,v,w) \to \bar{\mathcal{B}}(u,v)$, which is given by Eq.(A.35) with $\mathcal{L}$ replaced by $\bar{\mathcal{L}}$.

To derive the scaling for the shear modulus, we follow the same steps described in the last paragraph. Now we explore the connection between G and the transverse response χ_{T}. Equation (A.27) leads to

$$G = \frac{1}{2\,q}\frac{\partial {\chi_{\mathrm{T}}}^{-1}}{\partial q}, \tag{A.36}$$

which is valid near both jamming and RP. Using Eq. (A.30), we then find,

$$\begin{aligned} G &\approx \chi_0^{-1}\frac{1}{2\,q}|\delta p|^{\gamma_{\mathrm{T}}}\frac{\partial \bar{\mathcal{L}}^{-1}}{\partial q} \\ &= \frac{(\chi_0 {q_0}^2)^{-1}}{2\,((q/q_0)/|\delta p|^{\nu})}|\delta p|^{\gamma_{\mathrm{T}}-2\nu}\frac{\partial \bar{\mathcal{L}}^{-1}}{\partial((q/q_0)/|\delta p|^{\nu})}, \end{aligned} \tag{A.37}$$

so that,

$$\frac{G}{G_0} \approx |\delta p|^{\beta_{\mathrm{G}}}\mathcal{G}\left(\frac{q/q_0}{|\delta p|^{\nu}}, \frac{\omega/\omega_0}{|\delta p|^{z\nu}}\right), \tag{A.38}$$

where G_0 is a nonuniversal scaling factor,

$$\beta_{\mathrm{G}} = \gamma_{\mathrm{T}} - 2\,\nu, \tag{A.39}$$

with $\gamma_{\mathrm{T}} = 2$ and $\nu = 1/2$ for RP (see Table A.1). The universal scaling function

$$\mathcal{G}(u, v) = \frac{1}{2\,u}\frac{\partial}{\partial u}\left[\frac{1}{\bar{\mathcal{L}}(u, v)}\right]. \tag{A.40}$$

As expected, the scaling of G near both RP and jamming is the same as the scaling behavior of B near RP.

To extract the scaling behavior for the bulk and shear viscosities, we use the definitions $\zeta = B''(\omega)/\omega$ and $\eta = G''(\omega)/\omega$, so that,

$$\frac{\zeta}{\zeta_0} = |\delta p|^{-\gamma_{\mathrm{B}}}\mathcal{Z}\left(\frac{q/q_0}{|\delta p|^{\nu}}, \frac{\omega/\omega_0}{|\delta p|^{z\nu}}, \frac{\delta p_{\mathrm{B}}/\delta_0}{|\delta p|^{\varphi}}\right), \tag{A.41}$$

$$\frac{\eta}{\eta_0} = |\delta p|^{-\gamma_{\mathrm{G}}}\mathcal{E}\left(\frac{q/q_0}{|\delta p|^{\nu}}, \frac{\omega/\omega_0}{|\delta p|^{z\nu}}\right), \tag{A.42}$$

where ζ_0 and η_0 are nonuniversal scaling factors,

$$\gamma_{\mathrm{B}} = (2 + z)\,\nu - \gamma, \tag{A.43}$$

$$\gamma_{\mathrm{G}} = (2 + z)\,\nu - \gamma_{\mathrm{T}}, \tag{A.44}$$

with the exponents z and ν on the r.h.s. of Eqs. (A.42) and (A.44) corresponding to the ones listed in Table A.1 for RP, and

$$\mathcal{Z}(u, v, w) = \frac{1}{v} \operatorname{Im}\left[\mathcal{B}(u, v, w)\right], \tag{A.45}$$

$$\mathcal{E}(u, v) = \frac{1}{v} \operatorname{Im}\left[\mathcal{G}(u, v)\right], \tag{A.46}$$

are the universal scaling functions. Near RP, $\mathcal{Z}(u, v, w) \to \bar{\mathcal{Z}}(u, v)$, which is given by Eq. (A.45) with $\mathcal{B}$ replaced by $\bar{\mathcal{B}}$. As expected, $\mathcal{E}$ does not change near rigidity percolation.

A.5.3 Density Response

The derivation of the density response Π proceeds from the equations of motion, in a way that is similar to the derivation of χ_{L} [36]. Whereas $\chi_{\mathrm{L}} \equiv u_{\mathrm{L}}/f_{\mathrm{L}}$ is defined in Fourier space as the ratio of the longitudinal part of the displacement field u_{L} to its conjugate external field f_{L}, the density response can be defined as $\Pi \equiv n/h$, where n is the density and h is the density conjugate field. For small displacements,

$$n \equiv n_0 \left(1 - i\, q\, u_{\mathrm{L}}\right) \tag{A.47}$$

where n_0 is a constant given by the average background density. The appropriate conjugate field in Fourier space that linearly couples to the density in the Hamiltonian is $h \equiv f_{\mathrm{L}}/(i\, q\, n_0)$. Recasting the equation of motion for u as an equation of motion for n leads to a factor of q^2 originating from the divergence operator in Eq.(A.47) and another factor of q that is present in the definition of h. Thus,

$$\Pi = d' q^2 \chi_{\mathrm{L}}, \tag{A.48}$$

where d' is a constant.

Equations (A.48) and (A.17) lead to

$$\Pi \approx \chi_0 \, {q_0}^2 d' \left(\frac{q/q_0}{|\delta p|^{\nu}} \right)^2 |\delta p|^{2\,\nu} \, |\delta p|^{-\gamma} \mathcal{L}, \tag{A.49}$$

resulting in the scaling form:

$$\frac{\Pi}{\Pi_0} \approx |\delta p|^{-(\gamma-2\nu)} \mathcal{P}\left(\frac{q/q_0}{|\delta p|^{\nu}}, \frac{\omega/\omega_0}{|\delta p|^{z\nu}}, \frac{\delta p_{\mathrm{B}}/\delta_0}{|\delta p|^{\varphi}} \right), \tag{A.50}$$

which reduces to

$$\frac{\Pi}{\Pi_0} \approx |\delta p|^{-(\gamma-2\nu)} \bar{\mathcal{P}}\left(\frac{q/q_0}{|\delta p|^{\nu}}, \frac{\omega/\omega_0}{|\delta p|^{z\nu}} \right), \tag{A.51}$$

near RP, where Π_0 is a nonuniversal scaling factor, and

$$\mathcal{P}(u, v, w) = u^2 \mathcal{L}(u, v, w), \tag{A.52}$$

$$\bar{\mathcal{P}}(u, v) = u^2 \bar{\mathcal{L}}(u, v). \tag{A.53}$$

A.5.4 Correlation functions

We end this section with derivations of the scaling behavior of the Ursell function $S_{nn}(q, \omega)$ (the structure factor for isotropic fluids at nonzero q) and the scaling behavior of the density-density correlation function in real space: $S_{nn}(r, r', t, t') = \langle n(r, t) n(r', t') \rangle - \langle n(r, t) \rangle \langle n(r', t') \rangle$.

Using the fluctuation-dissipation theorem [36, 210],

$$\omega \, S_{nn}(q, \omega) = 2 \, T \, \mathrm{Im} \left[\Pi(q, \omega) \right], \tag{A.54}$$

where T is the temperature, and Eq. (A.50), we obtain

$$\begin{aligned} S_{nn}(q, \omega) &\approx \Pi_0 \frac{2\,T}{\omega} \, \mathrm{Im} \left[|\delta p|^{-(\gamma-2\nu)} \mathcal{P} \right] \\ &= \frac{2\,T\,\Pi_0\,{\omega_0}^{-1}}{(\omega/\omega_0)/|\delta p|^{z\nu}} \, |\delta p|^{-z\nu-(\gamma-2\nu)} \mathrm{Im} \left[\mathcal{P} \right], \end{aligned} \tag{A.55}$$

so that

$$\frac{S_{nn}(q,\omega)}{\tilde{S}_0} \approx |\delta p|^{-[\gamma+(z-2)\nu]} \times \mathcal{S}\left(\frac{q/q_0}{|\delta p|^{\nu}}, \frac{\omega/\omega_0}{|\delta p|^{z\nu}}, \frac{\delta p_{\rm B}/\delta_0}{|\delta p|^{\varphi}}\right), \tag{A.56}$$

which reduces to:

$$\frac{S_{nn}(q,\omega)}{\tilde{S}_0} \approx |\delta p|^{-[\gamma+(z-2)\nu]} \bar{\mathcal{S}}\left(\frac{q/q_0}{|\delta p|^{\nu}}, \frac{\omega/\omega_0}{|\delta p|^{z\nu}}\right), \tag{A.57}$$

near RP, where $\tilde{S}_0$ is a nonuniversal scaling factor, and

$$\mathcal{S}(u,v,w) = \frac{1}{v}\mathrm{Im}\left[\mathcal{P}(u,v,w)\right], \tag{A.58}$$

$$\bar{\mathcal{S}}(u,v) = \frac{1}{v}\mathrm{Im}\left[\bar{\mathcal{P}}(u,v)\right]. \tag{A.59}$$

The two-time density-density correlation function $S_{nn}(r-r',t-t')$ is given by,

$$\begin{aligned} S_{nn}(r-r',t-t') &= \int d\omega \int d\mathbf{q}\, e^{-i\omega(t-t')+i\mathbf{q}\cdot(r-r')} \\ &\quad \times S_{nn}(q,\omega) \\ &= \int d\left(\frac{\omega/\omega_0}{|\delta p|^{z\nu}}\right) \int d\left(\frac{\mathbf{q}/{q_0}^D}{|\delta p|^{\nu}}\right) |\delta p|^{(z+D)\nu} \omega_0\, {q_0}^D \\ &\quad \times \exp\left\{ i\left[\frac{\mathbf{q}/q_0}{|\delta p|^{\nu}} \cdot \frac{(r-r')/\ell_0}{|\delta p|^{-\nu}} - \frac{\omega/\omega_0}{|\delta p|^{z\nu}} \frac{(t-t')/t_0}{|\delta p|^{-z\nu}} \right] \right\} \\ &\quad \times S_{nn}(q,\omega), \end{aligned} \tag{A.60}$$

where $\ell_0 \equiv {q_0}^{-1}$ and $t_0 \equiv {\omega_0}^{-1}$ are nonuniversal scaling factors. Using Eq. (A.56), we then obtain

$$\frac{S_{nn}(r,r',t,t')}{S_0} \approx |\delta p|^{(2+D)\nu-\gamma} \times \mathcal{S}\left(\frac{(r-r')/\ell_0}{|\delta p|^{-\nu}}, \frac{(t-t')/t_0}{|\delta p|^{-z\nu}}, \frac{\delta p_{\rm B}/\delta_0}{|\delta p|^{\varphi}}\right), \tag{A.61}$$

which reduces to

$$\frac{S_{nn}(r,r',t,t')}{S_0} \approx |\delta p|^{(2+D)\nu-\gamma} \times \bar{\mathcal{S}}\left(\frac{(r-r')/\ell_0}{|\delta p|^{-\nu}}, \frac{(t-t')/t_0}{|\delta p|^{-z\nu}}\right), \tag{A.62}$$

near RP, where

$$\mathcal{S}(\rho, s, w) = \int d\mathbf{u}\, dv\, e^{i(u\cdot\rho - vs)}\, \frac{\mathrm{Im}\,\mathcal{P}(u, v, w)}{v}, \tag{A.63}$$

$$\bar{\mathcal{S}}(\rho, s) = \int d\mathbf{u}\, dv\, e^{i(u\cdot\rho - vs)}\, \frac{\mathrm{Im}\,\bar{\mathcal{P}}(u, v)}{v}. \tag{A.64}$$

Note that Eqs. (A.61) and (A.62) lead to natural definitions of diverging length and time scales, $\ell = |\delta p|^{-\nu}\ell_0$ and $\tau = |\delta p|^{-z\nu}t_0$, respectively. Interestingly, the time scale divergence is the same for jamming and RP, with $z\nu = 1$ for undamped dynamics, and 2 for overdamped dynamics. As it should be anticipated, our characteristic length scale diverges as $|\delta p|^{-1}$ for jamming, and as $|\delta p|^{-1/2}$ for RP. These divergences should be compared with traditional definitions of $\ell_c \sim |\Delta z|^{-1/2}$ and $\ell^* \sim |\Delta z|^{-1}$, as discussed in the literature [56, 57, 58, 38, 39].

A.6 Connections with experiments

The scaling behavior for quantities such as the moduli, viscosities, and correlation functions derived in Sec. A.5 provide an approach for experimentally validating our results. These quantities are commonly measured in a number of relevant experimental systems including emulsions, foams, colloidal particles and granular materials [14, 211, 212, 213, 214, 215, 216]. A careful experiment mapping out how one or more of these quantities evolve upon approaching rigidity could be compared to the critical exponents or even the analytical forms of our universal scaling functions near the jamming and rigidity percolation transitions.

One approach for experimental validation is to directly fabricate disordered

elastic networks such as those shown in Fig. A.1 using 3D printers or laser-cut 2D sheets [207]. A number of networks could be created at different distances from the RP or jamming point. A set of experiments apply compression or shear could then measure the bulk or shear moduli. Measuring how the moduli change with distance from RP or jamming should then allow experimental measurement of both the critical scaling exponents and the universal functions.

The scaling forms we derive might also apply to common experimental glass-formers such as colloidal suspensions. The density-density correlation function provide an accessible path to experimentally validate our universal scaling function. Recent advances in locating colloidal particles using optical microscopy allow highly precise measurements of particle positions and even local stresses [60, 61, 62, 63]. These techniques can be applied to settling system of colloidal silica particles to observe the approach to jamming. Measurements of the two-time density-density correlation function for volume fractions approaching either RP or jamming could be compared to our analytical forms and used to experimentally measure the critical exponents involved. Alternatively, experimental scattering data could allow for relatively easy comparison with our structure factor derivations above. Either approach would allow fitting to our universal scaling functions.

A number of difficulties still remain for this experimental validation approach. One obstacle is noise in experimental measurements of the density-density correlation function. While state-of-the-art methods for locating particles are very precise, the density-density correlation function still becomes noisy at longer ranges so measurements of correlation scaling will require much care. Additionally, the scaling variables δp_{B} and δp are defined based on knowledge

of the volume fraction for jamming and rigidity percolation. The jamming and rigidity percolation volume fractions are well known for monodisperse hard spheres, but are different for a binary sample (which is often needed to prevent crystalization) and may have to be calculated for any specific sample. Since our universal scaling form applies to a whole class of systems, we remain confident that the right system and experimental protocol could experimentally validate our results.

A.7 Summary

In this paper, we have presented a detailed analysis of the universal scaling behavior of disordered viscoelastic materials near the onset of rigidity. Combining an Ansatz for the longitudinal dynamic response with a semi-analytical effective-medium theory, we have been able to extract critical exponents and explicit formulas for universal scaling functions associated with a variety of quantities, such as elastic moduli, viscosities and correlation functions. We expect these scaling forms to apply to a large number of systems, from colloidal suspensions and soft gels to the density fluctuations in certain classes of strange metals [65].

Possible extensions of our analysis include the incorporation of ingredients such as an anisotropic distribution of bonds, which plays an important role in the behavior of colloidal suspensions undergoing shear thickening or shear jamming transitions [68]. Other extensions involve the inclusion of thermal effects [217, 218], normal forms or corrections to scaling at the upper critical dimension [49], and an annealed [34] or partially-annealed [64] distribution of

bonds; the latter might be better suited for a description of the fluid phase. Finally, it would be interesting to investigate the effects on the critical scaling of jamming or RP caused by quenched random fields modeling active behavior.

A.8 Acknowledgments

We thank Andrea Liu, Bulbul Chakraborty, Daniel Hexner, Eleni Katifori, Emanuela del Gado, Itay Griniasty, Matthieu Wyart, Meera Ramaswamy, Peter Abbamonte, Sean Ridout, Tom Lubensky and Xiaoming Mao for useful conversations. This work was supported in part by NSF DMR-1719490 (SJT and JPS), NSF CBET Award # 2010118 (DBL, ES, JPS, and IC) and NSF CBET Award # 1509308 (ES and IC). DBL also thanks ICTP-SAIFR for partial financial support through FAPESP grant # 2016/01343-7. DC is supported by a faculty startup grant at Cornell University.

APPENDIX B

APPENDIX OF CHAPTER 3

This Appendix is a reformatted version of the S.I. of [65].

B.1 Supplementary Information

B.1.1 Effective medium theory

As noted in the main text, we model the system as a layered structure consisting of two-dimensional randomly populated lattices of harmonic springs. The local deformations associated with the configurations (e.g. compression) are assumed to capture the fluctuations associated with an underlying electronic liquid; see Fig. B.1. We make an analogy between the strongly overdamped plasmon in a class of strange metals and the strongly overdamped phonon in viscoelastic systems near the onset of rigidity. One of the features of rigidity percolation (and jamming) is a nearly flat density of states at the transition, which corresponds to an anomalously large number of low-energy excitations into which an excited phonon can decay. This is captured in randomly populated networks analytically by an effective-medium theory known as the coherent potential approximation (CPA) [2].

In this model, we begin with a fully occupied lattice with unit elastic coefficients (harmonic springs) and randomly dilute the lattice, keeping each bond with probability p. To study the dynamics of the disordered system, the CPA self-consistently replaces the Green's function of this randomly populated lattice with a spatially homogeneous disorder-averaged Green's function. The self-

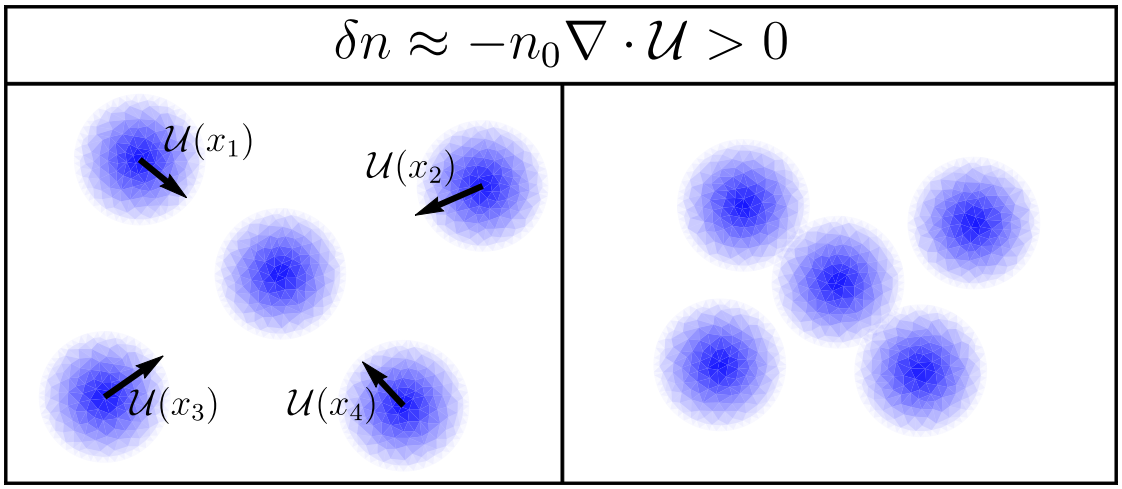

Figure B.1: The density-density response is connected to longitudinal fluctuations of the displacement. Shown here is a local compression wave increasing the local density of charged particles; the precise composition of the charged low-energy excitations is not known.

energy calculated in this framework is typically recast as a frequency-dependent elastic coefficient $\mathcal{K}(\omega)$. More generally, given several bond occupation probabilities $\{p_\alpha\}$, the CPA gives frequency-dependent elastic coefficients for each sublattice $\{\mathcal{K}_\alpha(\omega)\}$, where $\alpha = 1, 2\ldots$ is the sublattice index. This method faithfully reproduces the zero-frequency athermal phase diagram and phase transitions predicted by Maxwell's constraint counting arguments, where the number of constraints is equal to the number of degrees of freedom [2]. There is also experimental evidence that it properly reproduces the low-frequency behavior of other microscopically disordered systems undergoing rigidity transitions, such as soft gels [219, 220].

A specific type of phase transition that these randomly populated lattices can undergo is broadly known as *rigidity percolation*, when a disordered elastic network loses rigidity in a continuous fashion at $p = p_c$. This can be seen by examining the effective bulk modulus B and the shear modulus G of a bond-diluted lattice, defined by how the potential energy of the lattice U changes in

response to small linearized strains u_{ij}:

$$\Delta U = \frac{B}{2}\left(u_{xx}+u_{yy}\right)^2 + 2G\left[u_{xy}^2 + \frac{1}{4}\left(u_{xx}-u_{yy}\right)^2\right]. \tag{B.1}$$

The predicted zero-frequency bulk and shear moduli of these diluted lattices grow continuously from 0 across such a transition, as p grows larger than p_c. The density-density response near jamming is discontinuous across the critical point due to the jump in the bulk modulus, as opposed to the response near RP. The MEELS phenomenology is better captured in terms of RP, even though the nature of the anomalous low-energy excitations in the vibrational density of states is the same for both. This paper focuses on the *universal* behavior of *rigidity percolation*, that is, the characteristics of the phase transition that do not depend on the underlying microscopic lattice geometry.

For a single sublattice in two dimensions, the self-consistent equation for the elastic coefficients reads

$$\frac{p-\mathcal{K}(\omega)}{1-\mathcal{K}(\omega)} = \frac{1}{z}\frac{1}{s_{\mathrm{BZ}}}\int_{\mathrm{BZ}} \mathrm{d}^2 q\ \mathrm{Tr}\left[D\left(q,\mathcal{K}(\omega)\right)\left(D\left(q,\mathcal{K}(\omega)\right)-\omega^2 I\right)^{-1}\right] \tag{B.2}$$

where p is as defined earlier, $D(...)$ is the dynamical matrix, and z is the average number of bonds per unit cell. The derivation of the more general form of this expression can be found, for instance, in the supplemental material of [2].

By expanding the dynamical matrix for a general 2D isotropic lattice in the long-wavelength limit as

$$D_{ij}\left(\mathcal{K}(\omega)\right) = B\left(\mathcal{K}(\omega)\right) q^2 \hat{q}_i \hat{q}_j + G\left(\mathcal{K}(\omega)\right) q^2 \delta_{ij}, \tag{B.3}$$

we can evaluate the integral and solve the self-consistency equations. The combination $K_{\mathrm{L}} \equiv B + G$ is the only combination of moduli that enters the longitudinal response (and the density-density response), and must be proportional

to the only microscopic coupling in the problem $\mathcal{K}$. Writing the self-consistent equation for K_{L} and expanding to linear order in the distance to the continuous critical point $\delta p \equiv p - p_c$, one finds an expression involving only certain invariant scaling combinations. The coupling is found as the self-consistent solution to

$$\pm 1 - \widetilde{K}_{\mathrm{L}\pm} = \frac{\widetilde{\omega}'^2}{\widetilde{K}_{\mathrm{L}\pm}} \log\left(-\frac{\widetilde{K}_{\mathrm{L}\pm}}{\widetilde{\omega}'^2 \widetilde{Z}}\right), \tag{B.4a}$$

$$\widetilde{K}_{\mathrm{L}\pm} \equiv \frac{K_{\mathrm{L}\pm}}{K_{\mathrm{L}0}\,|\delta p|}, \tag{B.4b}$$

$$\widetilde{\omega}' \equiv \frac{\omega}{\omega_0'\,|\delta p|}, \tag{B.4c}$$

$$\widetilde{Z} \equiv Z_0\,|\delta p|\,. \tag{B.4d}$$

Here $K_{\mathrm{L}0}$, ω_0', and Z_0 are non-universal constants of order unity, and we choose their values from the bond-diluted mechanical triangular lattice with nearest-neighbor bonds for all plots. The + and − in the self-consistent equations refer to the "solid" ($p > p_c$) and "floppy" ($p < p_c$) sides of the transition, respectively. Asymptotically close to the transition, the solution to the above self-consistent effective medium equation is given by

$$\widetilde{K}'_{\mathrm{L}\pm}(\widetilde{\omega}'') = \pm 1 + \sqrt{1 - \widetilde{\omega}''^2}, \tag{B.5}$$

with $\widetilde{K}'_{\mathrm{L}\pm} \equiv K_{\mathrm{L}\pm}/K''_{\mathrm{L}0}\,|\delta p|$ and $\widetilde{\omega}'' \equiv \omega/\omega_0'' \left(|\delta p| \,/\, \left|\log\left(|\delta p|\right)\right|^{1/2}\right)$. The logarithm that appears in this scaling variable for the frequency is unique to 2 dimensions and does not affect the qualitative results of any of our calculations; this will be elaborated upon in a future manuscript [108]. The imaginary part of the square root should be interpreted as non-positive for causality reasons. The dissipation that is calculated within the CPA framework aims to capture phonon scattering off of "defects" introduced by the disorder. The vanishing of the imaginary part of $K_{\mathrm{L}}(\omega)$ at small but finite frequency does not survive universal corrections to

scaling; when the full CPA self-consistency equation is solved on the solid side ($\delta p > 0$), then $\mathrm{Im}\,(K_\mathrm{L}) < 0$ for all $\omega > 0$.

B.1.2 Universal scaling of the density-density response

The frequency-dependent elastic coefficient derived in the previous section can be used to determine the effective bulk and shear moduli of the elastic medium, which can be used to determine the long-wavelength density-density response. The form of our long-wavelength density-density response is calculated as follows: the equation of motion for an isotropic elastic sheet without external damping reads

$$\rho\,\ddot{\mathcal{U}} = B\nabla\,(\nabla\cdot\mathcal{U}) + G\nabla^2\mathcal{U} + \mathbf{f}^{\mathrm{ext}} \tag{B.6}$$

where ρ is the (constant) average background density and $\mathcal{U}$ is a small displacement field. B and G are proportional to $\mathcal{K}\,(\omega)$, and are hence frequency-dependent and complex. Assuming the local perturbation due to the external forcing field to be small, we expand $n \approx n_0\,(1-\nabla\cdot\mathcal{U}) = \rho/m\,(1-\nabla\cdot\mathcal{U})$; see Fig. B.1.

We then use the definition of the susceptibility as the change in the density as a result of the perturbing conjugate field, $\Pi \equiv -\delta n/\delta h$. Note that the additional negative sign in front of the susceptibility compared to [9, 45] is related to differing definitions for the susceptibility; we adopt the experimentalists' convention [66] where the imaginary part is negative for positive frequencies. Just as $\mathcal{U}$ and f are thermodynamic conjugates (because they enter the energy density as

$\mathcal{U} \cdot f$), so are $\delta n_q = i n_0 q \cdot \mathcal{U}_q$ and $\delta h_q = f_q^{\text{Lext}} / i n_0 q$. Thus,

$$\left(-\rho\omega^2 + (B+G)\, q^2\right) \delta n_q = n_0^2 q^2 \delta h_q, \tag{B.7}$$

$$\Pi \equiv -\frac{\delta n_q}{\delta h_q} = \frac{\rho^2 q^2}{m^2} \frac{1}{\rho\omega^2 - K_L(\omega)\, q^2}. \tag{B.8}$$

This allows us to write a universal form for the density-density response at rigidity percolation on both sides of the transition:

$$\widetilde{\Pi} = \frac{\widetilde{q}^2}{\widetilde{\omega}''^2 - \left(\sqrt{1 - \widetilde{\omega}''^2} \pm 1\right) \widetilde{q}^2} \tag{B.9}$$

where the appropriate scaling is found to be $\widetilde{q} \equiv q / q_0 \left(|\delta p|^{1/2} / \left| \log\left(|\delta p|\right) \right|^{1/2} \right)$ and $\widetilde{\Pi} \equiv \Pi\, |\delta p| / \Pi_0$. The $O(1)$ constants q_0 and Π_0 are non-universal. Since the scaling of B, G, and ω near rigidity percolation has already been fixed by the self-consistency equation, the scaling of q is found by balancing powers of δp in the denominator of the expression for Π. In practice, the corrections to scaling that fix the imaginary part at low frequencies are significant enough (they vanish as $\sim \left| \log |\delta p| \right|^{-1/2}$) that we numerically solve the self-consistent equations with $\widetilde{Z}$ included to find a more faithful representation of the CPA predictions. Finally, the effects of the long-ranged Coulomb interaction are added using the RPA (as described in the main text):

$$\chi(q, \omega) = \frac{\Pi(q, \omega)}{1 - V(q)\Pi(q, \omega)} \tag{B.10}$$

with the 3D Coulomb interaction $V(q) = 4\pi e^2 / q^2$.

The qualitative features that the CPA predicts for χ reflect what is expected of a lattice near a rigidity transition: sharply defined quasiparticles exist only at the longest wavelengths, and rapidly broaden with increasing q into an incoherent bump at a frequency $\Delta\omega_\star$ set by the distance to the rigidity percolation transition. If we are near the critical point, experimental probes of the response

will inevitably probe only the region of large $\widetilde{q}$, which leads to a q-independent shape of the response. In this model, a coherent quasiparticle can still be found near the center of the BZ.

For large values of $\widetilde{q}$, there is a range of frequencies where $\chi'' \sim \omega^{-1}$ decays slowly. For an experimental probe, this may indicate the violation of f-sum rules. However, at frequencies large enough, χ'' eventually decays as $\sim \omega^{-3}$ as predicted by Drude theory. Although the paradigm of proximity to a critical point with a large number of anomalously low-frequency modes serves to explain the q-independent shape of the response outside of the very center of the BZ, the shapes of the universal forms of the electronic response do not have the plateaus measured by the experiment. Because we have control over how our response depends on the distance to the critical point, we can investigate how long-wavelength disorder in a sample, represented by a distribution of distances to the critical point δp, modifies the observed form of the density-density response.

B.1.3 Averaging over the long-wavelength sample disorder

We imagine an experimental sample prepared on average close to a critical point δp, where different regions of the sample are allowed to have slightly different distances to the critical point with spread σ. The effect of this long-wavelength disorder is then represented by averaging the response over many distances to the critical point using a Gaussian of center δp and width σ:

$$\overline{\chi_{\delta p}(q,\omega)} = \int_{-\infty}^{\infty} d(\Delta p')\, P_\sigma(\Delta p')\, \chi_{\delta p'}(q,\omega) \tag{B.11}$$

$$P_\sigma[\Delta p'] = \frac{1}{\sqrt{2\pi\sigma^2}} e^{-(\Delta p')^2/2\sigma^2}, \tag{B.12}$$

where $\chi_{\delta p}(q, \omega)$ is the response at a fixed distance (δp) from RP, and we choose a Gaussian distribution, $P_\sigma[\Delta p]$, with width σ and $\Delta p' \equiv \delta p' - \delta p$. One could imagine other methods for averaging over the effect of the long-wavelength disorder. In this case, we adopt the procedure where the susceptibility (related to an inverse stiffness at zero frequency) is estimated as an arithmetic mean of the susceptibilities of different portions of the sample; this means that a large susceptibility in any portion of the sample corresponds to a large average susceptibility. One could also estimate the susceptibility as the inverse of the average inverse susceptibility, which would suppress the susceptibility if there is a small susceptibility in any portion of the sample. For an inhomogeneous medium, the effective susceptibility is bounded between these two options [221].

The solution to the full self-consistency equations including the corrections to scaling cannot be written in terms of elementary functions, so we estimate the convolution by picking many values of δp, computing χ'' over a range of frequencies by solving the full self-consistency equations, and performing an appropriate weighted average of the χ'' at the experimental values of q (which correspond to asymptotically large $\widetilde{q}$ for windows of δp very close to the critical point). These averaged responses $\overline{\chi}''$ are compared with the measured imaginary part of the density-density response from the experiment. We seek to describe the universal behaviour of the electronic response, and so we will not capture the additional *lattice* phonon seen in the experimental data at the lowest frequencies in [67]. The plots in Fig. B.2 are generated near rigidity percolation using a width of $\sigma = 1.2 \times 10^{-3}$ in probability space. The central distances to RP chosen are $\delta p = 1.0 \times 10^{-3}$ and $\delta p = 1.4 \times 10^{-3}$ and exhibit q-independence over a selected range of frequencies for $q \gg |\delta p|^{1/2} \,/\, \left|\log\left(|\delta p|\right)\right|^{1/2}$.

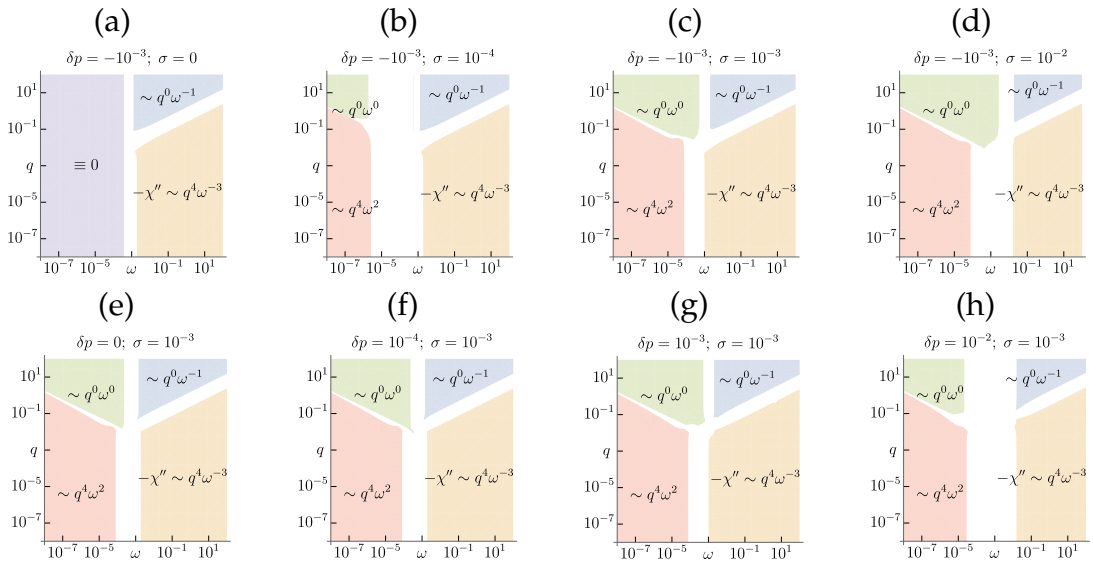

Figure B.2: Scaling regimes of the disorder-averaged susceptibilities near the rigidity transition. Plots (a)–(d) show fixed $\delta p = -10^{-3}$ near the transition on the liquid side with increasing σ, demonstrating the emergence of the disorder-averaged plateau. Plots (e)–(h) show the effect of varying δp into the solid side at fixed $\sigma = 10^{-3}$. In this case, the disorder-averaging becomes less relevant and the peak shifts into higher frequencies with the predicted scaling. The region of exactly 0 imaginary part in (a) is eliminated by corrections to scaling. Plots are similar at large q on the solid and liquid sides.

Without disorder averaging, for $q \gg |\delta p|^{1/2} / \left|\log\left(|\delta p|\right)\right|^{1/2}$, the susceptibility has a broad bump near $\omega_\star$ associated with the decay of the quasiparticle into the anomalous low-frequency modes. When disorder averaging is performed, a sequence of these bumps leads to the emergence of a low-frequency plateau terminating near $\omega_\star$. Above the plateau, this theory predicts a region where $\chi'' \sim \omega^{-1}$ crossing over into a region where $\chi'' \sim \omega^{-3}$ (the high-frequency Drude scaling). In the experiment, an exponent $1 \leq \alpha \leq 3$ is measured out to the highest frequencies.

The imaginary part of the susceptibility χ'' is odd in ω but contains a plateau that extends down to the lowest frequencies with increasing q. This results in a sharp feature at the lowest frequencies where the plateau ends and the response

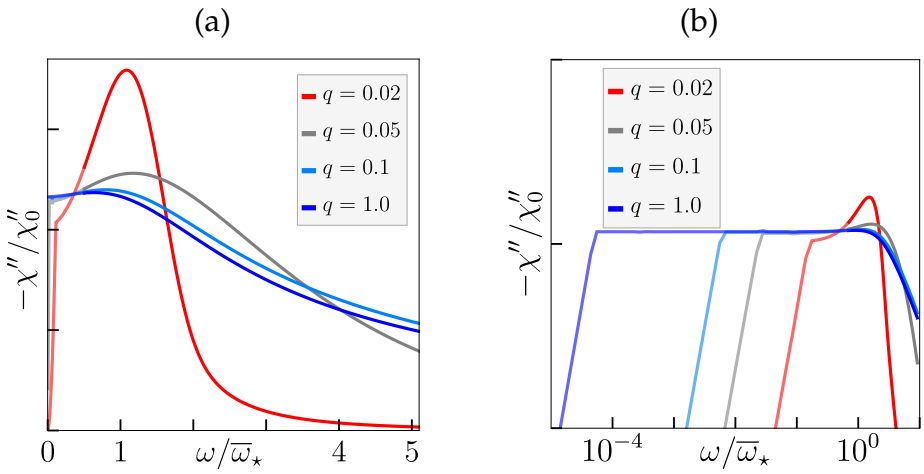

Figure B.3: Low frequency behavior of the disorder-averaged response, including an anomalous "sharp" feature at the lowest frequencies where the plateau crosses over into a power-law regime enforcing $\chi''(q, 0) = 0$. (a) is shown on a linear-linear scale, while (b) is shown on a log-log scale.

crosses over into power-law behavior to ensure $\chi''(q, 0) = 0$. The location of this feature can be deduced from Fig. B.2, where the green ($-\chi'' \sim q^0\omega^0$) and red ($-\chi'' \sim q^4\omega^2$) regions touch. Plots of the lowest frequency behavior are shown below in Fig. B.3 for the sake of completeness. In the experiment, the low frequency behavior shows a prominent feature tied to the lattice phonons, which is not included in our present theory.

APPENDIX C

APPENDIX OF CHAPTER 4

This is a reformatted version of the supplementary material of [108].

C.1 Scaling variables in terms of isotropic elastic sheet parameters

Here we expound upon the calculation mentioned in the main text that eventually leads to the universal scaling functions for the vanishing modulus. We take the perspective of a long-wavelength limit of a bond percolation CPA that is explicitly isotropic at long-wavelengths; this recovers the CPA for amorphous spring networks developed in [44]. First, we write the dynamical matrix and Green's function for an isotropic elastic sheet, with Lamé parameters λ and μ.[1] This is typically done in the reverse order using the constitutive relations (i.e. coarse-graining a lattice system with dynamical matrix $\mathbf{D}$), recovering the long-wavelength stiffness tensor $K_{ijk\ell}$. For a lattice with real-space unit cell volume V and n sites in the unit cell, we have

$$K_{ijk\ell} = \frac{n}{V}\left[\frac{1}{2}\frac{\partial^2 \mathbf{D}^{\mathrm{SS}}}{\partial q_j \partial q_\ell} - \frac{\partial \mathbf{D}^{\mathrm{SF}}}{\partial q_j}\left(\mathbf{D}^{\mathrm{FF}}\right)^{-1}\frac{\partial \mathbf{D}^{\mathrm{FS}}}{\partial q_\ell}\right]_{ik}\Bigg|_{\mathbf{q}=\mathbf{0}}, \tag{C.1}$$

where the dynamical matrix is written in the center-of-mass basis and the labels S and F represent the "slow" and "fast" normal modes [222] (essentially separating the acoustic modes from the optical). We are interested mainly in a

[1] We find it easier to work with Lamé parameters than with the bulk and shear moduli because the forms of the transverse and longitudinal parts of the Green's function and dynamical matrix are dimension-independent when written in terms of the Lamé parameters. However, μ and λ will be viscoelastic generalizations of their static versions in the same way that $\mu(\omega)$ is the viscoelastic generalization of the static shear modulus.

scaling that picks out low-frequency behavior, so we focus on the case $n = 1$ with no fast modes (investigating how the more general form interacts with the CPA is a fruitful avenue for future work, and is necessary to fully understand the jamming behavior of e.g. the system studied in [2]). In this case, the relation simply reads

$$K_{ijk\ell} = \frac{1}{2V} \frac{\partial^2 D_{ik}}{\partial q_j \partial q_\ell}\bigg|_{\mathbf{q}=\mathbf{0}}. \tag{C.2}$$

Using the form of $K_{ijk\ell}$ for an isotropic elastic medium, we find

$$\begin{aligned} \mathbf{D}(q) &= V(\lambda + 2\mu) q^2 \, \hat{q}_i \hat{q}_j + V\mu q^2 \left(\delta_{ij} - \hat{q}_i \hat{q}_j\right), \\ \mathbf{G}(q,\omega) &= \frac{1}{V(\lambda + 2\mu) q^2 - \mathrm{w}'} \, \hat{q}_i \hat{q}_j + \\ &\quad + \frac{1}{V\mu q^2 - \mathrm{w}'} \left(\delta_{ij} - \hat{q}_i \hat{q}_j\right). \end{aligned} \tag{C.3}$$

The frequency variable is taken to be $\mathrm{w}' \equiv m\omega^2$ for undamped dynamics and $\mathrm{w}' \equiv i\Gamma\omega$ for overdamped dynamics (in principle one can have a bulk viscosity ζ and shear viscosity η; this eventually gets reabsorbed into a definition of the scaling variable). This decomposition is convenient because the longitudinal and transverse parts are orthogonal:

$$\begin{aligned} \left(\hat{q}_i \hat{q}_j\right)\left(\hat{q}_j \hat{q}_k\right) &= \hat{q}_i \hat{q}_k, \\ \left(\delta_{ij} - \hat{q}_i \hat{q}_j\right)\left(\delta_{jk} - \hat{q}_j \hat{q}_k\right) &= \left(\delta_{ik} - \hat{q}_i \hat{q}_k\right), \\ \left(\hat{q}_i \hat{q}_j\right)\left(\delta_{jk} - \hat{q}_j \hat{q}_k\right) &= 0. \end{aligned} \tag{C.4}$$

We can compute the integrand that appears in the CPA self-consistent equation (Equation 4.7) for this isotropic sheet:

$$\mathbf{DG} = \frac{(\lambda + 2\mu) q^2}{(\lambda + 2\mu) q^2 - \mathrm{w}} \hat{q}_i \hat{q}_k + \frac{\mu q^2}{\mu q^2 - \mathrm{w}} \left(\delta_{ik} - \hat{q}_i \hat{q}_k\right), \tag{C.5}$$

so

$$\mathrm{Tr}\left(\mathbf{DG}\right) = \frac{(\lambda + 2\mu) q^2}{(\lambda + 2\mu) q^2 - \mathrm{w}} + (d-1) \frac{\mu q^2}{\mu q^2 - \mathrm{w}}. \tag{C.6}$$

where we have redefined $\mathrm{w} \equiv \mathrm{w}'/V = \rho\omega^2$ or $i\gamma\omega$. Using the fact that the shear modulus is being considered as the only independent modulus that is being depleted, we can write $\lambda/\lambda_\mathrm{F} = \mu/\mu_\mathrm{F}$ and so

$$\mathrm{Tr}\,(\mathbf{DG}) = \frac{(\lambda_\mathrm{F}/\mu_\mathrm{F} + 2)\,\mu q^2}{(\lambda_\mathrm{F}/\mu_\mathrm{F} + 2)\,\mu q^2 - \mathrm{w}} + (d-1)\frac{\mu q^2}{\mu q^2 - \mathrm{w}}. \tag{C.7}$$

Now we rearrange the integral a bit.

$$\begin{aligned}
\frac{1}{\widetilde{z}} \fint_\mathrm{BZ} \mathrm{d}^d q\ \mathrm{Tr}\,(\mathbf{DG}) &= \frac{1}{\widetilde{z}} \frac{1}{s_\mathrm{BZ}} \int_\mathrm{BZ} \mathrm{d}^d q\ \mathrm{Tr}\,(\mathbf{DG}) \\
&= \frac{1}{\widetilde{z}} \frac{S_{d-1}}{V_d q_\mathrm{D}^d} \int_0^{q_\mathrm{D}} \mathrm{d}q\ q^{d-1}\ \mathrm{Tr}\,(\mathbf{DG}) \\
&= \frac{1}{\widetilde{z}} \frac{d}{q_\mathrm{D}^d} \int_0^{q_\mathrm{D}} \mathrm{d}q\ q^{d-1}\ \mathrm{Tr}\,(\mathbf{DG})
\end{aligned} \tag{C.8}$$

where S_{d-1} is the surface area of the unit $d-1$ sphere embedded in d-dimensional space and V_d is the volume of the d-dimensional ball; we have used the fact that $S_{d-1}/V_d = d$ in all dimensions d. Now we subtract $p_c = d/\widetilde{z}$ from either side of the self-consistent equation. On the side involving just the modulus, the result is

$$\begin{aligned}
\frac{(p - d/\widetilde{z}) - (1 - d/\widetilde{z})\,\mu/\mu_\mathrm{F}}{1 - \mu/\mu_\mathrm{F}} &= \frac{\delta p - |\delta p|\,M}{1 - |\delta p|\,M/(1 - d/\widetilde{z})} \\
&\approx \delta p - |\delta p|\,M, \\
M &\equiv \frac{\mu/\mu_0}{|\delta p|}, \\
\mu_0 &\equiv \frac{\mu_\mathrm{F}}{(1 - d/\widetilde{z})}.
\end{aligned} \tag{C.9}$$

We are justified in ignoring the denominator because it contributes terms with one higher power in $|\delta p|$ when written in terms of the scaling variables. When we eventually carefully consider the side involving the frequency, we will find terms that scale as $|\delta p|$ and $|\delta p|^{d/2}$, indicating we are safe to ignore the contribution from the denominator until $d = 4$. Even above $d = 4$, there are more relevant terms that dictate the appropriate scaling behavior of the real part of the modulus, and the low-frequency imaginary part cannot be fixed by including further

polynomial terms like these in the self-consistent equation. We describe this physically important range of frequencies with a dangerously irrelevant variable. Note that the exponents on the invariant scaling combination combining μ and δp are independent of dimension; this is reflected in the RG flow equations that we write down.

Now we subtract p_c from the side involving the frequency. We write

$$\begin{aligned}\frac{d}{\widetilde{z}} = \frac{1}{\widetilde{z}} \fint_{\mathrm{BZ}} \mathrm{d}^d q \, \frac{(\lambda + 2\mu)\, q^2 - \mathrm{w}}{(\lambda + 2\mu)\, q^2 - \mathrm{w}} + \\ + \frac{(d-1)}{\widetilde{z}} \fint_{\mathrm{BZ}} \mathrm{d}^d q \, \frac{\mu q^2 - \mathrm{w}}{\mu q^2 - \mathrm{w}}\end{aligned} \tag{C.10}$$

and subtract the first piece from the longitudinal contribution and the second piece from the transverse contributions. This only serves to replace the numerators $(\lambda + 2\mu)q^2 \to \mathrm{w}$ and $\mu q^2 \to \mathrm{w}$, giving us

$$\begin{aligned}\frac{1}{\widetilde{z}} \frac{d}{q_{\mathrm{D}}^d} \int_0^{q_{\mathrm{D}}} \mathrm{d}q \, \frac{\mathrm{w} q^{d-1}}{(\lambda_{\mathrm{F}}/\mu_{\mathrm{F}} + 2)\, \mu q^2 - \mathrm{w}} + \\ + \frac{1}{\widetilde{z}} \frac{d(d-1)}{q_{\mathrm{D}}^d} \int_0^{q_{\mathrm{D}}} \mathrm{d}q \, \frac{\mathrm{w} q^{d-1}}{\mu q^2 - \mathrm{w}}\end{aligned} \tag{C.11}$$

or

$$\begin{aligned}\frac{1}{\widetilde{z}} \frac{d}{q_{\mathrm{D}}^d} \int_0^{q_{\mathrm{D}}} \mathrm{d}q \, \frac{q^{d-1}}{\frac{(\lambda_{\mathrm{F}}/\mu_{\mathrm{F}}+2)}{\mathrm{w}} \mu q^2 - 1} + \\ + \frac{1}{\widetilde{z}} \frac{d(d-1)}{q_{\mathrm{D}}^d} \int_0^{q_{\mathrm{D}}} \mathrm{d}q \, \frac{q^{d-1}}{\frac{\mu}{\mathrm{w}} q^2 - 1}.\end{aligned} \tag{C.12}$$

We now perform a substitution $\xi = (q/q_{\mathrm{D}})^2$. This serves the dual purpose of nondimensionalizing the integration variable and casting the integrals into a canonical form to be identified with a special function. The integrals become

$$\begin{aligned}-\frac{d}{2\widetilde{z}} \int_0^1 \mathrm{d}\xi \, \frac{\xi^{d/2-1}}{1 - \xi \frac{\mu}{\mathrm{w_L}}} - \frac{d\,(d-1)}{2\widetilde{z}} \int_0^1 \mathrm{d}\xi \, \frac{\xi^{d/2-1}}{1 - \xi \frac{\mu}{\mathrm{w_T}}}, \\ \mathrm{w_L} \equiv \frac{\mathrm{w}}{(\lambda_{\mathrm{F}}/\mu_{\mathrm{F}} + 2)\, q_{\mathrm{D}}^2}, \quad \mathrm{w_T} \equiv \frac{\mathrm{w}}{q_{\mathrm{D}}^2}.\end{aligned} \tag{C.13}$$

Now each of these integrals are of the form

$$\begin{aligned}\int_0^1 \mathrm{d}\xi \frac{\xi^{d/2-1}}{1-\xi z} &= \\ &= \int_0^1 \mathrm{d}\xi\, \xi^{d/2-1}\,(1-\xi)^{(d/2+1)-d/2-1}\,(1-\xi z)^{-1} \\ &= \mathrm{B}\left(\frac{d}{2},1\right)\,{}_2\mathrm{F}_1\left(1,\frac{d}{2};\frac{d}{2}+1;z\right) \\ &= \frac{2}{d}\,{}_2\mathrm{F}_1\left(1,\frac{d}{2};\frac{d}{2}+1;z\right)\end{aligned} \tag{C.14}$$

where $\mathrm{B}(z_1,z_2)$ is the beta function and ${}_2\mathrm{F}_1(a,b;c;z)$ is the ordinary hypergeometric function, as can be verified in 9.111 of [141] (and using the beta function identity $\mathrm{B}(z,1) = 1/z$). The frequency-dependent part of Equation 4.7 in the isotropic case (with p_c subtracted out) is then exactly

$$\begin{aligned}-\frac{1}{\widetilde{z}}\,{}_2\mathrm{F}_1\left(1,\frac{d}{2};\frac{d}{2}+1;\frac{\mu}{\mathrm{w_L}}\right) - \\ -\frac{(d-1)}{\widetilde{z}}\,{}_2\mathrm{F}_1\left(1,\frac{d}{2};\frac{d}{2}+1;\frac{\mu}{\mathrm{w_T}}\right).\end{aligned} \tag{C.15}$$

The parameter μ is found self-consistently and is some complex number in the appropriate scaling limit. The imaginary parts of the viscoelastic moduli are nonpositive to respect the causality of the Green's function. As mentioned in the main text, taking the scaling limit amounts to sending the argument of the hypergeometric functions to ∞, so we are interested in expansions of ${}_2\mathrm{F}_1(\alpha,\beta;\gamma;z)$ about its branch point at $z=\infty$. For this we look at the second identity in 9.132 of [141], assume d is not even for now and write

$$\begin{aligned}\frac{\Gamma\left(\frac{d}{2}\right)^2}{\Gamma\left(\frac{d}{2}+1\right)\Gamma\left(\frac{d}{2}-1\right)}\,{}_2\mathrm{F}_1\left(1,\frac{d}{2};\frac{d}{2}+1;\frac{\mu}{\mathrm{w_L}}\right) = \\ \left(-\frac{\mathrm{w_L}}{\mu}\right)\,{}_2\mathrm{F}_1\left(1,1-\frac{d}{2};2-\frac{d}{2};\frac{\mathrm{w_L}}{\mu}\right) + \\ +\Gamma\left(\frac{d}{2}\right)^2\frac{\Gamma\left(1-\frac{d}{2}\right)}{\Gamma\left(\frac{d}{2}-1\right)}\left(-\frac{\mathrm{w_L}}{\mu}\right)^{d/2}.\end{aligned} \tag{C.16}$$

The hypergeometric function involving $z = \mathrm{w_L}/\mu$ is 1 for $z = 0$ and can otherwise be expanded in a power series in z, which contributes terms higher-order in $|\delta p|$. Writing out the side with the frequency dependence now, grouping terms with the same powers of $\mathrm{w_{L/T}}$:

$$\begin{aligned} &\approx \frac{1}{\widetilde{z}} \frac{\Gamma\left(\frac{d}{2}+1\right)\Gamma\left(\frac{d}{2}-1\right)}{\Gamma\left(\frac{d}{2}\right)^2} \frac{\mathrm{w_L}+(d-1)\mathrm{w_T}}{\mu} - \\ &-\frac{1}{\widetilde{z}}\Gamma\left(\frac{d}{2}+1\right)\Gamma\left(1-\frac{d}{2}\right)\frac{\mathrm{w_L}^{d/2}+(d-1)\mathrm{w_T}^{d/2}}{(-\mu)^{d/2}}. \end{aligned} \tag{C.17}$$

The scaling variables asymptotically close to the critical point are now ready to be defined, but they depend upon whether we are above or below $d = 2$. We investigate each case separately below.

C.1.1 Scaling variables above 2 dimensions

First, assume $d > 2$ so that the first term contributes the leading-order frequency behavior. Then we define a scaling for the frequency f:

$$|\delta p|\, F \equiv \frac{1}{\widetilde{z}} \frac{\Gamma\left(\frac{d}{2}+1\right)\Gamma\left(\frac{d}{2}-1\right)}{\Gamma\left(\frac{d}{2}\right)^2} \frac{\mathrm{w_L}+(d-1)\mathrm{w_T}}{\mu}. \tag{C.18}$$

This corresponds to:

$$\begin{aligned} F &= \frac{f/f_0}{|\delta p|}, \\ f_0 &= q_\mathrm{D}^2 \frac{\Gamma\left(\frac{d}{2}\right)^2}{\Gamma\left(\frac{d}{2}+1\right)\Gamma\left(\frac{d}{2}-1\right)} \frac{\widetilde{z}/\mu_\mathrm{F}}{\frac{1}{\lambda_\mathrm{F}+2\mu_\mathrm{F}}+(d-1)\frac{1}{\mu_\mathrm{F}}}, \end{aligned} \tag{C.19}$$

essentially setting $f_0 = c^2 q_\mathrm{D}^2$, where c is a weighted combination of the longitudinal and transverse sound speeds in the undepleted membrane.

This definition of the scaling variable also makes the first term of the frequency-dependent side of the self-consistent equation $|\delta p|\, F$. These scaling

variables are then inserted into the other term, and the variable U is defined so that the final term is $+|\delta p|\, U(-F)^{d/2}$ (note that $\Gamma(1-d/2)$ is negative for $2 < d < 4$). This gives us

$$\begin{aligned} U &\equiv u/u_0\, |\delta p|^{d/2-1}\,, \\ u/u_0 &= \widetilde{z}^{d/2-1} \frac{\Gamma\left(\frac{d}{2}+1\right)\left(-\Gamma\left(1-\frac{d}{2}\right)\right)\Gamma\left(\frac{d}{2}\right)^d}{\left(\Gamma\left(\frac{d}{2}+1\right)\Gamma\left(\frac{d}{2}-1\right)\right)^{d/2}} \times \\ &\times \left(\frac{\left(\frac{1}{\lambda_\mathrm{F}+2\mu_\mathrm{F}}\right)^{d/2} + (d-1)\left(\frac{1}{\mu_\mathrm{F}}\right)^{d/2}}{\left(\left(\frac{1}{\lambda_\mathrm{F}+2\mu_\mathrm{F}}\right) + (d-1)\left(\frac{1}{\mu_\mathrm{F}}\right)\right)^{d/2}} \right). \end{aligned} \tag{C.20}$$

The large prefactor involving Γ functions can be simplified to bring the expression into the form

$$\begin{aligned} u/u_0 &= -\widetilde{z}^{d/2-1} \left(\frac{d-2}{d}\right)^{d/2} \frac{\pi d}{2} \csc\left(\frac{\pi d}{2}\right) \times \\ &\times \left(\frac{\left(\frac{1}{\lambda_\mathrm{F}+2\mu_\mathrm{F}}\right)^{d/2} + (d-1)\left(\frac{1}{\mu_\mathrm{F}}\right)^{d/2}}{\left(\left(\frac{1}{\lambda_\mathrm{F}+2\mu_\mathrm{F}}\right) + (d-1)\left(\frac{1}{\mu_\mathrm{F}}\right)\right)^{d/2}} \right) \end{aligned} \tag{C.21}$$

where the term involving csc is negative for $2 < d < 4$. The self-consistent equation for $d > 2$ defining the universal scaling function is then (dividing both sides by $|\delta p|$)

$$\pm 1 - M = F + U\,(-F)^{d/2}\,, \tag{C.22}$$

as claimed in the main text.

C.1.2 2 dimensions as a limit

To take the limit $d \to 2$, we first factor out one power of $-F$ from the self-consistent equation valid for $d > 2$. We then define

$$F' \equiv \frac{F}{\Gamma\left(\frac{d}{2}-1\right)} \tag{C.23}$$

to remove the divergence in the definition of F while retaining the same critical exponents (for now). The equation becomes

$$\begin{aligned} &\pm 1 - M = \\ &\quad -F'\left(\left(-F'\Gamma\left(\frac{d}{2}-1\right)\right)^{d/2-1} U - 1\right)\Gamma\left(\frac{d}{2}-1\right). \end{aligned} \tag{C.24}$$

Bring U inside the power of $d/2-1$ and write it as $U^{2/(d-2)} = (u/u_0)^{2/(d-2)}|\delta p|$. Then define $(u/u_0)'^{2/(d-2)} \equiv (u/u_0)^{2/(d-2)}\,\Gamma(d/2-1)$. The self-consistent equation becomes

$$\begin{aligned} &\pm 1 - M = \\ &\quad -F'\left(\left(-(u/u_0)'^{\frac{2}{2-d}} F'\,|\delta p|\right)^{d/2-1} - 1\right)\Gamma\left(\frac{d}{2}-1\right), \end{aligned} \tag{C.25}$$

as claimed in the main text. Now we need only to compute $u_2/u_{02} = \lim_{d\to 2^+}(u/u_0)'^{2/(d-2)}$. This yields

$$u_2/u_{02} = \widetilde{z}\,\frac{\mu_{\mathrm{F}}^{\frac{\mu_{\mathrm{F}}}{\lambda_{\mathrm{F}}+3\mu_{\mathrm{F}}}}\,(\lambda_{\mathrm{F}}+2\mu_{\mathrm{F}})^{\frac{\lambda_{\mathrm{F}}+2\mu_{\mathrm{F}}}{\lambda_{\mathrm{F}}+3\mu_{\mathrm{F}}}}}{\lambda_{\mathrm{F}}+3\mu_{\mathrm{F}}}. \tag{C.26}$$

The self-consistent equation in $d = 2$ is then

$$\pm 1 - M = -F' \log\left(-(u_2/u_{02})F'\,|\delta p|\right), \tag{C.27}$$

but as mentioned in the main text, this is not written in terms of the proper scaling variables. This result can also be derived without hypergeometric functions by directly performing the integral in $d = 2$, but it becomes less clear how this result is continuously connected to $d = 3$, or $d < 2$. It can also be understood (equivalently) as the branch point of the hypergeometric function at $z = \infty$ transforming from a power-law-like branch to a logarithmic branch for d even. This kind of resonance behavior, where the term with the exponent $d/2$ interacts with another term with an integer power to give a logarithm, happens in every even dimension. For even dimensions above 2, the logarithm is associated with a

correction that vanishes close to the critical point, but it is necessary to retain to understand the low-frequency imaginary part of the viscoelastic modulus.

In the right scaling variables, we can absorb this additional logarithmic divergence into the definition of the invariant scaling combination involving f in $d = 2$, giving

$$\pm 1 - M = F_2, \tag{C.28}$$

by analogy to the scaling variable for f in all dimensions $d > 2$. We can examine what this implies about how f scales with δp. We have

$$F_2 = -F' \log\left(-(u_2/u_{02})F' \left|\delta p\right|\right) \tag{C.29}$$

or

$$(u_2/u_{02})F_2 \left|\delta p\right| = -(u_2/u_{02})F' \left|\delta p\right| \log\left(-(u_2/u_{02})F' \left|\delta p\right|\right) \tag{C.30}$$

where F_2 is the invariant scaling combination. We invert this with the W function:

$$-(u_2/u_{02})F' \left|\delta p\right| = \frac{(u_2/u_{02})F_2 \left|\delta p\right|}{W\left((u_2/u_{02})F_2 \left|\delta p\right|\right)} \tag{C.31}$$

reinstalling the definition of $F' = f/f_0'/\left|\delta p\right|$, we have (up to constants)

$$f \sim \frac{(u_2/u_{02})F_2 \left|\delta p\right|}{W\left((u_2/u_{02})F_2 \left|\delta p\right|\right)} \tag{C.32}$$

in $d = 2$, which is also supported by the RG flow equations.

C.1.3 Scaling variables below 2 dimensions

Below 2 dimensions, the term involving $\mathrm{w}_{\mathrm{L/T}}^{d/2}$ is dominant at low frequencies. We define a scaling variable for the frequency f:

$$|\delta p|\,(-F_d)^{d/2} \equiv \frac{1}{\widetilde{z}}\Gamma\left(\frac{d}{2}+1\right)\Gamma\left(1-\frac{d}{2}\right)\times \\ \times\frac{\mathrm{w}_{\mathrm{L}}^{d/2}+(d-1)\,\mathrm{w}_{\mathrm{T}}^{d/2}}{(-\mu)^{d/2}} \tag{C.33}$$

Note that for $d<2$, $\Gamma\left(1-d/2\right)$ is now positive. This corresponds to:

$$\begin{aligned} F_d &= \frac{f/f_{0d}}{|\delta p|^{2/d}}, \\ f_{0d} &= q_{\mathrm{D}}^2\frac{1}{\Gamma\left(\frac{d}{2}+1\right)^{2/d}\Gamma\left(1-\frac{d}{2}\right)^{2/d}}\times \\ &\times\frac{\widetilde{z}^{2/d}/\mu_{\mathrm{F}}}{\left(\left(\frac{1}{\lambda_{\mathrm{F}}+2\mu_{\mathrm{F}}}\right)^{d/2}+(d-1)\left(\frac{1}{\mu_{\mathrm{F}}}\right)^{d/2}\right)^{2/d}}, \end{aligned} \tag{C.34}$$

another constant that is similar to $c^2q_{\mathrm{D}}^2$. This sets the first term in the self-consistent equation to be $-|\delta p|\,(-F_d)^{d/2}$. We again insert the definitions of the scaling variable F_d into the remaining term, and define an additional variable U_d so that the final term is $-|\delta p|\,U_dF_d$. This gives us

$$\begin{aligned} U_d &\equiv (u_d/u_{0d})\,|\delta p|^{2/d-1}\,, \\ u_d/u_{0d} &= \widetilde{z}^{2/d-1}\frac{-\Gamma\left(\frac{d}{2}-1\right)}{\Gamma\left(\frac{d}{2}\right)^2\Gamma\left(\frac{d}{2}+1\right)^{2/d-1}\Gamma\left(1-\frac{d}{2}\right)^{2/d}}\times \\ &\times\frac{\left(\frac{1}{\lambda_{\mathrm{F}}+2\mu_{\mathrm{F}}}\right)+(d-1)\left(\frac{1}{\mu_{\mathrm{F}}}\right)}{\left(\left(\frac{1}{\lambda_{\mathrm{F}}+2\mu_{\mathrm{F}}}\right)^{d/2}+(d-1)\left(\frac{1}{\mu_{\mathrm{F}}}\right)^{d/2}\right)^{2/d}}. \end{aligned} \tag{C.35}$$

Note that for $d<2$, $\Gamma\left(d/2-1\right)$ is now negative. The self-consistent equation for $d<2$ defining the universal scaling function is then (dividing both sides by $|\delta p|$)

$$\pm 1-M=-\left(-F_d\right)^{d/2}-U_dF_d, \tag{C.36}$$

as claimed in the main text.

C.1.4 Scaling in even dimensions greater than 2

To understand the scaling in even dimensions $d > 2$ one needs to retain three terms from the evaluation of the integral: the dominant piece from the hypergeometric function, the non-analytic piece going as $\sim (-\mathrm{w}/\mu)^{d/2}$, and the $\lfloor d/2 \rfloor$th term of the power series expansion of the hypergeometric function (note that the first and third of these coincide when $d = 2$). The latter two terms will interact in the limit $d/2 \to k^+$ for k an integer > 1 and produce a logarithmic singularity in a way similar to the 2 dimensional case. Keeping these terms, and writing things in terms of scaling variables valid above $d > 2$ gives

$$\pm 1 - M = F - \widehat{U}_d \, (-F)^{\lfloor d/2 \rfloor} + U \, (-F)^{d/2} \, . \tag{C.37}$$

Here $\widehat{U}_d$ is an invariant scaling combination associated with some other irrelevant variable $\sim |\delta p|^{\lfloor d/2 \rfloor - 1}$. As in dimension 2, pull out a factor of $\widehat{U}_d \, (-F)^{\lfloor d/2 \rfloor}$ from the last two terms, and one finds

$$\begin{aligned} \pm 1 - M = F + \\ + \widehat{U}_d \, (-F)^{\lfloor d/2 \rfloor} \left(\frac{U}{\widehat{U}_d} \, (-F)^{d/2 - \lfloor d/2 \rfloor} - 1 \right) . \end{aligned} \tag{C.38}$$

Similar to the case in $d = 2$, we can redefine $\widehat{U}_d$ to $\widehat{U}'_d$ to pull out a divergence in even dimensions, and take the limit as $d/2 \to \lfloor d/2 \rfloor$ to recover (making the δp dependence of the irrelevant variables explicit)

$$\begin{aligned} \pm 1 - M = F + \\ + c_d \, |\delta p|^{\lfloor d/2 \rfloor - 1} \, (-F)^{\lfloor d/2 \rfloor} \log \left(-u_d F \, |\delta p| \right) . \end{aligned} \tag{C.39}$$

This shows that the scaling exponents for all relevant variables in $d > 2$ are the same; the F term sets the scaling and the remaining term is a correction that vanishes. The only novelty is that the non-analyticity that fixes the low-frequency

imaginary part is now a logarithmic singularity, rather than a power-law singularity. As in other $d > 2$ this correction term must be retained to capture the low-frequency dissipation in the microscopically undamped case. As in other integer dimensions, the self-consistent integral can be expressed directly in terms of rational functions and logarithms (without referring to special functions) to verify these formulas.

C.1.5 Density of states scaling

The density of states is given in the undamped case as

$$D(\omega) = \frac{\omega}{\pi} \int_{\mathrm{BZ}} \mathrm{d}^d q \, \mathrm{Im}\left(\mathrm{Tr}\left(\mathbf{G}\right)\right). \tag{C.40}$$

This is evaluated for an isotropic system similarly to the previous section:

$$\begin{aligned} D(\omega) = \frac{\omega}{\pi V} \mathrm{Im}\Bigg[\int_0^{q_\mathrm{D}} \mathrm{d}q \, \frac{S_{d-1} q^{d-1}}{(\lambda_\mathrm{F}/\mu_\mathrm{F} + 2)\,\mu q^2 - \mathrm{w}} + \\ + (d-1) \int_0^{q_\mathrm{D}} \mathrm{d}q \, \frac{S_{d-1} q^{d-1}}{\mu q^2 - \mathrm{w}} \Bigg]. \end{aligned} \tag{C.41}$$

A trick to eliminate more tedious manipulation is to multiply and divide by a particular factor:

$$\begin{aligned} D(\omega) = \frac{\omega}{\pi} \frac{\widetilde{z} V_d q_\mathrm{D}^d}{V \mathrm{w}} \mathrm{Im}\Bigg[\frac{d}{\widetilde{z} q_\mathrm{D}^d} \int_0^{q_\mathrm{D}} \mathrm{d}q \, \frac{\mathrm{w} q^{d-1}}{(\lambda_\mathrm{F}/\mu_\mathrm{F} + 2)\,\mu q^2 - \mathrm{w}} + \\ + (d-1) \frac{d}{\widetilde{z} q_\mathrm{D}^d} \int_0^{q_\mathrm{D}} \mathrm{d}q \, \frac{\mathrm{w} q^{d-1}}{\mu q^2 - \mathrm{w}} \Bigg]. \end{aligned} \tag{C.42}$$

The term in brackets can be identified, to leading order in the scaling variables, as

$$D(\omega) \approx \frac{\omega}{\pi} \frac{\widetilde{z} V_d q_\mathrm{D}^d}{V \mathrm{w}} \mathrm{Im}\left[\delta p - |\delta p| \, M\right] = -|\delta p| \, \frac{\widetilde{z} V_d q_\mathrm{D}^d}{\pi m \omega} \mathrm{Im}\left[M\right] \tag{C.43}$$

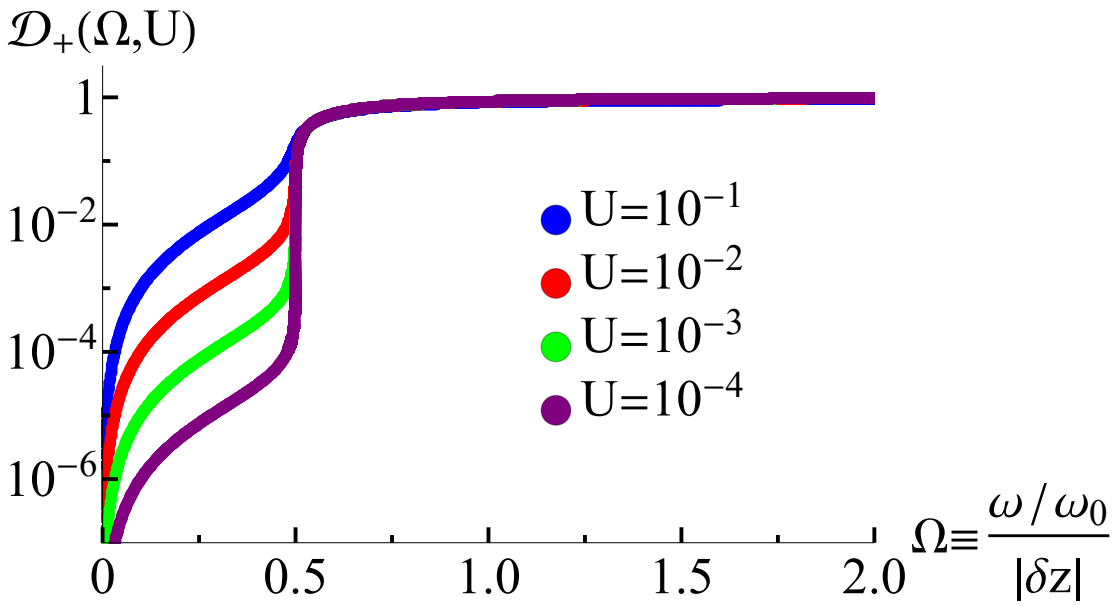

Figure C.1: **Density of states for a nearly floppy 3D viscoelastic membrane**. The dangerously irrelevant variable controls the low-frequency density of states in the undamped case. The rescaled density of states has a square-root cusp at $U = 0$ ($\delta p = 0$) [2, 9]; as discussed in section 4.2.4, the continuum CPA, and our universal scaling limit, do not show the ω^4 contribution to the density of states found from quasilocalized modes [138]. See Figure 4.3 for the excess density of states $\mathcal{D}(\Omega, U)/\Omega^2$.

For $d > 2$, this gives the following scaling form (written in terms of scaling variables for ω rather than for $f = \mathrm{w}/\mu$):

$$\begin{aligned} D(\omega) &= D_0 \mathcal{D}(\Omega, U), \\ \mathcal{D}(\Omega, U) &= -\frac{\mathrm{Im}\left[\mathcal{M}(\Omega, U)\right]}{\Omega} \end{aligned} \tag{C.44}$$

where D_0 is a non-universal constant. This remarkably simple scaling form is true within the CPA [52], but not in general. Setting $U = 0$ allows us to exactly evaluate this; in this scaling limit there is only a nonzero density of states for $\Omega > 1/2$ and it is flat at high frequency. We have

$$\mathcal{D}(\Omega, 0) = \frac{\sqrt{4\Omega^2 - 1}}{2\Omega}. \tag{C.45}$$

The density of states is shown for $d = 3$ and various values of U in Figure C.1.

For $d < 2$, we have:

$$\begin{aligned} D(\omega) &= \frac{D_{0d}}{|\delta p|^{1/d-1/2}} \mathcal{D}_d\left(\Omega_d, U_d\right), \\ \mathcal{D}_d\left(\Omega_d, U_d\right) &= -\frac{\operatorname{Im}\left[\mathcal{M}_d\left(\Omega_d, U_d\right)\right]}{\Omega_d}. \end{aligned} \tag{C.46}$$

$\omega D(\omega)$ can also be written in terms of F and U. This leads, using Equation 4.31 for $d > 2$, to

$$\begin{aligned} \omega D(\omega) &= D_0' \left|\delta p\right| \mathcal{D}(F, U), \\ \mathcal{D}\left(F, U\right) &= -\operatorname{Im}\left[\mathcal{M}\left(F, U\right)\right] \end{aligned} \tag{C.47}$$

For $d < 2$, we use Equation 4.32 to write

$$\begin{aligned} \omega D(\omega) &= D_{0d}' \left|\delta p\right| \mathcal{D}_d\left(F_d, U_d\right) \\ \mathcal{D}_d\left(F_d, U_d\right) &= -\operatorname{Im}\left[\mathcal{M}_d\left(F_d, U_d\right)\right]. \end{aligned} \tag{C.48}$$

In $d = 2$, we use Equation 4.35 to write

$$\begin{aligned} \omega D(\omega) &= D_{02} \left|\delta p\right| \mathcal{D}_2\left(F_2\right), \\ \mathcal{D}_2\left(F_2\right) &= -\operatorname{Im}\left[\mathcal{M}_2\left(F_2\right)\right]. \end{aligned} \tag{C.49}$$

This properly incorporates all of the logarithmic corrections yielding the theory curves on Figure C.2. For the triangular lattice in two dimensions (see next section for all specifics of lattice constants and microscopic stiffness parameters), we can reinstall the non-universal constants in the definitions of the scaling variables to make a direct comparison to the numerically determined density of states. To highlight the logarithmic shifts, we define $M_{\mathrm{T}} \equiv \mu / \left|\delta p\right|$ and $\Omega_{\mathrm{T}} \equiv \omega / \left|\delta p\right|$. In these variables, the asymptotic form of the density of states for an elastic sheet with the same long-wavelength parameters as the triangular lattice is

$$D_2 = -\frac{32\pi}{3\sqrt{3}} \frac{\operatorname{Im}\left(M_{\mathrm{T}}\right)}{\Omega_{\mathrm{T}}}, \tag{C.50}$$

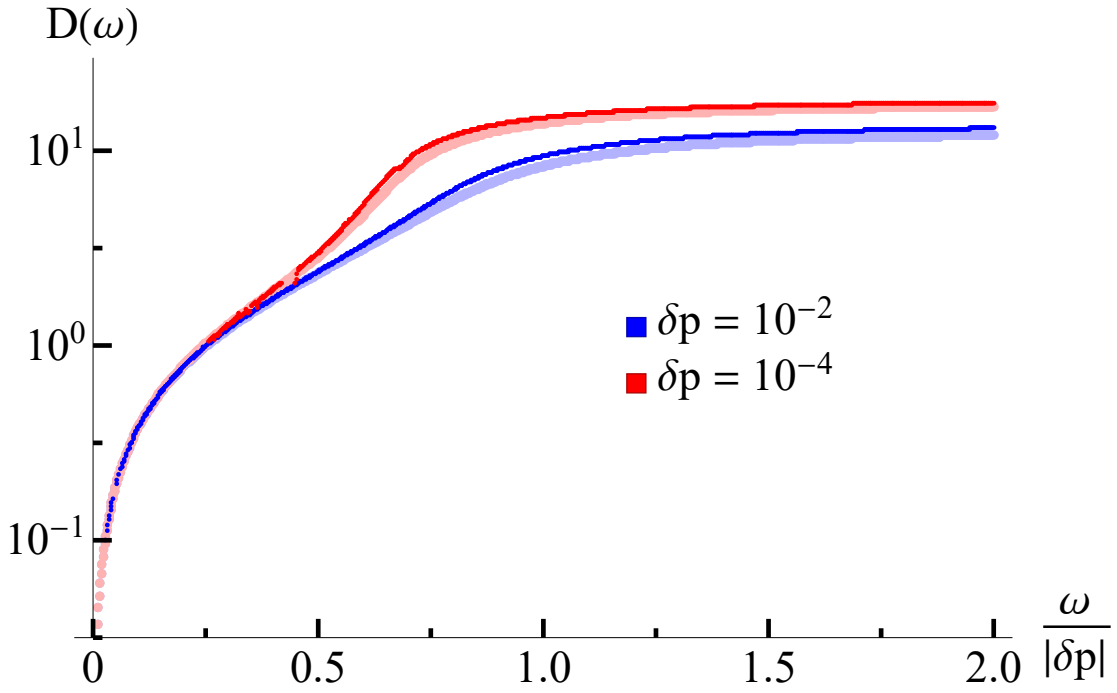

Figure C.2: **Density of states for the diluted triangular lattice computed within the CPA**. We plot rescaled numerical solutions (thin lines) against our scaling solutions (thick lines) at two distances from the critical point $\delta p = \left\{10^{-2}, 10^{-4}\right\}$, again demonstrating nice agreement with the scaling form. The shift in the rescaled frequency Ω_{T}^{*} where we cross over to a flat density of states and the vertical shift in the location of the plateau are both due to logarithmic corrections present in the upper critical dimension.

where M_{T} is the solution to

$$\pm 1 - \frac{4}{3\sqrt{3}} M_{\mathrm{T}} = -\frac{1}{3\pi\sqrt{3}} \frac{\Omega_{\mathrm{T}}^2}{M_{\mathrm{T}}} \log\left(-\frac{3^{1/4}}{4\pi} \frac{\Omega_{\mathrm{T}}^2}{M_{\mathrm{T}}} |\delta p|\right). \tag{C.51}$$

(See Appendix C.4 for details.) The plot of the comparison is shown in Figure C.2 for $\delta p = 10^{-2}$ and $\delta p = 10^{-4}$. The slow leftward drift of the onset of the plateau in the DOS and the upward drift of the location of the plateau in the DOS are both related to $d = 2$ being the upper critical dimension of the theory.

One often identifies the excess soft modes in glassy systems by plotting the density of vibrational states divided by the expected form from a Debye model of a crystal. This amounts to dividing the universal scaling function $\mathcal{D}$ by Ω^{d-1} in

dimension d; as the density of states is flat for $\Omega \gtrsim 1$, these plots unsurprisingly show a bump (Figure 4.3).

C.1.6 Green's function scaling

For completeness, we report the scaling form of the Green's function. For the case of the continuous transition, we write the long-wavelength form associated with an elastic sheet:

$$\begin{aligned} V\mathbf{G}(q,\omega) = &\frac{1}{(\lambda+2\mu)\,q^2 - \mathrm{w}}\;\hat{q}_i\hat{q}_j + \\ &+ \frac{1}{\mu q^2 - \mathrm{w}}\left(\delta_{ij} - \hat{q}_i\hat{q}_j\right). \end{aligned} \tag{C.52}$$

This can be rewritten in terms of f:

$$\begin{aligned} V\mathbf{G}(q,\omega) = &\frac{1}{\mu\left((\lambda_\mathrm{F}/\mu_\mathrm{F}+2)\,q^2 - f\right)}\;\hat{q}_i\hat{q}_j + \\ &+ \frac{1}{\mu\,(q^2 - f)}\left(\delta_{ij} - \hat{q}_i\hat{q}_j\right) \end{aligned} \tag{C.53}$$

so q^2 and f have identical scaling asymptotics in all dimensions (this can also be seen from the RG flow Equations 4.28). The non-universal constants that set the scale for q differ for the transverse and longitudinal parts, but the form of the universal scaling function is identical: in dimensions $d > 2$,

$$\begin{aligned} Q \equiv \frac{q/q_0^{\mathrm{L/T}}}{|\delta p|^{1/2}}, \quad G_{\mathrm{L/T}}(q,\omega) = \frac{G_0^{\mathrm{L/T}}}{|\delta p|^2}\mathcal{G}(Q,F,U), \\ \mathcal{G}(Q,F,U) = \frac{1}{\mathcal{M}(F,U)\,(Q^2 - F)}. \end{aligned} \tag{C.54}$$

Similarly, in dimensions $d < 2$, we have

$$\begin{aligned} Q_d \equiv \frac{q/q_{0d}^{\mathrm{L/T}}}{|\delta p|^{1/d}}, \quad G_{\mathrm{L/T}}(q,\omega) = \frac{G_{0d}^{\mathrm{L/T}}}{|\delta p|^{1+2/d}}\mathcal{G}_d(Q_d,F_d,U_d), \\ \mathcal{G}_d(Q_d,F_d,U_d) = \frac{1}{\mathcal{M}_d(F_d,U_d)\left(Q_d^2 - F_d\right)}. \end{aligned} \tag{C.55}$$

In $d = 2$ there are similar logarithmic corrections to the scaling variables as in all other linear response quantities.

These forms imply diverging length scales at the transition: $\ell_c \sim |\delta p|^{-1/2}$ for $d > 2$, $\ell_c \sim |\delta p|^{-1/d}$ for $d < 2$, and $\ell_c \sim |\delta p|^{-1/2} \left|\log |\delta p|\right|^{1/2}$ in $d = 2$ (noted also in Table 4.2). If a phonon has a wavelength shorter than ℓ_c, it is strongly overdamped. In the case of jamming, the transverse shear mode is associated with a diverging length scale of the type analyzed here and elsewhere [9, 45] but the longitudinal mode has a different scaling.

C.2 Renormalization group flows from scaling combinations

Here we detail the procedure of writing down our deduced renormalization-group flow equations, (Section 4.2.5). First, we take for granted that the wavevector, as an inverse length, coarse grains as

$$\frac{\mathrm{d}q}{\mathrm{d}\ell} = q. \tag{C.56}$$

This can be taken as a definition of the coarse-graining procedure. Let us first focus on flows above the upper critical dimension and ignore the irrelevant variable. The frequency variables scale as $f \equiv w/\mu \sim \delta p$, and the modulus scales as $\mu \sim \delta p$. From the form of the Green's function, $\left(\mu q^2 - \mu f\right)^{-1} \sim \delta p^{-\gamma}$, which means that $q \sim \delta p^{1/2}$ gives a nontrivial scaling limit. These mean-field power laws determine the coefficients on the linear parts of the flow equations, i.e. the terms linearized about the hyperbolic fixed point above $d = 2$. We have for $d > 2$ the

normal form:

$$\begin{aligned}
\frac{\mathrm{d}q}{\mathrm{d}\ell} &= q, \\
\frac{\mathrm{d}\delta p}{\mathrm{d}\ell} &= 2\delta p, \\
\frac{\mathrm{d}\mu}{\mathrm{d}\ell} &= 2\mu, \\
\frac{\mathrm{d}f}{\mathrm{d}\ell} &= 2f.
\end{aligned} \tag{C.57}$$

Now we include the effects of an upper critical dimension of 2. Assuming that a variable that was originally irrelevant undergoes a transcritical bifurcation and becomes relevant below $d = 2$, we can write the flow equations with help from normal form theory [49]. Normal form theory tells us the minimal number of terms we need to keep assuming we have made an analytic change of coordinates, i.e., we have preserved information about the singularity close to the critical point. We write a flow equation for this speculative coupling u irrelevant above 2 dimensions that undergoes a bifurcation and flows to a new stable point for $d < 2$. We must keep terms linear in u that appear in the other flow equations; these serve to modify the critical exponents below the upper critical dimension. We have

$$\begin{aligned}
\frac{\mathrm{d}q}{\mathrm{d}\ell} &= q, \\
\frac{\mathrm{d}\delta p}{\mathrm{d}\ell} &= 2\delta p - \lambda_p u\, \delta p, \\
\frac{\mathrm{d}\mu}{\mathrm{d}\ell} &= 2\mu - \lambda_\mu u\, \mu, \\
\frac{\mathrm{d}f}{\mathrm{d}\ell} &= 2f - \lambda_f u\, f, \\
\frac{\mathrm{d}u}{\mathrm{d}\ell} &= \frac{1}{A}(2-d)\, u - u^2
\end{aligned} \tag{C.58}$$

where $A > 0$ and we rescale u to set the coefficient of the quadratic term in its flow equation to -1. As this theory is simple and exactly solvable, we have

many *resonances* where there are integer relationships between coefficients in the RG flow equations. We will ignore these for now, but normal form theory gives a prescription to keep additional terms in the flow equations. These are then tuned to capture what would otherwise be interpreted as large corrections to scaling. We check directly that the coefficient D on the cubic term of the flow for u, $+Du^3$, is 0 through a calculation similar to the one performed in Appendix C.3. The critical value of u below $d = 2$ is $u_c = (2-d)/A$. We know that, below $d = 2$, $f \sim \delta p^{2/d}$ and so $q \sim \delta p^{1/d}$. After coarse-graining for a while, we can set $u = u_c$ in the flow equations to get accurate exponents for the invariant scaling combinations. We write

$$\begin{aligned}
\frac{\mathrm{d}\log q}{\mathrm{d}\log \delta p} &= \frac{1}{2-\lambda_p u_c} = \frac{1}{2-\lambda_p (2-d)/A} = \frac{1}{d}, \\
\frac{\mathrm{d}\log \mu}{\mathrm{d}\log \delta p} &= \frac{2-\lambda_\mu u_c}{2-\lambda_p u_c} = \frac{2-\lambda_\mu (2-d)/A}{2-\lambda_p (2-d)/A} = 1, \\
\frac{\mathrm{d}\log f}{\mathrm{d}\log \delta p} &= \frac{2-\lambda_f u_c}{2-\lambda_p u_c} = \frac{2-\lambda_f (2-d)/A}{2-\lambda_p (2-d)/A} = \frac{2}{d}.
\end{aligned} \tag{C.59}$$

These are solved by

$$\lambda_\mu = \lambda_p = A, \quad \lambda_f = 0. \tag{C.60}$$

We now look at how u scales with δp: above $d = 2$, we have

$$\frac{\mathrm{d}\log u}{\mathrm{d}\log \delta p} = \frac{(2-d)}{2A} = -\frac{1}{A}\left(\frac{d}{2} - 1\right). \tag{C.61}$$

Below $d = 2$, we have (expanding about the stable RG fixed point $\delta u = u - u_c$)

$$\frac{\mathrm{d}\log \delta u}{\mathrm{d}\log \delta p} = -\frac{(2-d)}{dA} = -\frac{1}{A}\left(\frac{2}{d} - 1\right). \tag{C.62}$$

The positive constant A sets the scale of u_c for $d < 2$. We will determine $A = 1$ by looking at the scaling implied by the RG flow equations in 2 dimensions and choosing A to match the asymptotic scaling found for the frequency directly in $d = 2$ from the CPA.

C.3 Scaling for frequency in 2 dimensions

Here we derive the scaling of f with δp in the upper critical dimension $d = 2$; other scalings (such as the one for q) follow similarly. This closely follows the Supplemental Material of [49]. We will use

$$\begin{aligned} \frac{\mathrm{d}u}{\mathrm{d}\ell} &= -u^2, \\ \frac{\mathrm{d}\delta p}{\mathrm{d}\ell} &= 2\delta p - A\, u\, \delta p, \\ \frac{\mathrm{d}f}{\mathrm{d}\ell} &= 2f. \end{aligned} \tag{C.63}$$

Divide the flow equation for δp by the flow equation for u to find

$$\frac{\mathrm{d}\delta p}{\mathrm{d}u} = \frac{2\delta p - Au\delta p}{-u^2}. \tag{C.64}$$

This is integrated to give

$$\log\left(\frac{\delta p}{\delta p_0}\right) = 2\left(\frac{1}{u} - \frac{1}{u_0}\right) + A\log\left(\frac{u}{u_0}\right). \tag{C.65}$$

It is useful to define a variable

$$s \equiv \frac{1}{u}. \tag{C.66}$$

We coarse-grain to $\delta p = 1$. Then

$$-\log\left(\delta p_0\right) = 2\left(s - s_0\right) - A\log\left(\frac{s}{s_0}\right). \tag{C.67}$$

Rearrange this into a particular form:

$$\begin{aligned} -\frac{2}{A}s + \log\left(-\frac{2}{A}s\right) &= \log\left(y\left(s_0\right)\delta p_0^{1/A}\right), \\ y(s_0) &\equiv -\frac{2}{A}s_0 \exp\left(-\frac{2}{A}s_0\right). \end{aligned} \tag{C.68}$$

Note that this form is one of the definitions of the Lambert W function,

$$W(z) + \log\left(W(z)\right) = \log(z). \tag{C.69}$$

Hence,

$$-\frac{2}{A}s = W\left(y(s_0)\delta p_0^{1/A}\right) \tag{C.70}$$

or

$$s = -\frac{A}{2}W\left(y(s_0)\delta p_0^{1/A}\right). \tag{C.71}$$

Now we use the flow equation for u directly, coarse-graining from $\ell_0 = 0$ to ℓ:

$$\ell = \frac{1}{u} - \frac{1}{u_0} = s - s_0. \tag{C.72}$$

We are now prepared to determine how f_0 varies with δp_0 in the upper critical dimension. Directly integrating the flow equation for f, we find

$$\frac{f}{f_0} = e^{2\ell} = e^{2(s-s_0)} = \frac{e^{2s}}{e^{2s_0}}. \tag{C.73}$$

All δp_0 dependence is through s (not s_0). So to find our invariant scaling combination (or the functional dependence of f_0 on δp_0), we write

$$f_0 \sim e^{-2s}. \tag{C.74}$$

Inserting our functional form for s, using the relation

$$e^{a\,W(z)} = \frac{z^a}{W(z)^a}, \tag{C.75}$$

and calling the argument of the W function z, we have

$$f_0 \sim e^{AW(z)} \sim \frac{z^A}{W(z)^A}. \tag{C.76}$$

(We assume A is an integer, which we will see in a moment, to ignore further branch subtleties). Reinstalling the definition of z, and calling $x(u_0) = y(s_0)$, we have

$$f_0 \sim \frac{\left(x(u_0)\delta p_0^{1/A}\right)^A}{W\left(x(u_0)\delta p_0^{1/A}\right)^A} = \frac{x(u_0)^A\,\delta p_0}{W\left(x(u_0)\delta p_0^{1/A}\right)^A}, \tag{C.77}$$

Comparing this with the scaling of f determined from the asymptotics of the theory in $d = 2$ allows us to identify $A = 1$. This gives the result for the flow

equations and the invariant scaling combination in the main text. Note that $f \sim \delta p$ (as it does in $d > 2$) with additional log and log-log corrections coming from the W function.

C.4 Details of the triangular lattice numerics

Here we directly compare our continuum, isotropic expansion of the CPA to the lattice CPA for the bond-diluted triangular lattice. (As noted earlier, the rigidity transition of the diluted triangular lattice is not described correctly by our CPA analysis [117]. The static critical exponents for the triangular lattice have lengths which scale as $|\delta p|^{-\nu}$ and moduli which scale as $|\delta p|^{f}$, with $\nu \sim 1.3 \pm 0.2$ and $f \sim 2.2 \pm 0.3$; CPA predicts $\nu = 1/2$ and $f = 1$, and log corrections.)

To make this comparison with no numerically determined fitting parameters, we must know the values of the *non-universal* constants μ_0, $f_{02} \equiv \lim_{d\to 2^+} f_0 \Gamma(d/2-1)$, and u_2/u_{02}. We take the triangular lattice with nearest-neighbor bonds of strength k and bond length $a = 1$. The dynamical matrix is

$$\mathbf{D} = \begin{pmatrix} D_{xx} & D_{xy} \\ D_{yx} & D_{yy} \end{pmatrix} \tag{C.78}$$

with

$$\begin{aligned} D_{xx} = 4k\Bigg(&\sin^2\left(\frac{q_x}{2}\right) + \frac{1}{4}\sin^2\left(\frac{q_x}{4} + \frac{\sqrt{3}}{4}q_y\right) + \\ &+ \frac{1}{4}\sin^2\left(\frac{q_x}{4} - \frac{\sqrt{3}}{4}q_y\right)\Bigg), \end{aligned} \tag{C.79}$$

$$\begin{aligned} D_{xy} = D_{yx} = \sqrt{3}k\Bigg(&\sin^2\left(\frac{q_x}{4} + \frac{\sqrt{3}}{4}q_y\right) - \\ &- \sin^2\left(\frac{q_x}{4} - \frac{\sqrt{3}}{4}q_y\right)\Bigg), \end{aligned} \tag{C.80}$$

$$D_{yy} = 3k\Bigg(\sin^2\left(\frac{q_x}{4} + \frac{\sqrt{3}}{4}q_y\right) + \\ + \sin^2\left(\frac{q_x}{4} - \frac{\sqrt{3}}{4}q_y\right)\Bigg). \tag{C.81}$$

The Brillouin zone is a hexagon with side length $4\pi/3$, so the area of the Brillouin zone is $s_{\mathrm{BZ}} = 8\pi^2/\sqrt{3}$ and so $q_{\mathrm{D}} = \sqrt{8\pi/\sqrt{3}}$. For small q_x and q_y, we expand the dynamical matrix to quadratic order and find

$$\begin{aligned} D_{xx} &= \frac{3}{8}k\left(q_x^2 + q_y^2\right) + \frac{3}{4}kq_x^2 + O(q^4), \\ D_{xy} = D_{yx} &= \frac{3}{4}kq_xq_y + O(q^4), \\ D_{yy} &= \frac{3}{8}k\left(q_x^2 + q_y^2\right) + \frac{3}{4}kq_y^2 + O(q^4). \end{aligned} \tag{C.82}$$

The long-wavelength isotropic form of the dynamical matrix is

$$\mathbf{D}(q) = V(\lambda + 2\mu)\, q^2\ \hat{q}_i\hat{q}_j + V\mu q^2\left(\delta_{ij} - \hat{q}_i\hat{q}_j\right). \tag{C.83}$$

with $V = \sqrt{3}/2$ (a hexagon with side length $1/\sqrt{3}$). Comparing the two, we find that the triangular lattice is isotropic at long wavelengths with $\lambda = \mu = \sqrt{3}k/4$. The triangular lattice has an average of $\widetilde{z} = 3$ bonds per site, identifying $p_c = 2/3$. This is all of the information we need to make the comparison between the triangular lattice CPA numerics and the asymptotic scaling forms for the weakened isotropic elastic sheet. Measuring the stiffnesses in units of k, we have

$$\begin{aligned} \lambda_{\mathrm{F}} = \mu_{\mathrm{F}} &= \frac{\sqrt{3}}{4}, \\ \widetilde{z} &= 3, \\ d &= 2. \end{aligned} \tag{C.84}$$

This leads to

$$\begin{aligned} \mu_0 \equiv \frac{\mu_{\mathrm{F}}}{1 - d/\widetilde{z}} &= \frac{3\sqrt{3}}{4}, \\ f_{02} &= \frac{6\pi\sqrt{3}}{\rho}, \\ u_2/u_{02} &= \frac{3^{7/4}}{4}. \end{aligned} \tag{C.85}$$

Setting ρ arbitrarily to 2 (which sets the microscopic mass m to $\sqrt{3}$), we have an *ansatz* for the scaling form of the viscoelastic modulus of the diluted triangular lattice, rescaling to $M_\mathrm{T} = \mu/|\delta p|$ and $\Omega_\mathrm{T} = \omega/|\delta p|$:

$$\pm 1 - \frac{4}{3\sqrt{3}} M_\mathrm{T} = -\frac{1}{3\pi\sqrt{3}} \frac{\Omega_\mathrm{T}^2}{M_\mathrm{T}} \log\left(-\frac{3^{1/4}}{4\pi} \frac{\Omega_\mathrm{T}^2}{M_\mathrm{T}} |\delta p|\right). \tag{C.86}$$

This is compared with the full CPA for the bond-diluted triangular lattice:

$$\frac{p - k/k_\mathrm{F}}{1 - k/k_\mathrm{F}} = \frac{1}{\tilde{z}} \fint_\mathrm{BZ} \mathrm{d}^2 q \, \mathrm{Tr}\,(\mathbf{DG}), \tag{C.87}$$

where all expressions are for the full triangular lattice (hexagonal BZ, dynamical matrix and Green's function with triangular lattice symmetry, etc.) and $k_\mathrm{F} = 1$. The diluted triangular lattice's effective long-wavelength shear modulus is then $\mu = \sqrt{3}k/4$, and $\mu/|\delta p|$ is compared with M_T (Figure 4.4). Any discrepancies that can be seen by eye are due to corrections to scaling from higher-order terms in the dynamical matrix and Green's function, which are generically anisotropic. These corrections vanish close to the critical point, and the behavior of this anisotropic triangular lattice near the critical point predicted by the CPA is well-described by this emergent isotropic theory.

APPENDIX D

APPENDIX OF CHAPTER 5

This appendix is a reformatted version of the appendices of [117].

D.1 Bond filling protocol

One method for filling the lattice is to choose some number of bonds n to randomly occupy, and set $p = n/N$, where N is the total number of possible bonds. This has the disadvantage that changes in p can only be measured to a sensitivity $1/N$. To characterize the behavior very close to the critical point, we instead fill our lattice in a way that is statistically equivalent, but allows measurements at continuous values of p. In the isotropic case, the algorithm is as follows: first, a random number s_i taken uniformly between 0 and 1 is assigned to each bond i. At a filling parameter value p, all bonds i with assigned random numbers $s_i < p$ are filled, and the independent components of the linear elasticity tensor are measured through applied shears. For different random number seeds, the "jumps" in the linear moduli associated with the addition of single stress-supporting bonds to the rigid backbone occur at different values of p (which are not multiples of $1/N$). When the measurements are averaged over several random number seeds, we find that the measurements of moduli quickly converge to a smooth function of p at a given system size L, except at the smallest values of p. This algorithm is modified to include our anisotropy parameter r in a straightforward way.

We start by picking a random number seed, and then assigning a (uniformly

chosen) random number s_i between 0 and 1 to each bond. The bonds are assigned and then sorted based on a key, k_i, which corresponds to the value of bond occupation fraction p for which the bond would be added based on the anisotropy parameter r:

$$k_i^x = \frac{(2+r)s_i^x}{3r}, \quad k_i^y = \frac{(2+r)s_i^y}{3}, \tag{D.1}$$

where s_i^x are assigned to bonds in the horizontal direction and s_i^y are assigned to the other bonds. The bonds are then removed according to their keys, highest to lowest. Note that this formulation allows for finding the bond configuration while continuously varying both p and r.

D.2 Numerical methods

We minimize the energy given in Equation (5.19), which can be equivalently written as

$$E = \frac{1}{2}\boldsymbol{u}^\top H \boldsymbol{u}, \quad H_{ij} = \frac{\partial^2 E}{\partial u_i \partial u_j}, \tag{D.2}$$

where H is the Hessian matrix and $\boldsymbol{u}$ is a length $N \times d$ vector containing the displacements from the initial node position.

To handle periodic boundary conditions, we split the Hessian into two parts: H_{pbc}, which is computed using only the bonds that span across the network, and H_{in} with bonds which do not. The energy is therefore computed as:

$$E = \frac{1}{2}\boldsymbol{u}^\top H_{\text{in}} \boldsymbol{u} + \frac{1}{2}(\boldsymbol{u}+\boldsymbol{c})^\top H_{\text{pbc}}(\boldsymbol{u}+\boldsymbol{c}), \tag{D.3}$$

in which $\boldsymbol{c}$ "corrects" the displacements for nodes that are connected across the network and depends on the particular strain. The energy is then minimized by

finding a zero-force configuration, solving the following linear system:

$$(H_{\text{in}} + H_{\text{pbc}})\boldsymbol{u}_{\text{relaxed}} = -H_{\text{pbc}}\boldsymbol{c} \tag{D.4}$$

An affine displacement is used as an initial guess. The sparsity structure allows matrices to be stored in compressed sparse row format, reducing memory usage and improving the speed of operations. A Cholesky factorization for $(H_{\text{in}} + H_{\text{pbc}})$ is computed [167] and used as a preconditioner. For large system sizes, we use GPUs to accelerate numerical computations, such as matrix factorizations and matrix-vector products.

We note that for systems that have under-constrained nodes, the null space of $(H_{\text{in}} + H_{\text{pbc}})$ has a non-zero dimension; as such we do not consider the non-affinity parameter (which sums the squared displacements from an affine transformation) as a method of analysis or for extracting critical exponents.

D.3 Details of finite-size effects

To obtain a consistent estimate of p_c^{∞} and ν, we consider the distribution of the rigidity percolation threshold for each modulus at isotropy ($r = 1$). We take p_c^{ijkl} to be the smallest value of p at which C_{ijkl} is rigid. For a given system size L, the value of p_c^{ijkl} is sampled from an underlying distribution:

$$p_c^{ijkl}(L) \sim \rho_L^{ijkl}, \quad \rho_L^{ijkl} \in \Delta[0, 1]. \tag{D.5}$$

Histograms of p_c^{ijkl} are plotted in Fig. D.1. As the system size increases, the distributions become increasingly sharp and the means shift systematically. In

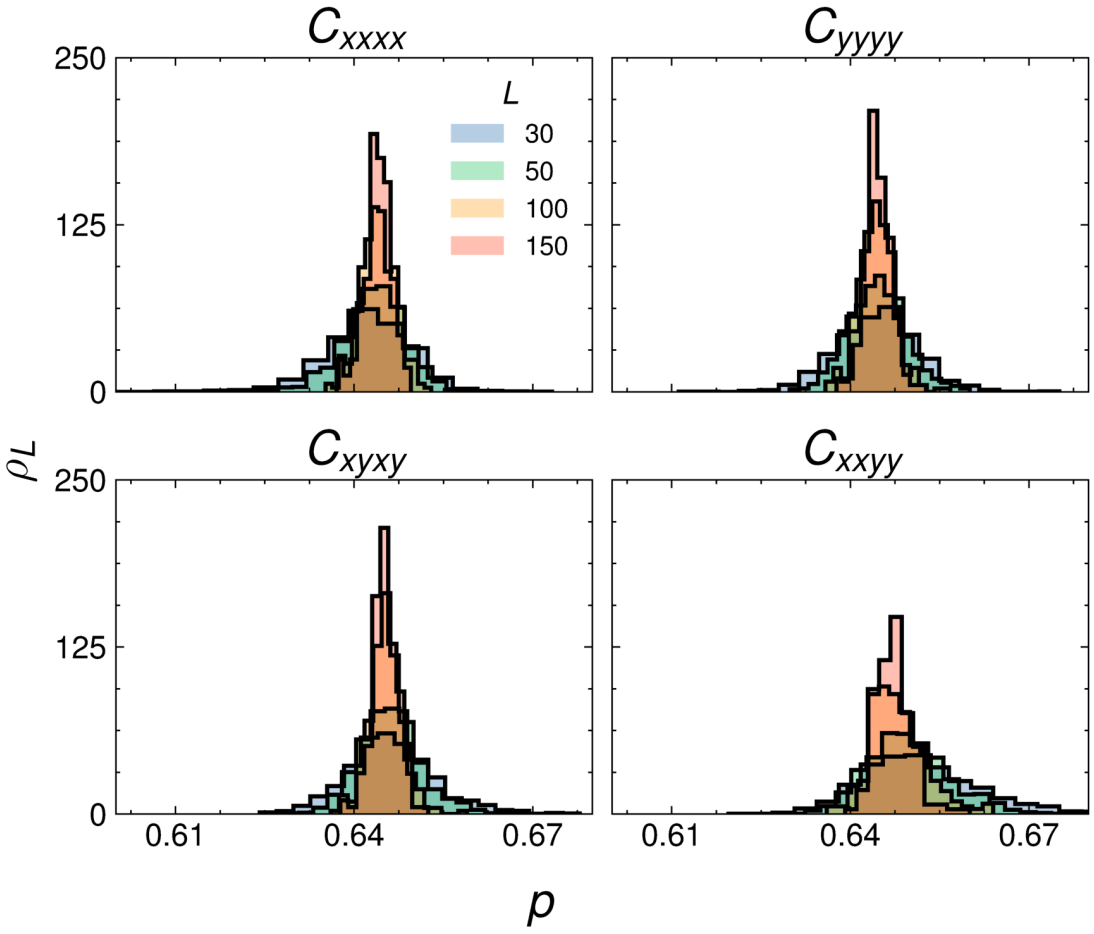

Figure D.1: **Histograms of rigidity percolation threshold p_c as a function of system size L at isotropy.** The estimated density functions for each independent elastic modulus are plotted. Each distribution becomes increasingly sharp with larger system size.

the limit of infinite system size, we assume that each distribution converges to a delta function about p_c^{∞}.

For each system size, we compute both the means $\langle p_c^{ijkl} \rangle_L$ and standard deviations σ_L^{ijkl} of each distribution. We expect systematic shifts in the means and standard deviations (i.e., the first and second moments) to scale as a power law

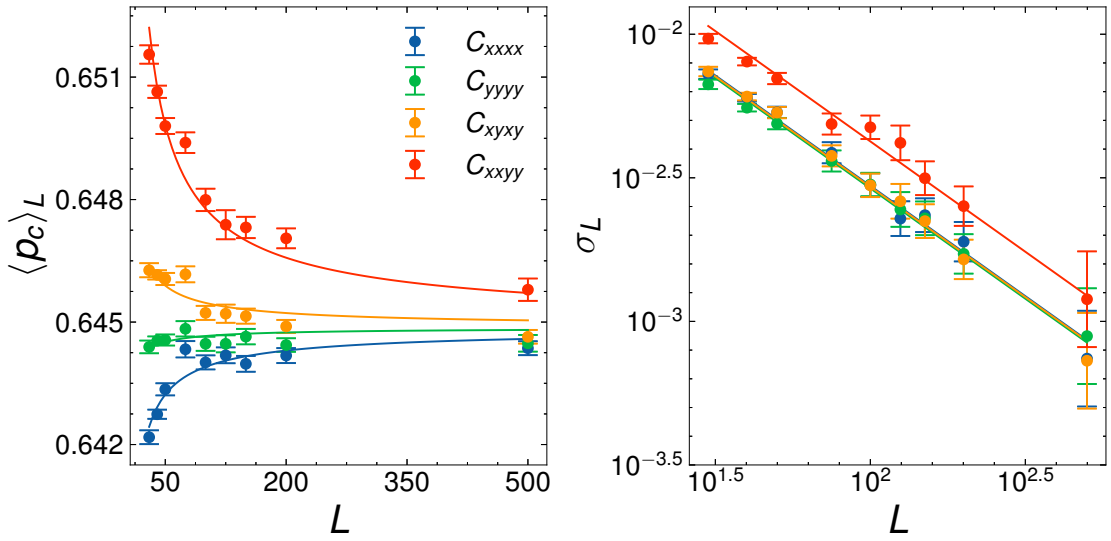

Figure D.2: **(left) Mean of p_c and (right) standard deviations of the p_c distribution at isotropy as a function of system size.** The fitted curves match those in Equation D.6 and the fitted lines on the right figure have slope $-1/\nu$.

with respect to L governed by a single critical exponent ν:

$$\begin{aligned} \langle p_c^{ijkl} \rangle_L - p_c^{\infty} &\sim L^{-1/\nu} \\ \sigma_L^{ijkl} &\sim L^{-1/\nu} \end{aligned} \tag{D.6}$$

We perform a joint non-linear least squares fit [223], with p_c^{∞} and ν the same for all curves (we assume they are equal for each modulus at isotropy). Figure D.2 depicts $\langle p_c^{ijkl} \rangle_L$ (left) and σ_L^{ijkl} (right) as a function of L. The fits give an estimate of $p_c^{\infty} = 0.645 \pm 0.002$ and $\nu = 1.3 \pm 0.2$.

Furthermore, we find a universal scaling function for the distributions ρ_L^{ijkl} with respect to our previously defined scaling variable $X \equiv (\delta p) L^{1/\nu}$:

$$\rho_L^{ijkl}(p) \sim L^{1/\nu} \mathcal{R}_{ijkl}(X). \tag{D.7}$$

We find that X collapses the density functions, with the resulting histograms shown in Fig. D.3.

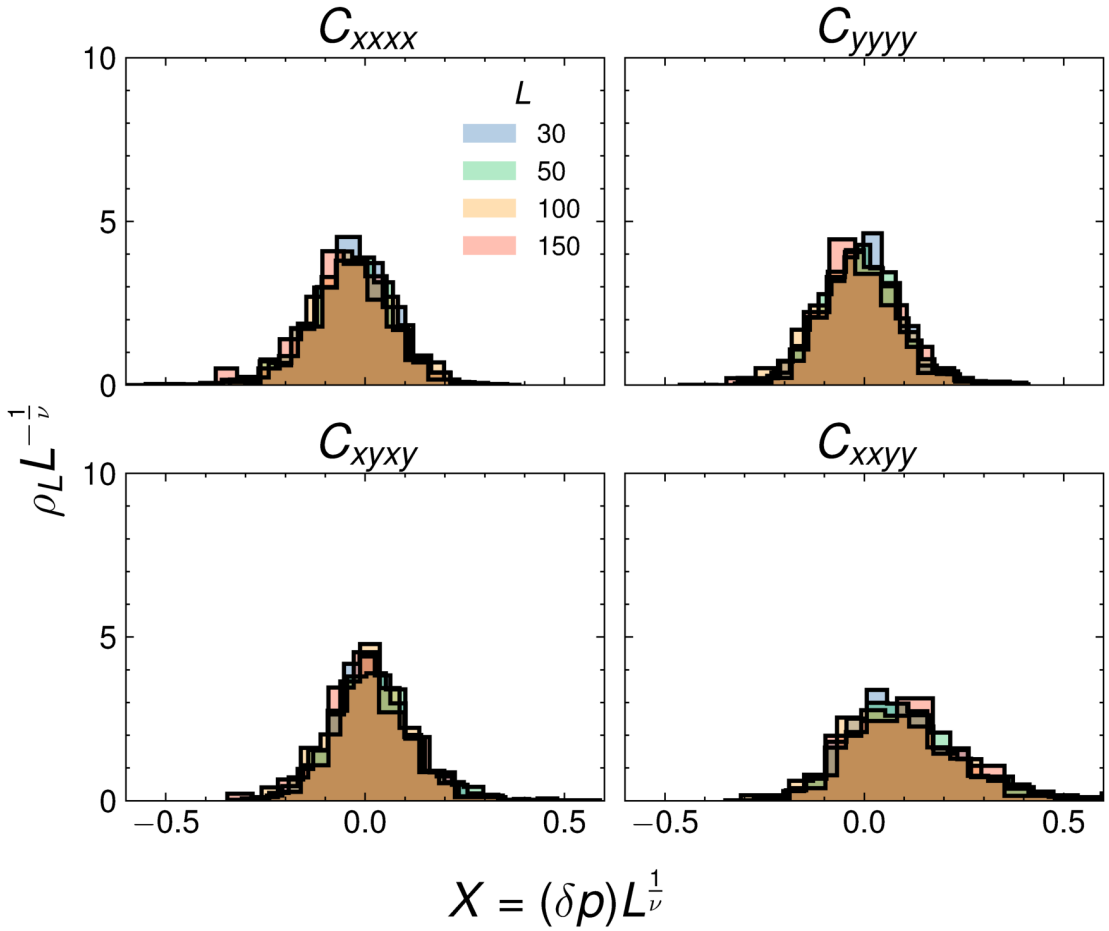

Figure D.3: **Universal scaling of rigidity distributions at isotropy for each independent modulus.** The histograms all collapse when plotted against the scaling variable X.

D.4 Details of modulus scaling collapse

At isotropy, each modulus grows as a power law above rigidity percolation threshold $C_{ijkl} \sim (\delta p)^{f^{\text{iso}}}$. Figure D.4 depicts the uncollapsed finite-size scaling data at isotropy; the systematic deviations are clear.

We find the exponent f^{iso} by considering the largest available system size ($L = 500$) and performing a least-squares fit of the modulus, finding a range of f^{iso} as we vary p_c slightly. With $f^{\text{iso}} = 2.2$, $p_c^{\infty} = 0.646$, and $\nu = 1.3$, we plot

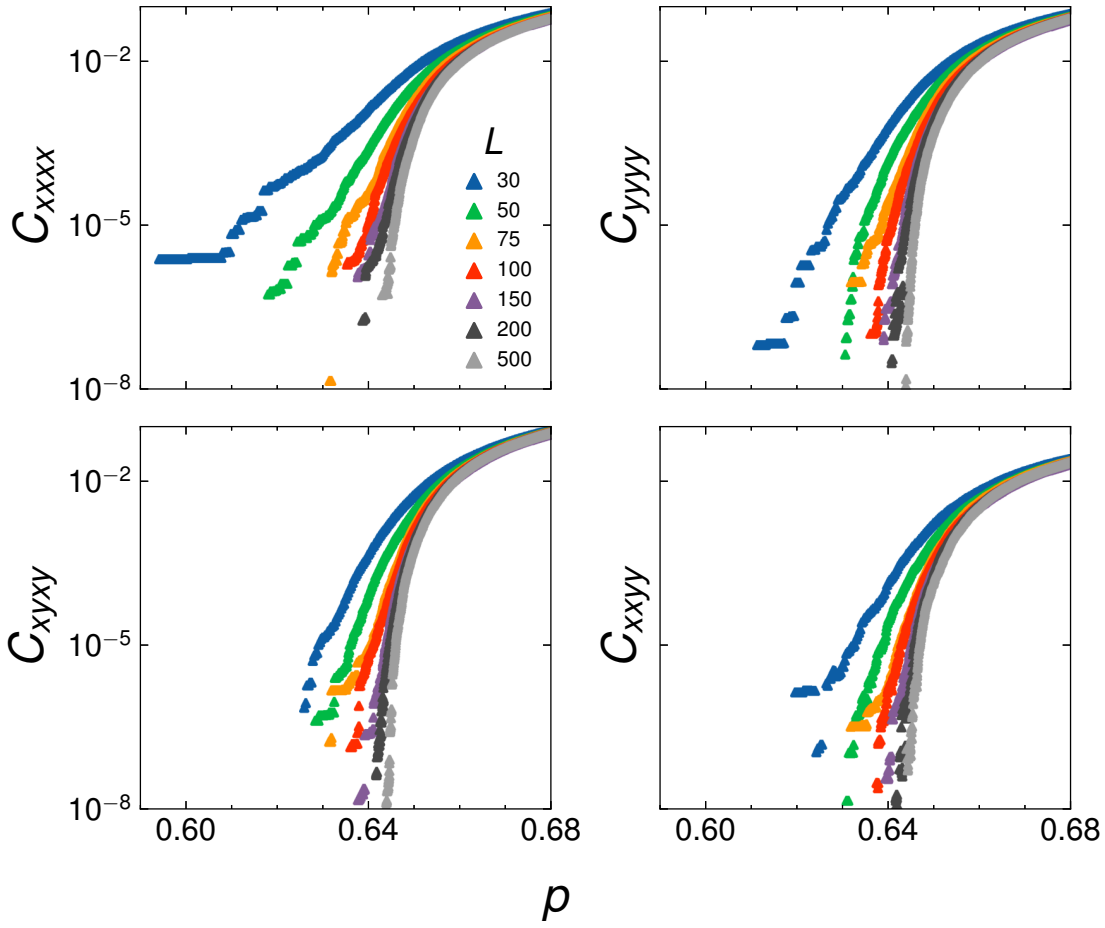

Figure D.4: **Unscaled modulus data across various system sizes at isotropy** ($r = 1$)**.** The smaller system sizes have a higher probability of becoming rigid at lower values of p.

the data against the proposed scaling variables and find a nice collapse for all independent moduli, shown in Fig. D.5. The number of samples we average over ranges from 10^4–10^2 for system sizes $L \in [30, 200]$ and 20 samples of $L = 500$.

Using the value of $f^{\text{iso}} = 1.4 \pm 0.1$ and $\nu = 1.4 \pm 0.2$ quoted in [5], we find best collapse with $p_c^{\infty} = 0.65$ shown in Fig. D.6, which gives good collapse for lower values of system size, but does not collapse the modulus for our largest system.

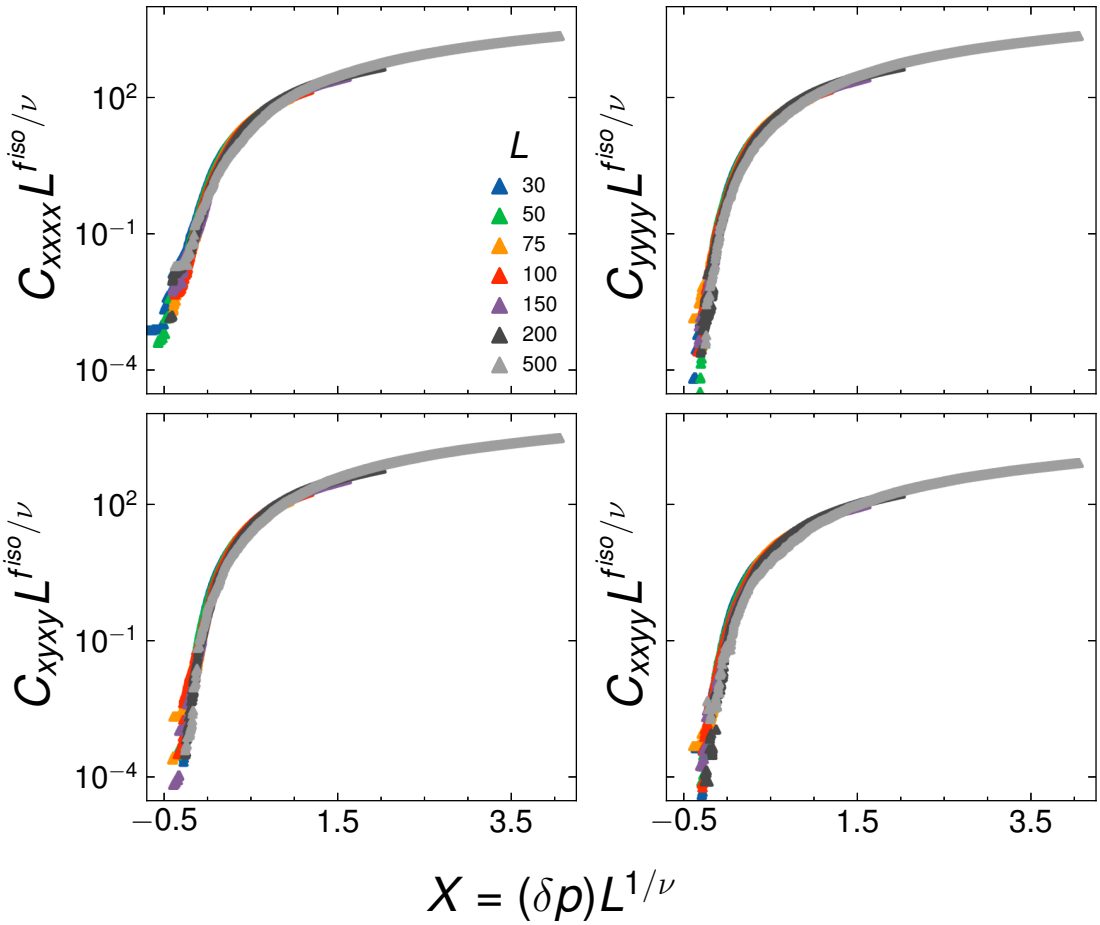

Figure D.5: **Universal scaling function of all independent elastic moduli at isotropy ($r = 1$).** The independent components of the elasticity tensor each collapse onto a single curve C^{iso}_{ijkl} when plotted against the finite-size scaling variable $X \equiv (\delta p)L^{1/\nu}$. In this isotropic case, there are only two independent moduli in the long-wavelength elasticity tensor (B and G, for instance).

D.5 Separation of phase transitions

Here we present our numerical evidence for the separation of the two phase transitions (one for C_{xxxx}, and at least one additional for C_{ijkl} with $ijkl \neq xxxx$) as $L \to \infty$. We do this by analyzing the systematic dependence on L of the distributions of p_c for each modulus away from isotropy, i.e., we perform large numbers of simulations at various system sizes for fixed $r = 1.5$ (away from

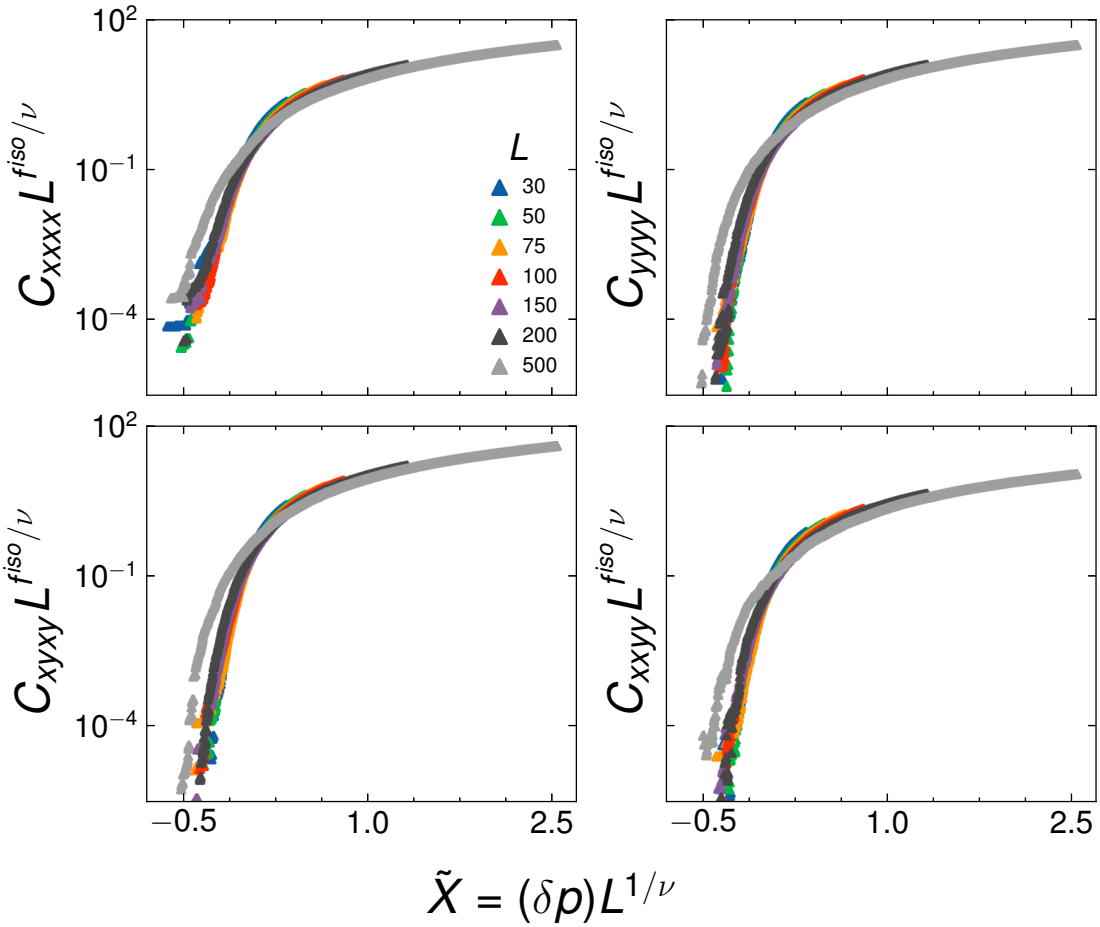

Figure D.6: **Universal scaling function of all independent elastic modulus using previously reported exponents [5].** The data for the range $L \in [30, 200]$ comparable to the earlier work does give a good collapse. Having the larger system size ($L = 500$) explains why we find different exponents.

isotropy) and examine how these distributions depend upon L. An example of these distributions can be seen in Fig. D.7, where at $L = 75$ (first column) the distributions of p_c for the C_{xxxx} and the C_{yyyy} moduli have significant overlap, but when we look at $L = 200$ (second column) the distributions are beginning to separate for $r > 1$.

Sample-to-sample, there are lattices that can support rigidity in some shear directions but not others. There are two basic scenarios. (1) In the case where including anisotropy ends up simply giving analytic corrections to scaling that

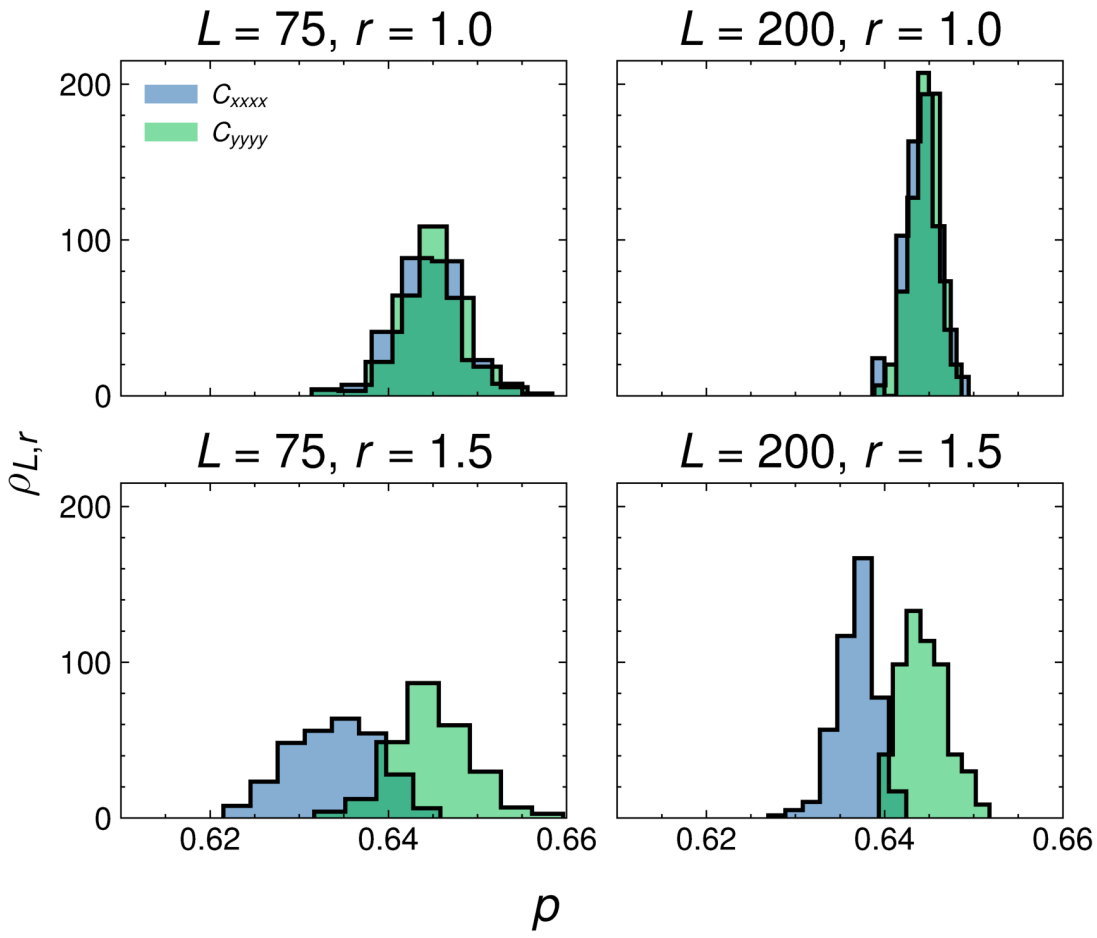

Figure D.7: **Histograms of rigidity percolation threshold p_c for C_{xxxx} (blue) and C_{yyyy} (green) for the same system size.** The means are consistent at isotropy ($r = 1$) and distinct from each other at higher anisotropy ($r = 1.5$).

bend a single phase boundary, all moduli will vanish at the same location at $L = \infty$, but the amplitudes of the finite-size effects may be different. Singling out the C_{yyyy} modulus for the sake of comparison, this means that

$$\left\langle p_c^{ijkl} \right\rangle_L - \langle p_c^{yyyy} \rangle_L \sim L^{-1/\nu}. \tag{D.8}$$

This is the same as the asymptotic scaling for the spreads of these distributions, $\sigma_L^{ijkl} \sim L^{-1/\nu}$, as all distributions are controlled by the exponents of the isotropic critical point in this supposition. If we measure the separation between the means as a function of system size in terms of the number of standard

deviations of the distribution at that system size, using the more democratic $\sigma_L^2 = (\sigma_L^{ijkl})^2 + (\sigma_L^{yyyy})^2$, then, we should find

$$\frac{\left\langle p_c^{ijkl} \right\rangle_L - \langle p_c^{yyyy} \rangle_L}{\sqrt{(\sigma_L^{ijkl})^2 + (\sigma_L^{yyyy})^2}} \sim c_{ijkl}, \tag{D.9}$$

for some constant c_{ijkl}, which is flat as a function of system size.

(2) In the case where including anisotropy leads to genuinely new critical phenomena and a pair of phase transitions, the finite-size effects of the mean and standard deviation are controlled by the finite-size scaling exponent of each anisotropic rigidity transition ν^{aniso}. If we split into a pair of phase transitions, then the spreads σ_{ijkl} of each distribution will narrow with increasing L, but the separation of the means is asymptotically constant as $L \to \infty$. This would make

$$\frac{\left\langle p_c^{ijkl} \right\rangle_L - \langle p_c^{yyyy} \rangle_L}{\sqrt{(\sigma_L^{ijkl})^2 + (\sigma_L^{yyyy})^2}} \sim L^{1/\nu^{\text{aniso}}}, \tag{D.10}$$

where ν^{aniso} is the largest of the (potentially different) finite-size scaling exponents associated with the new, anisotropic transition.

We begin by performing this measurement of the separations between the distributions of p_c for all moduli at the isotropic transition, where all moduli vanish at the same location in p as $L \to \infty$ (Fig. D.8 (left)).

As expected, this measure of the separation in the means is flat for the isotropic case as a function of system size, confirming that these moduli vanish at the same asymptotic location and that the finite-size effects controlling the mean and the standard deviation have the same systematic dependence on L.

When we perform the same analysis for the anisotropic case ($r = 1.5$), we see systematic growth in this measure as a function of system size (Fig. D.8 (right,

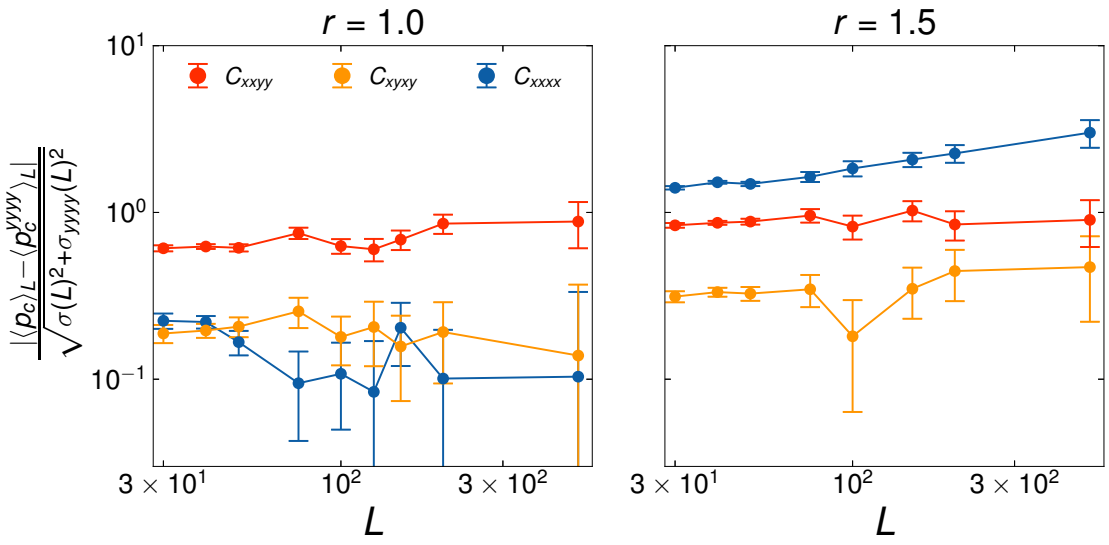

Figure D.8: **Separation of rigidity percolation threshold mean $\langle p_c \rangle$ from that of the C_{yyyy} modulus as a function of system size at isotropy (left) and anisotropy (right).**

blue)), suggesting that the locations of p_c for different moduli are genuinely different in the thermodynamic limit. This is moderately strong quantitative evidence for the information that can roughly be seen by eye in Fig. D.7.

D.6 Estimate of anisotropic scaling exponents

At infinite system size, the phase diagram curves in Fig. A.2 contain important information about the critical exponent ζ near the isotropic transition. We find ζ by fitting the differences between the C_{xxxx} curves and the C_{ijkl} curves (where $ijkl \neq xxxx$) to a power law, resulting in a value of $\zeta = 0.25 \pm 0.1$. The individual phase boundaries have an important linear correction to scaling, as the unstable eigenvector is not along the r-axis, but has a slope m. Hence the two phase boundaries are of the form $\delta p = m(r - r_c) + W(r - r_c)^{1/\zeta}$, with a fixed value of W defining a curve along which the invariant scaling combination is constant.

Because ζ is small, this correction cannot be neglected. By fitting the differences between the phase boundaries, we bypass this linear correction to scaling.

Furthermore, we can consider the standard deviations of the rigidity percolation threshold distributions (as in Appendix D.3) for $r > 1$ and consider a scaling function with respect to our scaling variable $Y = (r-1)L^{\zeta/\nu}$

$$\sigma^{ijkl}(L, r) \sim L^{-1/\nu} \mathcal{S}_{ijkl}((r-1)L^{\zeta/\nu}) \tag{D.11}$$

We find that standard deviation is best collapsed with $\zeta = 0.25 \pm 0.1$, shown in Fig. D.9. The determined value of the exponent ζ appears to collapse $\sigma L^{1/\nu}$ for all moduli except for C_{xxxx} at larger values of the scaling variable. We also note the nice overlap of data performed at different values of (r, L) but the same value of the scaling variable Y.

We can in principle use information from these collapse plots to make a prediction for the value of the finite-size scaling exponent close to the anisotropic phase transition ν^{aniso}. First, we note that if we fix $r > 1$ and send $L \to \infty$, the spread in the distributions of p_c will narrow as $\sigma \sim L^{-1/\nu^{\text{aniso}}}$, as the finite-size effects are (at large enough system sizes) controlled by the critical exponents of the anisotropic critical point. In the scaling function for the distributional spreads of p_c, this corresponds to the asymptotic limit $Y \to \infty$. Forcing the asymptotics of the numerically determined crossover scaling function to agree with the asymptotics expected at the anisotropic critical point will give us a prediction for ν^{aniso}.

Suppose this scaling function has asymptotic behavior $\mathcal{S}_{ijkl}(Y) \sim Y^{\alpha}$ at large Y. Then in the limit $L \to \infty$ with $r > 1$ fixed,

$$\sigma L^{1/\nu} \sim Y^{\alpha} \sim L^{\zeta\alpha/\nu} \text{ and } \sigma \sim L^{-1/\nu^{\text{aniso}}} \tag{D.12}$$

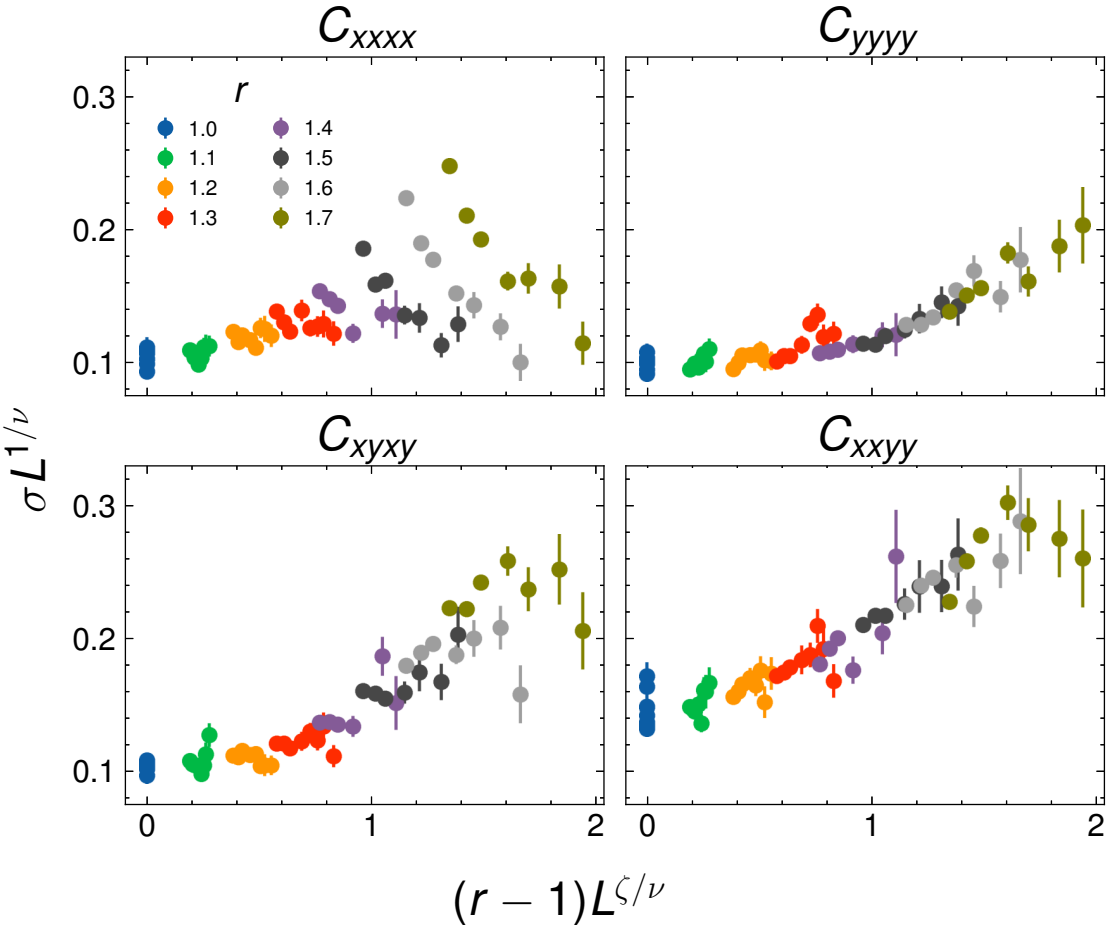

Figure D.9: **Universal scaling of rigidity distributions near isotropy for each independent modulus.** The widths of the histograms all collapse onto a single curve when plotted against the finite-size scaling variable Y. There appear to be deviations in the collapse of the C_{xxxx} modulus at higher values of Y.

together give

$$\nu^{\text{aniso}} = \frac{\nu}{1-\zeta\alpha}, \tag{D.13}$$

where ν is the value of the finite-size scaling exponent at the isotropic fixed point. With $\alpha = 1.0 \pm 0.5$, this gives a prediction of $\nu^{\text{aniso}} = 1.7$, but values between $1.2 - 3.2$ are consistent with our error bars reported in Table 5.1. This is ultimately due to the poor numerical determination of ζ and α. These could also in principle be different for the different $ijkl$; this would be detected through different values of α for each modulus since both ν and ζ are properties of the

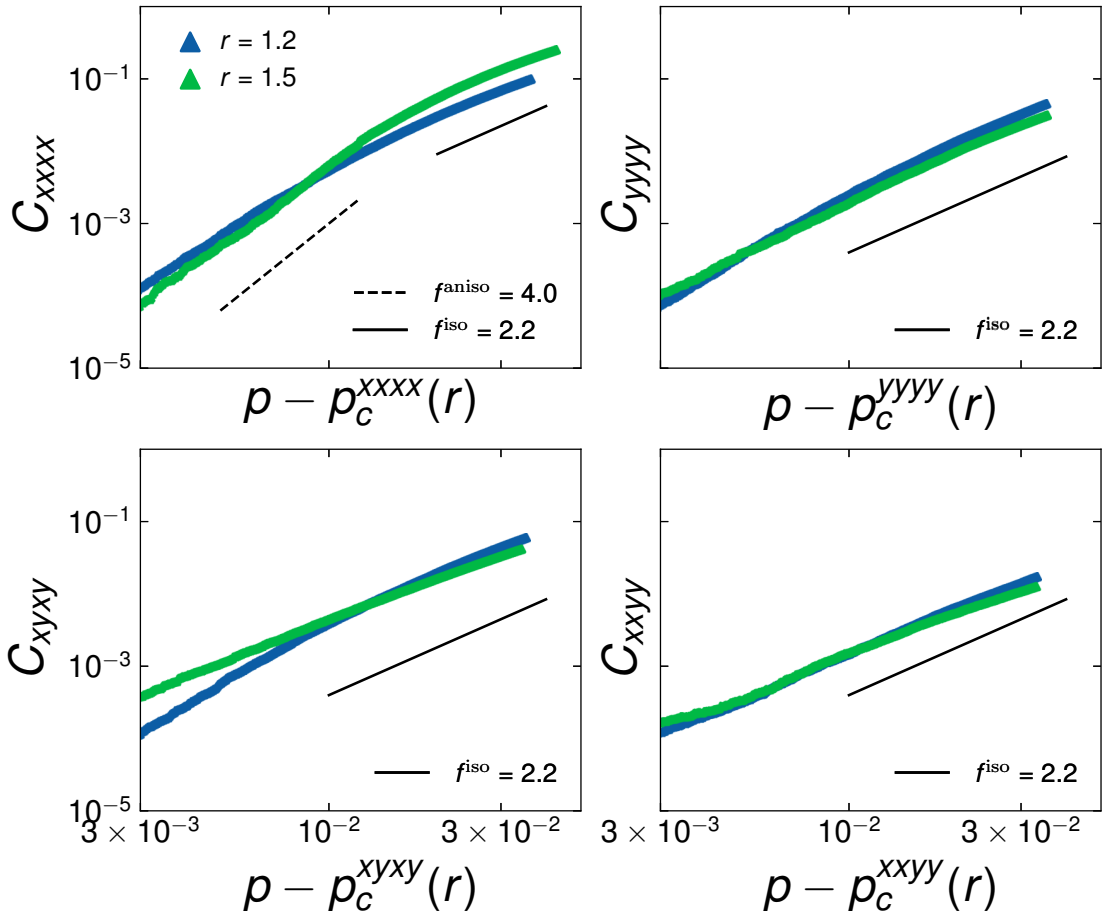

Figure D.10: **Estimate of anisotropic scaling exponent of each modulus from our largest system size.** The behavior of the C_{xxxx} modulus suggests a crossover between the anisotropic and isotropic scaling exponents, whereas for the other moduli, the behavior appears to be governed by the same isotropic exponent.

isotropic fixed point.

We estimate the exponent with which each modulus vanishes at their corresponding anisotropic phase transition (f_{ijkl}^{aniso}) by considering our largest system size at two values of r away from isotropy ($r = 1.2$ and $r = 1.5$). The location of the phase transition is determined by averaging the value of p with which each modulus for each lattice becomes rigid.

To search for which value of ζ best collapses the two variable scaling func-

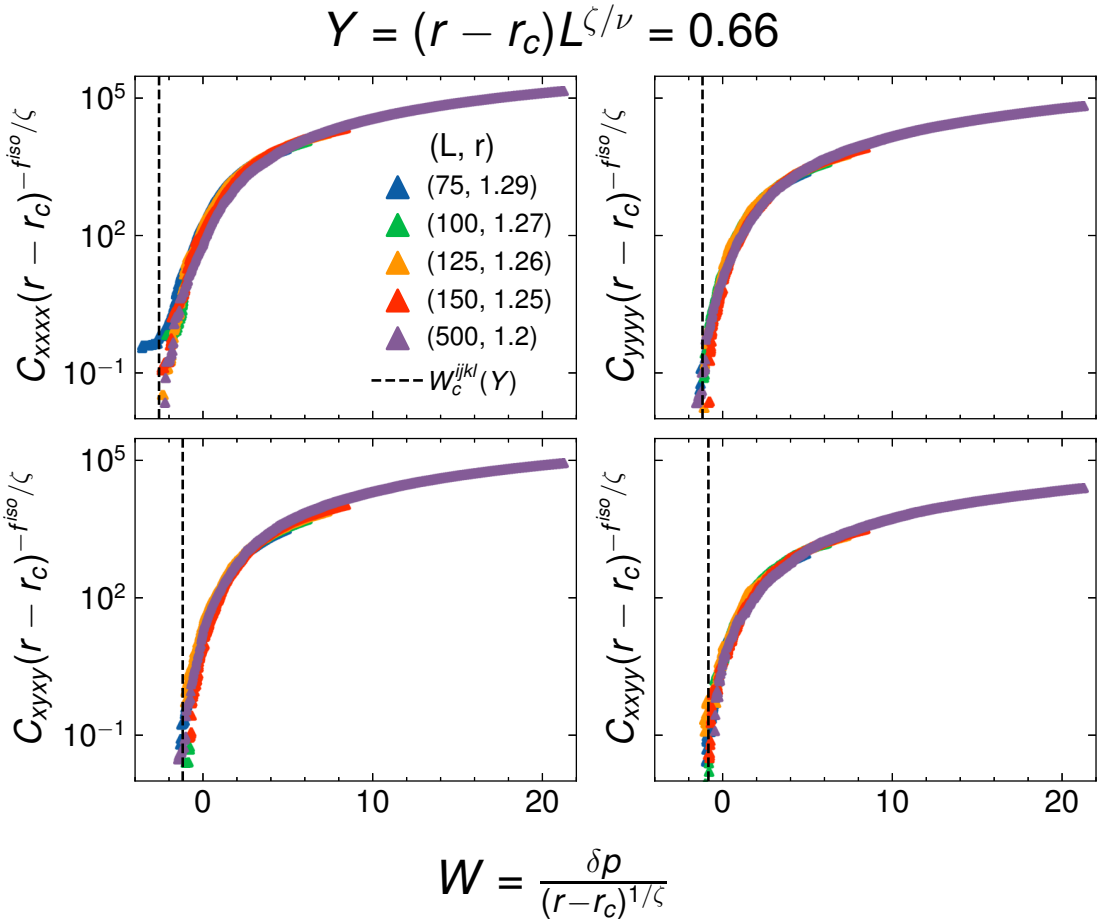

Figure D.11: **Scaling collapse of all the moduli at constant** $Y = 0.66$**.** The estimate of W_c is shown with the dashed black line.

tion, we obtain simulations of constant Y across various system sizes. We test a value of ζ by first fixing our largest system size and then solving for the value of r as a function of system size that results in the same value of Y. Figures D.11 and D.12 show a scaling collapse of all the moduli with $\zeta = 0.25$ and with a constant value of $Y = 0.66$ and $Y = 1.65$, respectively. The scaling function for each modulus vanishes at a given value of W, which we denote as $W_c^{ijkl}(Y)$, as it is dependent on the value of Y. We note that further away from isotropy ($Y = 0$), there are additional corrections to scaling, resulting in a worse collapse at higher values of Y.

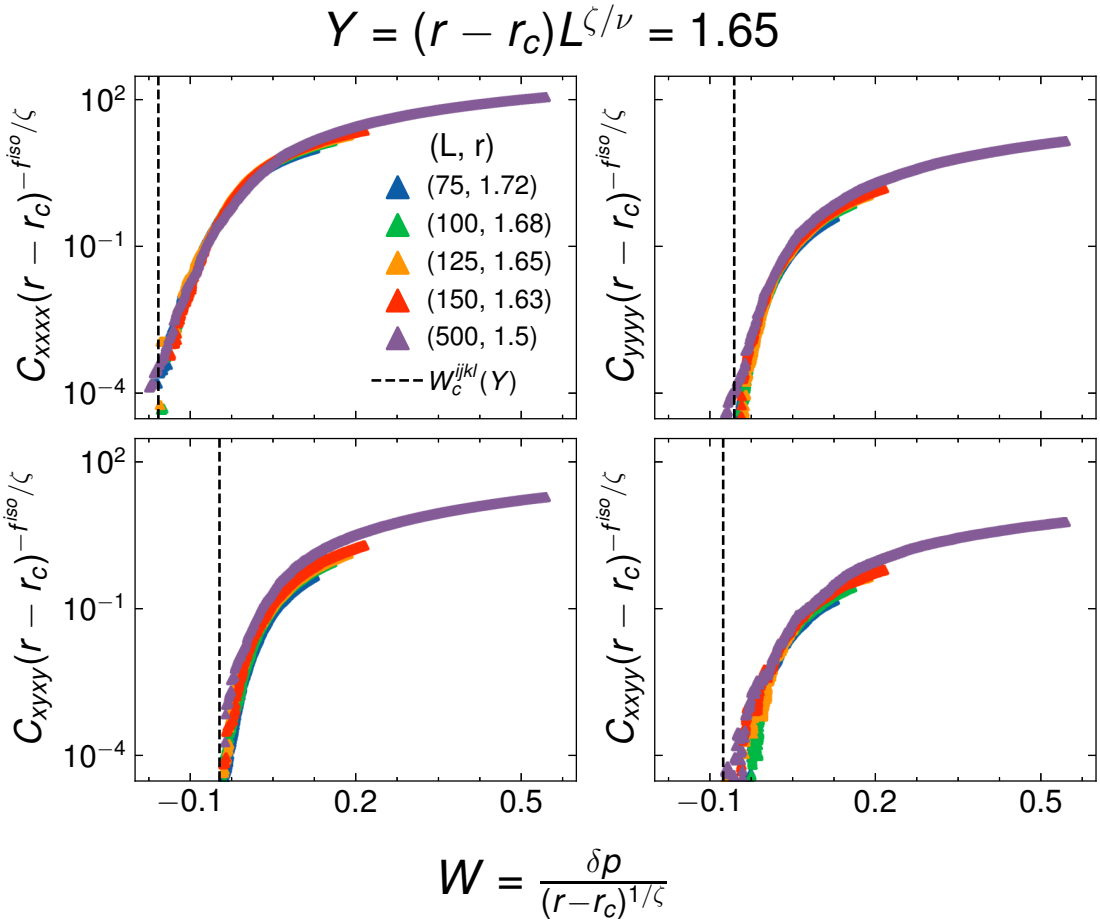

Figure D.12: **Scaling collapse of all the moduli at a constant** $Y = 1.65$**.** The estimate of W_c is shown with the dashed black line.

We again obtain an estimate of the scaling exponents in Figures D.13 and D.14 by plotting the rescaled moduli as a function of distance from W_c. The plots suggest crossover for the C_{xxxx} modulus, with f^{aniso}_{xxxx} governing the behavior for lower values of $W - W_c$ and f^{iso} for the high $W - W_c$ regime. Furthermore, the other three moduli appear to vanish with a critical exponent indistinguishable from f^{iso} within our estimated error bars.

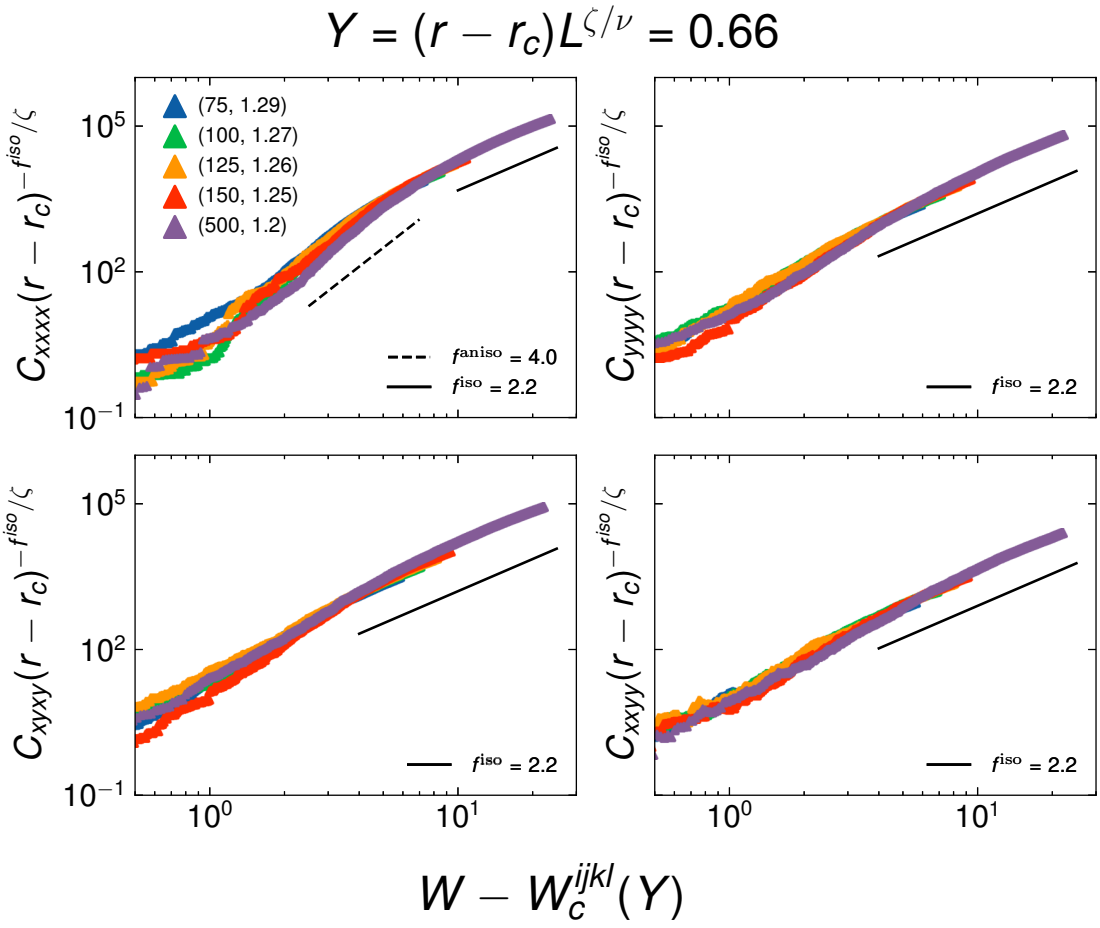

Figure D.13: **Estimate of anisotropic scaling exponent of each modulus at a constant** $Y = 0.66$**.** The simulation data is the same as found in Fig. D.11.

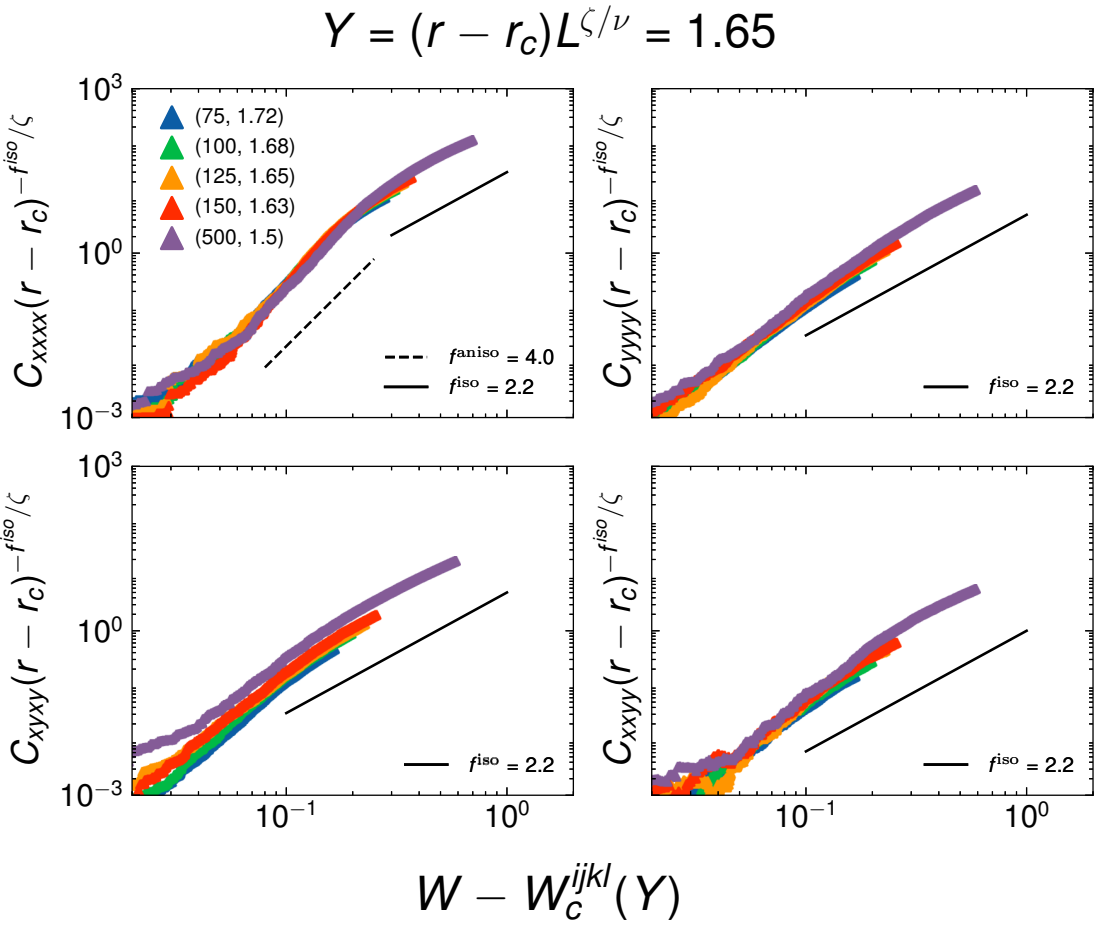

Figure D.14: **Estimate of anisotropic scaling exponent of each modulus at a constant** $Y = 1.65$**.** The simulation data is the same as found in Fig. D.12.

APPENDIX E

APPENDIX OF CHAPTER 6

This appendix is a reformatted version of the appendix of the manuscript to be submitted to Physical Review B or E.

E.1 Contour plots of error in expansion for $\chi(a, g)$

The relative error that the expansion in Equation 6.62 makes with the experimental value of $\chi(a, g)$ can be plotted in the original LPA coordinates, giving contour plots of the relative error. First, we show the result of directly integrating A^{-1} until its asymptotic value as a function of the starting LPA coordinates (a, g) as a contour plot in Figure E.1.

As required, the susceptibility diverges as one approaches the critical manifold, with a leading power law related to the eigenvalues of the fixed point that attracts flows on the critical manifold. We then plot the relative error associated with higher and higher order truncations of Equation 6.62. The relative errors associated with truncating Equation 6.62 to order Δa^0, $\Delta a^{\omega\nu}$, Δa^1, $\Delta a^{2\omega\nu}$, and $\Delta a^{1+\omega\nu}$ are shown as Figures E.2, E.3, E.4, E.5, and E.6, respectively. The relative error improves order by order especially along the critical manifold. The expansion fails in an interesting region near the Gaussian fixed point.

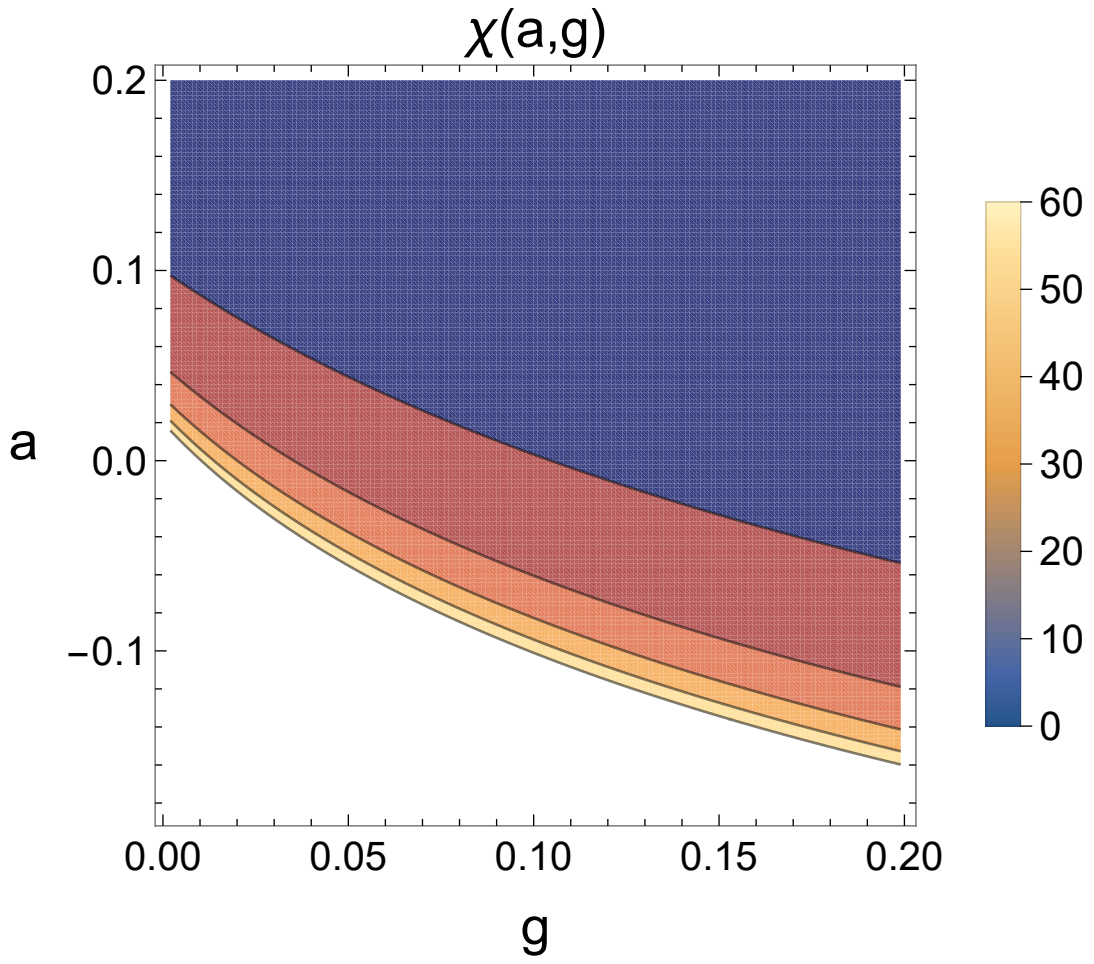

Figure E.1: The numerically determined values of $\chi(a, g)$ as a function of the starting LPA coordinate. As required, the susceptibility diverges upon approaching the critical manifold.

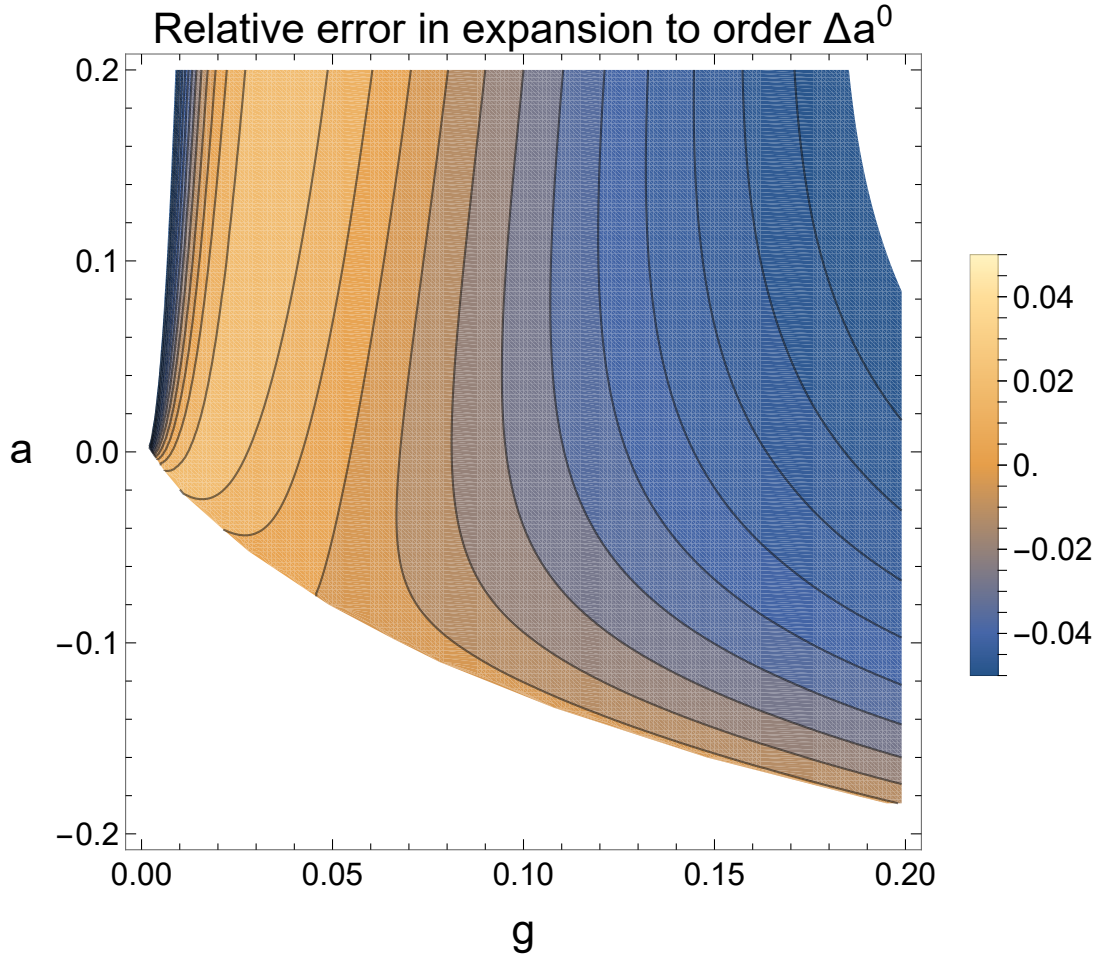

Figure E.2: The relative error that the expansion of Equation 6.62 truncated to order Δa^0 makes with a direct integration of $\chi(a, g)$ shown as a contour plot in (a, g).

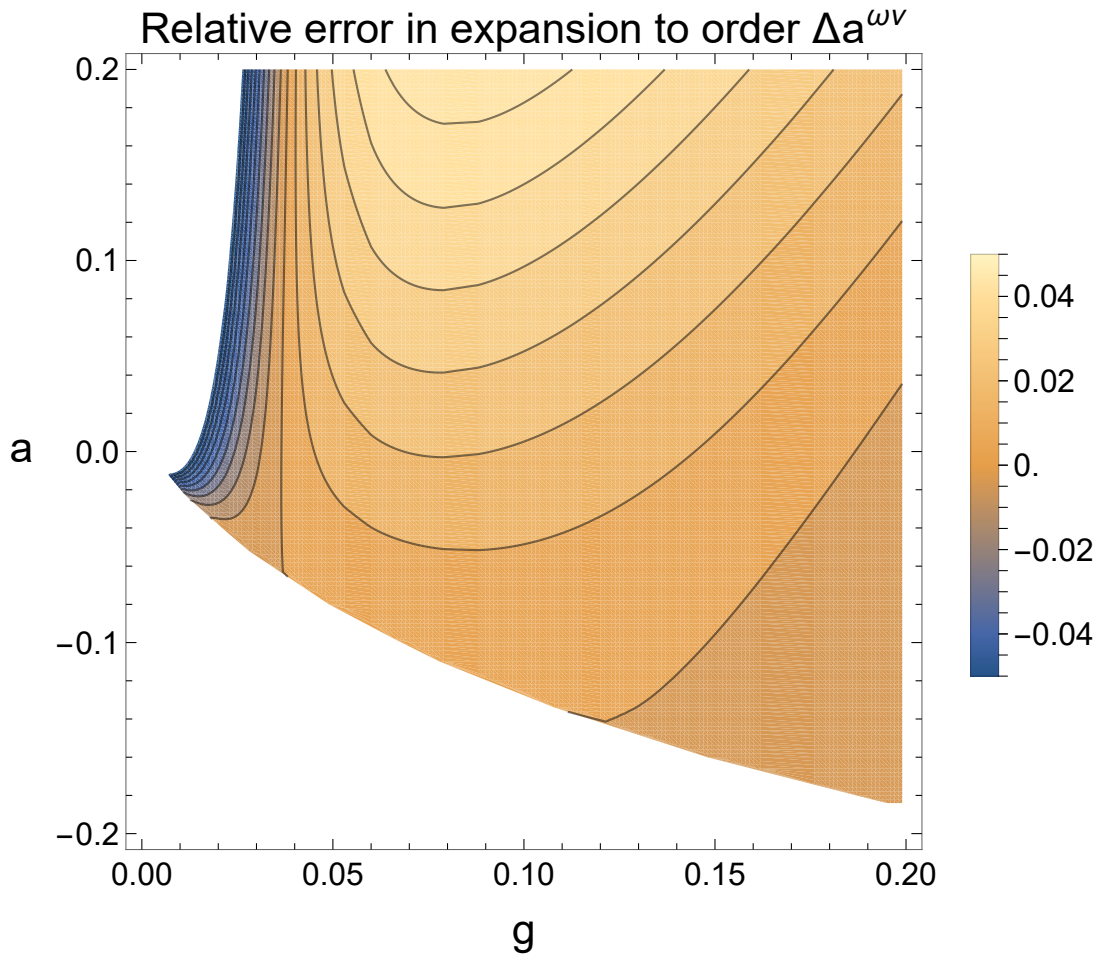

Figure E.3: The relative error that the expansion of Equation 6.62 truncated to order $\Delta a^{\omega\nu}$ makes with a direct integration of $\chi(a, g)$ shown as a contour plot in (a, g).

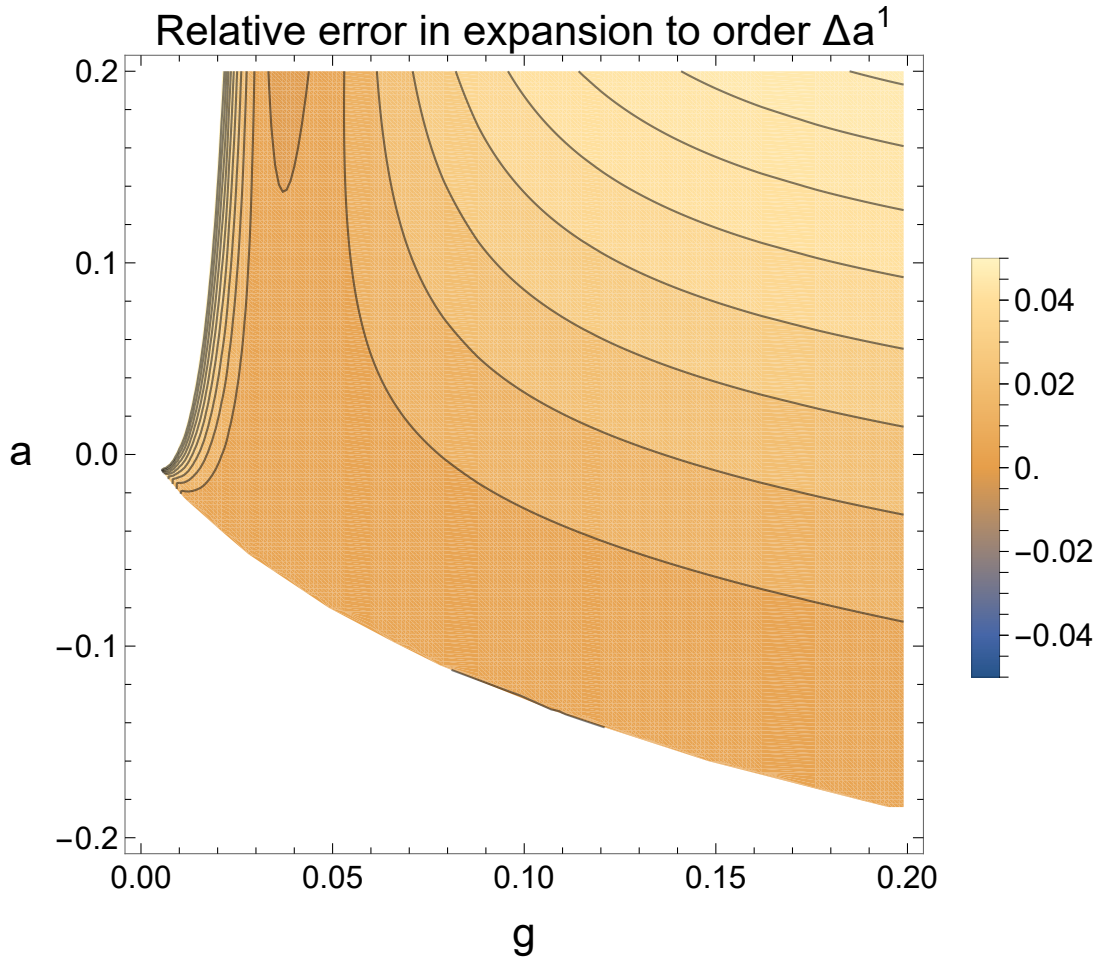

Figure E.4: The relative error that the expansion of Equation 6.62 truncated to order Δa^1 makes with a direct integration of $\chi(a, g)$ shown as a contour plot in (a, g).

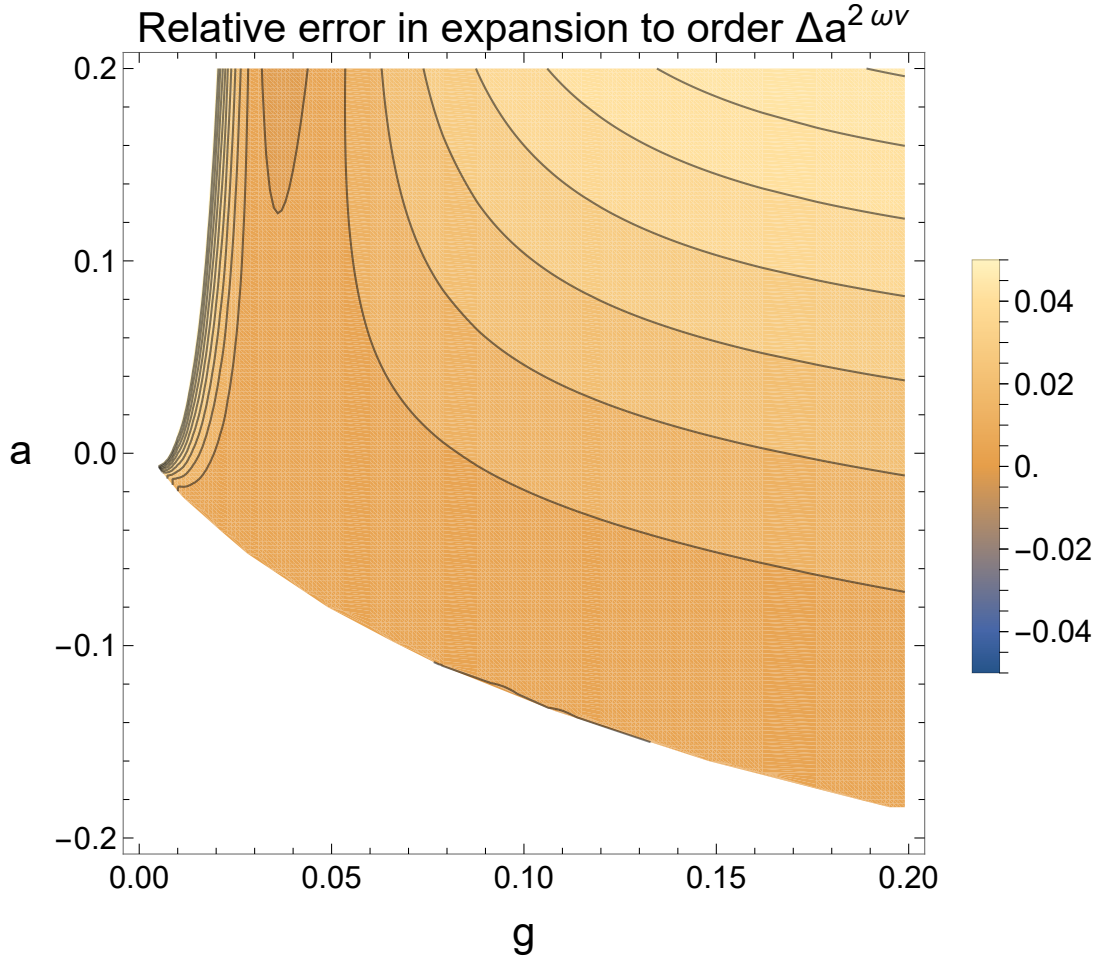

Figure E.5: The relative error that the expansion of Equation 6.62 truncated to order $\Delta a^{2\omega\nu}$ makes with a direct integration of $\chi(a, g)$ shown as a contour plot in (a, g).

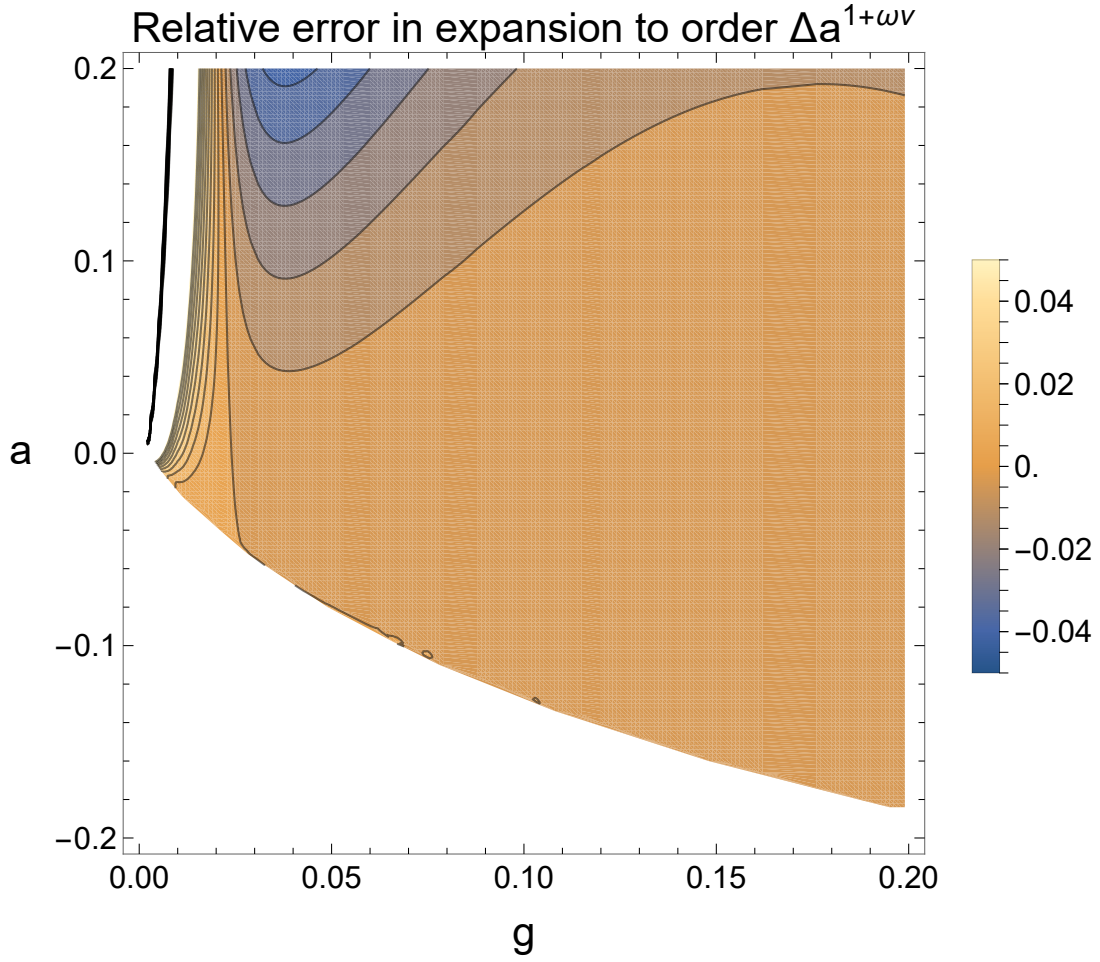

Figure E.6: The relative error that the expansion of Equation 6.62 truncated to order $\Delta a^{1+\omega\nu}$ makes with a direct integration of $\chi(a, g)$ shown as a contour plot in (a, g).

APPENDIX F

APPENDIX OF CHAPTER 7

This appendix is a reformatted version of the supplementary information of the manuscript to be submitted to Physical Review E.

F.1 Supplementary information

To complement the full analysis in the main text following [180], we include an image of each inequivalent type of defect in each symmetry-allowed ordered phase, along with a defect combination table for the finite groups. For simplicity, most defects are shown as point defects in 2D but can also be thought of as cores of line defects in 3D. Often there is freedom in choosing the coordinate system that is pinned to a defect and transported along the path of transformations in the order parameter space, so what is provided is one possible way of labelling the defects up to automorphism.

F.1.1 Isotropic *I* phase

The isotropic phase is the most symmetric, with all of SO(3) being a symmetry. The connected order parameter space is SO(3)/SO(3) which is the trivial topological space. There is only one orientation possible, and all homotopy groups are trivial.

F.1.2 Vector V phase

The connected order parameter space for the vector phase is $\mathrm{SO}(3)/C_\infty = S^2$. This can be visualized as an arrow of unit length at each point in space. The fundamental group is trivial (can't lasso a basketball), indicating that there are no nontrivial line defects in 3D. However, the second homotopy group is nontrivial, suggesting the existence of nontrivial point defects in 3D. These are the well-known skyrmions, characterized by their wrapping number $Q \in \mathbb{Z}$. Topological index +1, +2, and −1 are shown below. Plotted are the representatives

$$\mathbf{m} = \{\cos(Q\phi)\sin(\theta),\ \sin(Q\phi)\sin(\theta),\ \cos(\theta)\} \tag{F.1}$$

where Q is the topological charge. That this wraps S^2 in configuration space exactly Q times for $|Q| > 0$ can be seen by considering that the longitude slices $\phi \in ((n-1)\,2\pi/|Q|, n2\pi/|Q|)$, $n = 1, \ldots, Q$, each individually cover S^2 and cannot be "combed out." The topological index can also be explicitly computed by performing a stereographic projection of the field $\mathbf{m}$ to $(x, y) \in \mathbb{R}^2$ and computing

$$Q_{\mathrm{sk}} \equiv -\frac{1}{4\pi}\int \mathrm{d}x\,\mathrm{d}y\,\left(\partial_x\mathbf{m}\times\partial_y\mathbf{m}\right)\cdot\mathbf{m} = Q\int \mathrm{d}x\,\mathrm{d}y\,\frac{1}{\pi\left(1+x^2+y^2\right)^2} = Q. \tag{F.2}$$

F.1.3 Nematic N phase

The (uniaxial) nematic phase is the only phase in the diagram that can support topologically stable line *and* point defects, and these interact in nontrivial ways. The phase can be visualized by placing rods with circular cross section at each point in space. The order parameter space is $\mathbb{R}\mathrm{P}^2$, which can support only one topologically nontrivial kind of line defect. The topologically distinct point defects are labelled by the positive integers $\mathbb{Z}_+$, since the point defects can be

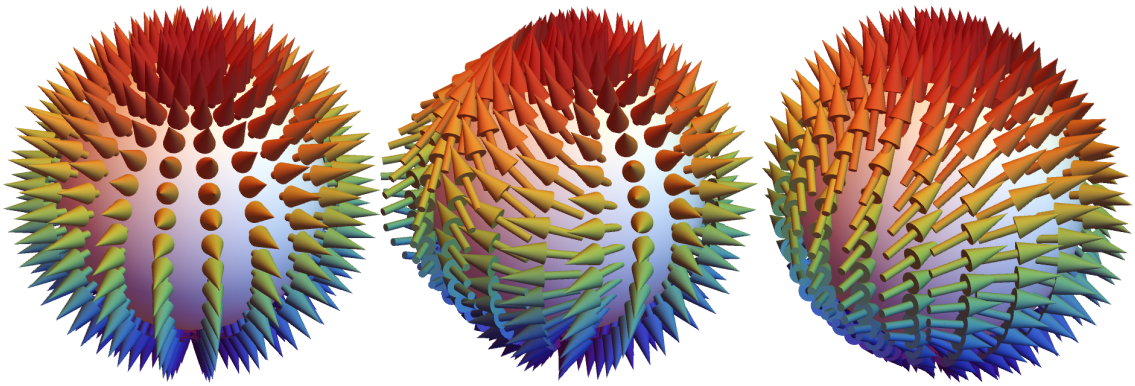

Figure F.1: Sketches of skyrmion point defects in the vector V phase. The skyrmions have charges (a) $Q = +1$, (b) $Q = +2$, and (c) $Q = -1$.

transported around the line defects to change their sign. See section VII.E.3 of [180] for a complete treatment of this phase.

F.1.4 Tetrahedratic T phase

The tetrahedratic T phase has symmetry group equal to the tetrahedral point group T, representing symmetries of a tetrahedron. The molecules can hence be visualized as tetrahedra. There are no stable point defects because the symmetry group of the molecule is discrete but $\pi_1(\mathrm{SO}(3)/T) \cong 2T$ which is a non-abelian group of order 24. Because the first homotopy group is non-abelian, we must compute the conjugacy classes to find the unambiguous labelling of the defects. There are 7 conjugacy classes and hence 6 distinct types of defect. One can think of all defects as combinations of $2\pi/3$ rotations about an axis normal to a face and π rotations about axes that pass through the centers of two edges not sharing a face.

For simplicity, a reference configuration of the tetrahedron is chosen and all

	$\mathbf{C_0}$	$\overline{\mathbf{C_0}}$	$\mathbf{C_Q}$	$\mathbf{C_{w_1}}$	$\mathbf{C_{-w_1}}$	$\mathbf{C_{w_2}}$	$\mathbf{C_{-w_2}}$
$\mathbf{C_0}$	C_0	$\overline{C_0}$	C_Q	C_{w_1}	C_{-w_1}	C_{w_2}	C_{-w_2}
$\overline{\mathbf{C_0}}$	$\overline{C_0}$	C_0	C_Q	C_{-w_1}	C_{w_1}	C_{-w_2}	C_{w_2}
$\mathbf{C_Q}$	C_Q	C_Q	$6C_0 + 6\overline{C_0} + 4C_Q$	$3C_{w_1} + 3C_{-w_1}$	$3C_{w_1} + 3C_{-w_1}$	$3C_{w_2} + 3C_{-w_2}$	$3C_{w_2} + 3C_{-w_2}$
$\mathbf{C_{w_1}}$	C_{w_1}	C_{-w_1}	$3C_{w_1} + 3C_{-w_1}$	$3C_{w_2} + C_{-w_2}$	$C_{w_2} + 3C_{-w_2}$	$4C_0 + 2C_Q$	$4\overline{C_0} + 2C_Q$
$\mathbf{C_{-w_1}}$	C_{-w_1}	C_{w_1}	$3C_{w_1} + 3C_{-w_1}$	$C_{w_2} + 3C_{-w_2}$	$3C_{w_2} + C_{-w_2}$	$4\overline{C_0} + 2C_Q$	$4C_0 + 2C_Q$
$\mathbf{C_{w_2}}$	C_{w_2}	C_{-w_2}	$3C_{w_2} + 3C_{-w_2}$	$4C_0 + 2C_Q$	$4\overline{C_0} + 2C_Q$	$3C_{w_1} + C_{-w_1}$	$C_{w_1} + 3C_{-w_1}$
$\mathbf{C_{-w_2}}$	C_{-w_2}	C_{w_2}	$3C_{w_2} + 3C_{-w_2}$	$4\overline{C_0} + 2C_Q$	$4C_0 + 2C_Q$	$C_{w_1} + 3C_{-w_1}$	$3C_{w_1} + C_{-w_1}$

Table F.1: Combination rules for defects in the tetrahedratic T-phase. When there are multiple classes resulting from the product of two conjugacy classes, then the resulting defect depends on the path along which two defects are brought together.

representatives of defects are drawn as rotations about the $(1/\sqrt{3}, 1/\sqrt{3}, 1/\sqrt{3}) \equiv \mathbf{a}_1$ axis (passing through the center of a face and a vertex) and the $(1, 0, 0) \equiv \mathbf{a}_2$ axis (passing through the centers of two edges not sharing a face). With a fixed choice of reference configuration, one can enumerate choices of defects from $2T$:

$$C_{w_1} : w_{++++} = (1 + i\sigma_x + i\sigma_y + i\sigma_z)/2 = \exp\left(i\left(\frac{\pi}{3}\right)\mathbf{a}_1 \cdot \sigma\right) = \frac{2\pi}{3} \text{ rotation about } \mathbf{a}_1.$$

$$C_{-w_1} : w_{----} = (-1 - i\sigma_x - i\sigma_y - i\sigma_z)/2 = \exp\left(i\left(-\frac{2\pi}{3}\right)\mathbf{a}_1 \cdot \sigma\right) = -\frac{4\pi}{3} \text{ rotation about } \mathbf{a}_1.$$

$$C_{w_2} : w_{+---} = (1 - i\sigma_x - i\sigma_y - i\sigma_z)/2 = \exp\left(i\left(-\frac{\pi}{3}\right)\mathbf{a}_1 \cdot \sigma\right) = -\frac{2\pi}{3} \text{ rotation about } \mathbf{a}_1.$$

$$C_{-w_2} : w_{-+++} = (-1 + i\sigma_x + i\sigma_y + i\sigma_z)/2 = \exp\left(i\left(\frac{2\pi}{3}\right)\mathbf{a}_1 \cdot \sigma\right) = \frac{4\pi}{3} \text{ rotation about } \mathbf{a}_1.$$

$$C_Q : i\sigma_x = \exp\left(i\left(\frac{\pi}{2}\right)\mathbf{a}_2 \cdot \sigma\right) = \pi \text{ rotation about } \mathbf{a}_2.$$

$\overline{C_0} : -1 = \exp\left(i\left(\pi\right)\mathbf{a}_2 \cdot \sigma\right) = 2\pi$ rotation about $\mathbf{a}_2$. (Note any other axis also works.)

F.1.5 Biaxial phases: $N + 2$, N_T, $(N_T + 2)^*$

The biaxial phases have symmetry group equal to D_2, representing symmetries of a rectangular parallellepiped. There are no stable point defects because the

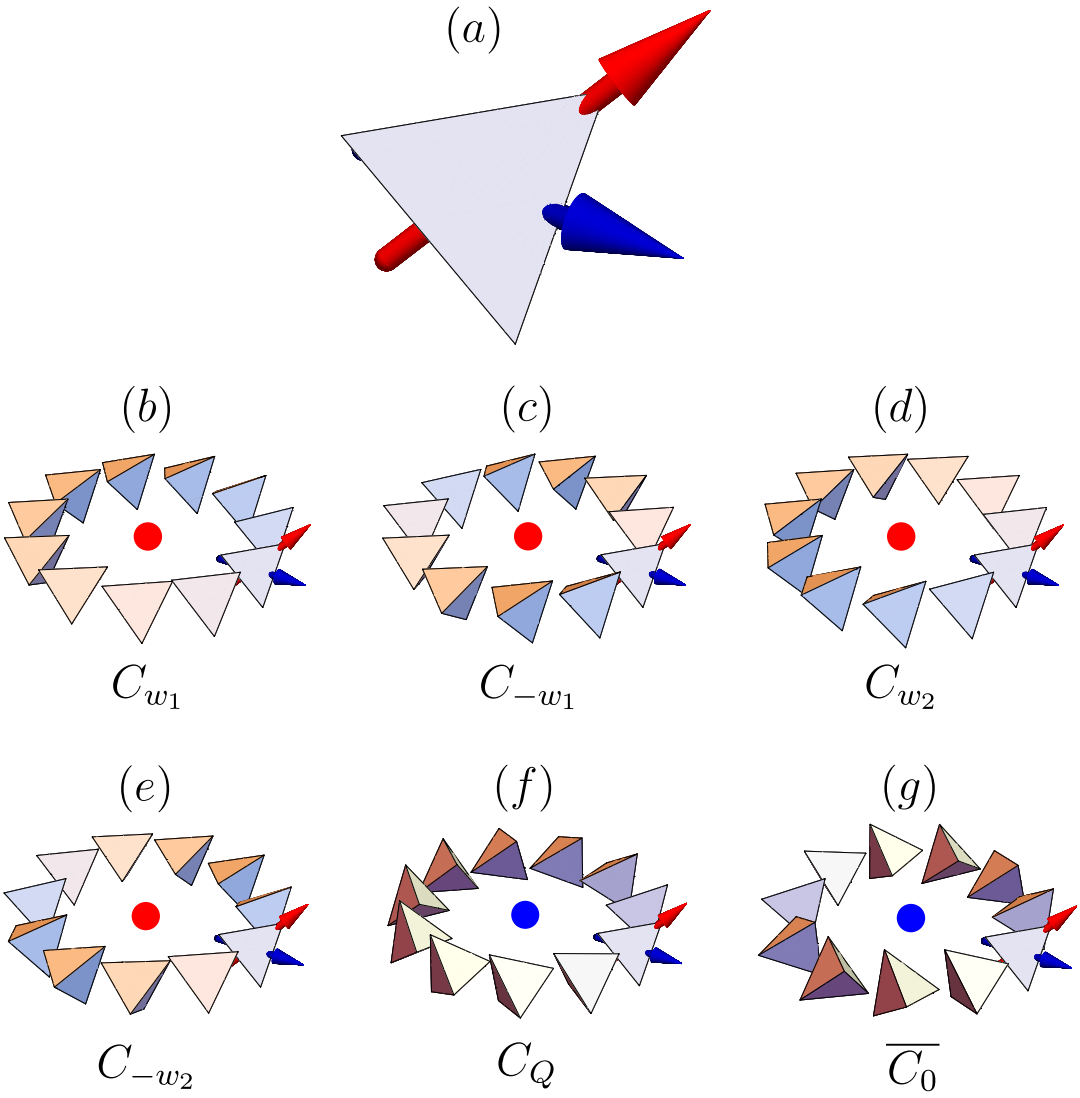

Figure F.2: Sketches of defects of each class in the tetrahedratic T-phase. (a) A reference configuration of an object with the symmetry of the T-phase. (b – g) Examples of each type of defect given the reference configuration, labelled according to the conjugacy classes of the binary tetrahedral group $2T$.

	$\mathbf{C_0}$	$\overline{\mathbf{C_0}}$	$\mathbf{C_x}$	$\mathbf{C_y}$	$\mathbf{C_z}$
$\mathbf{C_0}$	C_0	$\overline{C_0}$	C_x	C_y	C_z
$\overline{\mathbf{C_0}}$	$\overline{C_0}$	C_0	C_x	C_y	C_z
$\mathbf{C_x}$	C_x	C_x	$2C_0 + 2\overline{C_0}$	$2C_z$	$2C_y$
$\mathbf{C_y}$	C_y	C_y	$2C_z$	$2C_0 + 2\overline{C_0}$	$2C_x$
$\mathbf{C_z}$	C_z	C_z	$2C_y$	$2C_x$	$2C_0 + 2\overline{C_0}$

Table F.2: Combination rules for defects in the biaxial phases $N+2$, N_T, $(N_T+2)^*$.

symmetry group of the molecule is discrete but $\pi_1(\mathrm{SO}(3)/D_2) \cong \mathbb{H}$ (the quaternions) which is a non-abelian group of order 8. Because the first homotopy group is non-abelian, we must compute the conjugacy classes to find the unambiguous labelling of the defects. There are 5 conjugacy classes and hence 4 distinct types of defect. These involve swirling by π around each of the non-equivalent axes together with a full 2π swirl (about any axis). Fix a reference configuration, and call the three mutually orthogonal principal axes $\mathbf{e}_x$, $\mathbf{e}_y$, and $\mathbf{e}_x \times \mathbf{e}_y \equiv \mathbf{e}_z$. For this choice of reference configuration, we can then enumerate choices of defects from $\mathbb{H}$:

$$C_x : i\sigma_x = \exp\left(i\left(\frac{\pi}{2}\right)\mathbf{e}_x \cdot \sigma\right) = \pi \text{ rotation about } \mathbf{e}_x.$$

$$C_y : i\sigma_y = \exp\left(i\left(\frac{\pi}{2}\right)\mathbf{e}_y \cdot \sigma\right) = \pi \text{ rotation about } \mathbf{e}_y.$$

$$C_z : i\sigma_z = \exp\left(i\left(\frac{\pi}{2}\right)\mathbf{e}_z \cdot \sigma\right) = \pi \text{ rotation about } \mathbf{e}_z.$$

$\overline{C_0} : -1 = \exp(i(\pi)\,\mathbf{e}_z \cdot \sigma) = 2\pi$ rotation about $\mathbf{e}_z$. (Note any other axis also works.)

F.1.6 Triadic $N+3$ phase

The triadic $N+3$ phase has a symmetry group equal to D_3, representing symmetries of equilateral triangular prism. There are no stable point defects because

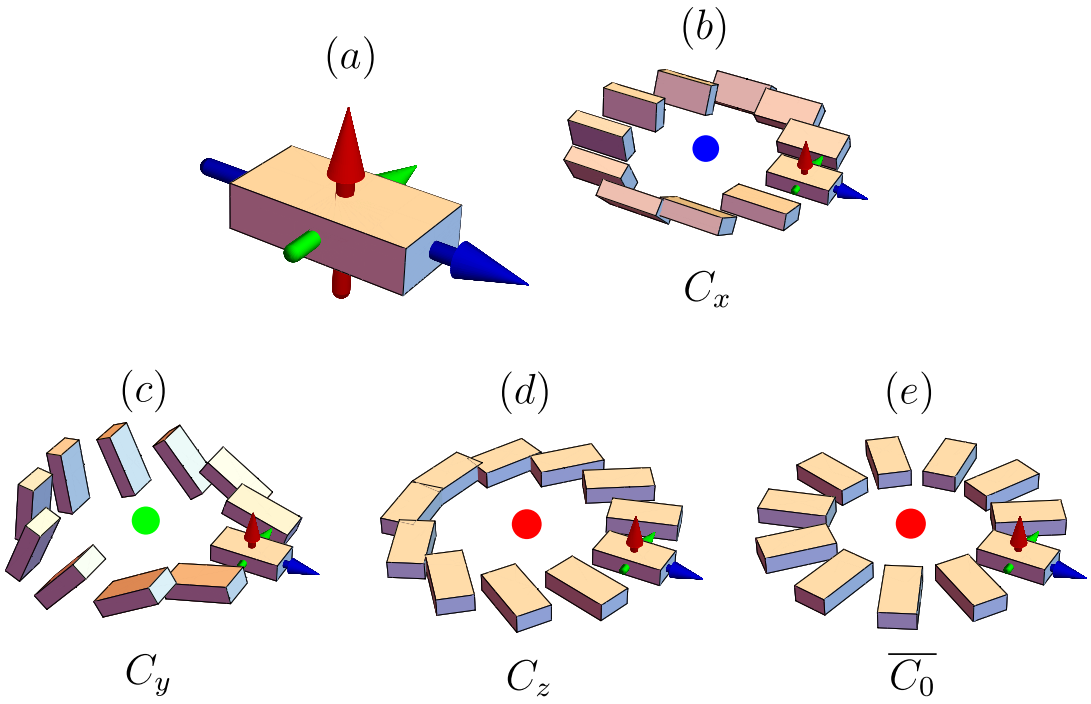

Figure F.3: Sketches of defects of each class in the biaxial phases. (a) A reference configuration of an object with the symmetry of these phases. (b – e) Examples of each type of defect given the reference configuration, labelled according to the conjugacy classes of the quaternions $\mathbb{H}$.

the symmetry group of the molecule is discrete but $\pi_1(\mathrm{SO}(3)/D_3) \cong \mathrm{Dic}_3$ (the 12-element dicyclic group) which is a non-abelian group of order 12. Because the first homotopy group is non-abelian, we must compute the conjugacy classes to find the unambiguous labelling of the defects. There are 6 conjugacy classes and hence 5 distinct types of defect. These involve swirling by $\pm n2\pi/3$ about the axis normal to the equilateral triangle ($n = 1, 2, 3$; the clockwise and counterclockwise swirls are topologically the same defect), a flip about an axis perpendicular to to the swirling one together with an even number of $2\pi/3$ swirls, and a flip about an axis perpendicular to to the swirling one together with an odd number of $2\pi/3$ swirls. For simplicity, a reference configuration of the triangular prism is chosen and all representatives of defects are drawn as rotations about the $\mathbf{e}_z$

	$\mathbf{C_0}$	$\overline{\mathbf{C_0}}$	$\mathbf{C_1}$	$\mathbf{C_2}$	$\mathbf{C}_{\text{even}}$	$\mathbf{C}_{\text{odd}}$
$\mathbf{C_0}$	C_0	$\overline{C_0}$	C_1	C_2	C_{even}	C_{odd}
$\overline{\mathbf{C_0}}$	$\overline{C_0}$	C_0	C_2	C_1	C_{odd}	C_{even}
$\mathbf{C_1}$	C_1	C_2	$2C_0 + C_2$	$2\overline{C_0} + C_1$	$2C_{\text{odd}}$	$2C_{\text{even}}$
$\mathbf{C_2}$	C_2	C_1	$2\overline{C_0} + C_1$	$2C_0 + C_2$	$2C_{\text{even}}$	$2C_{\text{odd}}$
$\mathbf{C}_{\text{even}}$	C_{even}	C_{odd}	$2C_{\text{odd}}$	$2C_{\text{even}}$	$3\overline{C_0} + 3C_1$	$3C_0 + 3C_2$
$\mathbf{C}_{\text{odd}}$	C_{odd}	C_{even}	$2C_{\text{even}}$	$2C_{\text{odd}}$	$3C_0 + 3C_2$	$3\overline{C_0} + 3C_1$

Table F.3: Combination rules for defects in the triadic $N + 3$ phase.

axis (the cylinder axis of the prism, about which rotations by multiples of $2\pi/3$ are symmetries) and the $\mathbf{e}_x$ axis (passing through the center of a rectangular face and the center of an opposite edge, about which rotations by multiples of π are symmetries). With a fixed choice of reference configuration, one can enumerate choices of defects from Dic_3:

$$C_1 : \left(1 + i\sigma_z\sqrt{3}\right)/2 = \exp\left(i\left(\frac{\pi}{3}\right)\mathbf{e}_z \cdot \sigma\right) = \frac{2\pi}{3} \text{ rotation about axis } \mathbf{e}_z.$$

$$C_2 : \left(-1 + i\sigma_z\sqrt{3}\right)/2 = \exp\left(i\left(\frac{2\pi}{3}\right)\mathbf{e}_z \cdot \sigma\right) = \frac{4\pi}{3} \text{ rotation about axis } \mathbf{e}_z.$$

$$C_{\text{even}} : i\sigma_x = \exp\left(i\left(\frac{\pi}{2}\right)\mathbf{e}_x \cdot \sigma\right) = \pi \text{ rotation about axis } \mathbf{e}_x.$$

$$C_{\text{odd}} : -i\sigma_x = \exp\left(i\left(-\frac{\pi}{2}\right)\mathbf{e}_x \cdot \sigma\right) = -\pi \text{ rotation about axis } \mathbf{e}_x.$$

$\overline{C_0} : -1 = \exp\left(i\left(\pi\right)\mathbf{e}_x \cdot \sigma\right) = 2\pi$ rotation about axis $\mathbf{e}_x$ (Note any other axis also works.)

F.1.7 Vortex $V + 3$ phase

The vortex $V + 3$ phase has symmetry C_3 and molecules can be visualized as a pyramid with an equilateral triangular base and other sides equal but not equilateral. There are no stable point defects but $\pi_1\left(\text{SO}(3)/C_3\right) \cong \mathbb{Z}_6$ and so there are five stable line defects that add like the integers modulo 6. The defect labelled

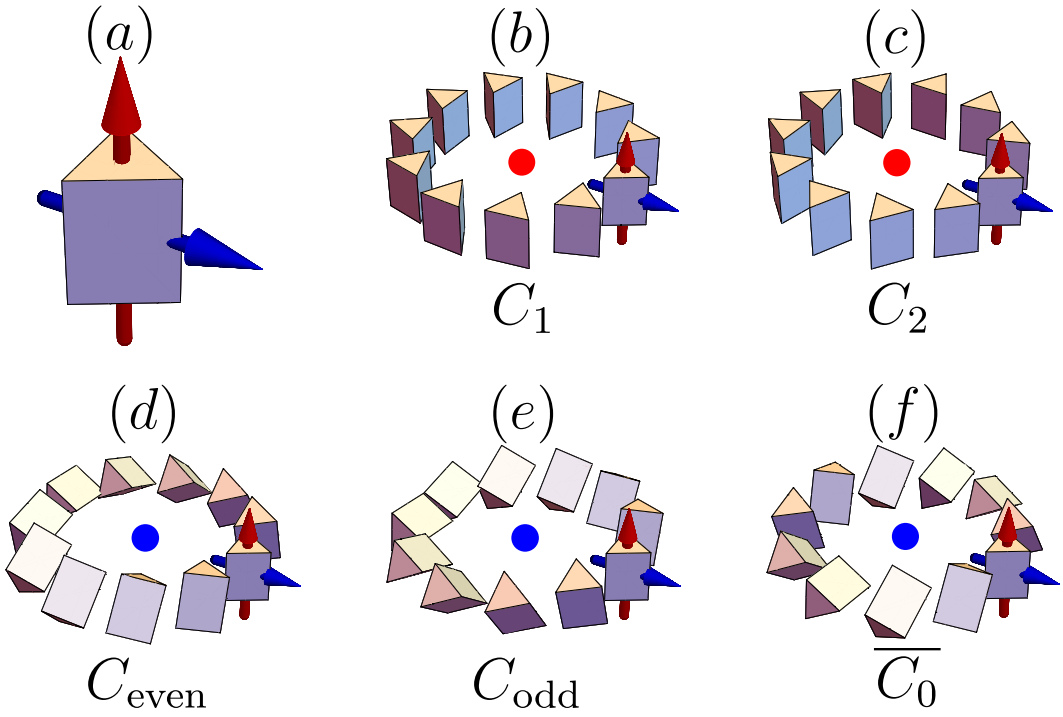

Figure F.4: Sketches of defects of each class in the triadic $N + 3$ phase. (a) A reference configuration of an object with the symmetry of the $N + 3$ phase. (b – f) Examples of each type of defect given the reference configuration, labelled according to the conjugacy classes of Dic_3.

by 3_+ is its own inverse and represents a full 2π swirl, much like the lone type of defect in the $N + V$ phase. The defects labelled by 1_+ and 2_+ represent CCW 1/3 and 2/3 turns about an axis normal to the equilateral triangle, respectively. Their inverses, $5_+ \equiv -1_+$ and $4_+ \equiv -2_+$ represent CW 1/3 and 2/3 turns about that same axis, respectively.

If we choose a reference configuration of the pyramid and call $\mathbf{e}_z$ the axis about which rotations by $2\pi/3$ are a symmetry, the defects can be written as:

$$1_+ : \left(1 + i\sigma_z \sqrt{3}\right)/2 = \exp\left(i\left(\frac{\pi}{3}\right)\mathbf{e}_z \cdot \sigma\right) = \frac{2\pi}{3} \text{ rotation about } \mathbf{e}_z.$$

$$2_+ : \left(-1 + i\sigma_z \sqrt{3}\right)/2 = \exp\left(i\left(\frac{2\pi}{3}\right)\mathbf{e}_z \cdot \sigma\right) = \frac{4\pi}{3} \text{ rotation about } \mathbf{e}_z.$$

$3_+ : -1 = \exp\left(i\left(\pi\right)\mathbf{e}_z \cdot \sigma\right) = 2\pi$ rotation about $\mathbf{e}_z$. (Note any other axis also works.)

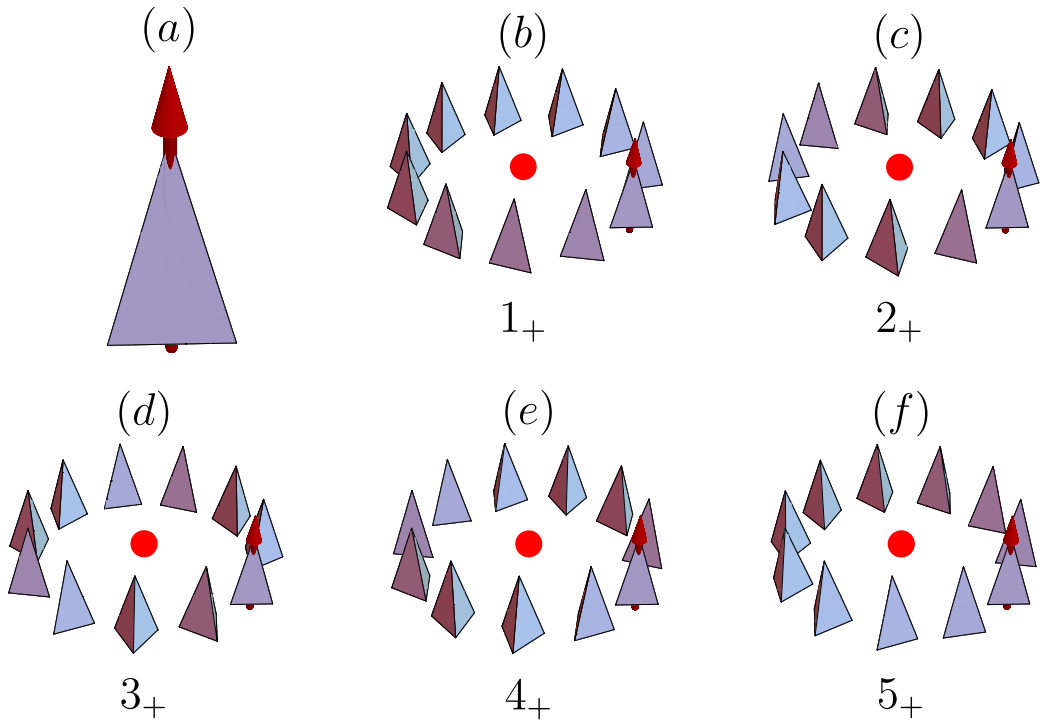

Figure F.5: Sketches of defects of each class in the vortex $V + 3$ phase. (a) A reference configuration of an object with the symmetry of the $V + 3$ phase. (b – f) Examples of each type of defect given the reference configuration, labelled according to the elements of $\mathbb{Z}_6$.

	$\mathbf{0}_+$	$\mathbf{1}_+$	$\mathbf{2}_+$	$\mathbf{3}_+$	$\mathbf{4}_+$	$\mathbf{5}_+$
$\mathbf{0}_+$	0_+	1_+	2_+	3_+	4_+	5_+
$\mathbf{1}_+$	1_+	2_+	3_+	4_+	5_+	0_+
$\mathbf{2}_+$	2_+	3_+	4_+	5_+	0_+	1_+
$\mathbf{3}_+$	3_+	4_+	5_+	0_+	1_+	2_+
$\mathbf{4}_+$	4_+	5_+	0_+	1_+	2_+	3_+
$\mathbf{5}_+$	5_+	0_+	1_+	2_+	3_+	4_+

Table F.4: Combination rules for defects in the vortex $V + 3$ phase.

$$4_+ \equiv -2_+ : \left(-1 - i\sigma_z \sqrt{3}\right)/2 = \exp\left(i\left(-\frac{2\pi}{3}\right)\mathbf{e}_z \cdot \sigma\right) = -\frac{4\pi}{3} \text{ rotation about } \mathbf{e}_z.$$

$$5_+ \equiv -1_+ : \left(1 - i\sigma_z \sqrt{3}\right)/2 = \exp\left(i\left(-\frac{\pi}{3}\right)\mathbf{e}_z \cdot \sigma\right) = -\frac{2\pi}{3} \text{ rotation about } \mathbf{e}_z.$$

	$\mathbf{0}_+$	$\mathbf{1}_+$	$\mathbf{2}_+$	$\mathbf{3}_+$
$\mathbf{0}_+$	0_+	1_+	2_+	3_+
$\mathbf{1}_+$	1_+	2_+	3_+	0_+
$\mathbf{2}_+$	2_+	3_+	0_+	1_+
$\mathbf{3}_+$	3_+	0_+	1_+	2_+

Table F.5: Combination rules for defects in the vortex phases $V + 2$ and $(V_T + 2)^*$.

F.1.8 Vortex $V + 2$, $(V_T + 2)^*$ phases

The vortex $V + 2$ and $(V_T + 2)^*$ phases have symmetry C_2 and molecules can be visualized as a pyramid with a rectangular (but not square) base. There are no stable point defects but $\pi_1(\mathrm{SO}(3)/C_2) \cong \mathbb{Z}_4$ and so there are three stable line defects that add like the integers modulo 4. The defect labelled by 2_+ is its own inverse and represents a full 2π swirl, much like the lone type of defect in the $N + V$ phase. The defect labelled by 1_+ represents a CCW 1/2 turn about an axis normal to the rectangle. Its inverse, $3_+ \equiv -1_+$ represents a CW 1/2 turn about that same axis. If we choose a reference configuration of the pyramid and call $\mathbf{e}_z$ the axis about which rotations by π are a symmetry, the defects can be written as:

$$1_+ : i\sigma_z = \exp\left(i\left(\frac{\pi}{2}\right)\mathbf{e}_z \cdot \sigma\right) = \pi \text{ rotation about } \mathbf{e}_z.$$

$2_+ : -1 = \exp\left(i\left(\pi\right)\mathbf{e}_z \cdot \sigma\right) = 2\pi$ rotation about $\mathbf{e}_z$. (Note any other axis also works.)

$$3_+ \equiv -1_+ : -i\sigma_z = \exp\left(i\left(-\frac{\pi}{2}\right)\mathbf{e}_z \cdot \sigma\right) = -\pi \text{ rotation about } \mathbf{e}_z.$$

F.1.9 $N + V$ phase

The $N + V$ phase is the least symmetric, with its order parameter space being all of SO(3). The phase can be represented by an object with no rotational symmetry at each point in space. There are no stable point defects, and $\pi_1(\mathrm{SO}(3)) = \mathbb{Z}_2$

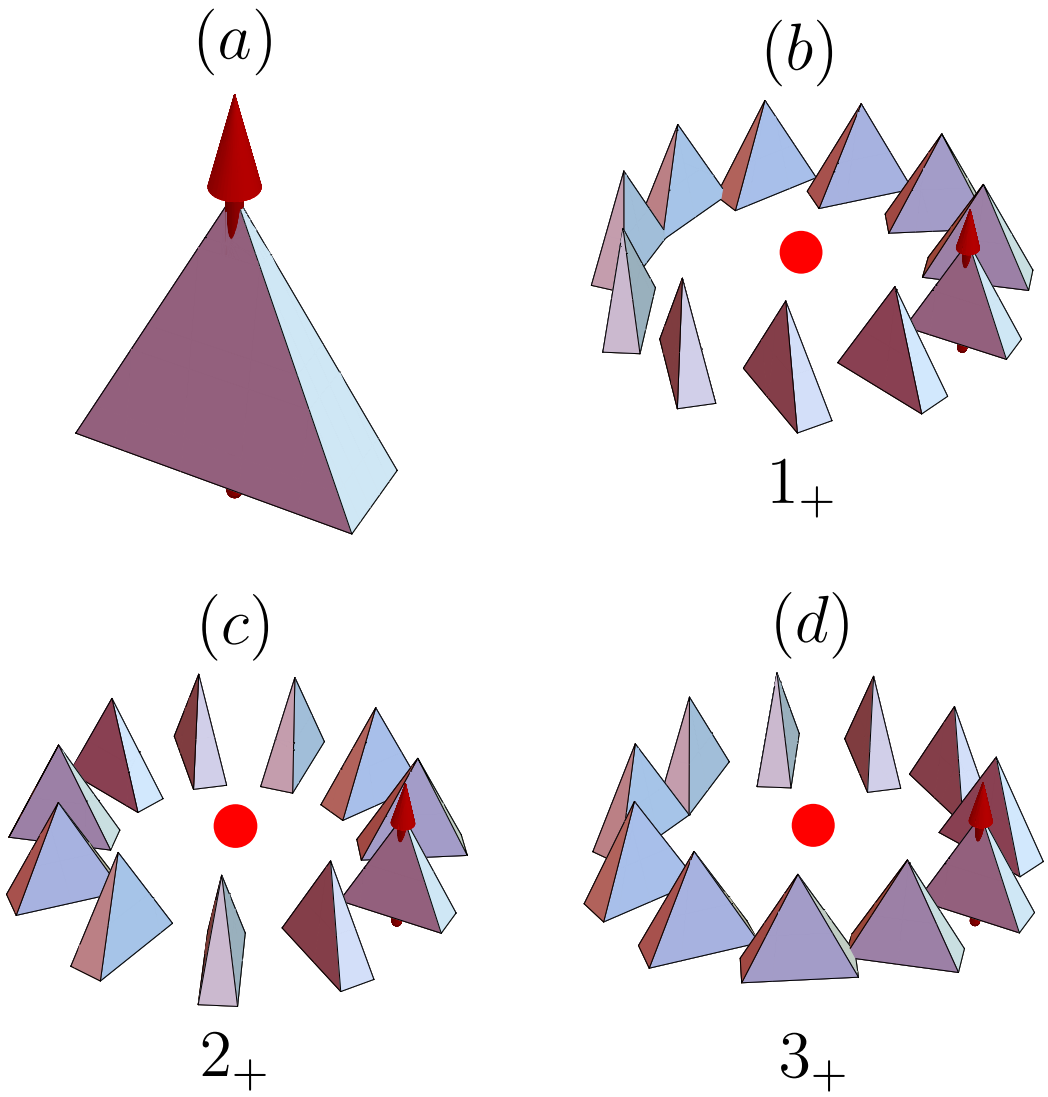

Figure F.6: Sketches of defects of each class in the $V + 2$ and $(V_T + 2)^*$ phases. (a) A reference configuration of an object with the symmetry of the $V + 2$ and $(V_T + 2)^*$ phases. (b – d) Examples of each type of defect given the reference configuration, labelled according to the elements of $\mathbb{Z}_4$.

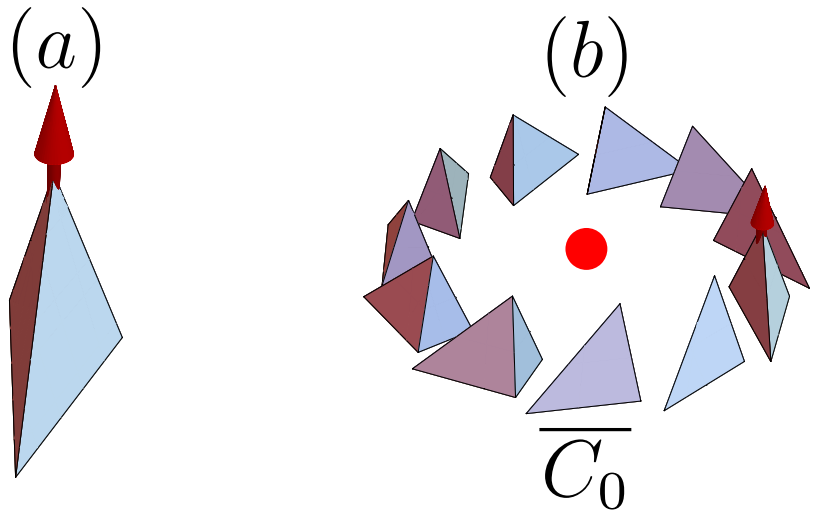

Figure F.7: Sketches of the lone defect in the $N + V$ phase. (a) A reference configuration of an object with no symmetries beyond the identity operation in SO(3). (b) The only defect given the reference configuration. The defects are labelled according to the elements of $\mathbb{Z}_2$ (i.e., the defect is labelled by the only non-identity element in the group).

	$\mathbf{C_0}$	$\overline{\mathbf{C_0}}$
$\mathbf{C_0}$	C_0	$\overline{C_0}$
$\overline{\mathbf{C_0}}$	$\overline{C_0}$	C_0

Table F.6: Combination rules for defects in the $N + V$ phase.

indicating there is only one type of line defect (a full 2π swirl). When two defects are brought together, they can be unravelled and the order parameter field can be patched. Choose any axis and call it $\mathbf{e}_1$. Then the only defect can be represented as

$\overline{C_0} : -1 = \exp(i(\pi)\,\mathbf{e}_1 \cdot \sigma) = 2\pi$ rotation about $\mathbf{e}_1$. (Note any other axis also works.)

BIBLIOGRAPHY

[1] Shechao Feng, M. F. Thorpe, and E. Garboczi. Effective-medium theory of percolation on central-force elastic networks. *Phys. Rev. B*, 31:276–280, Jan 1985.

[2] Danilo B. Liarte, Xiaoming Mao, Olaf Stenull, and T. C. Lubensky. Jamming as a multicritical point. *Phys. Rev. Lett.*, 122:128006, Mar 2019.

[3] T. Zhang, J. M. Schwarz, and Moumita Das. Mechanics of anisotropic spring networks. *Phys. Rev. E*, 90:062139, Dec 2014.

[4] Thomas Wyse Jackson, Jonathan Michel, Pancy Lwin, Lisa A. Fortier, Moumita Das, Lawrence J. Bonassar, and Itai Cohen. Structural origins of cartilage shear mechanics. *Science Advances*, 8(6):eabk2805, 2022.

[5] Chase P. Broedersz, Xiaoming Mao, Tom C. Lubensky, and Frederick C. MacKintosh. Criticality and isostaticity in fibre networks. *Nature Physics*, 7(12):983–988, December 2011.

[6] Jordan L. Shivers, Sadjad Arzash, Abhinav Sharma, and Fred C. MacKintosh. Scaling theory for mechanical critical behavior in fiber networks. *Phys. Rev. Lett.*, 122:188003, May 2019.

[7] Edan Lerner and Eran Bouchbinder. Scaling theory of critical strain-stiffening in disordered elastic networks. *Extreme Mechanics Letters*, 65:102104, 2023.

[8] Sihan Chen, Tomer Markovich, and Fred C. MacKintosh. Field theory for mechanical criticality in disordered fiber networks. *Phys. Rev. Lett.*, 133:028201, Jul 2024.

[9] Danilo B. Liarte, Stephen J. Thornton, Eric Schwen, Itai Cohen, Debanjan Chowdhury, and James P. Sethna. Universal scaling for disordered viscoelastic matter near the onset of rigidity. *Phys. Rev. E*, 106:L052601, Nov 2022.

[10] P. C. Hohenberg and B. I. Halperin. Theory of dynamic critical phenomena. *Rev. Mod. Phys.*, 49:435–479, Jul 1977.

[11] Fumiko Yonezawa and Kazuo Morigaki. Coherent Potential Approximation. Basic concepts and applications.

Progress of Theoretical Physics Supplement, 53:1–76, January 1973. _eprint: https://academic.oup.com/ptps/article-pdf/doi/10.1143/PTPS.53.1/5425626/53-1.pdf.

[12] Alexander Altland and Ben D. Simons. *Condensed Matter Field Theory*. Cambridge University Press, 2 edition, 2010.

[13] Sajeev John, H. Sompolinsky, and Michael J. Stephen. Localization in a disordered elastic medium near two dimensions. *Phys. Rev. B*, 27:5592–5603, May 1983.

[14] Andrea J. Liu and Sidney R. Nagel. The jamming transition and the marginally jammed solid. *Annual Review of Condensed Matter Physics*, 1(1):347–369, 2010.

[15] M.F. Thorpe. Continuous deformations in random networks. *Journal of Non-Crystalline Solids*, 57(3):355–370, 1983.

[16] James P. Sethna, Matthew K. Bierbaum, Karin A. Dahmen, Carl P. Goodrich, Julia R. Greer, Lorien X. Hayden, Jaron P. Kent-Dobias, Edward D. Lee, Danilo B. Liarte, Xiaoyue Ni, Katherine N. Quinn, Archishman Raju, D. Zeb Rocklin, Ashivni Shekhawat, and Stefano Zapperi. Deformation of crystals: Connections with statistical physics. *Annual Review of Materials Research*, 47(Volume 47, 2017):217–246, 2017.

[17] J. Clerk Maxwell. L. on the calculation of the equilibrium and stiffness of frames. *The London, Edinburgh, and Dublin Philosophical Magazine and Journal of Science*, 27(182):294–299, 1864.

[18] M.F. Thorpe, D.J. Jacobs, N.V. Chubynsky, and A.J. Rader. *Generic Rigidity of Network Glasses*, pages 239–277. Springer US, Boston, MA, 2002.

[19] R. C. Picu. Mechanics of random fiber networks—a review. *Soft Matter*, 7:6768–6785, 2011.

[20] Shang Zhang, Leyou Zhang, Mehdi Bouzid, D. Zeb Rocklin, Emanuela Del Gado, and Xiaoming Mao. Correlated rigidity percolation and colloidal gels. *Phys. Rev. Lett.*, 123:058001, Jul 2019.

[21] Danilo B. Liarte, O. Stenull, and T. C. Lubensky. Multifunctional twisted kagome lattices: Tuning by pruning mechanical metamaterials. *Phys. Rev. E*, 101:063001, Jun 2020.

[22] Xiaoming Mao and T. C. Lubensky. Coherent potential approximation of random nearly isostatic kagome lattice. *Phys. Rev. E*, 83:011111, Jan 2011.

[23] Danilo B Liarte, O Stenull, Xiaoming Mao, and T C Lubensky. Elasticity of randomly diluted honeycomb and diamond lattices with bending forces. *Journal of Physics: Condensed Matter*, 28(16):165402, mar 2016.

[24] Andrea J. Liu, Sidney R. Nagel, Wim van Saarloos, and Matthieu Wyart. 2989 The jamming scenario—an introduction and outlook. In *Dynamical Heterogeneities in Glasses, Colloids, and Granular Media*. Oxford University Press, July 2011. _eprint: https://academic.oup.com/book/0/chapter/155204450/chapter-ag-pdf/44955548/book_8915_section_155204450.ag.pdf.

[25] Dapeng Bi, Xingbo Yang, M. Cristina Marchetti, and M. Lisa Manning. Motility-driven glass and jamming transitions in biological tissues. *Phys. Rev. X*, 6:021011, Apr 2016.

[26] Yasaman Bahri, Jonathan Kadmon, Jeffrey Pennington, Sam S. Schoenholz, Jascha Sohl-Dickstein, and Surya Ganguli. Statistical mechanics of deep learning. *Annual Review of Condensed Matter Physics*, 11(1):501–528, 2020.

[27] Jorge Kurchan, Giorgio Parisi, and Francesco Zamponi. Exact theory of dense amorphous hard spheres in high dimension i. the free energy. *Journal of Statistical Mechanics: Theory and Experiment*, 2012(10):P10012, oct 2012.

[28] Jorge Kurchan, Giorgio Parisi, Pierfrancesco Urbani, and Francesco Zamponi. Exact Theory of Dense Amorphous Hard Spheres in High Dimension. II. The High Density Regime and the Gardner Transition. *The Journal of Physical Chemistry B*, 117(42):12979–12994, October 2013. Publisher: American Chemical Society.

[29] Patrick Charbonneau, Jorge Kurchan, Giorgio Parisi, Pierfrancesco Urbani, and Francesco Zamponi. Exact theory of dense amorphous hard spheres in high dimension. iii. the full replica symmetry breaking solution. *Journal of Statistical Mechanics: Theory and Experiment*, 2014(10):P10009, oct 2014.

[30] Alessio Zaccone and Enzo Scossa-Romano. Approximate analytical description of the nonaffine response of amorphous solids. *Phys. Rev. B*, 83:184205, May 2011.

[31] M. Schlegel, J. Brujic, E. M. Terentjev, and A. Zaccone. Local structure controls the nonaffine shear and bulk moduli of disordered solids. *Scientific Reports*, 6(1):18724, January 2016.

[32] T C Lubensky, C L Kane, Xiaoming Mao, A Souslov, and Kai Sun. Phonons and elasticity in critically coordinated lattices. *Reports on Progress in Physics*, 78(7):073901, jun 2015.

[33] Marco Baity-Jesi, Carl P. Goodrich, Andrea J. Liu, Sidney R. Nagel, and James P. Sethna. Emergent SO(3) symmetry of the frictionless shear jamming transition. *Journal of Statistical Physics*, 167(3):735–748, 2017.

[34] John Cardy. *Scaling and Renormalization in Statistical Physics*. Cambridge Lecture Notes in Physics. Cambridge University Press, 1996.

[35] E del Gado and X Mao. personal communication.

[36] P. M. Chaikin and T. C. Lubensky. *Principles of Condensed Matter Physics*. Cambridge University Press, 1995.

[37] James P. Sethna. *Statistical mechanics: entropy, order parameters, and complexity*. Oxford University Press, 2 edition, 2006.

[38] Karsten Baumgarten, Daniel Vaagberg, and Brian P. Tighe. Nonlocal elasticity near jamming in frictionless soft spheres. *Phys. Rev. Lett.*, 118:098001, Feb 2017.

[39] D. Hexner, S. R. Nagel, and A. J. Liu. "The length dependent elasticity for jammed systems," Poster presented at CECAM workshop, *Recent Advances on the Glass and Jamming Transitions* (2017).

[40] Carl P. Goodrich, Andrea J. Liu, and James P. Sethna. Scaling ansatz for the jamming transition. *Proceedings of the National Academy of Sciences*, 113, 2016.

[41] R. J. Elliott, J. A. Krumhansl, and P. L. Leath. The theory and properties of randomly disordered crystals and related physical systems. *Rev. Mod. Phys.*, 46:465–543, Jul 1974.

[42] Lawrence M. Schwartz, Shechao Feng, M. F. Thorpe, and Pabitra N. Sen. Behavior of depleted elastic networks: Comparison of effective-medium and numerical calculations. *Phys. Rev. B*, 32:4607–4617, Oct 1985.

[43] M. G. Yucht, M. Sheinman, and C. P. Broedersz. Dynamical behavior of disordered spring networks. *Soft Matter*, 9:7000–7006, 2013.

[44] Gustavo Düring, Edan Lerner, and Matthieu Wyart. Phonon gap and localization lengths in floppy materials. *Soft Matter*, 9:146–154, 2013.

[45] Danilo B. Liarte, Stephen J. Thornton, Eric Schwen, Itai Cohen, Debanjan Chowdhury, and James P. Sethna. Universal scaling for disordered viscoelastic matter II: Collapses, global behavior and spatio-temporal properties. *arXiv e-prints*, page arXiv:2202.13933, February 2022.

[46] James D Sartor, Sean A Ridout, and Eric I Corwin. Mean-field predictions of scaling prefactors match low-dimensional jammed packings. *Physical Review Letters*, 126(4):048001, 2021.

[47] Amnon Aharony and Michael E. Fisher. University in analytic corrections to scaling for planar ising models. *Phys. Rev. Lett.*, 45:679–682, Sep 1980.

[48] Amnon Aharony and Michael E. Fisher. Nonlinear scaling fields and corrections to scaling near criticality. *Phys. Rev. B*, 27:4394–4400, Apr 1983.

[49] Archishman Raju, Colin B. Clement, Lorien X. Hayden, Jaron P. Kent-Dobias, Danilo B. Liarte, D. Zeb Rocklin, and James P. Sethna. Normal form for renormalization groups. *Phys. Rev. X*, 9:021014, Apr 2019.

[50] Vincenzo Vitelli, Ning Xu, Matthieu Wyart, Andrea J. Liu, and Sidney R. Nagel. Heat transport in model jammed solids. *Phys. Rev. E*, 81:021301, Feb 2010.

[51] S. Köhler, G. Ruocco, and W. Schirmacher. Coherent potential approximation for diffusion and wave propagation in topologically disordered systems. *Phys. Rev. B*, 88:064203, Aug 2013.

[52] Eric DeGiuli, Adrien Laversanne-Finot, Gustavo Düring, Edan Lerner, and Matthieu Wyart. Effects of coordination and pressure on sound attenuation, boson peak and elasticity in amorphous solids. *Soft Matter*, 10:5628–5644, 2014.

[53] Silvio Franz, Giorgio Parisi, Pierfrancesco Urbani, and Francesco Zamponi. Universal spectrum of normal modes in low-temperature glasses. *Proceedings of the National Academy of Sciences*, 112(47):14539–14544, 2015.

[54] Kurt Binder and Walter Kob. *Glassy Materials and Disordered Solids*. WORLD SCIENTIFIC, revised edition, 2011.

[55] Leonardo E. Silbert, Andrea J. Liu, and Sidney R. Nagel. Vibrations and diverging length scales near the unjamming transition. *Phys. Rev. Lett.*, 95:098301, Aug 2005.

[56] Wouter G. Ellenbroek, Ellák Somfai, Martin van Hecke, and Wim van Saarloos. Critical scaling in linear response of frictionless granular packings near jamming. *Phys. Rev. Lett.*, 97:258001, Dec 2006.

[57] Edan Lerner, Eric DeGiuli, Gustavo Düring, and Matthieu Wyart. Breakdown of continuum elasticity in amorphous solids. *Soft Matter*, 10:5085–5092, 2014.

[58] Kamran Karimi and Craig E. Maloney. Elasticity of frictionless particles near jamming. *Phys. Rev. E*, 92:022208, Aug 2015.

[59] Donald J Jacobs and Michael F Thorpe. Generic rigidity percolation: the pebble game. *Physical review letters*, 75(22):4051, 1995.

[60] Eric R. Weeks, J. C. Crocker, Andrew C. Levitt, Andrew Schofield, and D. A. Weitz. Three-dimensional direct imaging of structural relaxation near the colloidal glass transition. *Science*, 287(5453):627–631, 2000.

[61] Neil Y. C. Lin, Matthew Bierbaum, Peter Schall, James P. Sethna, and Itai Cohen. Measuring nonlinear stresses generated by defects in 3D colloidal crystals. *Nature Materials*, 15(11):1172–1176, November 2016.

[62] Matthew Bierbaum, Brian D. Leahy, Alexander A. Alemi, Itai Cohen, and James P. Sethna. Light microscopy at maximal precision. *Phys. Rev. X*, 7:041007, Oct 2017.

[63] Brian D. Leahy, Neil Y.C. Lin, and Itai Cohen. Quantitative light microscopy of dense suspensions: Colloid science at the next decimal place. *Current Opinion in Colloid & Interface Science*, 34:32–46, 2018. Microscopy Methods: You Can Observe a Lot by Watching.

[64] E. do Carmo, D. B. Liarte, and S. R. Salinas. Statistical models of mixtures with a biaxial nematic phase. *Phys. Rev. E*, 81:062701, Jun 2010.

[65] Stephen J. Thornton, Danilo B. Liarte, Peter Abbamonte, James P. Sethna,

and Debanjan Chowdhury. Jamming and unusual charge density fluctuations of strange metals. *Nature Communications*, 14(1):3919, July 2023.

[66] M. Mitrano, A. A. Husain, S. Vig, A. Kogar, M. S. Rak, S. I. Rubeck, J. Schmalian, B. Uchoa, J. Schneeloch, R. Zhong, G. D. Gu, and P. Abbamonte. Anomalous density fluctuations in a strange metal. *Proceedings of the National Academy of Sciences*, 115(21):5392–5396, 2018.

[67] Ali A. Husain, Matteo Mitrano, Melinda S. Rak, Samantha Rubeck, Bruno Uchoa, Katia March, Christian Dwyer, John Schneeloch, Ruidan Zhong, G. D. Gu, and Peter Abbamonte. Crossover of charge fluctuations across the strange metal phase diagram. *Phys. Rev. X*, 9:041062, Dec 2019.

[68] Meera Ramaswamy, Itay Griniasty, Danilo B. Liarte, Abhishek Shetty, Eleni Katifori, Emanuela Del Gado, James P. Sethna, Bulbul Chakraborty, and Itai Cohen. Universal scaling of shear thickening transitions. *Journal of Rheology*, 67(6):1189–1197, October 2023. _eprint: https://pubs.aip.org/sor/jor/article-pdf/67/6/1189/18156366/1189_1_8.0000697.pdf.

[69] Robert P Behringer and Bulbul Chakraborty. The physics of jamming for granular materials: a review. *Reports on Progress in Physics*, 82(1):012601, nov 2018.

[70] Eric Brown and Heinrich M Jaeger. Shear thickening in concentrated suspensions: phenomenology, mechanisms and relations to jamming. *Reports on Progress in Physics*, 77(4):046602, apr 2014.

[71] Silke Henkes, Yaouen Fily, and M. Cristina Marchetti. Active jamming: Self-propelled soft particles at high density. *Phys. Rev. E*, 84:040301, Oct 2011.

[72] Aurelio Romero-Bermúdez, Alexander Krikun, Koenraad Schalm, and Jan Zaanen. Anomalous attenuation of plasmons in strange metals and holography. *Phys. Rev. B*, 99:235149, Jun 2019.

[73] Xuepeng Wang and Debanjan Chowdhury. Collective density fluctuations of strange metals with critical fermi surfaces. *Phys. Rev. B*, 107:125157, Mar 2023.

[74] David Pines and Philippe Nozières. *Theory of Quantum Liquids: Normal Fermi Liquids*. CRC Press, 2018.

[75] Sean Vig, Anshul Kogar, Matteo Mitrano, Ali A. Husain, Vivek Mishra, Melinda S. Rak, Luc Venema, Peter D. Johnson, Genda D. Gu, Eduardo Fradkin, Michael R. Norman, and Peter Abbamonte. Measurement of the dynamic charge response of materials using low-energy, momentum-resolved electron energy-loss spectroscopy (M-EELS). *SciPost Phys.*, 3:026, 2017.

[76] Ali A. Husain, Edwin W. Huang, Matteo Mitrano, Melinda S. Rak, Samantha I. Rubeck, Xuefei Guo, Hongbin Yang, Chanchal Sow, Yoshiteru Maeno, Bruno Uchoa, Tai C. Chiang, Philip E. Batson, Philip W. Phillips, and Peter Abbamonte. Pines' demon observed as a 3D acoustic plasmon in Sr2RuO4. *Nature*, 621(7977):66–70, September 2023.

[77] J. Levallois, M. K. Tran, D. Pouliot, C. N. Presura, L. H. Greene, J. N. Eckstein, J. Uccelli, E. Giannini, G. D. Gu, A. J. Leggett, and D. van der Marel. Temperature-dependent ellipsometry measurements of partial coulomb energy in superconducting cuprates. *Phys. Rev. X*, 6:031027, Aug 2016.

[78] Abhishek Nag, M. Zhu, Matías Bejas, J. Li, H. C. Robarts, Hiroyuki Yamase, A. N. Petsch, D. Song, H. Eisaki, A. C. Walters, M. García-Fernández, Andrés Greco, S. M. Hayden, and Ke-Jin Zhou. Detection of acoustic plasmons in hole-doped lanthanum and bismuth cuprate superconductors using resonant inelastic x-ray scattering. *Phys. Rev. Lett.*, 125:257002, Dec 2020.

[79] I. Bozovic, D. Kirillov, A. Kapitulnik, K. Char, M. R. Hahn, M. R. Beasley, T. H. Geballe, Y. H. Kim, and A. J. Heeger. Optical measurements on oriented thin $yba_2cu_3o_{7-\delta}$ films: Lack of evidence for excitonic superconductivity. *Phys. Rev. Lett.*, 59:2219–2221, Nov 1987.

[80] F. Slakey, M. V. Klein, J. P. Rice, and D. M. Ginsberg. Raman investigation of the $yba_2cu_3o_7$ imaginary response function. *Phys. Rev. B*, 43:3764–3767, Feb 1991.

[81] Debanjan Chowdhury, Antoine Georges, Olivier Parcollet, and Subir Sachdev. Sachdev-ye-kitaev models and beyond: Window into non-fermi liquids. *Rev. Mod. Phys.*, 94:035004, Sep 2022.

[82] Darshan G. Joshi and Subir Sachdev. Anomalous density fluctuations in a random $t-j$ model. *Phys. Rev. B*, 102:165146, Oct 2020.

[83] Aurelio Romero-Bermúdez, Alexander Krikun, Koenraad Schalm, and

Jan Zaanen. Anomalous attenuation of plasmons in strange metals and holography. *Phys. Rev. B*, 99:235149, Jun 2019.

[84] B. Keimer, S. A. Kivelson, M. R. Norman, S. Uchida, and J. Zaanen. From quantum matter to high-temperature superconductivity in copper oxides. *Nature*, 518(7538):179–186, Feb 2015.

[85] J. A. N. Bruin, H. Sakai, R. S. Perry, and A. P. Mackenzie. Similarity of scattering rates in metals showing $t-$linear resistivity. *Science*, 339(6121):804–807, 2013.

[86] Sean A. Hartnoll and Andrew P. Mackenzie. Planckian Dissipation in Metals. *arXiv e-prints*, page arXiv:2107.07802, July 2021.

[87] Andrea Damascelli, Zahid Hussain, and Zhi-Xun Shen. Angle-resolved photoemission studies of the cuprate superconductors. *Rev. Mod. Phys.*, 75:473–541, Apr 2003.

[88] S.-C. Wang, H.-B. Yang, A. K. P. Sekharan, H. Ding, J. R. Engelbrecht, X. Dai, Z. Wang, A. Kaminski, T. Valla, T. Kidd, A. V. Fedorov, and P. D. Johnson. Quasiparticle line shape of sr_2ruo_4 and its relation to anisotropic transport. *Phys. Rev. Lett.*, 92:137002, Apr 2004.

[89] O. Gunnarsson, M. Calandra, and J. E. Han. Colloquium: Saturation of electrical resistivity. *Rev. Mod. Phys.*, 75:1085–1099, Oct 2003.

[90] N. E. Hussey, K. Takenaka, and H. Takagi. Universality of the mott–ioffe–regel limit in metals. *Philosophical Magazine*, 84(27):2847–2864, 2004.

[91] Nicoletta I. Petridou, Bernat Corominas-Murtra, Carl-Philipp Heisenberg, and Edouard Hannezo. Rigidity percolation uncovers a structural basis for embryonic tissue phase transitions. *Cell*, 184(7):1914–1928.e19, 2021.

[92] M.-Carmen Miguel, Alessandro Vespignani, Michael Zaiser, and Stefano Zapperi. Dislocation jamming and andrade creep. *Phys. Rev. Lett.*, 89:165501, Sep 2002.

[93] Georgios Tsekenis, Nigel Goldenfeld, and Karin A Dahmen. Dislocations jam at any density. *Physical review letters*, 106(10):105501, 2011.

[94] Zohar Nussinov, Patrick Johnson, Matthias J. Graf, and Alexander V. Balatsky. Mapping between finite temperature classical and zero temperature quantum systems: Quantum critical jamming and quantum dynamical heterogeneities. *Phys. Rev. B*, 87:184202, May 2013.

[95] Thomas Bilitewski, Mike E. Zhitomirsky, and Roderich Moessner. Jammed spin liquid in the bond-disordered kagome antiferromagnet. *Phys. Rev. Lett.*, 119:247201, Dec 2017.

[96] Thomas Bilitewski, Mike E. Zhitomirsky, and Roderich Moessner. Dynamics and energy landscape of the jammed spin liquid. *Physical Review B*, 99(5), feb 2019.

[97] S. Thornton, D.B. Liarte, P. Abbamonte, J.P. Sethna, and D. Chowdhury. Supplementary information: Jamming and unusual charge density fluctuations of strange metals, 2023.

[98] Y. Kohsaka, C. Taylor, K. Fujita, A. Schmidt, C. Lupien, T. Hanaguri, M. Azuma, M. Takano, H. Eisaki, H. Takagi, S. Uchida, and J. C. Davis. An intrinsic bond-centered electronic glass with unidirectional domains in underdoped cuprates. *Science*, 315(5817):1380–1385, 2007.

[99] S. H. Pan, J. P. O'Neal, R. L. Badzey, C. Chamon, H. Ding, J. R. Engelbrecht, Z. Wang, H. Eisaki, S. Uchida, A. K. Gupta, K.-W. Ng, E. W. Hudson, K. M. Lang, and J. C. Davis. Microscopic electronic inhomogeneity in the high-Tc superconductor Bi2Sr2CaCu2O8+x. *Nature*, 413(6853):282–285, September 2001.

[100] C. J. Olson Reichhardt, E. Groopman, Z. Nussinov, and C. Reichhardt. Jamming in systems with quenched disorder. *Phys. Rev. E*, 86:061301, Dec 2012.

[101] A. L. Graves, S. Nashed, E. Padgett, C. P. Goodrich, A. J. Liu, and J. P. Sethna. Pinning susceptibility: The effect of dilute, quenched disorder on jamming. *Phys. Rev. Lett.*, 116, June 2016.

[102] Huba Péter, András Libál, Charles Reichhardt, and CJ Olson Reichhardt. Crossover from jamming to clogging behaviours in heterogeneous environments. *Scientific reports*, 8(1):1–9, 2018.

[103] Andy L. Zhang, Sean A. Ridout, Celia Parts, Aarushi Sachdeva, Cacey S. Bester, Katharina Vollmayr-Lee, Brian C. Utter, Ted Brzinski, and Amy L.

Graves. Jammed solids with pins: Thresholds, force networks, and elasticity. *Phys. Rev. E*, 106:034902, Sep 2022.

[104] Jörg Schmalian and Peter G. Wolynes. Stripe glasses: Self-generated randomness in a uniformly frustrated system. *Phys. Rev. Lett.*, 85:836–839, Jul 2000.

[105] Davide Facoetti, Giulio Biroli, Jorge Kurchan, and David R. Reichman. Classical glasses, black holes, and strange quantum liquids. *Phys. Rev. B*, 100:205108, Nov 2019.

[106] E. Tarquini, G. Biroli, and M. Tarzia. Critical properties of the anderson localization transition and the high-dimensional limit. *Phys. Rev. B*, 95:094204, Mar 2017.

[107] David Tong. *Lectures on Statistical Field Theory*, chapter 3. David Tong, 2010.

[108] Stephen J. Thornton, Itai Cohen, James P. Sethna, and Danilo B. Liarte. Universal scaling solution for a rigidity transition: Renormalization group flows near the upper critical dimension. *Phys. Rev. E*, 111:045508, Apr 2025.

[109] Patrick Charbonneau, Jorge Kurchan, Giorgio Parisi, Pierfrancesco Urbani, and Francesco Zamponi. Glass and jamming transitions: From exact results to finite-dimensional descriptions. *Annual Review of Condensed Matter Physics*, 8:265–288, 2017.

[110] Giorgio Parisi, Pierfrancesco Urbani, and Francesco Zamponi. *Theory of simple glasses: exact solutions in infinite dimensions*. Cambridge University Press, 2020.

[111] Patrick Charbonneau, Eric I. Corwin, Giorgio Parisi, and Francesco Zamponi. Universal microstructure and mechanical stability of jammed packings. *Physical review letters*, 109 20:205501, 2012.

[112] Patrick Charbonneau, Eric I. Corwin, Giorgio Parisi, and Francesco Zamponi. Jamming criticality revealed by removing localized buckling excitations. *Physical review letters*, 114 12:125504, 2015.

[113] M. L. Gardel, J. H. Shin, F. C. MacKintosh, L. Mahadevan, P. Matsudaira,

and D. A. Weitz. Elastic behavior of cross-linked and bundled actin networks. *Science*, 304(5675):1301–1305, 2004.

[114] D. A. Head, A. J. Levine, and F. C. MacKintosh. Distinct regimes of elastic response and deformation modes of cross-linked cytoskeletal and semiflexible polymer networks. *Phys. Rev. E*, 68:061907, Dec 2003.

[115] MF Thorpe. Rigidity percolation in glassy structures. *Journal of Non-Crystalline Solids*, 76(1):109–116, 1985.

[116] Michael F Thorpe and Phillip M Duxbury. *Rigidity theory and applications*. Springer Science & Business Media, 1999.

[117] William Y. Wang, Stephen J. Thornton, Bulbul Chakraborty, Anna R. Barth, Navneet Singh, Japheth Omonira, Jonathan A. Michel, Moumita Das, James P. Sethna, and Itai Cohen. Rigidity transitions in anisotropic networks: a crossover scaling analysis. *Soft Matter*, 21:3278–3289, 2025.

[118] Paul Meakin. Universality, nonuniversality, and the effects of anisotropy on diffusion-limited aggregation. *Phys. Rev. A*, 33:3371–3382, May 1986.

[119] Ojan Khatib Damavandi, Varda F. Hagh, Christian D. Santangelo, and M. Lisa Manning. Energetic rigidity. i. a unifying theory of mechanical stability. *Phys. Rev. E*, 105:025003, Feb 2022.

[120] Stephen J. Thornton, Danilo B. Liarte, and James P. Sethna. Universal scaling functions and upper critical dimension for a jamming transition. Unpublished., 2025.

[121] Carl P. Goodrich, Simon Dagois-Bohy, Brian P. Tighe, Martin van Hecke, Andrea J. Liu, and Sidney R. Nagel. Jamming in finite systems: Stability, anisotropy, fluctuations, and scaling. *Phys. Rev. E*, 90:022138, Aug 2014.

[122] Jorge Kurchan. personal communication.

[123] James P. Sethna. Scaling functions in disordered elastic materials, 2022. Lecture notes from the School on Disordered Elastic Systems at ICTP-SAIFR.

[124] M Lisa Manning and Andrea J Liu. A random matrix definition of the boson peak. *EPL (Europhysics Letters)*, 109(3):36002, 2015.

[125] Matthieu Wyart. Marginal stability constrains force and pair distributions at random close packing. *Physical review letters*, 109 12:125502, 2012.

[126] Edan Lerner, Gustavo During, and Matthieu Wyart. Low-energy non-linear excitations in sphere packings. *Soft Matter*, 9:8252–8263, 2013.

[127] Combe and Roux. Strain versus stress in a model granular material: A devil's staircase. *Physical review letters*, 85 17:3628–31, 2000.

[128] Yuliang Jin and Hajime Yoshino. A jamming plane of sphere packings. *Proceedings of the National Academy of Sciences*, 118, 2021.

[129] ME Cates, JP Wittmer, J-P Bouchaud, and Ph Claudin. Jamming, force chains, and fragile matter. *Physical review letters*, 81(9):1841, 1998.

[130] Corey S O'Hern, Stephen A Langer, Andrea J Liu, and Sidney R Nagel. Force distributions near jamming and glass transitions. *Physical review letters*, 86(1):111, 2001.

[131] Philip W. Anderson. Lecture notes of the Les Houches summer school, 1978.

[132] Florian Vogel, Philipp Baumgärtel, and Matthias Fuchs. Self-consistent current response theory of unjamming and vibrational modes in low-temperature amorphous solids. *Phys. Rev. X*, 15:011030, Feb 2025.

[133] Manuel Maier, Annette Zippelius, and Matthias Fuchs. Stress auto-correlation tensor in glass-forming isothermal fluids: From viscous to elastic response. *The Journal of Chemical Physics*, 149(8):084502, 2018.

[134] Annette Zippelius, Matthias Fuchs, Alberto Rosso, James P. Sethna, and Matthieu Wyart. *Emergent Dynamics in Glasses and Disordered Systems: Correlations and Avalanches*, chapter Chapter 15, pages 277–305. World Scientific Publishing, 2023.

[135] Jishnu N. Nampoothiri, Yinqiao Wang, Kabir Ramola, Jie Zhang, Subhro Bhattacharjee, and Bulbul Chakraborty. Emergent elasticity in amorphous solids. *Phys. Rev. Lett.*, 125:118002, Sep 2020.

[136] O. K. Damavandi, M. L. Manning, and J. M. Schwarz. Effective medium theory of random regular networks. *Europhysics Letters*, 138, May 2022.

[137] Y. Kakehashi. Many-body coherent potential approximation, dynamical coherent potential approximation, and dynamical mean-field theory. *Phys. Rev. B*, 66:104428, Sep 2002.

[138] Geert Kapteijns, Eran Bouchbinder, and Edan Lerner. Universal nonphononic density of states in 2d, 3d, and 4d glasses. *Phys. Rev. Lett.*, 121:055501, Aug 2018.

[139] R. M. Corless, G. H. Gonnet, D. E. G. Hare, D. J. Jeffrey, and D. E. Knuth. On the LambertW function. *Advances in Computational Mathematics*, 5(1):329–359, December 1996.

[140] Hideyuki Mizuno and Atsushi Ikeda. Phonon transport and vibrational excitations in amorphous solids. *Phys. Rev. E*, 98:062612, Dec 2018.

[141] Izrail Solomonovich Gradshteyn, I M Ryzhik, Daniel Zwillinger, and Victor Moll. *Table of integrals, series, and products; 8th ed.* Academic Press, Amsterdam, 2015.

[142] Carl P. Goodrich, Simon Dagois-Bohy, Brian P. Tighe, Martin van Hecke, Andrea J. Liu, and Sidney R. Nagel. Jamming in finite systems: Stability, anisotropy, fluctuations, and scaling. *Phys. Rev. E*, 90:022138, Aug 2014.

[143] Carl Goodrich. personal communication.

[144] Jorge V. José, Leo P. Kadanoff, Scott Kirkpatrick, and David R. Nelson. Renormalization, vortices, and symmetry-breaking perturbations in the two-dimensional planar model. *Phys. Rev. B*, 16:1217–1241, Aug 1977.

[145] Q. M. Zhang and J. Z. Larese. Melting of monolayer argon adsorbed on a graphite substrate. *Phys. Rev. B*, 43:938–946, Jan 1991.

[146] C. P. Broedersz and F. C. MacKintosh. Modeling semiflexible polymer networks. *Rev. Mod. Phys.*, 86:995–1036, Jul 2014.

[147] Silke Henkes and Bulbul Chakraborty. Statistical mechanics framework for static granular matter. *Phys. Rev. E*, 79:061301, Jun 2009.

[148] Yuxiao Zhang, M. J. Godfrey, and M. A. Moore. Marginally jammed states of hard disks in a one-dimensional channel. *Phys. Rev. E*, 102:042614, Oct 2020.

[149] Pierre Hohenberg. personal communication.

[150] P. C. Hohenberg and B. I. Halperin. Theory of dynamic critical phenomena. *Rev. Mod. Phys.*, 49:435–479, Jul 1977.

[151] Maria Chiara Angelini, Giorgio Parisi, and Federico Ricci-Tersenghi. Relations between short-range and long-range ising models. *Phys. Rev. E*, 89:062120, Jun 2014.

[152] G. Gori, M. Michelangeli, N. Defenu, and A. Trombettoni. One-dimensional long-range percolation: A numerical study. *Phys. Rev. E*, 96:012108, Jul 2017.

[153] G. Kotliar, P. W. Anderson, and D. L. Stein. One-dimensional spin-glass model with long-range random interactions. *Phys. Rev. B*, 27:602–605, Jan 1983.

[154] Hugo Perrin, Matthieu Wyart, Bloen Metzger, and Yoël Forterre. Nonlocal effects reflect the jamming criticality in frictionless granular flows down inclines. *Phys. Rev. Lett.*, 126:228002, Jun 2021.

[155] Sijie Tong, Rastko Sknepnek, and Andrej Kovsmrlj. Linear viscoelastic response of the vertex model with internal and external dissipation: Normal modes analysis. *Phys. Rev. Res.*, 5:013143, Feb 2023.

[156] Stavros Thomopoulos, Juan P. Marquez, Bradley Weinberger, Victor Birman, and Guy M. Genin. Collagen fiber orientation at the tendon to bone insertion and its influence on stress concentrations. *Journal of Biomechanics*, 39(10):1842–1851, 2006.

[157] Jesse L Silverberg, Aliyah R Barrett, Moumita Das, Poul B Petersen, Lawrence J Bonassar, and Itai Cohen. Structure-function relations and rigidity percolation in the shear properties of articular cartilage. *Biophysical journal*, 107(7):1721–1730, 2014.

[158] Moumita Das, D. A. Quint, and J. M. Schwarz. Redundancy and cooperativity in the mechanics of compositely crosslinked filamentous networks. *PLOS ONE*, 7(5):1–11, 05 2012.

[159] D. J. Jacobs and M. F. Thorpe. Generic rigidity percolation in two dimensions. *Phys. Rev. E*, 53:3682–3693, Apr 1996.

[160] Shechao Feng and Pabitra N. Sen. Percolation on elastic networks: New exponent and threshold. *Phys. Rev. Lett.*, 52:216–219, Jan 1984.

[161] J.D. Currey, K. Brear, and P. Zioupos. Dependence of mechanical properties on fibre angle in narwhal tusk, a highly oriented biological composite. *Journal of Biomechanics*, 27(7):885–897, 1994.

[162] S. Weiner and H. D. Wagner. The material bone: Structure-mechanical function relations. *Annual Review of Materials Research*, 28:271–298, August 1998.

[163] B.K. Hoffmeister, S.M. Handley, S.A. Wickline, and J.G. Miller. Ultrasonic determination of the anisotropy of young's modulus of fixed tendon and fixed myocardium. *Journal of the Acoustical Society of America*, 100 6:3933–40, 1996.

[164] A.A. de Aro, B. de Campos Vidal, and E.R. Pimentel. Biochemical and anisotropical properties of tendons. *Micron*, 43(2):205–214, 2012.

[165] Jonathan Michel, Gabriel von Kessel, Thomas Wyse Jackson, Lawrence J. Bonassar, Itai Cohen, and Moumita Das. Reentrant rigidity percolation in structurally correlated filamentous networks. *Phys. Rev. Res.*, 4:043152, Nov 2022.

[166] A. Sharma, A. J. Licup, K. A. Jansen, R. Rens, M. Sheinman, G. H. Koenderink, and F. C. MacKintosh. Strain-controlled criticality governs the nonlinear mechanics of fibre networks. *Nature Physics*, 12(6):584–587, June 2016.

[167] Yanqing Chen, Timothy A. Davis, William W. Hager, and Sivasankaran Rajamanickam. Algorithm 887: Cholmod, supernodal sparse cholesky factorization and update/downdate. *ACM Trans. Math. Softw.*, 35(3):22, Oct 2008.

[168] Jorge Nocedal and Stephen J. Wright. *Numerical Optimization*, chapter 5, pages 101–134. Springer, 2e edition, 2006.

[169] Ojan Khatib Damavandi, Varda F. Hagh, Christian D. Santangelo, and M. Lisa Manning. Energetic rigidity. ii. applications in examples of biological and underconstrained materials. *Phys. Rev. E*, 105:025004, Feb 2022.

[170] Aleksandar Donev, Robert Connelly, Frank H. Stillinger, and Salvatore Torquato. Underconstrained jammed packings of nonspherical hard particles: Ellipses and ellipsoids. *Phys. Rev. E*, 75:051304, May 2007.

[171] J. Wang, Z. Zhou, Q. Liu, T.M. Garoni, and Y. Deng. High-precision monte carlo study of directed percolation in $(d + 1)$ dimensions. *Physical Review E*, 88:042102, Oct 2013.

[172] Iwan Jensen. Low-density series expansions for directed percolation: I. a new efficient algorithm with applications to the square lattice. *Journal of Physics A: Mathematical and General*, 32(28):5233–5249, January 1999.

[173] A Hansen and S Roux. Application of 'logical transport' to determine the directed and isotropic percolation thresholds. *Journal of Physics A: Mathematical and General*, 20(13):L873, sep 1987.

[174] N. Dupuis, L. Canet, A. Eichhorn, W. Metzner, J.M. Pawlowski, M. Tissier, and N. Wschebor. The nonperturbative functional renormalization group and its applications. *Physics Reports*, 910:1–114, 2021. The nonperturbative functional renormalization group and its applications.

[175] Daniel F. Litim. Optimized renormalization group flows. *Phys. Rev. D*, 64:105007, Oct 2001.

[176] S Seide and Christof Wetterich. Equation of state near the endpoint of the critical line. *Nuclear Physics B*, 562(3):524–546, 1999.

[177] M. A. Stephanov. QCD phase diagram and the critical point. *International Journal of Modern Physics A*, 20(19):4387–4392, 2005.

[178] S. Borsányi, Z. Fodor, J. N. Guenther, R. Kara, S. D. Katz, P. Parotto, A. Pásztor, C. Ratti, and K. K. Szabó. Lattice QCD equation of state at finite chemical potential from an alternative expansion scheme. *Phys. Rev. Lett.*, 126:232001, Jun 2021.

[179] *Equilibrium Solutions, Stability, and Linearized Stability*, pages 5–19. Springer New York, New York, NY, 2003.

[180] N. D. Mermin. The topological theory of defects in ordered media. *Rev. Mod. Phys.*, 51:591–648, Jul 1979.

[181] T. C. Lubensky and Leo Radzihovsky. Theory of bent-core liquid-crystal phases and phase transitions. *Phys. Rev. E*, 66:031704, Sep 2002.

[182] Teruki Niori, Tomoko Sekine, Junji Watanabe, Tomoo Furukawa, and Hideo Takezoe. Distinct ferroelectric smectic liquid crystals consisting of achiral molecules with banana shape. *Molecular Crystals and Liquid Crystals Science and Technology. Section A. Molecular Crystals and Liquid Crystals*, 301(1):337–342, 1997.

[183] Noel A. Clark and Sven T. Lagerwall. Submicrosecond bistable electro-optic switching in liquid crystals. *Applied Physics Letters*, 36(11):899, June 1980.

[184] Darren R. Link, Giorgio Natale, Renfan Shao, Joseph E. Maclennan, Noel A. Clark, Eva Körblova, and David M. Walba. Spontaneous formation of macroscopic chiral domains in a fluid smectic phase of achiral molecules. *Science*, 278(5345):1924–1927, 1997.

[185] Dong Chen, Jan H. Porada, Justin B. Hooper, Arthur Klittnick, Yongqiang Shen, Michael R. Tuchband, Eva Korblova, Dmitry Bedrov, David M. Walba, Matthew A. Glaser, Joseph E. Maclennan, and Noel A. Clark. Chiral heliconical ground state of nanoscale pitch in a nematic liquid crystal of achiral molecular dimers. *Proceedings of the National Academy of Sciences*, 110(40):15931–15936, 2013.

[186] Dipak Patra and Arun Roy. Spontaneous breaking of chiral symmetry in achiral bent-core liquid crystals: Excluded volume effect. *Phys. Rev. E*, 107:034704, Mar 2023.

[187] Miklos Solymosi, Robert J. Low, Martin Grayson, Maureen P. Neal, Mark R. Wilson, and David J. Earl. Scaled chiral indices for ferroelectric liquid crystals. *Ferroelectrics*, 277(1):169–176, 2002.

[188] Philip J. Camp, Michael P. Allen, and Andrew J. Masters. Theory and computer simulation of bent-core molecules. *The Journal of Chemical Physics*, 111(21):9871–9881, December 1999. _eprint: https://pubs.aip.org/aip/jcp/article-pdf/111/21/9871/19166607/9871_1_online.pdf.

[189] Jeffrey Billeter, Alexander Smondyrev, George Loriot, and Robert Pelcovits. Phase-ordering dynamics of the gay-berne nematic liquid crystal. *Physical review. E, Statistical physics, plasmas, fluids, and related interdisciplinary topics*, 60:6831–40, 01 2000.

[190] R. Memmer, H.-G. Kuball, and A. Schönhofer. Computer simulation of chiral liquid crystal phases ii. the use of twisted boundary conditions. *Berichte der Bunsengesellschaft für physikalische Chemie*, 97(10):1193–1198, 1993.

[191] Yves Lansac, Prabal K. Maiti, Noel A. Clark, and Matthew A. Glaser. Phase behavior of bent-core molecules. *Phys. Rev. E*, 67:011703, Jan 2003.

[192] Dozov, I. On the spontaneous symmetry breaking in the mesophases of achiral banana-shaped molecules. *Europhys. Lett.*, 56(2):247–253, 2001.

[193] Chenhui Zhu, Michael R. Tuchband, Anthony Young, Min Shuai, Alyssa Scarbrough, David M. Walba, Joseph E. Maclennan, Cheng Wang, Alexander Hexemer, and Noel A. Clark. Resonant carbon *k*-edge soft x-ray scattering from lattice-free heliconical molecular ordering: Soft dilative elasticity of the twist-bend liquid crystal phase. *Phys. Rev. Lett.*, 116:147803, Apr 2016.

[194] Dong Chen, Michi Nakata, Renfan Shao, Michael R. Tuchband, Min Shuai, Ute Baumeister, Wolfgang Weissflog, David M. Walba, Matthew A. Glaser, Joseph E. Maclennan, and Noel A. Clark. Twist-bend heliconical chiral nematic liquid crystal phase of an achiral rigid bent-core mesogen. *Phys. Rev. E*, 89:022506, Feb 2014.

[195] V. Borshch, Y.-K. Kim, J. Xiang, M. Gao, A. Jákli, V. P. Panov, J. K. Vij, C. T. Imrie, M. G. Tamba, G. H. Mehl, and O. D. Lavrentovich. Nematic twist-bend phase with nanoscale modulation of molecular orientation. *Nature Communications*, 4(1):2635, November 2013.

[196] Vitaly P. Panov, Jang-Kun Song, Georg H. Mehl, and Jagdish K. Vij. The beauty of twist-bend nematic phase: Fast switching domains, first order fréedericksz transition and a hierarchy of structures. *Crystals*, 11(6), 2021.

[197] Z. Parsouzi, S. M. Shamid, V. Borshch, P. K. Challa, A. R. Baldwin, M. G. Tamba, C. Welch, G. H. Mehl, J. T. Gleeson, A. Jakli, O. D. Lavrentovich, D. W. Allender, J. V. Selinger, and S. Sprunt. Fluctuation modes of a twist-bend nematic liquid crystal. *Phys. Rev. X*, 6:021041, Jun 2016.

[198] L Radzihovsky and T. C Lubensky. Fluctuation-driven 1st-order isotropic-to-tetrahedratic phase transition. *Europhysics Letters (EPL)*, 54(2):206–212, apr 2001.

[199] Mario Liu. Hydrodynamic theory of biaxial nematics. *Phys. Rev. A*, 24:2720–2726, Nov 1981.

[200] Darren R. Link, Giorgio Natale, Renfan Shao, Joseph E. Maclennan, Noel A. Clark, Eva Körblova, and David M. Walba. Spontaneous formation of macroscopic chiral domains in a fluid smectic phase of achiral molecules. *Science*, 278(5345):1924–1927, 1997.

[201] Matthieu Wyart. On the rigidity of amorphous solids. *Ann Phys-Paris*, 30, 12 2005.

[202] Dapeng Bi, J. H. Lopez, J. M. Schwarz, and M. Lisa Manning. A density-independent rigidity transition in biological tissues. *Nature Physics*, 11(12):1074–1079, December 2015.

[203] Katia Bertoldi, Vincenzo Vitelli, Johan Christensen, and Martin van Hecke. Flexible mechanical metamaterials. *Nature Reviews Materials*, 2(11):17066, October 2017.

[204] Xiaoming Mao and Tom C. Lubensky. Maxwell lattices and topological mechanics. *Annual Review of Condensed Matter Physics*, 9(Volume 9, 2018):413–433, 2018.

[205] Michel Fruchart, Yujie Zhou, and Vincenzo Vitelli. Dualities and non-Abelian mechanics. *Nature*, 577(7792):636–640, January 2020.

[206] Carl P. Goodrich, Andrea J. Liu, and Sidney R. Nagel. The principle of independent bond-level response: Tuning by pruning to exploit disorder for global behavior. *Phys. Rev. Lett.*, 114:225501, Jun 2015.

[207] Jason W. Rocks, Nidhi Pashine, Irmgard Bischofberger, Carl P. Goodrich, Andrea J. Liu, and Sidney R. Nagel. Designing allostery-inspired response in mechanical networks. *Proceedings of the National Academy of Sciences*, 114(10):2520–2525, 2017.

[208] Siheng Chen and L. Mahadevan. Rigidity percolation and geometric information in floppy origami. *Proceedings of the National Academy of Sciences*, 116(17):8119–8124, 2019.

[209] D. R. Bland. *The Theory of Linear Viscoelasticity*. Dover Publications, 2016.

[210] R. Kubo, M. Toda, and N. Hashitsume. *Statistical Physics II*. Springer Berlin, 2012.

[211] T. G. Mason, J. Bibette, and D. A. Weitz. Elasticity of compressed emulsions. *Phys. Rev. Lett.*, 75:2051–2054, Sep 1995.

[212] A. Saint-Jalmes and D. J. Durian. Vanishing elasticity for wet foams: Equivalence with emulsions and role of polydispersity. *Journal of Rheology*, 43(6):1411–1422, November 1999. _eprint: https://pubs.aip.org/sor/jor/article-pdf/43/6/1411/12276122/1411_1_online.pdf.

[213] Zexin Zhang, Ning Xu, Daniel T. N. Chen, Peter Yunker, Ahmed M. Alsayed, Kevin B. Aptowicz, Piotr Habdas, Andrea J. Liu, Sidney R. Nagel, and Arjun G. Yodh. Thermal vestige of the zero-temperature jamming transition. *Nature*, 459(7244):230–233, May 2009.

[214] T. S. Majmudar, M. Sperl, S. Luding, and R. P. Behringer. Jamming transition in granular systems. *Phys. Rev. Lett.*, 98:058001, Jan 2007.

[215] A. R. Abate and D. J. Durian. Approach to jamming in an air-fluidized granular bed. *Phys. Rev. E*, 74:031308, Sep 2006.

[216] Aaron S. Keys, Adam R. Abate, Sharon C. Glotzer, and Douglas J. Durian. Measurement of growing dynamical length scales and prediction of the jamming transition in a granular material. *Nature Physics*, 3(4):260–264, April 2007.

[217] E. DeGiuli, E. Lerner, and M. Wyart. Theory of the jamming transition at finite temperature. *The Journal of Chemical Physics*, 142(16):164503, April 2015. _eprint: https://pubs.aip.org/aip/jcp/article-pdf/doi/10.1063/1.4918737/14823082/164503_1_online.pdf.

[218] Xiaoming Mao, Anton Souslov, Carlos I. Mendoza, and T. C. Lubensky. Mechanical instability at finite temperature. *Nature Communications*, 6(1):5968, January 2015.

[219] Mehdi Bouzid, Bavand Keshavarz, Michela Geri, Thibaut Divoux, Emanuela Del Gado, and Gareth H. McKinley. Computing the linear viscoelastic properties of soft gels using an optimally windowed chirp protocol. *Journal of Rheology*, 62(4):1037–1050, 2018.

[220] Jader Colombo and Emanuela Del Gado. Stress localization, stiffening, and yielding in a model colloidal gel. *Journal of Rheology*, 58(5):1089–1116, 2014.

[221] Robert V. Kohn and Graeme W. Milton. On bounding the effective conductivity of anisotropic composites. In J. L. Ericksen, David Kinderlehrer, Robert Kohn, and J.-L. Lions, editors, *Homogenization and Effective Moduli of Materials and Media*, pages 97–125, New York, NY, 1986. Springer New York.

[222] Wim van Saarloos, Vincenzo Vitelli, and Zorana Zeravcic. *Soft Matter. Concepts, Phenomena, and Applications*. Princeton University Press, Princeton and Oxford, 2023.

[223] Matthew Newville, Till Stensitzki, Daniel B. Allen, and Antonino Ingargiola. LMFIT: Non-Linear Least-Square Minimization and Curve-Fitting for Python, Oct 2015.